## Structural Characterization of Polymer-Based Flocculation of Humic Acid as a Tool for Optimizing Water Treatment

vorgelegt von

**Mingyu Yuan, M.Sc.** ORCID: 0009-0003-1911-6863

an der Fakultät II – Mathematik und Naturwissenschaften der Technischen Universität Berlin zur Erlangung des akademischen Grades

Doktorin der Naturwissenschaften - Dr. rer. nat. -

genehmigte Dissertation

#### Promotionsausschuss:

Vorsitzender: Prof. Dr. Peter Strasser (TU Berlin)

Gutachter: Prof. Dr. Michael Gradzielski (TU Berlin)

Gutachter: Prof. Dr. Matthias Karg (Universität Düsseldorf)

Tag der wissenschaftlichen Aussprache: 12. Dezember 2024

Berlin 2025

#### **Abstract**

The complexation/flocculation induced by cationic polyelectrolytes (cPE) is regarded as an effective method in conventional water treatment process for addressing negatively charged humic acid (HA), which exists ubiquitously in aquatic environments as a degradation product of plants and negatively affects the quality of drinking water.

The interaction between oppositely charged HA and cPE can be regarded as the formation of interpolyelectrolyte complexes (IPEC), where HA serves as the polyanion with high rigidity and polydispersity. IPEC of cationic polydiallyldimethylammonium chloride (PDADMAC) and HA was first studied with a focus on the Ca<sup>2+</sup> effects. This was accomplished by determining the phase behavior and characterizing the structures in solution through the use of light scattering and small-angle neutron scattering (SANS). This allowed for the probing of the formation of aggregates with a radius of 120–150 nm and a compaction in the size range of 10–50 nm within these aggregates with the addition of Ca<sup>2+</sup>. The presence of Ca<sup>2+</sup> was found to exert a considerable influence on both the macroscopic phase behavior and the mesoscopic complex structure.

Chitosan, a natural polymer derived from waste materials, has been identified as a promising candidate for altering synthetic cationic polyelectrolyte (cPEs) to develop an environmentally friendly flocculant. A library of different modified cationic (quaternized) chitosans (QCSs) with permanent charges was synthesized by the substitution of glycidyl trimethylammonium chloride (GTMAC). A comparison of the HA removal efficiency of QCS and the commercial synthetic PDADMAC revealed that with QCS the precipitation of HA was enhanced and occurred at a lower charge mixing ratio due to the intrinsic hydrophobic domain of QCS. By tailoring the degree of quaternization of QCS, a shift in the phase diagram was observed, which correlated with the aggregate structure.

Moreover, the kinetic process was obtained specifically for the initial stage, during which the HA complexes are immediately formed upon mixing. This process may ultimately determine the final flocculation performance and the removal efficiency of HA in water treatment. Time-resolved small-angle X-ray scattering (TR-SAXS) combined with stopped-flow was employed to probe the early-stage complex formation over a timescale of milliseconds. This approach facilitated the elucidation of the rate and efficacy with which HA can interact with diverse cationic polyelectrolytes, including quaternized chitosan with varying degrees of charged groups and PDADMAC, which is 100% charged. By systematically varying the type of cationic polyelectrolyte, the charge ratio between cPEs and humic acid, and additionally by adjusting the pH value, comprehensive insight into the initial formation process and factors controlling the final structures was obtained. This insight from colloid science is promising to optimize the water treatment process in industrial settings.

#### Zusammenfassung

Die durch kationische Polyelektrolyte (cPE) induzierte Komplexierung/Flockung gilt als wirksame Methode in konventionellen Wasseraufbereitungsverfahren zur Behandlung negativ geladener Huminsäure (HA), die als Abbauprodukt von Pflanzen in Gewässern allgegenwärtig ist und die Qualität des Trinkwassers beeinträchtigt.

Die Wechselwirkung zwischen gegensätzlich geladenen HA und cPE kann als Bildung von Interpolyelektrolytkomplexen (IPEC) betrachtet werden, wobei HA als Polyanion mit hoher Steifigkeit und Polydispersität dient. **IPEC** von kationischem Polydiallyldimethylammoniumchlorid (PDADMAC) und HA wurde zunächst mit Schwerpunkt auf die Ca<sup>2+</sup>-Effekte untersucht. Dazu wurde das Phasenverhalten bestimmt und die Strukturen in Lösung mit Hilfe von Lichtstreuung und Kleinwinkel-Neutronenstreuung (SANS) charakterisiert. Dies ermöglichte die Untersuchung der Bildung von Aggregaten mit einem Radius von 120-150 nm und einer Verdichtung im Größenbereich von 10-50 nm innerhalb dieser Aggregate bei Zugabe von Ca<sup>2+</sup>. Es wurde festgestellt, dass die Anwesenheit von Ca<sup>2+</sup> einen erheblichen Einfluss sowohl auf das makroskopische Phasenverhalten als auch auf die mesoskopische Komplexstruktur ausübt.

Chitosan, ein aus Abfallstoffen gewonnenes natürliches Polymer, wurde als vielversprechender Kandidat für die Veränderung synthetischer kationischer Polyelektrolyte (cPEs) zur Entwicklung eines umweltfreundlichen Flockungsmittels identifiziert. Eine Bibliothek verschiedener modifizierter kationischer (quaternisierter) Chitosane (QCS) mit permanenten Ladungen wurde durch die Substitution von Glycidyltrimethylammoniumchlorid (GTMAC) synthetisiert. Ein Vergleich der HA-Entfernungseffizienz von QCS und dem kommerziellen synthetischen PDADMAC ergab, dass die Ausfällung von HA mit QCS verbessert wurde und aufgrund der intrinsischen hydrophoben Domäne von QCS bei einem niedrigeren Ladungsmischungsverhältnis erfolgte. Durch Anpassung des Quaternisierungsgrads von QCS wurde eine Verschiebung des Phasendiagramms beobachtet, die mit der Aggregatstruktur korrelierte.

Darüber hinaus wurde der kinetische Prozess speziell für die Anfangsphase ermittelt, in der die HA-Komplexe unmittelbar nach dem Mischen gebildet werden. Dieser Prozess kann letztendlich die endgültige Flockungsleistung und die Entfernungseffizienz von HA bei der Wasseraufbereitung bestimmen. Die zeitaufgelöste Röntgenkleinwinkelstreuung (TR-SAXS) in Kombination mit einer gestoppten Strömung wurde eingesetzt, um die Komplexbildung in der Anfangsphase über eine Zeitskala von Millisekunden zu untersuchen. Dieser Ansatz erleichterte die Aufklärung der Geschwindigkeit und Wirksamkeit, mit der HA mit verschiedenen kationischen Polyelektrolyten interagieren kann, darunter quaternisiertes Chitosan mit unterschiedlichem Anteil an geladenen Gruppen und PDADMAC, das zu 100 % geladen ist. Durch systematisches Variieren der Art des kationischen Polyelektrolyts, des Ladungsverhältnisses zwischen cPEs und Huminsäure und zusätzlich durch Einstellen des pH-Werts wurden umfassende Erkenntnisse über den anfänglichen Bildungsprozess und die Faktoren, die die endgültigen Strukturen steuern, gewonnen. Diese Erkenntnisse aus der Optimierung Kolloidwissenschaft sind vielversprechend für die des Wasseraufbereitungsprozesses in der Industrie.

#### Dedicated to the Yangtze River,

by whose banks I grew up,

for which I pursued the study about water treatment.

#### **Acknowledgements**

I would like to first extend my deepest gratitude to my supervisor, Prof. Dr. Michael Gradzielski, for his invaluable support throughout my research journey. I am truly grateful for his prompt and attentive responses, as well as his dedicated efforts toward my project. His resilient and optimistic attitude in addressing scientific challenges has profoundly impacted my personal and professional development.

I extend my heartfelt thanks to Prof. Dr. Matthias Karg for graciously accepting to serve as a referee for my dissertation. Additionally, I am grateful to Prof. Dr. Peter Strasser for his role in chairing my defense.

I want to acknowledge Dr. Heri Bustamante for his expertise in practical water industry, which has significantly broadened the scope of our project. I am deeply grateful for his continuous encouragement and his warm welcome during my research visit to Sydney.

I would like to thank the German Research Foundation (DFG) for funding the project. I am grateful to have received the Scholarship for Completing a Doctoral Degree from the Advisory Board for Women's Advancement and Gender Equality at TU Berlin, which has been instrumental in reinforcing the importance of diversity and gender equality in academia.

I extend sincere thanks to Stranski Laboratorium for the joy and exchange during my whole PhD journey. Special appreciation goes to Petra for her tireless assistance with all paperwork, even before I joined the group. My gratitude also goes to Jana, the first person I met in the group, for her thorough introductions to our instruments and for the warmth she provided, literally and figuratively, by offering me a coat during the wonderful BBQs she organized. Special thanks to Olga and Chris for all their mentor on my research, and to Matteo for introducing me to Python for data analysis and contributing to my beamtime simultaneously. My academic journey would not have been possible without the constant emotional and financial support from my parents. Their encouragement and faith in me have been my foundation and inspiration. Special thanks to Yuxin, whose unwavering support has encouraged me to explore my potential without constraints. His presence, even from afar, has been like the theta solvent for a polymer chain that allowing me to neither expand nor contract while taking a lifelong random walk. My final thanks to Maomao (Catcat in Chinese), a little soft delicate ball of fur who is so smart and brave with an extraordinary inner world. Thank you for being my cherished family member over the past four years and I look forward to many more years together.

### **List of Contents**

Abstı	act	I
Zusaı	mmenfassung	. III
Ackn	owledgements	VII
List o	of Contents	. IX
1.	Introduction	1
1.1.	Water treatment for Humic acid removal	1
1.2.	Polyelectrolytes for water treatment	3
1.3.	IPEC formation in water treatment	5
1.4.	Motivation	7
2.	Methods	9
2.1.	Light Scattering.	9
2.2.	Small-angle Neutron Scattering.	. 10
2.3.	Small-angle X-ray Scattering	. 11
2.4.	Ultraviolet-visible Spectroscopy	. 13
2.5.	Laser light diffraction	. 13
2.6.	Zeta-Potential	. 14
2.7.	Fluorescence	. 15
2.8.	Jar test	. 15
3.	The Effect of Ca <sup>2+</sup> on the Interaction Between Humic Acid and poly	
(diall	yldimethylammonium chloride) (PDADMAC)	. 17
3.1.	Introduction	. 18
3.2.	Sample Preparation	. 22
3 3	Results and Disscussion	23

3.3.1. Phase I	Diagram	23
3.3.2. <i>ζ</i> -Poten	ntial	26
3.3.3. Remova	ral efficiency of humic acid	28
3.3.4. Static a:	and Dynamic Light Scattering (SLS, DLS)	31
3.3.5. Small-A	Angle Neutron Scattering (SANS)	35
3.3.6. Settling	g rate of humic acid precipitate	44
3.4. Conclusion		46
4. From Waste	e Treatment to Water Treatment: Application of Quaternised Ch	itosan in
Enhancing NOM	Flocculation	49
4.1. Introduction	n	49
4.2. Sample Prep	paration	52
4.3. Results and	Disscussion	54
4.3.1. Phase D	Diagram	54
4.3.2. Stability	ry of HA complexes	58
4.3.3. Remova	ral efficiency of HA	59
4.3.4. Fluores	scence Probe Studies	61
4.3.5. Floccul	lation of HA complexes via light diffraction	64
4.3.6 A Case	study from water filtration plant, Australia	68
4.4. Conclusion		74
5. In Situ Inve	estigation of Humic Acid - Quaternised Chitosan Complexation	via Time-
Resolved Small-ar	ingle X-ray Scattering	76
5.1. Introduction	n	76
5.2 Sample Pres	naration	80

5.3. Results a	and Disscussion	81
5.3.1. Influ	nence of the pH value	81
5.3.2. Influ	nence of the charge ratio	86
5.3.3. Influ	nence of the degree of the quaternization	92
5.4. Conclusi	on	97
6. Conclusi	ons & Outlook	101
List of Figures		107
List of Tables.		119
Appendix A.	Chapter 3	121
Appendix B.	Chapter 4	139
Appendix C.	Chapter 5	155
List of Doform		171

#### 1. Introduction

#### 1.1. Water treatment for Humic acid removal

The history of water treatment can be dated back to the time of ancient Egypt, when the first time alum was used for accelerating the settlement of suspended particles in water, illustrating humanity's longstanding need to purify water for consumption and use. Humic acid, accounting for approximately 60% of natural organic matter (NOM) in water, is a significant component of natural water bodies. It is formed through the biological degradation of organic life substance and plays a crucial role in the environmental chemistry of water. Although humic acid is itself non-toxic, its presence in water treatment systems poses significant challenges, particularly during the chlorination process—an essential step in most water treatment protocols. Chlorination of water containing humic acid can lead to the formation of harmful disinfection byproducts (DBPs). Additionally, the organic matter associated with humic acid can serve as a nutrient source for bacteria, potentially inducing bacterial regrowth in the urban water distribution system. This regrowth can compromise water quality and safety, requiring increased maintenance and additional chlorination, which in turn can lead to further DBP formation.

Humic acid is a complex mixture of aromatic compounds with heterogeneous nature and molecular weight ranging from 400 Da to 300 kDa.<sup>6</sup> The molecular structure of humic acid, as suggested by F. J. Stevenson<sup>7</sup>, effectively integrates aromatic carbon frameworks with a variety of functional groups, most notably carboxylic and phenolic groups.

**Figure 1.1.** Stevenson's model for humic acid composition effectively integrates several key components, offering a comprehensive framework that highlights the complex and heterogeneous nature of humic substances. Taken from <sup>8</sup>

The phenolic and carboxylic groups of humic acid molecules lead to the negative charge of humic acid, which prompt its complexation with various ions, a property extensively utilized in water treatment processes. Traditionally, aluminum (Al) and iron (Fe) salts have been used as coagulants to form microflocs with humic acids. <sup>9, 10</sup> The process can be explained by the DLVO theory that was named after Boris Derjaguin, Lev Landau, Evert Verwey and Theodoor Overbeek. <sup>11</sup> DLVO theory is a foundational concept in understanding the stability of colloidal dispersions, which primarily considers two types of forces that influence colloidal stability: Van der Waals forces, which attract particles towards each other, and electrical double layer forces, which create repulsion between particles as their charged layers interact. With the addition of positively charged multi-valent metal ions to negatively charged HA molecules, the repulsion among the HA molecules is reduced by achieving charge neutralization by reducing, thus effectively destabilizes the colloidal system and initiate coagulation. With increased dosages of positively charged multi-valent metal ions, these HA molecules can become restabilized due to charge reversal, subsequently becoming entangled in a flocculent hydroxide precipitate, a process known as 'sweep flocculation'9.

Despite their long-standing use, the traditional metal ion coagulants come with several drawbacks. A significant concern is the requirement for large amounts of coagulants, which consequently produce substantial quantities of sludge.<sup>12</sup> This sludge generation poses severe disposal and environmental challenges. Moreover, tailoring FeCl<sub>3</sub> molecules to interact effectively with various types of humic substances is challenging, potentially limiting the effectiveness of humic acid removal from water systems. Also, the 'sweep flocculation' process may not always be sufficient for practical applications that only small portion of natural organic matter (NOM) can be removed using this method, requiring the additional methods to address the remaining soluble NOM not captured by inorganic coagulants.<sup>13</sup>

#### 1.2. Polyelectrolytes for water treatment

The introduction of oppositely charged polymers, or polycations, helps aggregate coagulated particles and microflocs into larger flocculates that are more readily removed<sup>14</sup>. This combined approach, known as coagulation-flocculation, is highly favored in water purification for its effectiveness and low-cost.<sup>15-17</sup> Such type of polymer where a significant portion of the constitutional units are ionic or can become ionized is known as a polyelectrolyte<sup>18</sup>. Polyelectrolytes can be categorized into two main types based on the nature of their charged groups: polycations and polyanions. Polycations are polyelectrolytes that contain positively charged groups, whereas polyanions consist of negatively charged groups. Unlike uncharged polymers, the presence of ionic groups enables polyelectrolytes to interact strongly with water and other charged species, which can be utilized for humic acid removal in water treatment<sup>19</sup>. Charge density is a critical parameter for polyelectrolytes, which refers to the number of equivalents of charge per gram. This value is determined by the degree of charged groups and the molecular weight of the monomer unit within each polyelectrolyte.<sup>20</sup> High charge density can significantly enhance the solubility of a polyelectrolyte as well as its interaction with oppositely charged species, which are vital factors in the water treatment application.<sup>21</sup>

Understanding and controlling charge density allows for the optimication of polyelectrolytes to meet specific needs.

Many different cationic polymers have been employed and reviewed. 14, 22, 23 Copolymerization of dimethyl diallyl ammonium chloride and acryl amide was investigated to achieve a higher molecular weight<sup>24</sup>, as in general a high molecular weight has been found to be advantageous for flocculation. The reaction of epichlorohydrin and dimethylamine will form low molecular weight linear polymers, in which all the active sites are quaternary ammonium groups. <sup>25</sup> As for acrylamide, after random copolymerization with cationic ester acryloyloxyethyltrimethylammonium chloride, it can be widely applied in water treatment.<sup>26</sup> One of the conventional cationic polymers employed in modern water plants is poly(diallyldimethylammonium chloride) (PDADMAC). Developed over the past few decades, PDADMAC has become widely used due to its effectiveness for precipitating anionic natural organic matters (NOM).<sup>16</sup> Apart from above-mentioned synthetic polyelectrolytes, there are also several naturally occurring polymers such as cellulose or starch that exhibit inherent cationic properties or can be chemically modified to function as cationic polyelectrolytes. A very promising candidate is chitosan, as it is derived from chitin, a renewable resource abundantly available from the shell of seafood.<sup>27</sup> Because of protonation of the -NH<sub>2</sub> group on the C-2 position of the dglucosamine repeat unit, chitosan is soluble in aqueous acidic media. One disadvantage of chitosan that may hinder its application in water treatment is its insolubility at natural pH range, which can be overcome by chemical modification such as quaternization of chitosan or substitution of cationic groups. The modified chitosan can be converted from a pH-dependent to a permanent polyelectrolyte so that it is soluble in wider pH range with other advantages like antibacterial and nontoxic still remained.<sup>28-32</sup> These natural polyelectrolytes offer environmentally friendly alternatives to synthetic polymers, with additional benefits of biocompatibility and biodegradability.

#### 1.3. IPEC formation in water treatment

Interpolyelectrolyte complexes (IPECs) form when two polyelectrolytes of opposite charges are mixed together in solution, as recognized since the 1940s.<sup>33</sup> These complexes result from the electrostatic attraction between anionic and cationic polyelectrolytes, of which the formation occurs almost instantaneously, as first investigated by Stop-flow measurements that this process completes in less than 5 ms.<sup>34</sup> During this rapid interaction, any low molecular weight counterions that initially associated with the polymeric backbone are released, resulting in an increase in entropy for the entire system, which serves as the primary driving force for the complexation process.<sup>35</sup>

The formed structure of IPECs from two oppositely charged homopolyelectrolytes was proposed to consist of both ordered and disordered domains as shown in Figure. The ordered regions feature "ladder-like" sequences where the chains of the polyelectrolytes are neatly aligned; the disordered areas, e.g. "scrambled egg" domains, exhibit a less organized arrangement where the chains are randomly intertwined.<sup>36</sup>

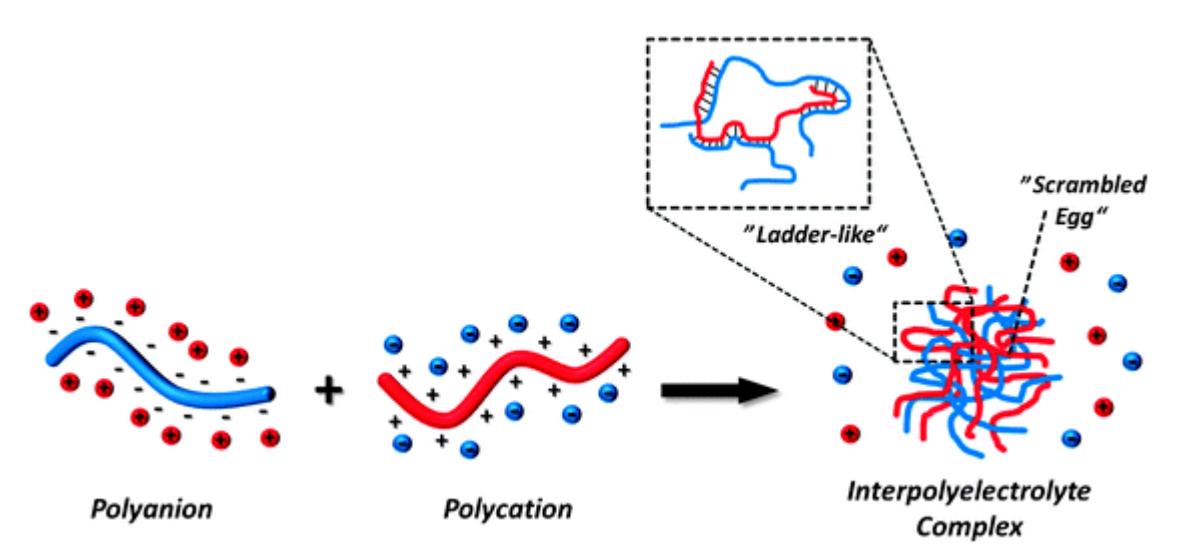


**Figure 1.2.** A schematic depiction of the formation of an interpolyelectrolyte complex (IPEC) between polycations and polyanions with the low molecular weight counterions that were previously balancing the charges of the polyelectrolytes are released into the solution. Taken from <sup>36</sup>.

From a colloidal point of view, the aggregation of humic acid (HA) in the presence of polycations can be described as IPEC formation of oppositely charged polyelectrolytes. In this process humic acid (HA) can be regarded as a polyanion rich in aromatic groups with high polydispersity<sup>8</sup>, e.g. exhibiting a wide range of molecular weights and sizes. At low dosage of polycations, the system can remain optically clear, involving the initial interactions and binding of the polycations to the negatively charged sites on HA molecules without the formation of visible particle. With further addition of polycations, significantly larger aggregates form so that facilitate flocculation, 'dangling' polymer segments of long-chain polymers adsorbed on particles can 'bridge' particles together and settle out of the solution.<sup>37,38</sup> Such phase separation is an indicator of reaching the charge neutralization point, where the stoichiometry between the positive and negative charges equates to one. It was also reported that when the bridging mechanism is too effective, achieving strong intermolecular connection, the intense flocculation happens way before reaching the charge neutralization point, as observed for the polycations induced bentonite flocculation<sup>39</sup> and Ca<sup>2+</sup> enhanced HA flocculation<sup>40</sup>.

The ratio can be precisely tuned during the preparation of interpolyelectrolyte complexes (IPECs) by adjusting the amount of each polyelectrolyte added. This adjustment is particularly effective for ideal linear polymers that have comparable chain lengths, allowing for predictable and controlled interactions<sup>41,42</sup>. However, for polyelectrolytes that are relatively ill-defined, for example HA molecules or modified chitosan with a broad distribution of molecular weights or structural irregularities, the neutralization point and the subsequent phase separation might shift.<sup>43</sup> This uncertainty introduces challenges in applying IPEC formation to achieve desired outcomes, particularly in applications such as water treatment where the efficiency of polyelectrolyte interactions is crucial.

#### 1.4. Motivation

The removal of negatively charged humic acid (HA) in conventional water treatment processes through flocculation and precipitation by cationic polyelectrolytes (cPEs) represents an effective method. However, the interactions between anionic HA and oppositely charged cPE involve a complex interplay of electrostatic forces and entropy, which are not yet fully understood in fundamental physico-chemical terms. This complexity arises because the process is not solely governed by the attraction between opposite charges but also by the configurational entropy changes related to polymer conformation and the counterion release during complexation. Understanding these interactions at a molecular level is crucial for optimizing the use of polyelectrolytes in water treatment, potentially leading to more efficient, targeted, and environmentally sustainable practices.

Based on the focus on investigating fundamental concepts of the interaction of humic acid with polymer-based flocculants, my doctoral research started from the most commonly employed cPE in water treatment polydiallyldimethylammonium chloride (PDADMAC), investigating its complexation with humic acid molecules in terms of fundamental mechanism of flocculation. To mimic the lime addition, i.e., addition of Ca<sup>2+</sup> ions in practical water treatment process, the role of Ca<sup>2+</sup> ions was specifically examined in determining the mesoscopic structure of formed complexes.

Apart from synthetic polymer-based flocculants in water treatment, the alternative flocculants were explored and developed by adopting polyelectrolytes derived from natural waste to manage HA removal, offering a more sustainable method for water treatment. By modifying chitosan that is obtained from waste exoskeleton of crustaceans (such as shrimp and crabs), its properties regarding water solubility, charge density as well as chain morphology were tailored to enhance complexation with humic acid molecules. From the perspective of colloidal chemistry, the motivation of this project is to gain a molecular-basis level understanding on

how the structure of the modified chitosan-based flocculants affect the interaction with HA, which is of great potential in the application of HA removal in water treatment.

Building on the development of a series of modified chitosan, the kinetics of its early-stage complex formation with humic acid in a timescale of ms was further probed, providing a comprehensive analysis of how the structural variations in cationic polyelectrolytes affects the overall complexation dynamics. This shall allow for rationalising the tendency for further flocculation and precipitation, the compactness of formed complexes, and the tendency to form long-term stably dispersed aggregates – all aspects of central importance for ultimately understanding the flocculation process.

Overall, the goal of this thesis is to bridge the gap between practical water treatment industrial and fundamental colloidal interactions research regarding HA flocculation, advancing the understanding of polymer-humic acid interactions and contributing to the field of environmental engineering from a theoretical standpoint. By elucidating these interactions and their kinetic profiles, the findings are expected to provide a foundation for the innovation and development of new polymer-based flocculant

#### 2. Methods

#### 2.1. Light Scattering

Static and Dynamic Light Scattering (SLS and DLS) were measured simultaneously using an ALV/CGS-3 instrument. The instrument is equipped with a He–Ne laser with a wavelength  $\lambda$  of 632.8 nm. Samples were measured inside a temperature-controlled toluene bath and measurements were done at 25 °C. Light scattering was recorded at several scattering angles  $\theta$ , ranging from 30° to 130° set by an ALV-SP goniometer. The data was analyzed with in-house software called SimplightQt. The intensity autocorrelation function  $g^{(2)}(\tau)$  was recorded via ALV 5000/E multiple  $\tau$  correlator from DLS measurements.

The SLS curves were recorded with the corresponding magnitude of the scattering vector q, with

$$q = \frac{4\pi n_0 \sin\left(\frac{\theta}{2}\right)}{\lambda} \tag{2.1}$$

where  $n_0$  is the refractive index of solution and  $\theta$  is the scattering angle.

The low-q region of the SLS curves, characteristic for the overall dimension of HA complexes, were analyzed with the Guinier approximation, in order to obtain the forward scattering intensity at zero angle  $I_0(q = 0)$  and the gyration radius  $R_g$ :

$$\lim_{\mathbf{q} \to 0} I = I_0 \exp\left(-\frac{q^2 R_g^2}{3}\right) \tag{2.2}$$

The DLS intensity autocorrelation functions  $g^{(2)}(\tau)$  were fitted with a stretched exponential function to determine the relaxation rate  $\Gamma$ :

$$g^{(2)}(\tau) - 1 = \beta \exp(-2(\Gamma \tau)^{\alpha})$$
 (2.3)

where  $\beta$  is the intercept of the correlation function (for this instrument it should ideally be 0.333),  $\alpha$  is the stretching exponent, and  $\Gamma$  is the relaxation rate.

From the slope of  $\Gamma$  versus  $q^2$ , a diffusion coefficient D can be calculated. With an assumption that the particles are spherical and non-interacting, the hydrodynamic radius  $R_h$  was derived from the Stokes–Einstein equation:

$$D = \frac{k_B T}{6\pi \eta R_h} \tag{2.4}$$

where  $k_B$  is the Boltzmann constant, T is the absolute temperature, and  $\eta$  is the solvent viscosity.

#### 2.2. Small-angle Neutron Scattering

Small angle neutron scattering (SANS) experiments were performed with the Sans2d time-of-flight SANS instrument at the ISIS Neutron and Muon Source (STFC, Rutherford Appleton Laboratory, UK). The experimental q-range covered was 0.0023-1 Å<sup>-1</sup> with two detectors at 4 and 8 m from the sample, respectively, and incident neutron wavelength ranging from 1.75 to 14.4 Å. Samples were measured in quartz cuvettes with an optical path length of 2 mm. A thermostatic sample changer was utilized for the experiment and measurements were done at 25 °C. Data reduction was performed with Mantid<sup>44</sup>, following the standard procedures for the instrument (detector efficiencies, measured sample transmissions, absolute scale using the scattering from a standard polymer, etc.)<sup>45</sup> and data analysis was performed with SasView Version 5.0.5, an open-source scattering analysis software.<sup>46</sup>

The SANS results were fitted by a shape-independent empirical two power law model, where the scattering intensity I(q) is given as:

$$I(q) = \begin{cases} Aq^{-p1} + background, & q \le q_c \\ Bq^{-p2} + background, & q > q_c \end{cases}$$
 (2.5)

where  $q_c$  is the location of the crossover from one slope to the other, A is a scaling coefficient that sets the overall intensity of the lower q power law region, p1 and p2 are the power law exponents at low q and high q, respectively. The scaling of the second power law region (coefficient B) is then automatically scaled to match the first by following formula:

$$B = \frac{Aq_c^{p2}}{q_c^{p1}} \tag{2.6}$$

During fitting A, q<sub>c</sub>, p1, and p2 were free parameters.

As a second model we also applied by a shape-independent Beaucage model<sup>47-49</sup>, which is generally very suited for describing structures with different levels or hierarchical organization and can reasonably approximate the scattering from many different types of particles, including fractal clusters, random coils, etc. The scattering intensity I(q) is given as:

$$I(q) = \sum_{i=1}^{N} \left[ G_i \exp\left(-\frac{q^2 R_{gi}^2}{3}\right) + B_i \exp\left(-\frac{q^2 R_{g(i+1)}^2}{3}\right) \left(\frac{1}{q_i^*}\right)^{P_i} \right]$$
 (2.7)

$$q_i^* = q \left[ erf\left(\frac{qR_{gi}}{\sqrt{6}}\right) \right]^{-3} \tag{2.8}$$

where  $G_i$  is the scaling pre-factor,  $B_i$  is the power law scattering pre-factor,  $R_g$  is the radius of gyration and  $P_i$  is the power law exponent. For pure humic acid solution under various ionic conditions a one-level Beaucage model (N = 1) was adopted; for the rest of sample sets where PDADMAC is involved, the two-level Beaucage model (N = 2) was utilized in which  $R_{g1}$  refers to radius of gyration at larger scale and  $R_{g2}$  refers to radius of gyration at smaller scale, i.e., local structure, respectively.

#### 2.3. Small-angle X-ray Scattering

Time-resolved small angle X-ray scattering were performed at both EMBL (Beamline P12, Hamburg, Germany) and ESRF (Beamline ID02, Grenoble, France) respectively.

At EMBL the Time-Resolved BioSAXS environment with Stopped-Flow Mixing (SFM-SAXS) mode was utilized by replacing conventional sample chamber to SFM-400 mixing device from Bio-Logic, as shown in **Figure 2.1**. Two sample-to-detector distances 2 and 3 m were utilized for trial experiments and it was for HA complexes with QCS2 and QCS3, a sample-to-detector distance of 3 meters was suitable, with an exposure time of 45 ms and an

exposure period of 500 ms, capturing 30 frames per mixing. Conversely, for the faster-reacting complexes where cPEs were QCS4 and PDADMAC, the sample-to-detector distance was reduced to 2 meters to enhance the temporal resolution. Here, the exposure time was shortened to 15 ms, with an exposure period of 20 ms, allowing for the collection of 100 frames mixing 2 s upon mixing. This adjustment in exposure times and periods was necessary due to the higher degree of charged groups in QCS4 and PDADMAC, which facilitated faster kinetics, necessitating increased time resolution to accurately capture the rapid complexation dynamics. At ESRF, a longer sample-to-detector distances of 10 m was utilized to probe the complexation process on a lower q range with similar stopped-flow rapid mixing device SFM-4000 from Biologic. Upon mixing, 40 frames were taken within 120s with an interval that varied in a geometrical progression. The total volume of each mixing was 252 µL at EMBL and 300 µL at ESRF, respectively. The procedure involved initially mixing the cationic polyelectrolyte solution with water, followed by rapid mixing with the 80 mg/L HA solution to achieve a final mixing ratio of 1:1. The flow rate for the mixing process was set at 6 mL/s to ensure effective complexation.

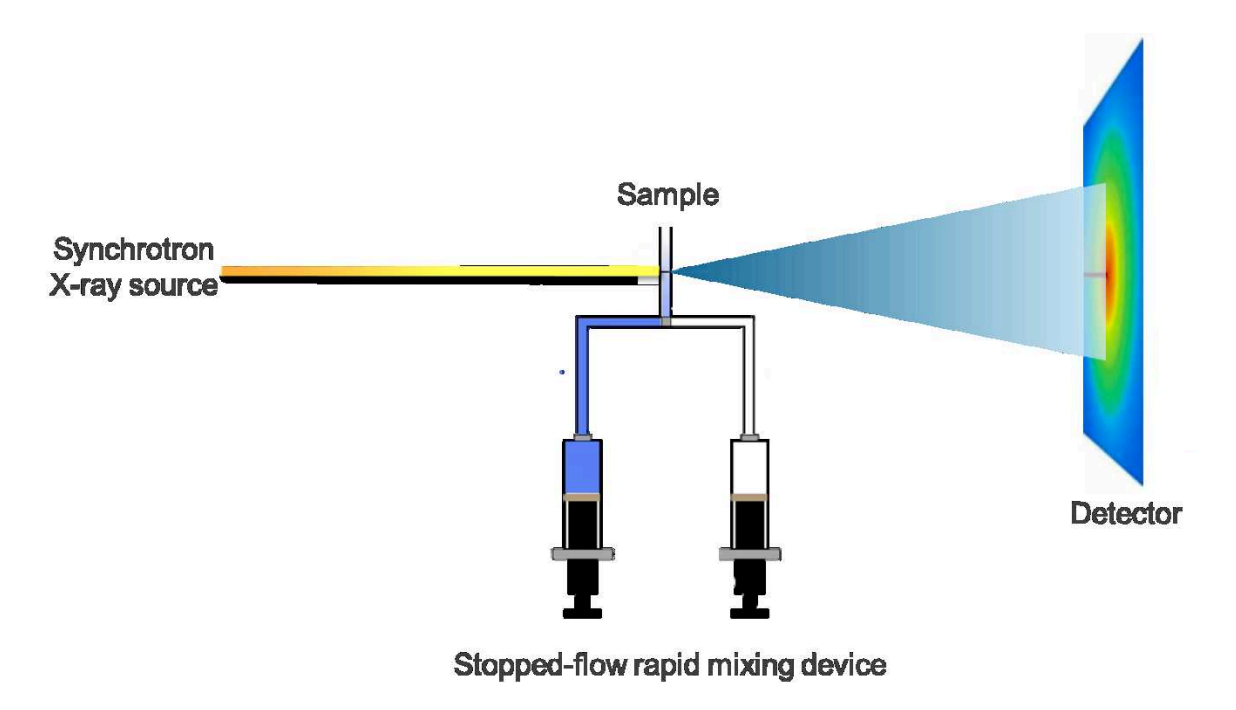


Figure 2.1. Setup for time-resolved SAXS combined with stopped-flow mixing.

The collected data was first converted to absolute scale, background subtracted as well as rebinned via custom python scripts to reduce noise and improve the statistical quality of the SAXS measurements. To calculate the scattering intensity in the absolute scale, the known scattering of water ( $I_{0,abs}$ (water) = 1.632.10<sup>-2</sup>cm<sup>-1</sup>, at 20°C), was used.<sup>50</sup> By dividing the relative intensity of the HA complexes with the experimental constant scattering of water and then multiplying by the absolute scattering of water one obtains the intensity of the HA complexes in absolute scale.<sup>51</sup>

#### 2.4. Ultraviolet-visible Spectroscopy

UV absorbance of HA solutions was measured using a Cary 50 UV-vis spectrometer with a 1 cm quartz cell. In particular, we took the absorbance observed at 254 nm (known as UV254) and for calibration measured HA solutions at pH 9 in the concentration regime of 0.1-10 mg/L. From the linear relationship between UV254 and the HA concentration (x in mg/L) the amount of HA in unknown solutions can be determined reliably and accordingly, the remaining HA can be quantitatively expressed as:

Remaining HA (%) = 
$$\left(\frac{C}{C_0}\right)$$
 \* 100% (2.9)

where C<sub>0</sub> is the original concentration of HA, typically 40 mg/L, and C is the concentration of HA remaining in the supernatant after precipitation, calculated from the UV-vis absorbance value at 254 nm.

#### 2.5. Laser light diffraction

Laser light diffraction is a widely recognized and highly efficient light scattering method used for particle size analysis across an extensive range, spanning from sub-micron to millimeter scales. It was utilized to monitor the development of HA complexes size during the flocculation process. A wet dispersing system CUVETTE was integrated with the laser diffraction sensor

HELOS (Sympatec) for dispersion, as shown in **Figure 2.2**. The measurement was conducted in the 50 ml cuvette with stirring rate 600 rpm to achieve adequate mixing. R5 lens with a measurable particle size range of 0.5/4.5-875 μm was selected to evaluate the particle size. A time-sliced measurement over 10 min with a resolution of 10 s was applied upon the mixing of humic acid solution and cPEs for time-resolved investigation on the flocculation process. The temperature was 25 °C and the time 0 was defined as 30 s after mixing.

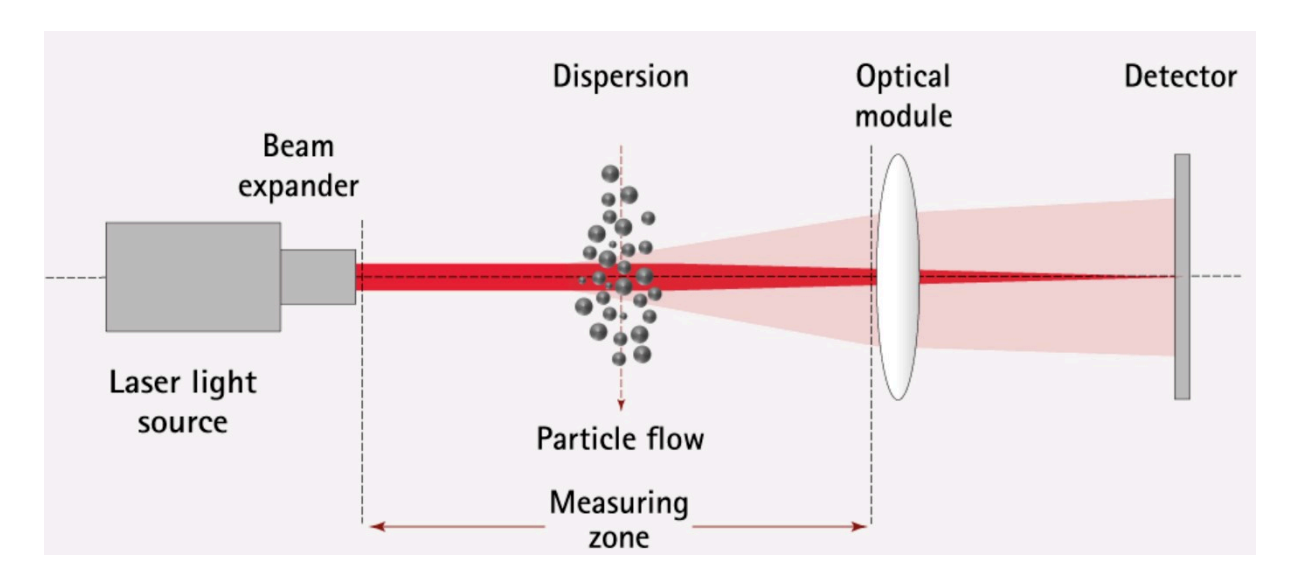


Figure 2.2. Laser light diffraction experimental setup. Taken from<sup>52</sup>

#### 2.6. Zeta-Potential

 $\zeta$ -potential measurements were performed using a Litesizer 500 (Anton Paar) at 298 K and a wavelength of 658 nm with a laser power of 40 mW.  $\zeta$ -potential was measured by electrophoretic light scattering (ELS), that measures the electrophoretic mobility  $U_E$  as

$$\zeta = \frac{3\eta \ U_E}{2\varepsilon f(\kappa\alpha)} \tag{2.10}$$

where  $\eta$  is dynamic viscosity,  $U_E$  is electrophoretic mobility,  $\epsilon$  is dielectric constant and  $f(\kappa\alpha)$  is the Debye factor, which was set to a value of 1.5 for particles suspended in aqueous solutions according to the Smoluchowski approximation.

#### 2.7. Fluorescence

Fluorescence measurements were carried out using a Hitachi F-4500 fluorescence spectrometer in emission scan mode. The excitation wavelength was established at 340 nm, and the emission spectra were recorded over a range from 355 to 650 nm at a scan rate of 240 nm/min. Both the excitation and emission slits were configured to 5 nm.

The samples for investigation were specifically prepared using an aqueous solution of Prodan, at a concentration of 1 µmol/L in D<sub>2</sub>O. To prepare this solution, a small amount of ethanol-based Prodan solution (1 mmol/L) was added to a vial, followed by the evaporation of the ethanol under controlled conditions. Subsequently, the required volume of filtered D<sub>2</sub>O was added to the residue to achieve the desired concentration. The use of Prodan, a solvatochromic compound, allows for the assessment of the polarity of the surrounding environment based on its fluorescence properties. This approach is particularly useful for studying the microenvironmental changes in biological and chemical system.

#### 2.8. Jar test

Jar test was conducted by mixing 500 ml of water sample from the plant in a series of 1L beakers. 1g/L PDADMAC solutions were then added to each beaker at different dosages that varied from 1 mg/L to 6 mg/L to determine the optimal dosage for water treatment. The raw water sample was stirred at 120 rpm for 60 seconds to ensure sample homogeneity, followed by the addition and mixing of PDADMAC. Mixing was continued at 120 rpm for an additional 60 seconds then the stirring speed was reduced to 30 rpm, and the samples were allowed to undergo flocculation for 30 minutes to promote the aggregation of suspended particles with PDADMAC. After the flocculation stage, the rotation was turned off, and the samples were left undisturbed for 30 minutes to allow precipitation to occur. For tests where FeCl<sub>3</sub> was involved, FeCl<sub>3</sub> was added to each beaker upon finishing the initial mixing at a dosage of 5 mg/L,

consistent with the dosage used at the Orchard Hill Water Plant and was mixed for 1 minute. Subsequently, polyelectrolytes were added to each beaker at an optimal dosage of 3 mg/L and follow the above-mentioned protocols.

After the 30 min of quiescent settling, samples were then carefully collected from the medium height of each beaker for further characterization before filtered through 1.2  $\mu$ m membrane. UV<sub>254</sub> absorbance was measured using a UV-1900i Spectrophotometer from Shimadzu with a 1 cm quartz cell.  $\zeta$ -potential measurements were performed using a Zetasizer Nano particle analyzer Nano ZS (Malvern) at 25 °C and equipped with 10mW 632.8nm 'red' laser. Total organic carbon (TOC) was measured by analytikjena multi N/C 3100 by multiWin and Turbidity was measured by 2100Q Portable Turbidimeter.

# 3. The Effect of Ca<sup>2+</sup> on the Interaction Between Humic Acid and poly (diallyldimethylammonium chloride) (PDADMAC)

This chapter is based on the publication:

Yuan, Mingyu, Heriberto Bustamante, Najet Mahmoudi, and Michael Gradzielski. "Colloidal Chemistry in Water Treatment: The Effect of Ca<sup>2+</sup> on the Interaction between Humic Acid and Poly (diallyldimethylammonium chloride) (PDADMAC)." In: Langmuir (2024). DOI: 10.1021/acs.langmuir.3c03029.

#### Authorship contribution statement:

M.G. conceived and led the project. M.G. and M.Y. designed the experiments. M.Y. performed the sample preparation, characterization, and data analysis. H.B. participated in the data discussion as well as the reviewing and editing of the manuscript. N.M. directed SANS experiments and participated in the discussion and data curation.

#### 3.1. Introduction

The production of clean drinking water is one of the main challenges for humanity. Normal surface water contains large amounts of natural organic matter (NOM) that arise from natural biological degradation of organic life substances and mostly is composed of humic substances, but may vary largely with respect to its detailed composition.<sup>3</sup> NOM might partly be toxic but will become even more so during the necessary disinfection process, in which conventionally chlorine (Cl<sub>2</sub>) is used as a disinfectant, in form of disinfection by-products (DBPs), for instance trihalomethanes (THM).<sup>4</sup> Humic acid (HA), as the main component (~ 60 wt%) of NOM<sup>2</sup>, is a complex mixture of a large number of organic molecules with Mw ranging from 400 Da to 300 kDa. 6 It is composed of a large variety of organic macromolecules with carboxylic and phenolic groups, which contribute mostly to negative surface charge and reactivity of humic acid. 8 The various approaches to remove NOM from drinking water have been reviewed recently. 16, 53, 54 Traditionally the main treatment in water purification is addition of an inorganic coagulant (Fe<sup>III</sup>) or AlIII), which typically is followed by the addition of a polycation, such as poly(diallyldimethylammonium chloride) (PDADMAC). 15-17 It is well established that by adding positively charged multi-valent metal ions at relatively low pH value, charge neutralization is achieved that reduces the repulsion between predominantly negatively charged HA molecules, so that this colloidal system is destabilized enough to start coagulation. At higher pH values (usually the case in practice of water treatment and achieved by lime addition, i.e. addition of Ca2+ ions), the hydrolysis of metal ions becomes the main reaction and NOM is removed by precipitation.9 However, such 'sweep flocculation' may not be sufficient enough for practical usage as for example, in some water treatment plants in Australia only around 20-30% of the NOM can be removed<sup>13</sup>, which necessitates additional use of polycations to remove the remaining soluble NOM that has not been removed by inorganic coagulant (Fe<sup>III</sup> or Al<sup>III</sup>) yet. When oppositely charged polymers (i.e. polycations) are added, coagulated particles and microflocs are brought together to form flocculates which can be removed easily. The

combination of these two steps is called coagulation-flocculation, which is widely used in water purification because of its high efficiency, simple operation as well as low cost. <sup>19, 55</sup> It might be noted that there are methods like membrane filtration that can be used for water purification <sup>56</sup> and one may also substitute chlorine by ozone <sup>57</sup> or UV-treatment <sup>58</sup> for sterilization, thereby avoiding the risk of chlorinated DBP. However, at the current state the coagulation-flocculation method, due to its ease of large-scale application, as well as associated low cost, still remains the most largely employed method for water treatment.

From a colloidal point of view the interaction of polycation and HA is the formation of a classical interpolyelectrolyte complex (IPEC)<sup>35</sup> of oppositely charged polyelectrolytes, as known from the 1940s.<sup>33</sup> In this process HA can be regarded as polyanion with high polydispersity, rich in aromatic groups and rather rigid as a macromolecule.<sup>59</sup> Polymer binding plays an important role in the complexation between HA and PE, which can be regarded to be largely irreversible as it is unlikely for all complexed segments in a long polymer chain to be detached simultaneously<sup>60</sup>. Based on a mechanism recognized since the 1950s<sup>37</sup>, when the polymer chain is long enough to project into solutions, those 'dangling' polymer segments adsorbed on particles can 'bridge' particles together to form strong flocculates. Several previous studies reported the HA removal with PE as a function of PE dosage and pH level. 14, 61, 62 Basically the optimum HA removal happens when the PE dosage reaches the level required for charge neutralization, which is at relatively high pH value and the high ionization of HA molecules is favorable for complete complexation with PE. In addition, HA removal can be enhanced by PE with higher charge density while the effect of molecular weight, Mw, of PE (typically in the range of 50 kDa to 150 kDa) was negligible above a certain critical value of  $M_{\rm w}$ .<sup>21</sup>

Additionally, the presence of metal cations can significantly influence the aggregation behavior of HA and modulate its interactions with polyelectrolytes.<sup>61</sup> The variation in aggregate sizes of humic acid under different temperatures, cation conditions, and pH values was studied using

dynamic light scattering (DLS), which revealed particle diameters ranging from 100 to 500 nm, contingent upon the source of the HA.<sup>63</sup> It was observed that higher temperatures within the ambient range result in larger humic acid aggregates, which can be attributed to temperature-induced clouding phenomena.<sup>64</sup> Also, acidification leads to the contraction of HA aggregates as the repulsion between negatively charged sites diminishes. With continued acidification, intermolecular aggregation is induced, ultimately resulting in precipitation.

The complexation of HA with metal ions has been widely studied.<sup>65</sup> For example, potentiometric titrations indicate that the presence of Ca<sup>2+</sup> reduces the charge of humic acid, likely due to the binding of Ca<sup>2+</sup> ions to the carboxylic acid groups.<sup>66</sup> An initial reduction in the size of humic acid aggregates was observed upon the addition of up to 0.5 mM Mg<sup>2+</sup> ions to a 20 mg/L HA solution, indicative of charge neutralization and internal crosslinking by the added cations, resulting in intramolecular contraction and the formation of a more compact structure. Continuing this trend upon further acidification and additional Mg<sup>2+</sup> ions led to intermolecular aggregation. While intramolecular contraction occurred with both Mg<sup>2+</sup> and Na+ ions, it was more pronounced with the divalent cations. Notably, intermolecular aggregation was observed only with Mg<sup>2+</sup>, suggesting that monovalent cations like Na<sup>+</sup> are unable to induce intermolecular associations.<sup>63</sup> With trivalent ions the HA aggregation was further prompted as formation of pseudomicelles in aqueous humic acid was reported in the presence of Lu<sup>3+</sup>.67 Such comparison among various ions was also clarified by a molecular dynamic (MD) simulation study<sup>68</sup> which suggest that trivalent Eu<sup>3+</sup> and bivalent Sr<sup>2+</sup> may facilitate the formation of interand intramolecular bridges between negatively charged HA molecules to promote coagulation, whereas monovalent Cs<sup>+</sup> cannot form intermolecular bridges.

Ca<sup>2+</sup> ions, commonly present in raw water and frequently added as lime during the water treatment process, have been extensively studied to understand their effects within traditional water treatment settings. Notably, research has demonstrated that using CaCl<sub>2</sub> as a co-coagulant can reduce the consumption of aluminum sulfate (Al<sub>2</sub>(SO4)<sub>3</sub>) by approximately 20%, while still

achieving similar removal efficiencies for natural organic matter (NOM) at pH levels above 6.<sup>69</sup> Interestingly, although Ca<sup>2+</sup> can compress the electric double layers and neutralize negatively charged HA molecules, the charge neutralization point is not achieved solely through the addition of Ca<sup>2+</sup> to HA. The enhancing effect of Ca<sup>2+</sup> on HA removal using polyaluminium chloride (PAC) is only noticeable when the coagulant quantity is insufficient.<sup>70</sup> Despite its potential significance, the effect of Ca<sup>2+</sup> on the interaction between HA and cationic polyelectrolytes (PE) has been less extensively studied. This interaction is crucial as it represents a fundamental step in the complex process of water treatment.

To address this gap in knowledge, our study investigated the impact of Ca<sup>2+</sup> presence on the phase behavior and structures formed by humic acid (HA) in conjunction with varying concentrations of high molecular weight (500 kDa) PDADMAC at pH 9. At this pH, both carboxylic and phenolic groups of HA are largely dissociated, ensuring a high surface charge, a condition that aligns closely with those commonly found in water treatment processes. We used purified HA to ensure more defined and reproducible experimental conditions. The Ca<sup>2+</sup> concentrations we explored ranged from 0 to 0.25 mM, matching the typical Ca<sup>2+</sup> levels found in surface waters, which generally contain 1-2 mg/L (0.025-0.05 mM) but can rise to 100 mg/L (2.5 mM) in areas with limestone deposits. <sup>71,72</sup> The mesoscopic structure of HA-PDADMAC complexes across various concentrations of Ca<sup>2+</sup> was explored using a combination of static and dynamic light scattering (SLS and DLS) as well as small-angle neutron scattering (SANS). Additionally, the macroscopic sedimentation of HA flocs was monitored through long-term UV-Vis measurements. The impact of Ca<sup>2+</sup> was also compared with that of other ions such as Na<sup>2+</sup> and Mg<sup>2+</sup>, allowing for an examination of both generic effects attributable to ionic strength and specific influences of Ca<sup>2+</sup>.

## 3.2. Sample Preparation

Humic acid (HA) was purchased from Sigma-Aldrich (product number 53680-50G, technical grade) and subsequently purified to eliminate fulvic acid (FA) and humin. This involved dissolving the raw HA in a NaOH solution with a pH exceeding 12, followed by dual filtration using LLG-Qualitative filter paper (pore size 5 to 13 μm) and LABSOLUTE micro glass fibre filters (particle retention 1.20 μm). To precipitate HA, 35% HCl was added to the filtered solution to reduce the pH to 1. The resulting HA slurry was isolated by centrifugation and then freeze-dried to produce a black HA powder. Polydiallyldimethylammonium chloride (PDADMAC) with a molecular weight of 400–500 kDa was acquired from Sigma-Aldrich as a 20 wt% solution in water and was freeze-dried prior to use. A stock solution of PDADMAC was prepared at 0.01 wt%, assuming each repeating unit carries a single charge (Mw(charge) = 161.67 g/mol), equating to a nominal charge concentration of 0.625 mM.

For all samples, excluding those for Small Angle Neutron Scattering (SANS), the HA concentration was maintained at 40 mg/L, corresponding to a nominal charge concentration of 0.135 mM, as determined from the average molecular weight of the charged unit derived from titration data (Mw(charge) = 296 g/mol; referenced in **Figure A.1**). The pH of HA solutions was adjusted to 9.0 using 0.1 M NaOH solutions before the introduction of PDADMAC. The PDADMAC concentration was varied to achieve a specific nominal charge ratio Z, defined as Z = [charges of PDADMAC] / [charges of HA]. Appropriate quantities of NaCl, MgCl<sub>2</sub>, and CaCl<sub>2</sub> were added as calculated. All samples were prepared using Milli-Q water (18.2 M $\Omega$ ·cm at 25°C) or D<sub>2</sub>O (99.9% isotopic purity, Deutero GmbH) for SANS tests, and all measurements were conducted at least 24 hours post-preparation at a constant temperature of 298 K.

## 3.3. Results and Discussion

The aim of this work was to elucidate in detail the phase behavior of complexes formed by humic acid (HA) and the polycation PDADMAC (500 kDa) and in particular, how this process is affected by the presence of Ca<sup>2+</sup> ions, which are automatically present in the process of water treatment under real conditions (e. g., the concentration of Ca<sup>2+</sup> has an average value of 15 mg/L (0.375 mM) in the Nepean water treatment plant (WTP) in the Sydney area). Here we were first interested in the changes in macroscopic phase behavior upon variation of Ca<sup>2+</sup> concentration, as well as in the ensuing flocculation process. This was complemented by thorough characterization of the structures of the soluble complexes, as well as of the precipitates formed. These are important aspects of the colloidal complexation process that are directly related to a central elementary step done in water treatment in water industry, which is the interaction of humic acid with polycations. Therefore, this investigation is supposed to give fundamental insights into these elementary steps involved in the practical and more complex process of water treatment.

### 3.3.1. Phase Diagram

As a first step we characterized in detail the macroscopic phase behavior of aqueous solutions of humic acid containing different amounts of Ca<sup>2+</sup> to which increasing amounts of PDADMAC were added, where the composition was described by the nominal charge ratio Z, which is defined as Z = [charges of PDADMAC]/ [charges of HA]. It should be noted that these are always potential charges, ignoring possible protonation of the HA. These series contained different, constant concentrations of Ca<sup>2+</sup> and we worked always with a HA concentration of 40 mg/L. Phase behavior of the mixed samples was visually examined 24 h after the preparation (**Figure A.2**), this time interval was chosen to allow for adequate equilibration and the manifestation of any latent phase transitions.

For the reference HA-PDADMAC system without Ca<sup>2+</sup> addition, the transition from the monophasic to the biphasic region can be observed at Z = 0.9, i.e., near the charge neutralization point arising from the complexation of negatively-charged humic acid molecules by positivelycharged PDADMAC molecules. With vanishing electrical repulsion between the HA molecules, the system becomes destabilized, flocs are formed and grow until finally macroscopic phase separation takes place. As the dosage of PDADMAC is further increased to Z = 1.6, the positive excess charges from PDADMAC restabilize the system so that soluble complexes of humic acid are formed, switching back to a monophasic region, where a clear brownish solution with water-like viscosity is observed. In the biphasic regime, solutions become turbid upon mixing and a dispersion of extremely fine flocs can be seen by naked eyes within ~30 minutes. With the agglomeration of fine flocs and further sedimentation, phase separation occurs within several hours resulting in a clear water-like supernatant and dark brown loosely-packed precipitate of humic acid. The visual appearance of samples 24 h after mixing is shown by photos given in Figure A.2. It should be noted that samples were always prepared such, that it was avoided to pass through the equimolar charge regime (Z = 1) during the mixing process. An interesting point is that formed precipitates in the biphasic region cannot become dissolved again by further addition of PDADMAC, for instance by moving the system to a Z value above 1.3 where the monophasic region is observed otherwise. Apparently, the formed precipitate is rather stable and its redispersion is kinetically hindered.

In comparison, when Ca<sup>2+</sup> is present in the system, the range of precipitation is shifted to much lower PDADMAC concentration (lower Z) for increasing Ca<sup>2+</sup> concentration and this effect is already seen for rather low concentrations of 0.125 and 0.25 mM. This is shown in the phase diagram depicted in **Figure 3.1** and one observes that for 0.125 mM Ca<sup>2+</sup> and 0.25 mM Ca<sup>2+</sup> the phase boundary appears at Z~0.62 and Z~0.52, respectively, while without Ca<sup>2+</sup> it is at Z~0.85, i.e., much less PDADMAC is required to achieve precipitation of HA. It should be noted that the Ca<sup>2+</sup> concentration here is directly in the range of the concentration of ionizable groups (i.e.

carboxylic and phenolic groups) of the HA, which is 0.135 mM, therefore sufficient to completely neutralize the HA. Given the affinity especially of the carboxylic groups to  $Ca^{2+}$  it is not surprising that here a rather strong neutralisation by the  $Ca^{2+}$  takes place that shifts the phase boundary substantially. From a practical point of view this is important, as it reduces the amount of PDADMAC needed within the water treatment process, and it might be noted that a similar effect of reduced need for  $Al_2(SO_4)_3$  in the presence of  $Ca^{2+}$  has been reported before. Very interesting in that context is that the upper phase boundary is not affected at all by the presence of  $Ca^{2+}$ , which indicates that for polyelectrolyte excess the phase behavior is dominated by the interaction with the polycation and the  $Ca^{2+}$  was liberated from any binding site on the HA. For the overall phase behavior it means that the width of the precipitation range is substantially increasing upon  $Ca^{2+}$  addition.

Interesting is that not only the lower phase boundaries shift, but also the consistency of the precipitate changes. Compared to the reference system without  $Ca^{2+}$ , the precipitates become more densely packed with enhanced structural stability that is less likely to be re-dispersed during agitation and transportation, as it might occur during the industrial water treatment. These changes are evident in the confocal microscopy images shown in **Figure A.3** and inset in **Figure 3.1**, which show much larger and more compact precipitated flocs in the presence of  $Ca^{2+}$ , typically forming agglomerates in the size range of 10-40  $\mu$ m. In contrast, the flocs obtained in the absence of  $Ca^{2+}$  look much fluffier and less compact. In addition, the procedure of fine flocs formation and agglomeration are observed much earlier during the mixing of HA and PDADMAC in the presence of  $Ca^{2+}$ , i.e.  $Ca^{2+}$  speeds up the precipitation of humic acid. Those changes indicate the capability of  $Ca^{2+}$  in leading to more effective precipitation.

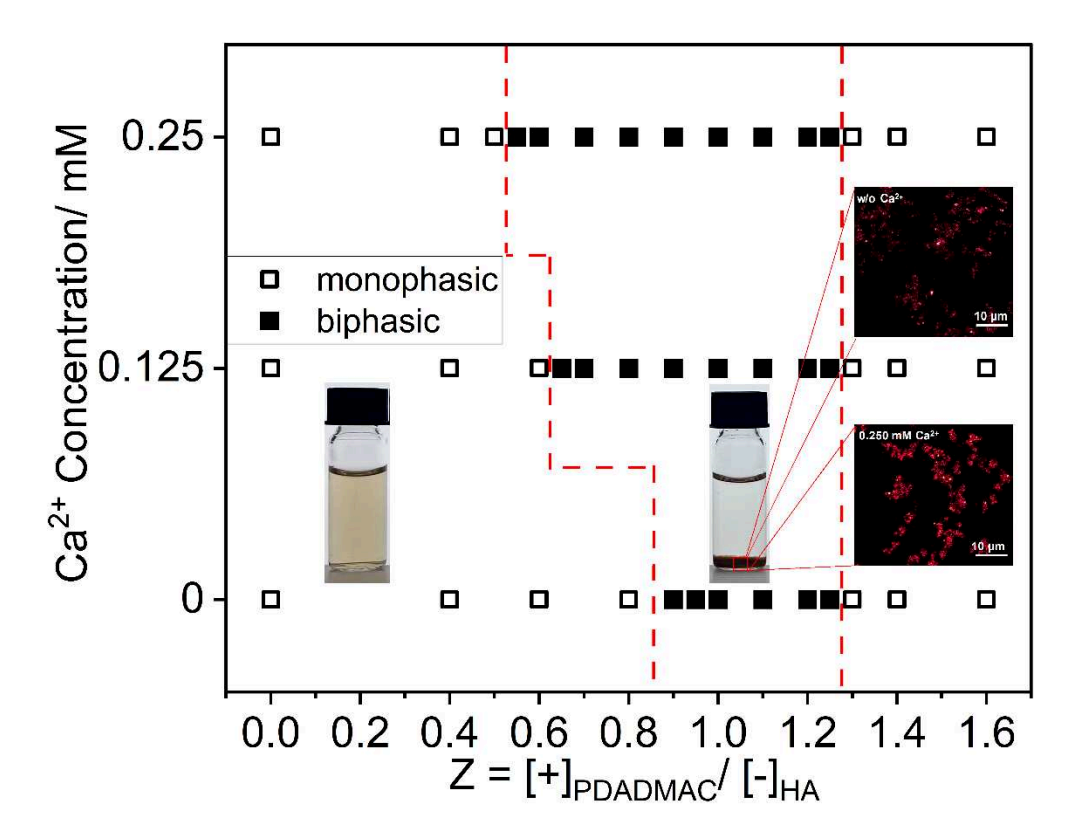


**Figure 3.1.** Phase diagram of 40 mg/L HA and added 500 kDa PDADMAC, the added amount being characterized by the nominal charge ratio Z = [+]/[-] for different concentrations of  $Ca^{2+}$  at pH 9.0. The inserts show confocal laser scanning microscopy (CLSM) images of precipitated flocs at Z = 1.0 with no  $Ca^{2+}$  and 0.250 mM  $Ca^{2+}$ , respectively.

#### 3.3.2. ζ-Potential

After having determined the macroscopic phase boundaries, we were now interested in quantifying the properties of the dispersed complexes, as a function of the composition of the systems. For that we measured the  $\zeta$ -potential, which is the parameter quantifying the electrostatic repulsion between the particles caused by their ionized groups. It has been used for a long time in water treatment facilities to determine colloidal stability and to optimize coagulant dosages.<sup>73, 74</sup> This was done both in the monophasic regions and for the supernatant in the biphasic region, the latter being of key importance in the removal process during water treatment.<sup>73, 74</sup> The measured  $\zeta$ -potential of all HA-PDADMAC complexes is shown in **Figure** 3.2 and tabulated values are given in **Table A.1** in Supporting Information. The  $\zeta$ -potential of

pure HA solutions without added PDADMAC was negative as expected considering its functional groups (-COOH, phenolic, etc). A continuous increase of the  $\zeta$ -potential can be observed as cationic PDADMAC is added to the system. When the charge ratio Z reaches 0.9 the  $\zeta$ -potential increases above -20 mV, i.e., into the range where interparticle repulsive forces become too weak to suppress coalescence or flocculation. With further addition of PDADMAC the  $\zeta$ -potential keeps increasing to over +10 mV and the system becomes monophasic again for Z above 1.3, due to the charge reversal taking place.

For HA solutions with added CaCl<sub>2</sub>, generally higher values of the  $\zeta$ -potential are measured, becoming systematically higher with increasing Ca<sup>2+</sup> concentration. Apparently, the cationic Ca<sup>2+</sup> is capable to complex with HA molecules and to neutralize its charge to a certain degree. This overall increase of the  $\zeta$ -potential is observed in the Z range up to 1.2, i.e. up to the upper boundary of the biphasic region. Interestingly, beyond this phase boundary the presence of the Ca<sup>2+</sup> has no longer an effect on the observed  $\zeta$ -potential. In the region of excess polycationic charge, the  $\zeta$ -potential depends only on the dosage of PDADMAC and is independent of the concentration of Ca<sup>2+</sup>, which indicated that here Ca<sup>2+</sup> is no longer bound to the aggregates and was substituted by the PDADMAC. Related specific prompting effects of Ca<sup>2+</sup> under inadequate coagulant conditions only were also observed for HA removal with inorganic coagulants, such as aluminum sulphate (Al<sub>2</sub>(SO4)<sub>3</sub>) and modified polyaluminium chloride (PAC)<sup>70</sup>.

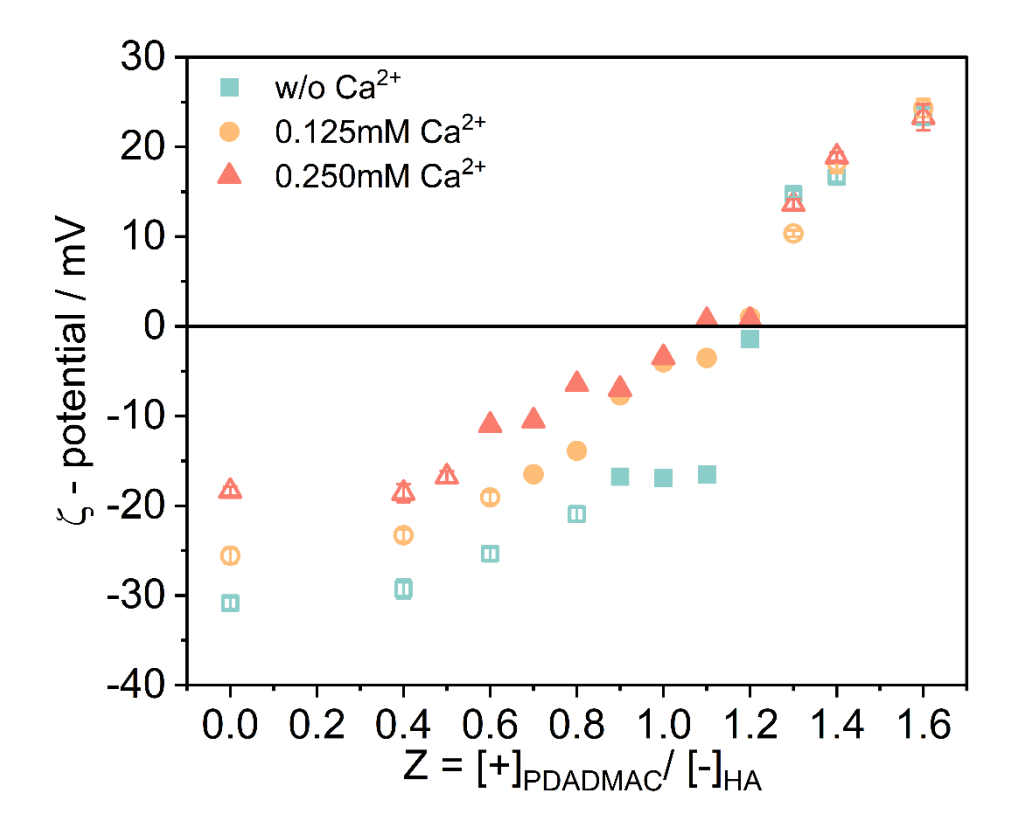


**Figure 3.2.**  $\zeta$ -potential for complexes of HA and 500 kDa PDADMAC for different Ca<sup>2+</sup> concentrations at different charge ratio Z (measurements done at pH 9 and 25 °C). Open symbols refer to monophasic regions while full symbols refer to the biphasic region. Error bars are given or are smaller than the symbol size.

#### 3.3.3. Removal efficiency of humic acid

For the purpose of quantifying the concentration of humic acid in the supernatant of biphasic solutions with precipitate, we employed UV-vis spectrometry as humic acid (HA) is known to absorb strongly in the UV range (see **Figure A.4** for a calibration curve). The absorbance at 254 nm (UV254) is a water quality test parameter that provides a quick measurement of the organic matter in water<sup>75</sup> (of course, limited to humic substances and similar compounds with conjugated aromatic rings that absorb in that region). It is typically expressed as [A/L] where A refers to the measured value of UV254 and L is the optical path length, which is the thickness of quartz cuvette. After having calibrated our system (for details see **Figure A.4**) a linear

correlation between HA concentration and UV254 was established and the amount of HA in the supernatant of the biphasic region can be determined reliably, as given in **Table A.2**.

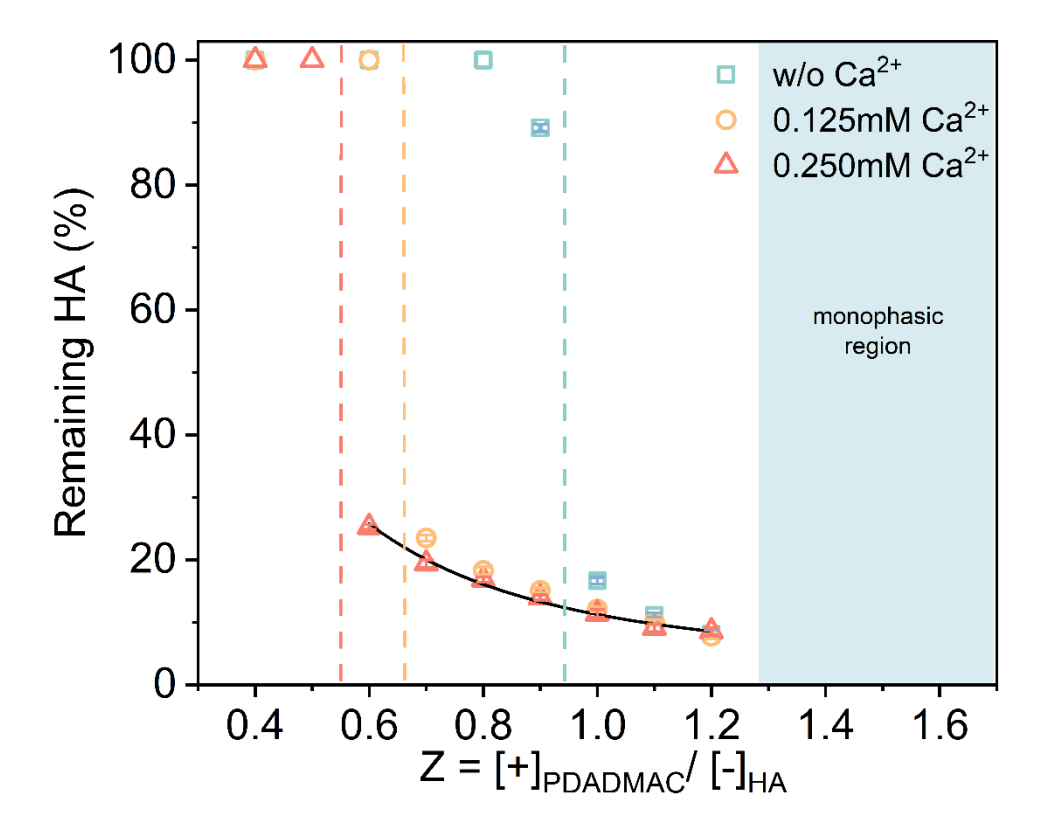


**Figure 3.3.** Remaining percentage of HA in the supernatant 24 hours after mixing at different charge ratio Z at 25 °C at pH 9 in the presence of different concentrations of Ca<sup>2+</sup> (open symbols: monophasic (100%), filled symbols: biphasic, crossed symbol: in a metastable state, partly precipitated). Error bars are given but always smaller than the symbol size.

In **Figure A.5**, the UV254 values of HA-PDADMAC systems 24 hours after mixing are shown as a function of charge ratio Z for varying  $Ca^{2+}$  concentrations (precipitates settled under gravity). As the charge ratio Z increased from 0 to 1.6, a huge drop of the UV-absorbance at 254 nm from ~1.8 to below 0.4 is observed near the charge neutralization point (Z=1), corresponding to a HA removal efficiency over 90%, showing that most of the humic acid was precipitated out, and which compares well to previous observations for the similar process with much higher Mw polycation<sup>21</sup>. For the biphasic region the concentration of the remaining HA was calculated and is shown in **Figure 3.3**. One observes that the concentration of remaining

HA decreases continuously with increasing Z. For all the systems with various  $Ca^{2+}$  concentration, the highest removal efficiency was obtained next to the upper phase boundary at Z=1.2, corresponding to a remaining HA concentration of around 8% (here the  $\zeta$ -potential is close to 0). In agreement with the phase diagram (**Figure 3.1**) at lower Z values, higher HA removal can be caused by increasing the concentration of  $Ca^{2+}$ . One also observes slightly lower values at a given Z with increasing  $Ca^{2+}$  concentration, but here the  $Ca^{2+}$  effect is rather small. It is interesting to note that the HA removal efficiency as a function of the charge ratio Z keeps increasing until the monophasic region is reached again, and without showing a minimum around the 'equimolar charge point'.

This behavior can be described with the classical solubility product according to K = [HA]\*[PDADMAC] (here one may choose concentrations in mass per volume, as that is the concentration easiest known and which is directly proportional to the concentration of charged units). Assuming a simple precipitation behavior in which a certain percentage x of the PDADMAC relative to the humic acid (HA) becomes precipitated out of solution, one arrives at eq. 3.1 (in the SI we also give the equation rewritten in terms of Z), where the subscript 0 indicates the respective initial concentrations of PDADMAC and HA. Experimentally we find from fitting this equation to the experimental data K equal to 57.4 mg<sup>2</sup>/L<sup>2</sup> and a value of x of 0.249, which means as charge ratio a value 0.585, which is quite a bit below the potentially expected equimolar ratio and indicates that for the destabilization of the HA only this larger fraction of PDADMAC is needed and the precipitate is in equilibrium with some excess PDADMA in solution. This model is in good agreement with the experiment data, as shown in Figure 3.3 as solid line that describes very well the observed behavior within the precipitation range. Of course, the model is restricted to the biphasic regime, as for Z values lower or higher than the phase boundary the complexes are colloidally stable again due to the excess PDADMAC. It might also be noted that x and K in eq. 11 are to some extent interrelated with

respect to their effect. Considering this and the finite precision of the [HA] values we could convince ourselves that the error of the fitted values of K and x should be about 10%.

$$[HA] = -\frac{[P]_0 - x \cdot [HA]_0}{2 \cdot x} + \sqrt{\left(\frac{[P]_0 - x \cdot [HA]_0}{2 \cdot x}\right)^2 + \frac{K}{x}}$$
(3.1)

## 3.3.4. Static and Dynamic Light Scattering (SLS, DLS)

In order to investigate the mesoscopic structure of HA-PDADMAC complexes, SLS and DLS measurements were carried out for HA-PDADMAC mixtures at constant HA concentration of 40 mg/L in the Z range where samples remain monophasic for at least 24 hours after mixing in the presence of different concentration of Ca<sup>2+</sup>.

The static intensity at zero angle,  $I_0$ , was determined from a Guinier fit and from it molecular weight  $M_w$  and radius of gyration  $R_g$  were calculated (see **Figure A.6** for SLS data). A slight increase of  $I_0$  of HA-PDADMAC complexes without  $Ca^{2+}$  can be observed as Z increases from 0 to 0.6, but the  $M_w$  of the aggregates remains almost constant, as shown in **Figure 3.4a**. This increase becomes more pronounced with higher  $Ca^{2+}$  content, whereas the  $M_w$  for the samples of the pure HA (Z=0) decreases with increasing  $Ca^{2+}$  content. It is also interesting to note that the Mw for samples with  $Ca^{2+}$  is highest for Z=1.3, i.e., for the samples just beyond the biphasic region. Also, it is interesting to note is that the  $M_w$  of the complexes does not vary very largely and remains in the range of  $3-12*10^8$  g/mol. This value indicates that about 150-500 PDADMAC molecules must be contained in the complexes close to the phase boundary of precipitation.

The radii of gyration  $R_g$  of the formed complexes obtained from SLS (**Figure 3.4b**) show generally rather constant values of 140-170 nm, with a slight tendency to decrease with increasing charge ratio Z. Moreover, at Z = 0 where only HA molecules and  $Ca^{2+}$  are dispersed in solution, HA complexes with 0.25 mM  $Ca^{2+}$  show the biggest  $R_g$  values, which drops

somewhat upon the addition of PDADMAC; whereas the  $R_g$  of HA complexes without  $Ca^{2+}$  shows only minor variations with charge ratio Z changing from 0 to 0.4. Interesting is also the observation that for the highest  $Ca^{2+}$  concentration of 0.25 mM one sees for the pure HA solution a lower scattering intensity and a minimum around 4-5  $10^{-2}$  nm<sup>-1</sup> (**Figure A.5c**). This would indicate a less compact structure (likely globular) with about 100 nm radius.

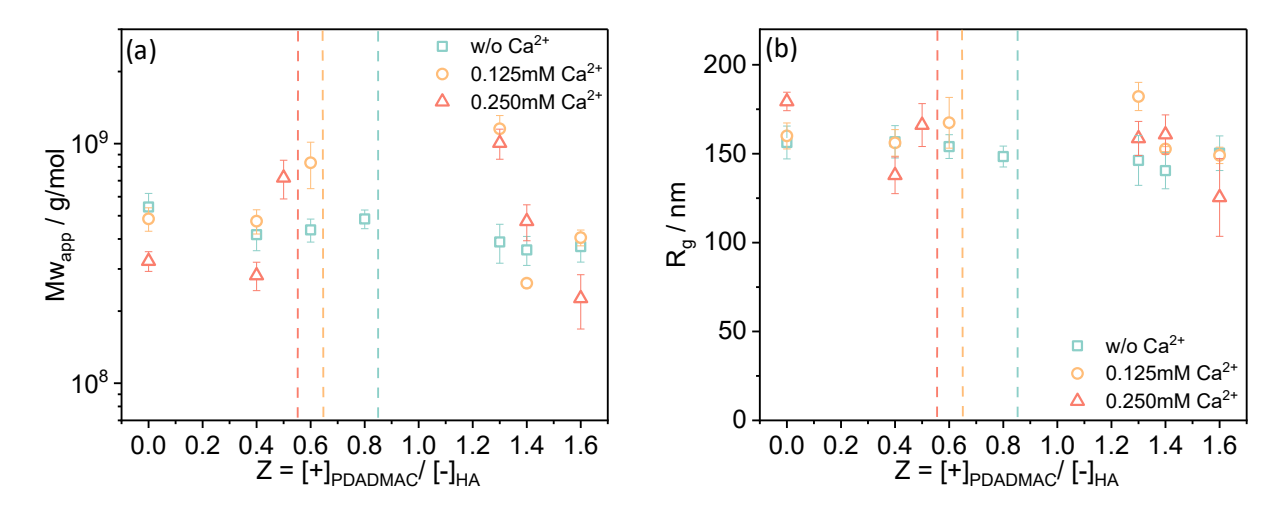


**Figure 3.4.** Static light scattering results: (a) Molecular weight Mw and (b) Radius of gyration Rg for HA-PDADMAC complexes under varying Ca<sup>2+</sup> concentrations as a function of the charge ratio Z at 25 °C.

The DLS data generally show monomodal intensity correlation functions (see **Figure 3.5a** for Z = 0 and **Figure A.8** for other Z values) that could be described well with a stretched exponential function (see eq. 3). Values of the characteristic stretching exponent  $\alpha$  for HA-PDADMAC complexes under varying  $Ca^{2+}$  concentrations at different charge ratio Z are ranging between 0.80 and 0.95 and are summarized in **Table A.3**, which indicates the presence of not too polydisperse aggregates. A pronounced decrease of  $\alpha$  is observed for HA-PDADMAC complexes with 0.25 mM  $Ca^{2+}$  upon approaching the charge neutralization point. This means that the aggregates become more polydisperse in the vicinity of the phase boundary. For pure HA this analysis yields a rather constant value of the hydrodynamic radius  $R_h$  of ~130 nm, irrespective of the  $Ca^{2+}$  concentration (**Figure 3.5b**). With the addition of PDADMAC,  $R_h$ 

of HA complexes decreases somewhat, which indicates a tendency for compaction, as the  $M_w$ at the same time remains constant or even increases (Figure 3.4a). With further addition of PDADMAC, i.e. in the region of excess polyelectrolyte, the aggregates are generally smaller than those of the pure HA and end up with similar size at Z = 1.6 (see Figure A.8b), irrespective of the Ca<sup>2+</sup> concentration. Apparently, here PDADMAC takes the main role in complexing with HA and therefore  $R_h$  is independent of the concentration of  $Ca^{2+}$ , as previously seen from the constant upper phase boundary and the values of the ζ-potential. Comparing the values of R<sub>h</sub> (Figure 3.5b) and Rg (Figure 3.4b), we may conclude that the aggregates are rather open with respect to their structure, as for such more star-like shaped or highly branched aggregates a higher value of R<sub>g</sub> than for R<sub>h</sub> is expected. The ratio of R<sub>g</sub> and R<sub>h</sub> is reported in **Figure A.9** with values of 1.2-1.6 found for all mixtures except those near the phase boundaries. However, these are also a bit less reliable as samples might not be long-time stable and typically precipitation was observed after several days. These rather high values for R<sub>g</sub>/R<sub>h</sub> indicate the presence of more open and fluffy structures. It can also be noted that in general the value for R<sub>g</sub>/R<sub>h</sub> increases with increasing Z value, thereby indicating that here less homogeneous aggregates are formed.

In summary, SLS and DLS show rather constant radii in the range of 120-150 nm for the aggregates present, irrespective of the Z value and the addition of Ca<sup>2+</sup>.

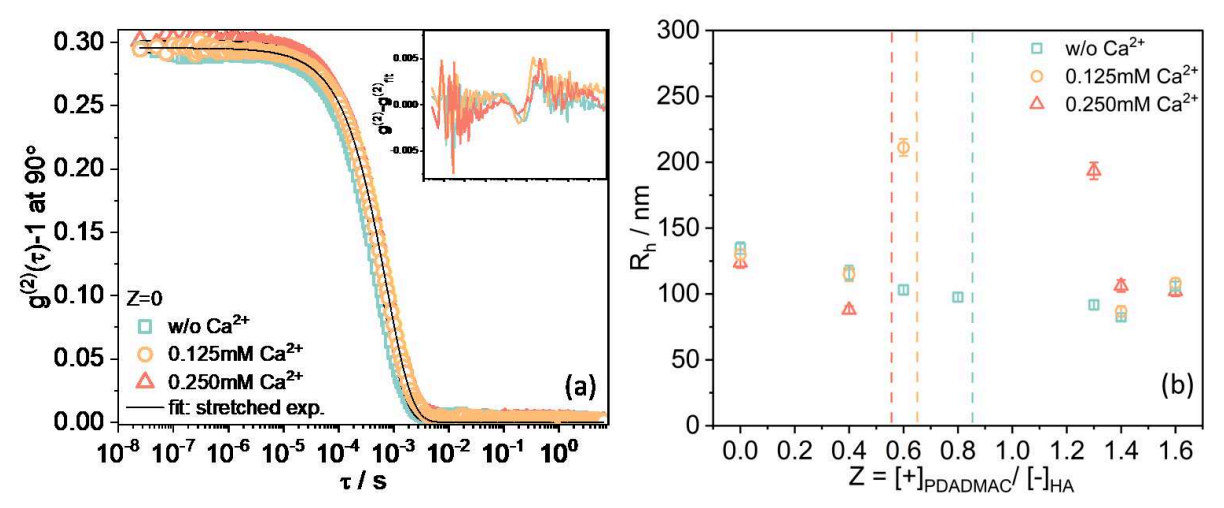


**Figure 3.5.** (a) Intensity auto-correlation functions from DLS experiments at 90° for HA solutions for varying  $Ca^{2+}$  concentrations at 25 °C and fits with a stretched exponential function (solid black line). The insets show the normalized fit residuals,  $(g^{(2)}-g^{(2)}_{fit})$ ; (b) Apparent hydrodynamic radii Rh for HA-PDADMAC complexes under varying  $Ca^{2+}$  concentrations at different charge ratio Z at 25 °C. Error bars for  $R_h$  are given.

Besides those DLS measurements for samples that remain monophasic at least for 24 hours, the HA-PDADMAC mixtures in the biphasic region, at Z =1.0 for varying Ca<sup>2+</sup> concentrations, were also measured 5 min after mixing, in order to look into the development of complexation at the initial stage (intensity autocorrelation functions shown in **Figure A.10**). Here the reliability of the data is not so high since precipitation sets in rapidly and sedimentation may affect the DLS results. However, the intensity correlation functions clearly show much longer correlation times for Ca<sup>2+</sup> addition, even after 5 min of mixing, indicating a fast formation of larger agglomerates. The hydrodynamic radii are 345 nm without Ca<sup>2+</sup> and 3630 and 5215 nm for 0.125 and 0.25 mM Ca<sup>2+</sup>, respectively, i.e., becoming much larger with increasing Ca<sup>2+</sup> concentration. This difference initiated our interest in the effect Ca<sup>2+</sup> effect on the rate of coagulation and floc formation, as well as the rate of settling of flocs, which will be discussed later in the manuscript.

## 3.3.5. Small-Angle Neutron Scattering (SANS)

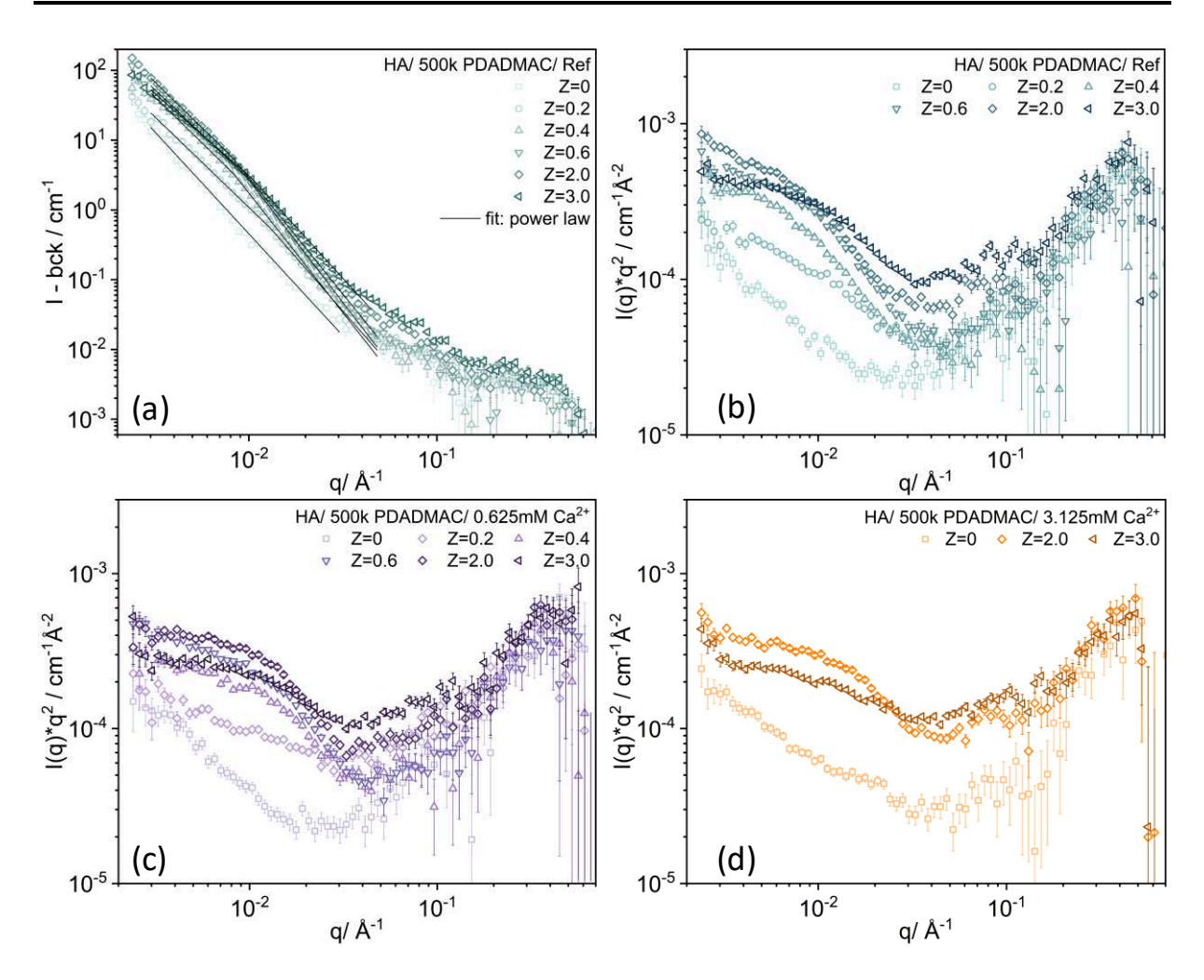
When light is adopted as the probing radiation, the q range is limited by the wavelength of the incident light, with which only the larger scale of HA-PDADMAC complexes can be investigated. As neutrons has a much longer wavelength compared to lights, SANS experiments were performed to further determine the mesoscopic structure of the soluble HA-PDADMAC complexes within the monophasic region with higher local resolution. The results from SLS represent the large-scale size of the aggregate while the results from SANS indicate the internal arrangement of local structures within a given aggregate. Figure A.11 displays the scattering pattern of HA-PDADMAC complexes obtained by plotting together SLS (low-q data) and SANS measurements (SANS curves are in absolute units and the SLS data were normalized to the SANS data by considering the corresponding contrast factor, for details see SI). There is good agreement of the absolute values and relative tendencies for both SANS and SLS curve and this combined plot shows the finite size of the aggregates studied by approaching a plateau in SLS, while SANS just sees a smaller size scale on which the matter is distributed according to a fractal law. Basically, SLS and SANS were used as complementary techniques to offer a more comprehensive understanding of the overall structure of HA-PDADMAC complexes. It should be noted that in order to achieve adequate scattering intensity a much higher concentration of 1.0 g/L HA was utilized in the SANS experiments. This increase of concentration of the system also leads to a broader biphasic region (see Figure A.12), which now ranged from Z = 0.8 to 1.4 without  $Ca^{2+}$  and Z = 0.2 to 1.4 for 3.125 mM  $Ca^{2+}$  (same HA/Ca ratio as for 40 mg/L HA system with 0.125 mM Ca<sup>2+</sup>). Accordingly, the charge ratio of samples selected for SANS differs slightly compared to the series for LS described above. For a broader comparison of the cation effect also samples with identical ionic strength with NaCl or MgCl<sub>2</sub> as salts were prepared. Figure A.12 shows the visual appearance of the measured samples and one observes the much faster precipitation in the case of addition of Ca<sup>2+</sup> and partly for Mg<sup>2+</sup>.

Figure 3.6 and Figure A.13 shows the SANS data of complexes formed by 1.0 g/L HA and different amounts of 500 kDa PDADMAC with mixing ratios Z ranging from 0 to 3, in the presence of different concentrations of CaCl<sub>2</sub> and without it. For the pure HA-PDADMAC system with no added salt, an increase of scattering intensity at lower q is observed with increasing charge ratio from 0 to 2, followed by a decrease of scattering intensity as Z reaches 3 (Figure 3.6a). That can be attributed to the formation of bigger complexes and in addition the total polymeric concentration increases due to the addition of the PDADMAC. The scattering curves at lower q also show a transition from the q<sup>-3</sup> power law behavior characteristic for pure humic acid solution to q<sup>-2.6</sup> behavior with increasing Z before reaching the phase boundary. Beyond the phase boundary this trend continues further to q<sup>-2.3</sup>, indicating the formation of apparently less densely packed structures on this larger size scale with increasing PDADMAC addition. In contrast, the slope at higher q increases with increasing Z until the phase boundary is reached and then for Z values beyond the phase boundary decreases again. This means that the complexes become more compact on a local scale in the vicinity of the biphasic region. The intensity and slope changes are seen more clearly in the Kratky-Porod plot shown in Figure **3.6b-d**. The presence of 0.625 mM Ca<sup>2+</sup> has only a small effect on the phase behavior and also the scattering curves (Figure 3.6c) look very similar to the case without added Ca<sup>2+</sup> (Figure **3.6**Error! Reference source not found.**b**). In contrast, for addition of 3.125 mM CaCl<sub>2</sub> precipitation at Z = 0.2, 0.4 and 0.6 happens quickly, thus only complexes in the PDADMAC excess region and pure HA-Ca $^{2+}$  complexes were measured. However, the SANS curves at Z = 2.0 and 3.0 look quite similar (Figure 3.6d), which means the addition of the Ca<sup>2+</sup> has only little effect on the complex structure. More details of the effect of PDADMAC addition are seen upon dividing the scattering data for

different Z values by the ones obtained for Z = 0 (**Figure A.14a-c**). For the case of no added  $Ca^{2+}$  and 0.625 mM  $Ca^{2+}$ , one clearly sees a marked increase of scattering intensity in the mid-q range  $(0.005-0.02 \text{ Å}^{-1})$  that becomes more marked with increasing PDADMAC addition and

then is most pronounced for samples beyond the biphasic region, i.e., for Z=2.0 and 3.0, where the scattering intensity increases by about a factor 8. This indicates that upon PDADMAC addition much more compact structural features in the size range of 10-50 nm are formed. In contrast, for the highest  $Ca^{2+}$  content (3.125 mM  $CaCl_2$ ) a much less pronounced increase of scattering intensity is seen (**Figure A.14c**). The effect of  $Ca^{2+}$  addition on the structure of the pure HA aggregates (Z=0) is seen more obviously in the Kratky-Porod plot in **Figure A.14d**, in the q-range below 0.05 Å<sup>-1</sup> the intensity is significantly higher for 3.125 mM  $Ca^{2+}$ . This means that at higher  $Ca^{2+}$  content the structures of the HA are already modified in a certain way that then is not much affected by PDADMAC addition and mostly the PDADMAC is attaching to the existing structures.

For the case of Z = 2.0 and 3.0 one can learn more about the effect of  $Ca^{2+}$  by comparing directly to the curves without added  $CaCl_2$  (**Figure A.15**). For Z = 2.0 the presence of  $Ca^{2+}$  leads to a peak at  $\sim 0.02$  Å<sup>-1</sup> that becomes somewhat more prominent for higher  $CaCl_2$  concentration, while at lower q the addition of  $Ca^{2+}$  leads to a reduction in scattering intensity. For Z = 3.0 a similar behavior is seen but much less pronounced and the peak is shifted to higher q of  $\sim 0.035$  Å<sup>-1</sup>. This can be interpreted such that here the addition of  $Ca^{2+}$  leads a local ordering of the aggregated mass on a scale of  $\sim 30$  nm.



**Figure 3.6.** SANS intensity as a function of the magnitude of the scattering vector q for complexes of HA and 500 kDa PDADMAC (a) without added salt (the curves with added CaCl<sub>2</sub> are shown in **Figure S13**). Kratky-Porod plots for: (b) without added salt; (c) with 0.625 mM CaCl<sub>2</sub>; (d) with 3.125 mM CaCl<sub>2</sub> (all measured at 25 °C).

To elucidate in more detail generic vs. specific ion effects on the mesoscopic structure of the complexes, in further experiments CaCl<sub>2</sub> was replaced by NaCl and MgCl<sub>2</sub>, while retaining the ionic strength at 9.375 mM. Consistent to previous literature claiming that Ca<sup>2+</sup> has a much larger effect than Mg<sup>2+</sup> on HA aggregation, macroscopic precipitation was observed in a much narrower range of charge ratios Z when replacing Ca<sup>2+</sup> by Mg<sup>2+</sup>, as shown in **Figure A.12**. This indicates much weaker binding of Mg<sup>2+</sup> to humic acid as reported previously.<sup>77</sup> When replaced by Na<sup>+</sup>, precipitation was further suppressed as no or much weaker intra- or intermolecular bridges should be formed with monovalent ions.

The scattering curves for the samples with different Z are summarized in Figure A.16. One observes rather similar changes of the scattering curves as a function of charge ratio Z for the different HA-PDADMAC complexes at all ionic conditions, irrespective whether using NaCl, MgCl<sub>2</sub>, or CaCl<sub>2</sub> (Figure 3.6). When grouping together the results at the same Z values (see Figure 3.7 and Figure A.17) for the different salts, the differences can be seen more clearly. For the simple system of pure HA (Ref) and different salts no obvious change in SANS can be seen, compared to pure HA solutions, only a somewhat higher scattering intensity is observed for Ca<sup>2+</sup>. This becomes better visible when normalized by the intensity of pure HA without added salt (I/I<sub>Ref</sub>) shown in Figure A.18. This suggests formation of somewhat more compact complexes here due to the presence of Ca<sup>2+</sup>. Furthermore, as Z increases from 2 to 3, a much more drastic intensity drop at lower q is seen for HA-PDADMAC-Na<sup>+</sup> complexes (Figure 3.7), which indicates that for the formation of larger complexes bivalent cations are required. The observed ion specificity aligns generically with the well-established Hofmeister effect.<sup>78</sup> Influenced by the strength and interaction of hydration shells, distinct aggregation behavior of HA in presence of Na<sup>+</sup>, Mg<sup>2+</sup>, and Ca<sup>2+</sup>, respectively, can be observed. However, the distinct role played here by Ca<sup>2+</sup> certainly arises from its strong interaction with the carboxylic groups of the HA. Certainly, also a further theoretical analysis of the electrostatic conditions in such complexes and during their formation process would be interesting, but is largely hampered by the rather ill-defined mesoscopic structure of humic acid and therefore appears out of scope at the given moment.

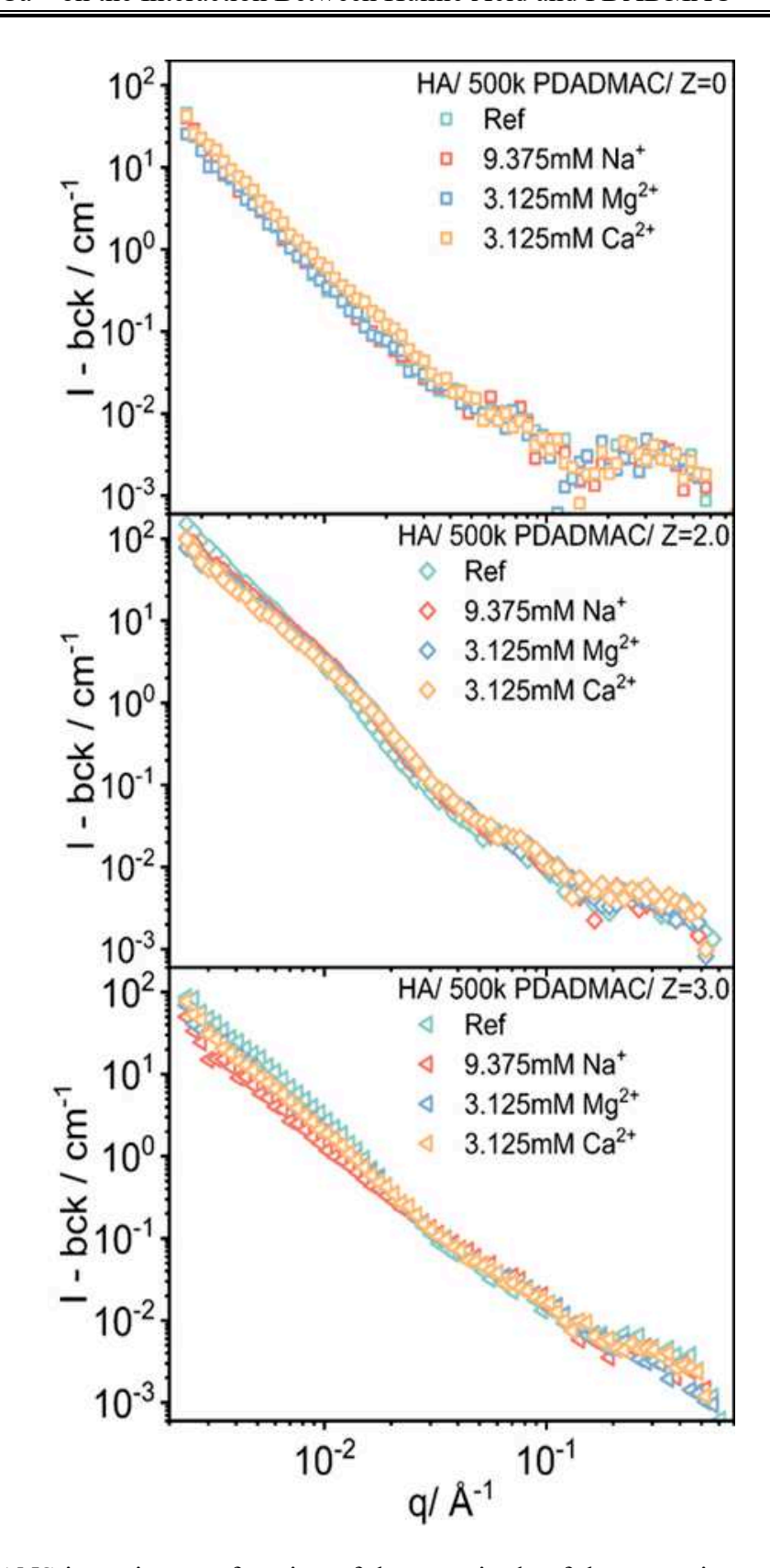


**Figure 3.7.** SANS intensity as a function of the magnitude of the scattering vector q for pure HA (Z = 0) under various ionic conditions and for HA-PDADMAC complexes under various ionic conditions at Z = 2 and 3, respectively (c(HA) = 1.0 g/L).

For a more quantitative interpretation, the SANS data of the HA-PDADMAC complexes was analyzed empirically by a two-power law model with all obtained parameters summarized in **Table 3.1.** For Z = 0, i.e. pure humic acid solution, under various ionic conditions only a single power law is observed, where the exponent p decreases only somewhat by switching from Na<sup>+</sup>, Mg<sup>2+</sup> to Ca<sup>2+</sup>, where the most strongly binding Ca<sup>2+</sup> shows the lowest value. As soon as PDADMAC is added a switch of the slope is seen in the q-range of 0.01-0.1 Å<sup>-1</sup>, the curve becoming steeper at higher q. Without added salt the initial slope (p1) is rather unaffected by the addition of PDADMAC and only becomes significantly smaller for Z = 3.0. In contrast, the second slope (p2) increases substantially upon PDADMAC addition until the phase boundary is reached and for the Z values beyond becomes smaller again. In the presence of Na<sup>+</sup> the same tendencies are seen, just with generally somewhat lower values. The addition of Mg<sup>2+</sup> has only a very small effect on p1, but markedly higher values for p2 are seen for Z values below the phase boundary, where the higher fractal dimension indicates a more compacted structure in that size range. For Ca<sup>2+</sup> only the Z range beyond the phase boundary was studied and shows here very similar values as seen for Mg<sup>2+</sup>. Interesting is the observation that for complexes at Z = 3 the addition of salt always leads to a substantial reduction of the slope at higher q (**Table** 3.1), which is most pronounced for the case of Na<sup>+</sup>. In general, that means that salt here leads to less compact aggregates on that length scale of 100-200 nm.

**Table 3.1.** Fitted power law exponent p1 at low q and p2 at high q, respectively of HA complexes with different charge ratio Z values under different ionic conditions, as determined from the SANS experiments.

Z	0	0.2		0.4		0.6		2		3	
	р	p1	p2	p1	p2	<b>p</b> 1	p2	p1	p2	p1	p2
ref	2.92	2.59	3.08	2.63	3.43	2.55	3.51	2.61	3.33	2.35	2.95
Na	2.9	2.44	2.98	2.44	3.30	2.52	3.47	2.31	3.25	2.29	2.08
Mg	2.86	2.57	3.27	2.60	3.81			2.30	3.12	2.32	2.48
<u>Ca</u>	2.76							2.25	2.98	2.29	2.50

As an alternative approach we analyzed our data with the Beaucage model to interpret the hierarchical structural levels of HA complexes and the corresponding fit parameters are summarized in **Table A.4**. Corresponding residuals for fit of SANS data for 500kDa PDADMAC-HA complexes under various ionic conditions at Z=2 with the two-power law model and Beaucage model, respectively can be found in **Figure A.19** and **Figure A.20**, as an example. Of course, in general the Beaucage is superior with respect to its fit quality, especially for pure humic acid solution under various ionic conditions a one-level Beaucage model was adopted, where the radius of gyration  $R_{g1}$  shows comparable values around 44 nm for the pure HA as reference system. The addition of  $Na^+$  or  $Mg^{2+}$  ions has no effect on this size, while the more strongly binding  $Ca^{2+}$  lead to an increase of  $R_{g1}$  to 56.1 nm, indicating a 'bridging effect' between HA molecules and  $Ca^{2+}$  even in absence of cationic electrolyte.

As discussed in previous sections that the addition of PDADMAC leads to a local densification of the structures in the complexes, the two-level Beaucage model was utilized for the sample sets where PDADMAC is involved (**Table A.4**). For the pure HA-PDADMAC system with no added salt, a steady increase for both R<sub>g1</sub> and R<sub>g2</sub> is observed as charge ratio increasing from 0 to 3, confirming the formation of bigger complexes due to the addition of PDADMAC. Here a jump-wise increase from 44 to 56 nm occurs already upon the addition of the smallest amount

of PDADMAC and then  $R_{g1}$  increases systematically up to 95.5 nm for the sample with PDADMAC excess. At the same time  $R_{g2}$  starts from 5.2 and goes up to 9.6 nm, being almost constantly a factor 10 smaller than  $R_{g1}$ . The appearance of this smaller scale structure indicates that the complexation by PDADMAC also leads to a densification of structures on this rather local level of 5-10 nm, which becomes larger with increasing amount of complexing PDADMAC. This is further corroborated by the fact that  $G_2$ , that quantifies the presence of these smaller compacted structures, increases substantially with increasing Z (**Table A.4**).

With the addition of Na<sup>+</sup> the HA-PDADMAC complexes R<sub>g1</sub> and R<sub>g2</sub> follow similar tendency until charge ratio 2, i.e. until the phase boundary is reached and above one no longer observes the increase of  $R_{g1}. \ When \ switch \ from the monovalent \ Na^+$  to bivalent  $Mg^{2^+}$  a pronounced higher value for  $R_{\rm g1}$  of 108 nm is seen when Z approaches the phase boundary, followed by rapid drop of  $R_{\rm gl}$  value by a factor of around 2 at the PDADMAC excess region, while radius of gyration at smaller scale R<sub>g2</sub> is less influenced by the charge ratio Z. For HA-PDADMAC complexes at both ionic conditions, at higher Z value, where PDADMAC is in excess, the considerable reduction of R<sub>g1</sub> compared to the salt-free condition indicates the shrinkage of HA complexes in the length scale of 50-100 nm; while the comparable  $R_{\rm g2}$  suggests that the structural rearrangement on a smaller scale is little affected. For Ca<sup>2+</sup>, due to precipitation, no soluble complexes could be studied with PDADMAC, but for HA-PDADMAC excess interesting the values for R<sub>g1</sub> and R<sub>g2</sub> are even a bit bigger than without added Ca<sup>2+</sup>. As explanation one could state that apparently for PDADMAC excess the ionic strength brought into the system by addition of Na<sup>+</sup> or Mg<sup>2+</sup> is weakening the binding of PDADMAC and HA, while for Ca<sup>2+</sup> the effect of ionic strength increase is counterbalance by its ability to contribute to bridging of HA molecules, thereby keeping the complexes large

### 3.3.6. Settling rate of humic acid precipitate

So far, we have been concerned with the equilibrium or steady-state behavior of the HA-PDADMAC complexes under various conditions. However, equally important for the process of HA removal by precipitation is the rate by which this takes place, i.e., the rate at which the coagulation takes place and precipitate forms and settles.

To monitor these processes, the time-dependent absorption changes at 254 nm of HA-PDADMAC mixtures were measured over a longer time period of 16 h, starting 3 minutes after mixing. The results are shown in Figure 3.8. For charge ratios Z=0.8 and Z=1.4, where no precipitation happened, constant absorbance values are observed throughout the whole 16 h observation window. The slightly higher absorbance at Z=1.4 is likely due to the higher concentration of dispersed material. For Z=1.0 and Z=1.2 precipitation can be observed and for these Z values HA removal efficiency around 83% and 92%, respectively, was achieved within 24 h after mixing (Figure 3.3). For these samples a gentle decline of absorbance at 254 nm can be observed at the very beginning followed by a much more rapid decrease after 1.5 or 4 h, respectively. For longer times the absorbance values decreased much more slowly and after 10-15 h reached values of around 0.5 and 0.3, respectively, which correspond to removal efficiencies of about 70% and 80%, respectively (Figure 3.8a; the values here after 15 h are a bit lower than after 24 h (Figure 3.3) as remaining dispersed flocs still settle during that time). At this moment the major part of HA was already precipitated out and phase separation could be observed clearly, with tiny amount of HA flocs remaining in the supernatant that will settle after longer times (see Figure 3.3). Interesting to note is that a slight excess of PDADMAC (Z = 1.2) makes the precipitation process to proceed much faster and efficient then under apparent equimolar conditions (Z = 1.0).

We then investigated further the effect of  $Ca^{2+}$  on the precipitation process. In **Figure 3.8b** we compare the absorbance (of the developing supernatant) as a function of time for the system at Z=1.0. Generically a similar decline-drop-plateau curve of the absorbance at 254 nm can be

seen. However, already the addition of 1 mg/L  $Ca^{2+}$  (0.025 mM), which corresponds to around one  $Ca^{2+}$  ion per 5.5 carboxylic groups from the HA molecules leads to a marked speeding up of the settling process. It is comparable to the one for 20% higher dosage of PDADMAC (Z = 1.2, **Figure 3.8a**), indicating the  $Ca^{2+}$  effect in promoting HA precipitation. The observed calcium effect on HA precipitation, as measured through time-resolved UV-vis technique, was systematically reproduced to ensure the reliability and consistency of our results. In summary, this study shows that the presence of  $Ca^{2+}$  during the precipitation process leads to a more marked removal of HA and also is speeding up this removal process. Bother effects are of high relevance to the practical use of polycations in the NOM removal in water industry.

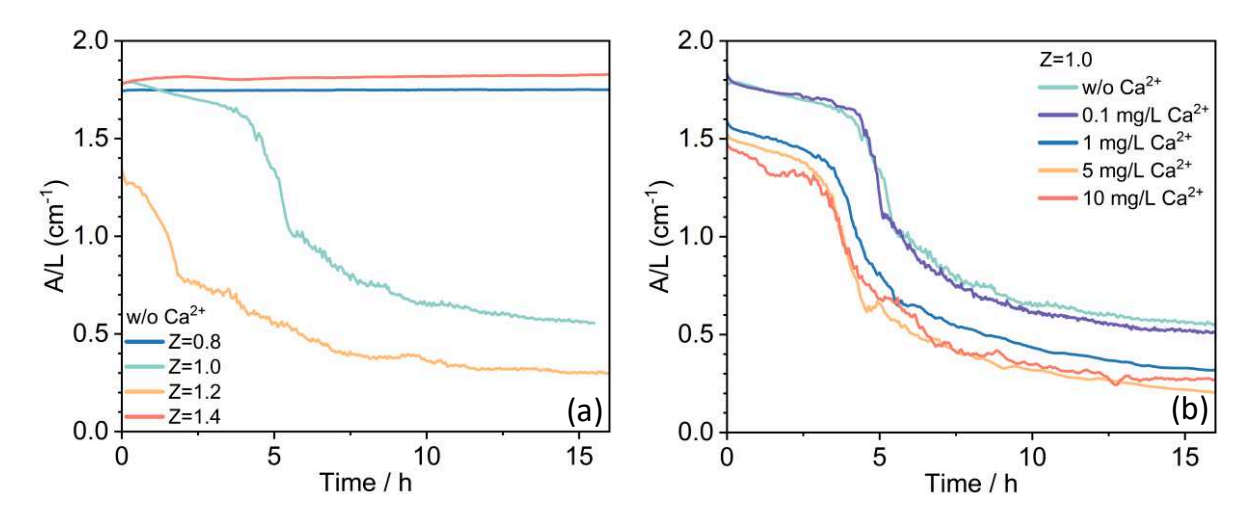


**Figure 3.8.** Time dependence of the HA-PDADMAC mixture absorbance at 254 nm with various (a) charge ratios Z (addition of PDADMAC) and (b) for different Ca<sup>2+</sup> concentrations at fixed charge ratio Z=1.

## 3.4. Conclusion

In this work, we studied systematically the interaction between oppositely charged humic acid (HA) and polycation polydiallyldimethylammonium chloride (PDADMAC), which is widely used in conventional water treatment, with a particular focus on the effect of Ca<sup>2+</sup> on the complexation process. The complexation of HA by polycation is an elementary step in water treatment, in which Ca<sup>2+</sup> will always be present to a certain extent. All these investigations were done at pH 9.0 to mimic the realistic conditions in a water plant. To obtain a comprehensive view of the behavior of this system, the ion concentration and the charge ratio Z between the HA and PDADMAC were varied.

A combination of UV-Vis and confocal microscopy was utilized to probe and quantify the phase behavior and morphology of the formed HA-PE precipitates as a function of mixing ratio for various  $Ca^{2+}$  concentrations. This investigation showed that the biphasic region is shifted to lower charge ratio Z already for rather small  $Ca^{2+}$  concentrations of 0.125 mM (actually close the 0.135 mM of charged HA units contained in our experiments), which means that a significantly lower amount of PDADMAC is needed for achieving the same effect. At the same time the packing density of HA flocs in the precipitate was enhanced by the presence of  $Ca^{2+}$ , which is presumably relevant for the floc strength of the precipitates. The amount of precipitated HA in the two-phase region is well described by a simple solubility law and does not depend to a significant extent on the presence of  $Ca^{2+}$ . In addition to the phase behavior, for HA-PDADMAC complexes with common charge ratio Z=1, a significantly faster precipitation process in the presence of  $Ca^{2+}$  was quantitatively verified via long-term UV-vis measurements.

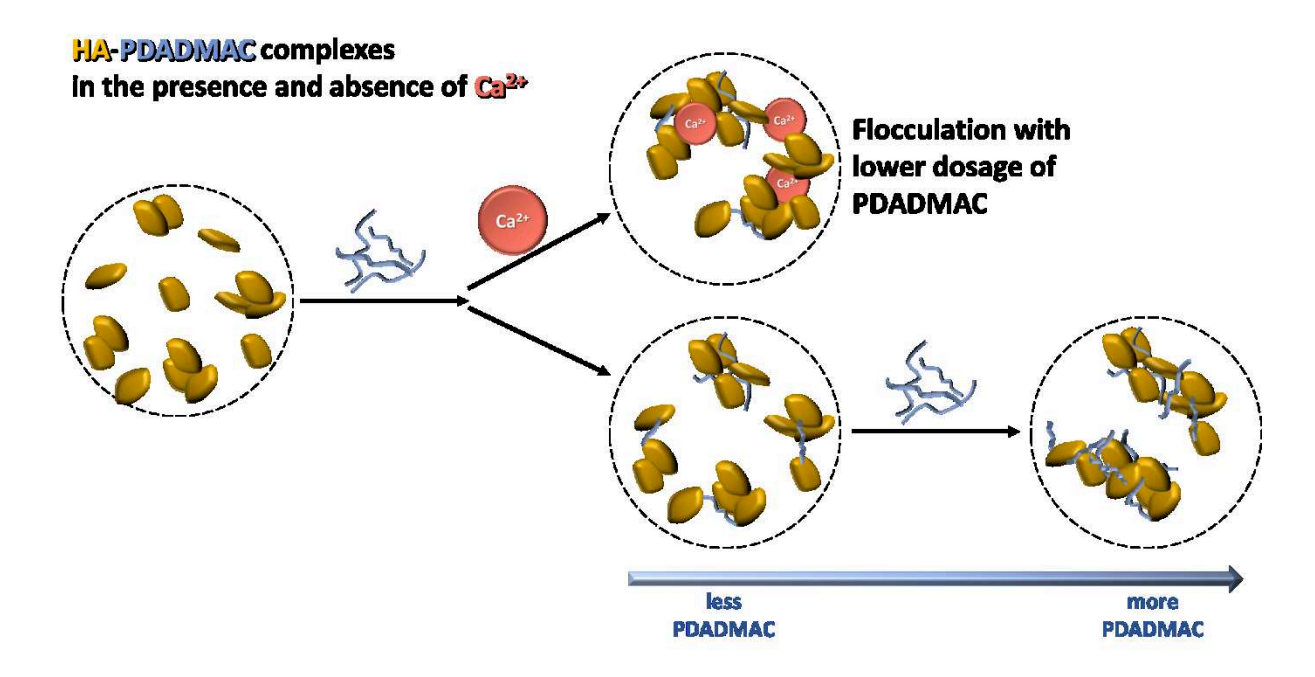


**Figure 3.9.** Schematic drawing of the complexation between cationic PDADMAC and anionic HA in the presence and absence of Ca<sup>2+</sup>, respectively.

Moreover, the colloidal structural characteristics of HA-PDADMAC complexes, to the extent of our knowledge, were for the first time studied by comprehensive scattering measurements including SLS, DLS, and small-angle neutron scattering (SANS). A slight decrease of the radii of gyration Rg of the formed complexes with increasing charge ratio Z was shown by SLS measurements, which became more pronounced in the presence of Ca<sup>2+</sup>. As the calculated Rg/Rh values are largely above 0.775, it implies a rather open structure of the HA-PDADMAC complexes. Further one has the 'bridging effect' from bivalent ion Ca<sup>2+</sup> and **Figure 3.9** depicts the complexation in the presence and absence of Ca<sup>2+</sup>. The SANS experiments showed a marked more compacted structure in the size range of 10-50 nm due to the addition of PDADMAC. Interestingly the addition of PDADMAC reduces the fractal dimension on a larger scale but increases it for smaller sizes, which demonstrates the local densification of the structures in the complexes. Here the presence of Ca<sup>2+</sup> has only a minor effect but the SANS experiments show a clearly discernible ordering effect, in the size range of 30 nm at PDADMAC excess. In

summary, that means that the main structural effect of PDADMAC addition is a compaction of aggregates on the structural range of 20-50 nm, further supported by the presence of  $Ca^{2+}$ . In order to elucidate the specific ion effects in more details on the mesoscopic structure of the complexes, HA-PDADMAC complexes under more ion conditions were probed with SANS, where the difference between the effect of monovalent ion and bivalent ions was clearly revealed. These experiments also showed that  $Ca^{2+}$  plays a special role here due to its very marked interaction with the carboxylic groups of the HA.

Those insights from colloid science may shed a light to the optimization of water treatment process in industrial fields. Also, it provides a reference characterization of HA-PE complexes as a basis of the development of PE from neutral resource to develop an environmentally-friendly solution.

## 4. From Waste Treatment to Water Treatment:

# **Application of Quaternised Chitosan in Enhancing NOM**

## **Flocculation**

## 4.1. Introduction

The production of clean drinking water is one of the main challenges for humanity. However, natural organic matter (NOM) in surface water, particularly humic acid (HA), leads to significant challenges in water treatment due to its widespread presence and complex chemical characteristics.<sup>3</sup> NOM contributes to color, taste, and odor issues in urban water system and forms disinfection by-products (DBPs) during the disinfection process with chlorine (Cl<sub>2</sub>), which are potential health hazards for public health.<sup>4</sup>

Flocculation is a widely used conventional method for the removal of NOM in water treatment facilities, where humic acid constitutes a major component of NOM.<sup>2</sup> Humic acid is a complex mixture of organic macromolecules ranging from 400 Da to 300 kDa<sup>6</sup> and contains a large number of carboxylic and phenolic groups, <sup>8</sup> which lead to the negative charges and thus contribute to its reactivity with flocculants, which are often cationic polyelectrolytes (cPE). The interaction between humic acid and cPE can be understood as the formation of a classical interpolyelectrolyte complex (IPEC), which is a concept well-established since the 1940s.<sup>33, 35</sup> For such systems involving oppositely charged polyelectrolytes, the primary mechanism is the resulting entropy gain due to the release of counterions during the complexation process.<sup>79</sup> The cPE molecules interact with negatively charged HA, reduce their electrostatic repulsion, thereby leading to the formation of larger aggregates and flocs. In addition, when the polymer chain of cPE is long enough, segments of the chain that dangle into the solution can adsorb onto neighboring particles, which is a process known as "bridging", <sup>37, 60</sup> These adsorbed segments

can then act as bridges, effectively linking particles together to form robust flocculates. This bridging effect enhances floc formation, leading to larger and more easily settling aggregates. The conventional polymeric flocculants used in practical water treatment are fully synthetic, including modified polyacrylamides (PAM)<sup>80-82</sup>, ammonium-based polycations<sup>83-85</sup> and poly(diallyldimethylammonium chloride) (PDADMAC)<sup>15-17</sup>, due to their high flocculation efficiency, low toxicity and low cost. Synthetic cationic polyelectrolytes (cPEs) play a vital role in the purification of water by promoting the aggregation of suspended particles into larger complexes, which can be more easily removed through sedimentation or filtration. However, environmental concerns have prompted the search for more sustainable alternatives, such as chitosan. As a biodegradable polymer, often derived from the shell of seafood, chitosan is increasingly considered in water treatment applications to address the environmental impacts associated with traditional chemical flocculants.<sup>86,87</sup>

One disadvantage of chitosan that hinders its general application in water treatment is its restricted solubility at natural pH range, as it only becomes soluble at pH below 6.3-6.5 because of the protonation of the amine group (pKa = 6.5). Addressing this issue, various methods have been developed to enhance chitosan's solubility by synthetic chemical methods. Grafting hydrophilic chains onto the chitosan backbone, as seen in PEGylated chitosan, not only improves solubility but broadens its potential for applications in pharmaceutical formulations due to a more variable biological functionality. 88,89 Another approach involves the introduction of quaternary ammonium groups. The simplest derivative is N,N,N-trimethyl chitosan (TMC), obtained via reaction with a methylating agent, e.g. methyl iodide<sup>90-93</sup>; in addition, grafting a quaternary-ammonium group as a side chain of the chitosan backbone also has been widely applied. For example, water-soluble chitosan derivatives were achieved by initially reacting chitosan with ethyl acrylate, followed by further modification through substitution reactions alcohols;94 alkyl grafting 3-chloro-2involving aliphatic diamines amino hydroxypropyltrimethylammonium chloride (CTA) has been reported to effectively improve the solubility of chitosan<sup>95, 96</sup> and success and extent of the modification can be determined by NMR.<sup>97</sup> Conjugating glycidyl trimethylammonium chloride (GTMAC) onto chitosan chains may also result in a derivative that is soluble in water at concentrations up to 25 g/L, for which the degree of quaternization of the resulting modified chitosan is related to the feed ratio of grafted species and chitosan. 98 These modifications increase both its solubility across a broader pH range and charge density, which are important parameters in the water treatment process. In our study, to develop an environmentally friendly and potentially more efficient solution, we explore the application of modified cationic chitosans, specifically quaternised chitosans (qCs) synthesized through the conjugation with glycidyl trimethylammonium chloride (GTMAC),98 as cationic polyelectrolytes (cPEs) in water treatment applications. By controlling the degree of GTMAC substitution, modified chitosans with different charge densities have been produced. We conducted a systematic investigation of the phase behavior of humic acid (HA) when interacting with a series of qCs, using poly(diallyldimethylammonium chloride) (PDADMAC), a fully charged linear polymer, as a reference cPE. Additionally, the kinetics of flocculation were investigated through laser light diffraction, enabling real-time monitoring of HA floc formation. Besides the established theory of charge neutralization and bridging, the flocculation mechanism of cationic polyelectrolytes can be further probed with a focus on their morphological characteristics. This insight is promising for the development of more efficient flocculant materials in industrial fields.

## 4.2. Sample Preparation

HA is Suwannee River Humic Acid Standard III purchased from International Humic Substances Society (IHSS). Raw water sample was collected from Nepean Water Filtration Plant from Australia without any pre-treatment. 150 kDa polydiallyldimethylammonium chloride (PDADMAC) (low molecular weight, 100–200 kDa) was purchased from Sigma-Aldrich as 20 wt.% solutions in water and freeze-dried before usage. Chitosan (low molecular weight, 50–190 kDa) was purchased from Sigma-Aldrich. To remove any possible residual chloride ions from its production, chitosan was precipitated, washed and freeze-dried before usage. All samples were prepared by Milli-Q water (18.2 MΩ·cm at 25°C).

For all samples the HA concentration was 40 mg/L, which corresponds to a nominal charge concentration of 0.157 mM at pH 9, as calculated from the averaged molecular weight of the charged unit determined from titration (Mw(charge) = 255 g/mol; see the titration curve in Figure S1). The pH of HA solutions was adjusted to 7.0 and 9.0 with 0.1 M NaOH solutions before the addition of cationic polyelectrolyte (PDADMAC and chitosan). The cationic polyelectrolyte concentration was varied to achieve a specific nominal charge ratio Z, which is defined as Z = [+]/[-] = [quaternised amino groups of chitosan]/[carboxylic and phenolic groupsof HA]. Of course, it has to be noted that the real charge of the macromolecules depends on pH, where at lower pH the HA becomes more neutralized and the free amino groups of the chitosan become increasingly protonated. In addition to pH, the charge state will also depend on the mixing ratio of the both components, due to their mutual interaction in the formed complexes. Water-soluble quaternary ammonium chitosan derivatives (QCS) were synthesized by grafting glycidyltrimethylammonium chloride (GTMAC) onto the glucosamine residues of chitosan polymers using a previously established method<sup>99</sup>. The mole ratio of GTMAC to chitosan was varied from 2:1 to 4:1 to produce quaternised chitosan with different degree of substitution (DS) ranging from 34.0% to 51.6%, respectively. Based on the GTMAC to chitosan molar ratios, the quaternised QCSs were designated as QCS2, QCS3, and QCS4, and contained 34.0, 42.4, and 51.6 mol% quaternisation. Further details are given in **Table 4.1**.

**Table 4.1.** Composition, feed ratio, ratios of the functional groups, molecular weights, and charge densities for the different samples of quaternised chitosans and PDADMAC (PDAD).

	GTMAC	—NH <sub>2</sub>	Ů	-N	Mw	Permanent charge density	
	QCS	1	—N CH₃	H OH	g/mol	g/mol e	
QCS2	2:1	39.00%	27%	34.00%	223.7	658	
QCS3	3:1	30.60%	27%	42.40%	236.3	558	
QCS4	4:1	21.40%	27%	51.60%	250.2	485	
PDAD	n/a		n/a		160	160	

## 4.3. Results and Discussion

#### 4.3.1. Phase Diagram

As a first step of our investigation, we thoroughly studied the macroscopic phase behavior of the polyelectrolyte complexes at a temperature of 25 °C and for a fixed HA concentration of 40 mg/L, which is somewhat above the typical concentration of HA in raw water, but allows for better experimental investigation. The polyelectrolyte concentration was varied to achieve a specific nominal charge ratio Z ranging from 0 to 1.2 and samples were studied at pH 7 and 9. The macroscopic phase behavior of aqueous solutions of humic acid containing different amounts of polyelectrolyte under these two pH conditions can be seen in **Figure 4.1**. For each sample set, the transition from the monophasic to the biphasic region can be seen, indicating the destabilization of the system as positively-charged polyelectrolyte molecules complex with negatively-charged humic acid molecules. With further increasing PE dosage the system can be restabilised thus switching back to the clear solution with water-like viscosity, same as the monophasic region for lower charge ratio value. However, a noteworthy observation is that once precipitates have formed in the biphasic region, they do not dissolve upon the subsequent addition of further cPEs. This suggests that the precipitates exhibit considerable stability, and their redispersion is kinetically constrained.

The two pH values at 7.0 and 9.0 were chosen as they are relevant to the practical situation in conventional water plants. At pH 9, the carboxylic groups are fully dissociated with phenolic groups being partially dissociated and the protonation of amino group of chitosan is negligible, i.e. the positive charge fully attributes to the permanent charge of substituted GTMAC molecules. In contrast, at pH 7, the degree of deprotonation for HA was decreased by around 20% compared to that at pH 9 as calculated from the titration curve of IHSS HA in **Table B.1**, which means that the tendency of HA to interact electrostatically will be somewhat reduced. At the same time, almost 20% amino groups from modified chitosan can be protonated (as calculated from the titration curve of unmodified chitosan in **Figure B.2**) thus adding extra

positive charges to the system. The combination of the dissolution behavior of these two species at pH 7 increases the overall charge ratio in the system, leading to effective phase separation at lower PE dosages (as the real Z would be larger). For example, the HA-PDADMAC system exhibits the transition from the monophasic to the biphasic region at Z=0.75 and 0.90, respectively, at pH levels of 7 and 9. Also, at pH 7 a biphasic region between charge ratio range 0.35-0.65 can be observed for HA-QCS2 system while at pH 9 it slightly shifted to larger charge ratio 0.45-0.7.

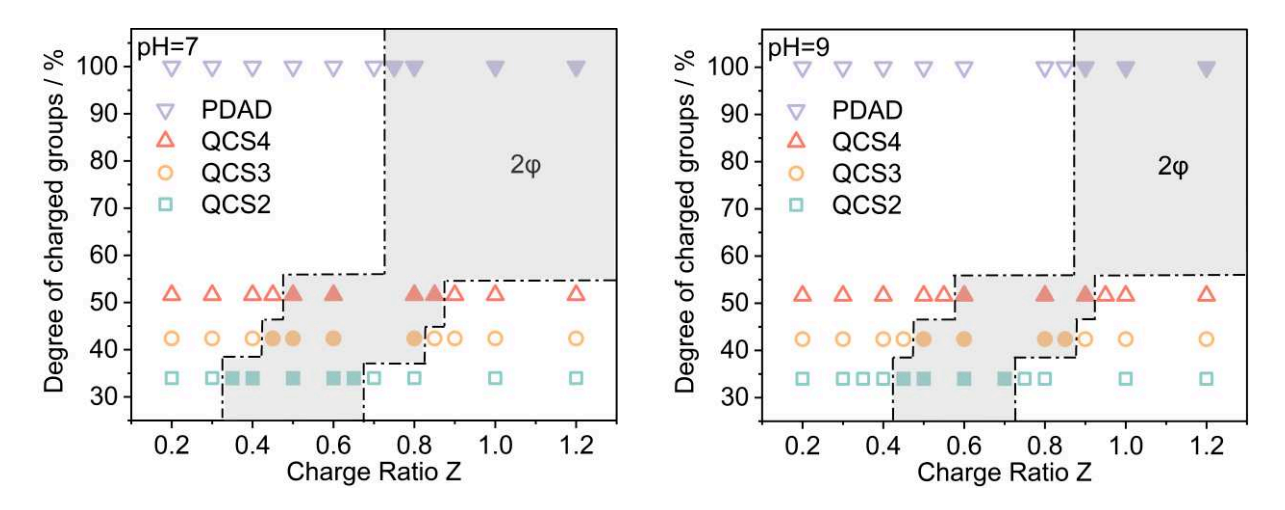


**Figure 4.1.** Phase diagram of 40 mg/L HA and added polyelectrolytes, the added amount being characterized by the nominal charge ratio Z (= [+]/[-]) at pH 7 and pH 9, respectively (T = 25 °C). Open symbols refer to monophasic regions while full symbols refer to the biphasic region.

Comparing the different cationic polyelectrolytes, one observes that PDADMAC, with its 100% charging, precipitates near the nominal charge neutralization point where the charge ratio Z = 1 at pH 9. The onset of precipitation is at Z = 0.9 or Z = 0.7 for pH 9 and 7, respectively, where this shift can simply be explained by the different degree of charge content of the HA. In contrast, modified chitosan, characterized to have a degree of charged groups ranging from 34% to 52%, shows precipitation much before reaching the stoichiometric charge neutralization point. This phenomenon may primarily be attributed to the much higher flexibility of the

charged group of QCS, compared to PDADMAC, where the charge is fixed to the polymer backbone (see **Figure 4.2**), but also to the fact that some of the amino groups of the chitosan may be charged in the complexes. This structural property should facilitate effective electrostatic interaction with the charged groups of the humic acid (HA), which are fixed within their aromatic structure and therefore not flexible themselves.

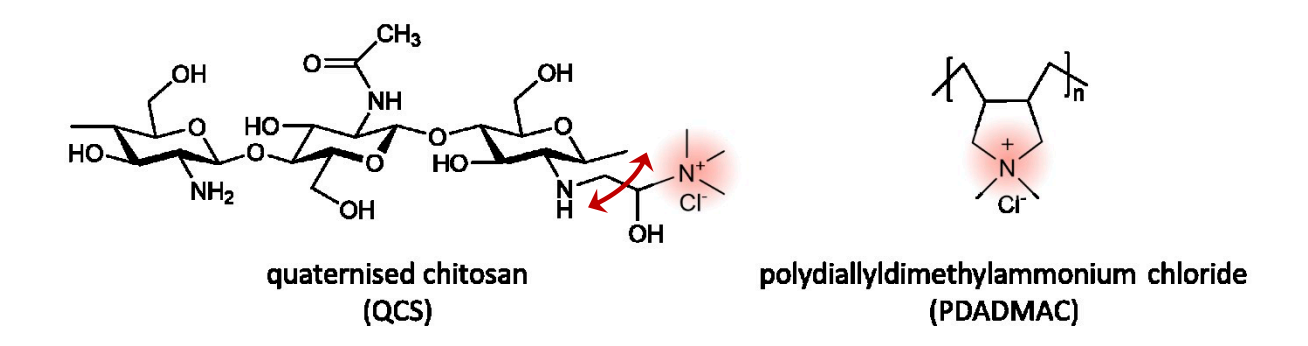


**Figure 4.2.** Structure of quaternised chitosan (QCS) and polydiallyldimethylammonium chloride (PDADMAC). The charged regions are highlighted.

In addition, one has a higher intrinsic hydrophobicity of the chitosan backbone and the QCS may interact more effectively with the hydrophobic components of HA molecules, thereby amplifying the heterocoagulation mechanism. The significance of hydrophobic interactions is further illustrated by comparing the different quaternised chitosans (QCS). A systematic shift of the phase behavior is seen and QCS2, which possesses the lowest degree of charged groups and consequently the highest hydrophobic character for a given charge ratio value, is shifted the most to the left in the phase diagram, where the transition from the monophasic to the biphasic occurs at Z=0.35 for pH 7; while for QCS3 and QCS4 it occurs at 0.45 and 0.50, respectively. This shift shows the critical role of hydrophobic interactions (and potentially interactions with the amino groups), which occurs in synergy with the charge neutralization mechanism, underscoring the complex interplay between hydrophobic and electrostatic forces in achieving effective coagulation as well as enhancing the phase separation. When plotting the

phase diagram over the concentration of added polyelectrolytes, as illustrated in **Figure B.4**, QCSs exhibit a biphasic region at a much higher concentration compared to PDADMAC due to its relatively lower charge density thereby requires higher dosages. When comparing between different QCSs, the relationship between the degree of GTMAC substitution and the phase behavior does not follow a linear pattern. Specifically, QCS3, which has a median degree of GTMAC substitution, unexpectedly exhibits the highest concentration range for the biphasic region among the QCSs, consisting with the trade-off between charge density and solubility in enhancing phase separation.

Furthermore, to visualize the interaction of humic acid and modified chitosans with varying degrees of substitution under different pH conditions, confocal microscopy was employed to observe the morphology of formed flocs. Examples of the flocs formed at pH 7 and 9 by the different QCSs with HA at charge ratio Z = 0.5 are shown in Figure 4.3, along with HA-PDADMAC flocs at charge ratio Z = 1.0, as there are no flocs formed at Z = 0.5. For QCS2 with the lowest degree of substitution of GTMAC, thus lowest charge density, a glossy and more homogeneous appearance and less distinct floc formation can be seen. In contrast, QCS4, which has the highest degree of substitution, leads to the formation of clearer and more densely packed flocs under both pH conditions. The denser floc formation at pH 7, as compared to pH 9, also indicates the favorable rearrangement of humic acid complexes in a more acidic environment. The results suggest that the degree of substitution not only influences the phase behavior but also affects the spatial packing density of flocs, which has potential implications on the floc strength, a parameter that requires precise control in the practical water treatment process to achieve efficient filtration 100. Interestingly for PDADMAC no significant effect of pH is seen, potentially due to the fact that its charge state does not change and therefore also its extent of interaction with the HA varies little.

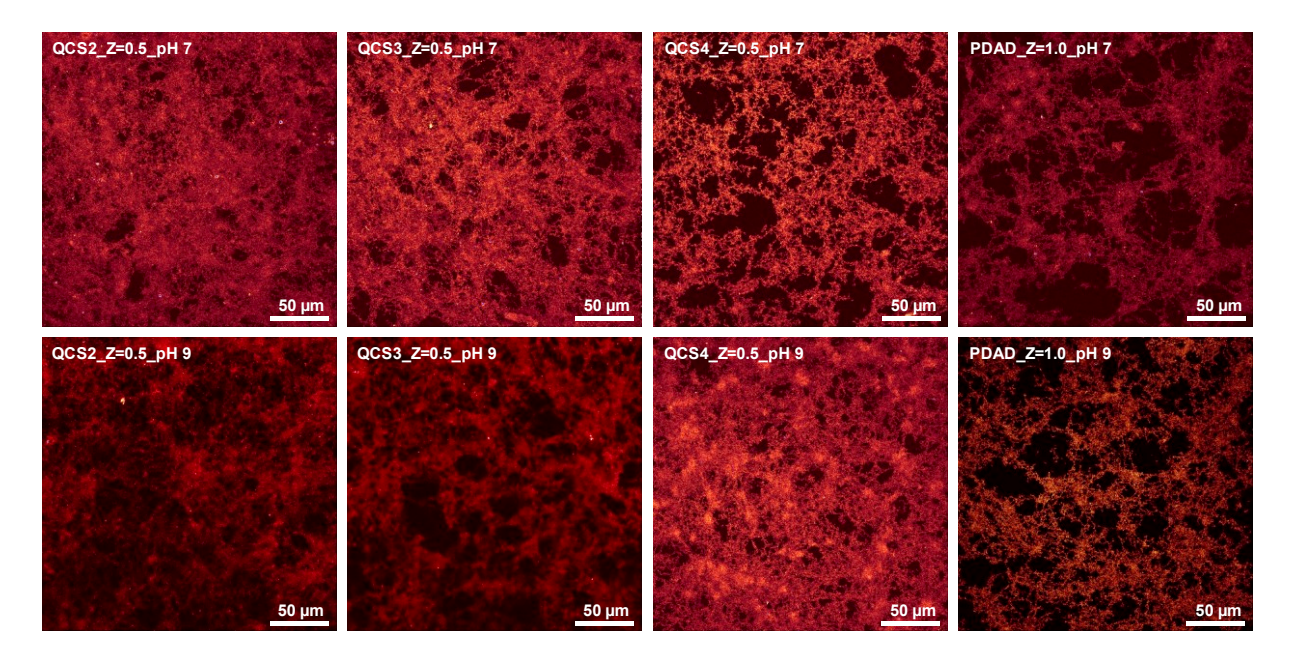


**Figure 4.3.** Confocal laser scanning microscopy (CLSM) images of precipitated flocs at Z = 0.5 for the different QCS with HA (size bar: 50  $\mu$ m).

# 4.3.2. Stability of HA complexes

The colloidal stability can be estimated by the  $\zeta$ -potential, which is the potential difference between the dispersion medium and stationary shear plane of the HA complexes. It has been used for a long time in water treatment facilities to determine colloidal stability and to optimize coagulant dosage.<sup>17, 101</sup> Tabulated values of HA complexes with different cationic polyelectrolytes are given in **Table B.1**. **Figure 4.2** shows a consistent increase of  $\zeta$ -potential for all cationic PEs added to the system. A higher value is always observed for pH 7, which is consistent with incomplete deprotonation of HA molecules and the partial protonation of amino groups of modified chitosans.

The values of  $\zeta$ -potential of modified chitosan with various charge densities are rather similar, whereas those in the reference PDADMAC system are much lower, as apparently the flexibility of the charged group on the QCS backbone allows for more effective neutralization of the negative charges on HA molecules and leads to a larger shift in the  $\zeta$ -potential. In addition, the ability of chitosan to form hydrogen bonds and to complex via hydrophobic interactions

potentially facilitates the formation of more stable HA complexes, effectively increasing the  $\zeta$ potential. In any case it is a very interesting observation that charge neutralization takes place
for much lower nominal charge compensation in the case of QCS compared to PDADMAC.

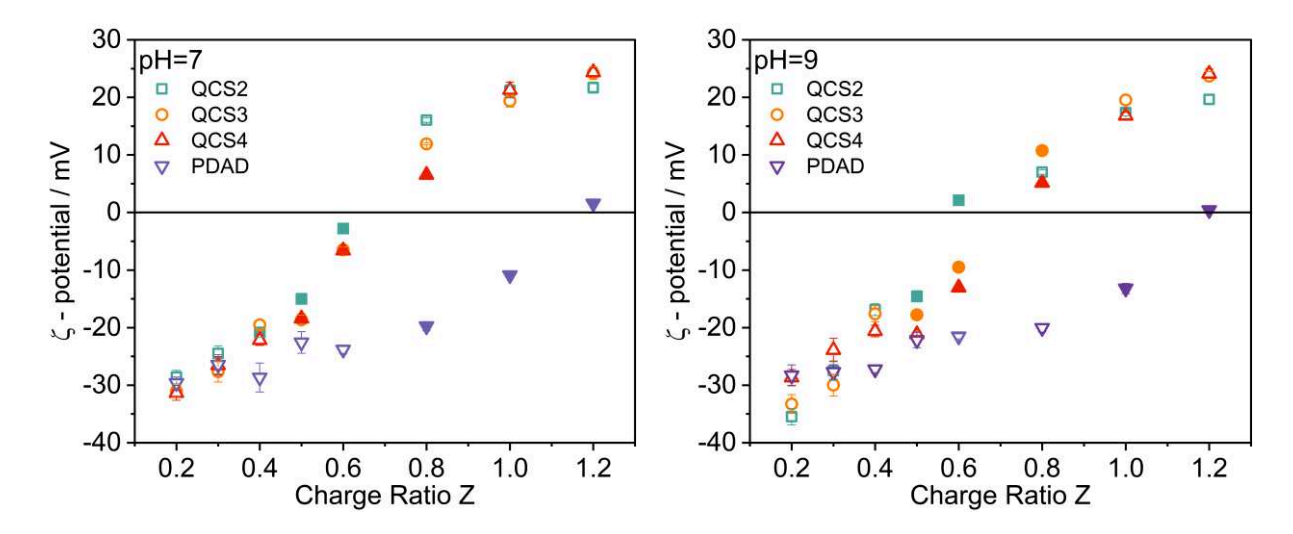


**Figure 4.4.** ζ-potential for complexes of HA and polyelectrolytes at different charge ratio Z at pH 7 and pH 9, respectively. (measurements done at 25 °C, full symbols denote samples located in the biphasic region, but measurements were done before precipitation sets in)

## 4.3.3. Removal efficiency of HA

Humic acid is known to absorb strongly in a certain UV range due to its conjugated aromatic rings, which leads to the utilization of the absorbance at 254 nm (UV254) as a water quality test parameter that provides a quick measurement of the HA content in water. <sup>102, 103</sup> As illustrated by the UV-vis spectra of humic acid solutions of different concentrations and the corresponding calibration curve in **Figure B.5** of the Supporting Information, a linear relationship between HA concentration and UV254 value can be derived to quantify the remaining HA after treatment for those biphasic sample sets, as seen in **Table B.2**.

In **Figure B.6**, the relationship between UV254 values of biphasic HA-PE systems 24 h after mixing and charge ratio Z is shown. The absorbance value can be further converted to the

concentration of the remaining HA, which is shown in **Figure 4.5**. Corresponding to the macroscopic phase behavior described before (**Figure 4.1**), in range of charge ratios Z from 0.8 to 1.2, a huge drop of the UV absorbance at 254 nm can be seen for HA-PDADMAC; while for the HA-QCS systems such phase separation occurs at lower charge ratio values, ranging from 0.4 to 0.8. It is observed that all QCS derivatives demonstrate similar removal efficiencies, albeit with a slight shift corresponding to the phase behavior. In addition, the removal efficiency increases somewhat with decreasing degree of quaternisation, i.e. in the row from QCS4 over QCS3 to QCS2. Apparently, a higher extent of hydrophobicity and lower charge density helps in the HA precipitation, becoming more efficient in agreement with the flocs observed in **Figure 4.4**. In absolute values the removal efficiency of PDADMAC is similar to that of QCS. Notably, the removal efficiency of all cationic polyelectrolytes is enhanced somewhat at pH 9 in comparison to pH 7. This increase in efficiency at a higher pH could be attributed to the higher degree of deprotonation of HA molecules, leading to stronger electrostatic interactions with the positively charged polyelectrolytes, thereby improving the aggregation and subsequent removal efficiency of HA.

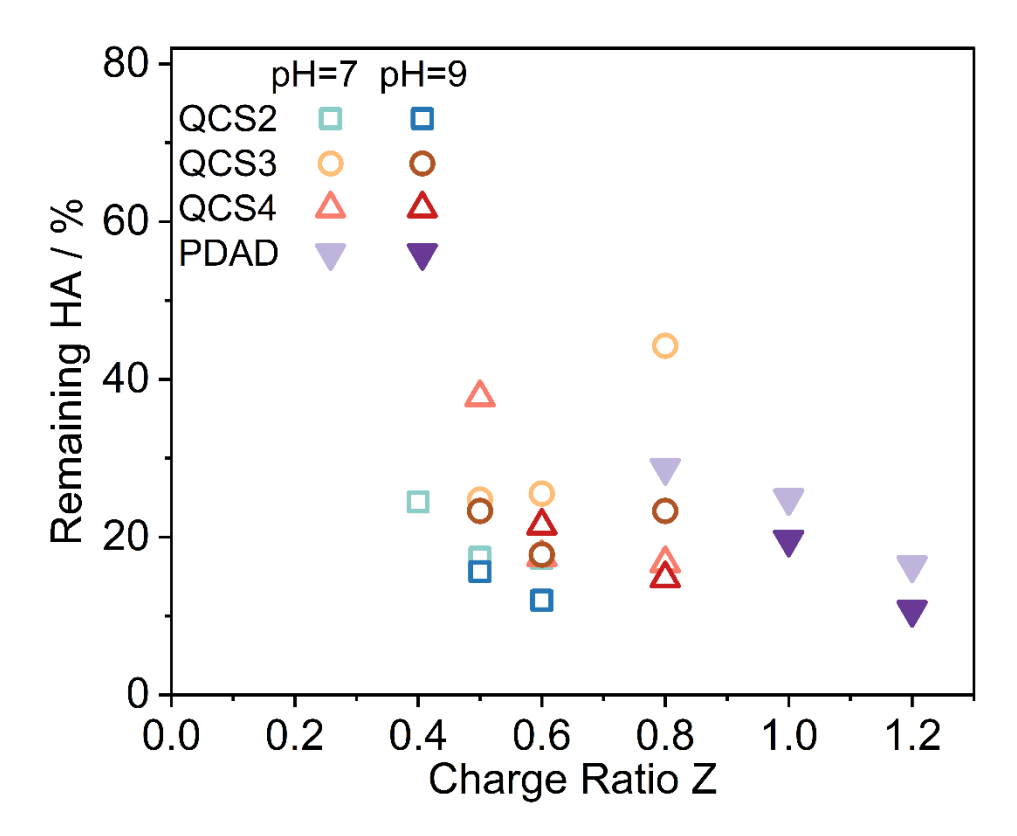


**Figure 4.5.** Remaining percentage of HA in the supernatant 24 hour after mixing HA and various polyelectrolytes under pH 7 and pH 9, respectively, at different charge ratio Z at 25 °C.

#### 4.3.4. Fluorescence Probe Studies

After having considered so far mostly the macroscopic behavior of the HA/polycation systems, we were now also interested in the question, to which extent hydrophobic domains may be formed within the complexes. To address this question we employed 6-propionyl-2-(dimethylamino)naphthalene (Prodan) as solvatochromic probe to study the local aggregation behavior, as Prodan reacts sensitive to its microenvironmental polarity. Accordingly, one can for instance study the aggregation behavior of LCST block copolymers by fluorescence spectroscopy with Prodan as polarity probe, via changes in fluorescence intensity and peak position. 106

Figure B.7 shows the fluorescence emission spectra of 1  $\mu$ M Prodan probe in the presence of varying concentrations of humic acid at pH values of 7 and 9 and the corresponding extracted wavelength of the maximum emission ( $\lambda_{max}$ ) and emission intensity ( $F_{max}$ ) are shown in **Figure** 

~ -

**4.6.** A slight shift of the spectra maximum  $\lambda_{max}$  to lower wavelength with increasing HA concentration is observed for both pH 7 and pH 9, indicating the presence of weakly hydrophobic domains within the HA aggregates. For both pH values one observes a substantial increase of fluorescence intensity of the Prodan signal for the addition of very small amounts of 5 mg/L HA but the signal then becomes smaller again for higher HA concentrations. The fluorescence intensity at pH 7 is always higher than at pH 9, indicating a less polar environment as more carboxylic and phenolic groups within HA are protonated. In addition, as shown in **Figure B.8**, the fluorescence spectrum of HA at 40 mg/L shows a broad peak around 450 nm that is independent of pH. Apparently, the intrinsic optical properties of HA are not affected by pH, while Prodan senses here a somewhat different microenvironment.

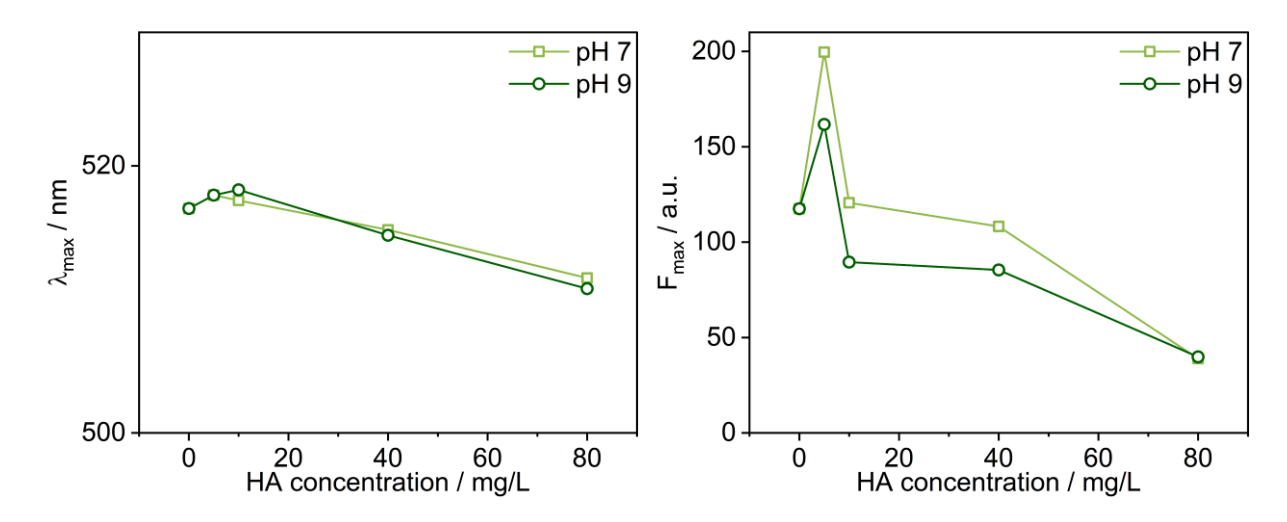


Figure 4.6. The extracted wavelength of the maximum emission ( $\lambda_{max}$ ) and its emission intensity ( $F_{max}$ ) of polarity-sensitive 1  $\mu$ M Prodan probe in varying concentration of humic acid, at pH 7 and pH 9, respectively.

For the investigation of the local polarity in the complexes of humic acid with various cPE, Prodan was added to HA-cPE complex solutions with different Z values and the emission spectra obtained are shown in **Figure B.9** and **Figure S9**. **Figure 4.7** shows the summarized extracted wavelength of the maximum emission ( $\lambda_{max}$ ) and its emission intensity ( $F_{max}$ ). All

samples were measured immediately after mixing and before macroscopic phase separation could set in.

Starting from the values seen for pure 40 mg/L HA solutions (Z=0), the addition of cPE to HA solutions leads only to small changes of the peak position ( $\lambda_{max}$ ) while the peak intensity ( $F_{max}$ ) shows more marked changes (**Figure B.9** and **Figure B.10**). This indicates that the polarity of the microenvironment of Prodan changes only rather little upon HA complexation by cPEs. This clearly shows that this complexation does not result in the formation of hydrophobic domains. The change of  $\lambda_{max}$  at pH 9 is more pronounced, especially for QCS4 with its degree of quaternization of 51.6%. The shift of the peak to ~525 nm suggests even an increase in polarity upon addition of QCS4.

In addition, the corresponding emission intensity (F<sub>max</sub>) for all complexes at pH 9 was lower compared to those at pH 7, thereby confirming the formation of a more polar environment of the Prodan that aligns with findings from pure humic acid solution at pH 9. All complexes showed a tendency for decreasing intensity as the charge ratio Z increased, especially at pH 9 the decreasing intensity is marked for PDADMAC and even more pronounced for the highly charged QCS4 and QCS3. Such Prodan quenching can be attributed to the more extensive interaction within the complexes, where a more compact structure is formed that potentially limits the mobility of Prodan<sup>40, 107</sup>. The slowing down of intensity attenuation followed by a plateau at higher charge ratio suggests that once humic acid molecules are largely complexed with polycations, further addition of polycations does not promote intermolecular interactions among HA molecules, but leads to the formation of larger supramolecular HA aggregates without significantly influencing Prodan quenching. Similar phenomenon have been seen in previous research, demonstrating the interactions between Prodan and HA in the presence of cations for instance Na<sup>+</sup>, Ca<sup>2+</sup> and Mg<sup>2+</sup>, where cation concentrations below the HA charge density significantly reduce PRODAN quenching, while higher concentrations do not further diminish this effect significantly. 108 The variation for different polyelectrolytes at pH 7,

however, was subtle and small, indicating that the effect of polymer structure to aggregation behavior in terms of hydrophobicity is screened by the HA domain, which have less activating site for cationic polyelectrolyte at lower pH value.

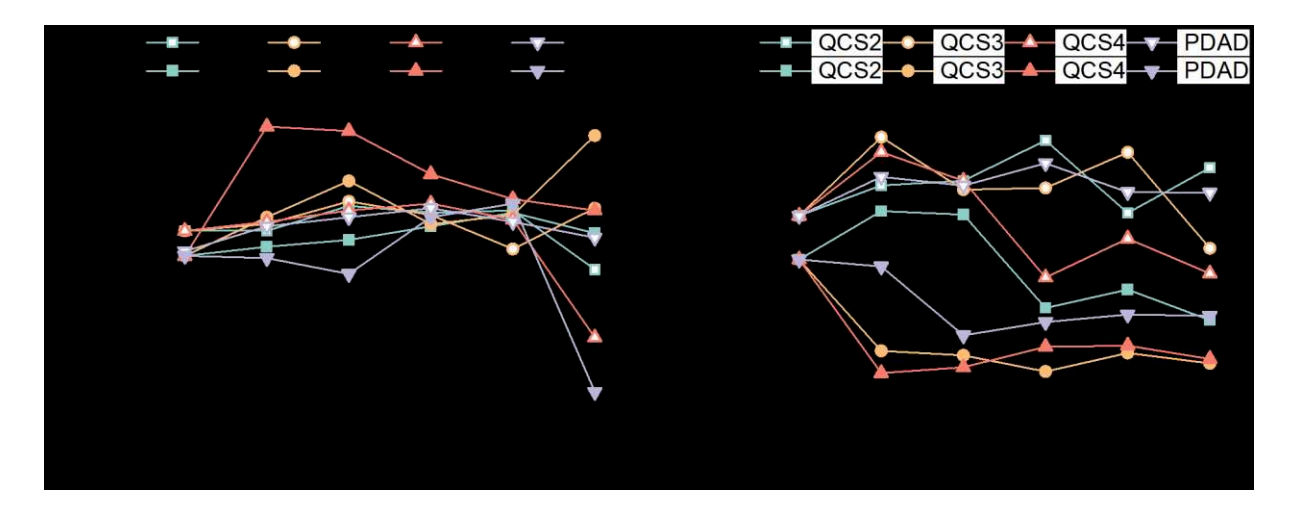


Figure 4.7. The extracted wavelength of the maximum emission ( $\lambda_{max}$ ) and its emission intensity ( $F_{max}$ ) of polarity-sensitive 1  $\mu$ M Prodan probe in varying concentration of humic acid, at pH 7 (open symbols) and pH 9 (full symbols), respectively.

### 4.3.5. Flocculation of HA complexes via light diffraction

To monitor the flocculation processes of HA with the different polycations, a time-sliced laser light diffraction experiment was done. It is necessary to mention that in laser diffraction measurements, the optical concentration of the sample is a critical parameter that must be precisely controlled around 20% to obtain reliable data. The optical concentration is the measure of obscuration of the center of the laser detector caused by the particles in the laser beam. It is calculated using the formula:

$$C_{opt} = (I_{ref} - I_{mes}) / I_{ref}$$

where  $C_{opt}$  is the optical concentration  $I_{ref}$  is the mean intensity in the detector center during the reference measurement and  $I_{mes}$  is the mean intensity in the detector center during the measurement.

However, achieving the appropriate optical concentration can be challenging, especially for certain sample sets, which are too turbid or too transparent. For instance, direct measurement of systems with 40 mg/L humic acid often results in optical concentrations that exceed the instrument's measurement range, leading to inaccurate data and risk of damaging the instrument. To circumvent these limitations, humic acid was initially mixed with various polycations to form preliminary structures at a controlled concentration of 40 mg/L for 30 s. Subsequently, the mixture was diluted with water to a final concentration of 10 mg/L HA. This step was performed to ensure that the flocculation process fell within the detectable range for subsequent measurements. This approach then mitigates the issues associated with high or low optical concentrations.

**Figure B.11 and Figure B.12** illustrate the laser diffraction particle size distribution curves recorded for HA complexes formed by various QCSs and PDADMAC with charge ratio Z of 0.4 at pH 7 and charge ratio Z of 0.5 at pH 9, respectively.

To facilitate a more quantitative analysis, the change of particle size over time were further empirically examined using a logistic growth model<sup>109</sup>, as shown in **Figure 4.8**. This model, of which the initial growth stage is approximately exponential, followed by slower process and ends with a plateau indicating the saturation state, is consistent with the observation of the particle size development over time. All the parameters derived from this analysis are listed in

## Table B.3.

For all the sample sets, the later stage is characterized by roughly exponential growth in the particle size x(50%) and levelling off to a final value within this timeframe of this experiment. One observes a state of quasi-stability during this phase, indicative of a slowed or attenuated growth rate. Only for the HA complexes formed by QCS2 with a charge ratio Z of 0.4 at pH 7 already for the first data point a rather large size is seen, indicating that substantial growth has already occurred before. Correspondingly, the inflection point for this set occurred at -17.1 s, meaning that a larger part of the growth process is not captured by this model. HA-QCS3

complexes with same charge ratio Z of 0.4 at pH 7 displayed a slightly lower final value of x(50%) of 34.24  $\mu$ m, with a higher growth rate of 0.017 s<sup>-1</sup>. The inflection point at 106.5 s for this set indicates that the midpoint of growth occurred well within our observation period, allowing for a complete capture of the growth kinetics from initiation to near saturation. Switching to QCS4 with the highest degree of GTMAC substitution, this sample set presented the smallest final x(50%) value of 30.49  $\mu$ m among the three, yet it exhibited the fastest growth rate of 0.020 s<sup>-1</sup> and the latest inflection point of 141.35 s, which reflects a slower initial growth phase followed by a rapid catch-up in size increase to reach the midpoint of growth later than the other sets. Effectively this system shows an incubation time for the particle growth, which to a lesser extent is also seen for QCS3.

Differences in the behavior of various QCS systems were also evident at higher pH of 9.0 with charge ratio Z=0.5, among which HA-QCS3 complexes exhibited the highest final x(50%) of 51.12  $\mu$ m, indicating the capacity of QCS3 to achieve larger size under similar pH conditions compared to the other modified chitosans. HA-QCS4 complexes showed the highest growth rate at  $0.016~s^{-1}$  and the latest inflection point, similar to the situation at pH 7 suggesting a delayed but rapid growth phase. Such delayed nucleation phenomena of HA complexes with higher charged QCS species could be attributed to its highest solubility, which on the other hand, benefits the following flocculation process as its higher charge density prompts the further interaction with HA molecules. Conversely, PDADMAC, which exhibits the highest charge density, it complexes with HA (see trend diagram in **Figure B.13**) display the smallest final x(50%) of 24.01  $\mu$ m with charge ratio Z=0.8 at pH 7; similarly, HA-PDADMAC complexes with charge ratio Z=1.0 at pH 9 exhibit an final x(50%) value of 27.33  $\mu$ m. For both sample environments the inflection points occurred at around -45 s, demonstrates the quickest flocculation kinetics.

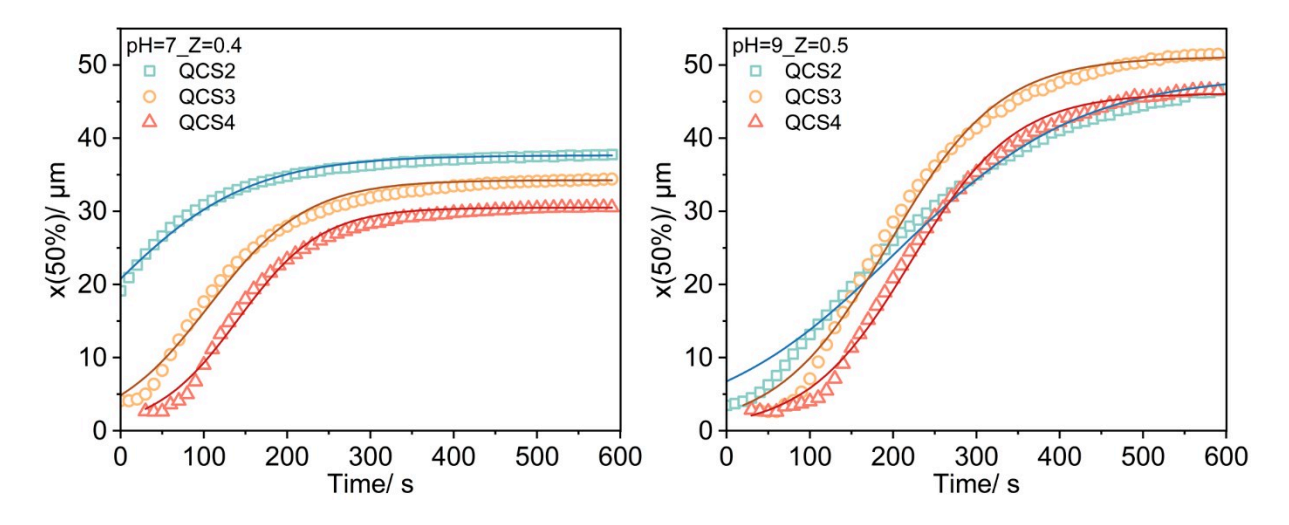


**Figure 4.8.** The trend diagram of the median particle size (x(50%)) for complexes of HA and various QCSs with charge ratio Z=0.4 at pH 7 and charge ratio Z=0.5 at pH 9. Solid lines are fits with a logistic growth model.

Additionally, the influence of pH on the flocculation dynamics of HA complexes with the same QCS at an identical charge ratio Z was investigated, the corresponding change of x(50%) over time is shown in **Figure B.14**. In general, in the more basic environment larger HA aggregates are formed. For instance, the HA-QCS4 complexes exhibited a higher maximum x(50%) value of 46.14  $\mu$ m at pH 9, in contrast to 39.05  $\mu$ m at pH 7. However, there was a notable reversal in the inflection points between the different pH levels. At pH 7, the time to reach half-maximal x(50%) was 43.35 seconds, whereas at pH 9, it extended significantly to 221.16 seconds. This phenomenon was also seen for HA-QCS2 complexes at charge ratio Z =0.4 and means that the flocculation process was significantly retarded by the higher pH.

# 4.3.6 A Case study from water filtration plant, Australia

Prior to treatment, the raw water sample received from water plant was characterized. The characterization included analysis of physical parameters such as pH and  $\zeta$ -potential, as well as chemical composition including the presence of total organic carbon (TOC). This initial characterization served as a reference point for evaluating the effectiveness of the treatment processes, as tabulated in **Table B.4** .

For water treated by PDADMAC, the UV254 results indicated that the optimal dosage of PDADMAC for water treatment was found to be 3 mg/L, where  $\zeta$ -potential was measured to near 0 and TOC showed the lowest value of 2.22 mg/L. However, no floc can be observed and it ends up with the blurry colloidal solution without phase separation, as shown in the **Figure B.15**. Interestingly, for PDADMAC as coagulant, the optimal dosage can be roughly 'predicted' by calculating the charge neutralization point. According to the measured TOC value of raw water 3.16mg/L, the humic acid concentration can be roughly converted as of 5.79 mg/L and the PDADMAC concentration when charge ratio Z [+]<sub>PDADMAC</sub>/ [-]  $_{HA}$  = 1 can be calculated, which is 3.13 mg/L that aligns well with the experimental results.

Similar experiments were conducted with a series of quaternized chitosans with different degrees of substitutions (QCS) to assess their potential as an alternative polyelectrolyte for water treatment. In contrast to PDADMAC that is failed to induce flocculation even at its optimal dosage, QCS3 (quaternized chitosan with medium degree of charged groups of 42.4%) is capable to induce flocculation at extremely low dosage down to 0.25 mg/L, as seen in **Figure B.16**. This phenomenon suggests the capability of quaternized chitosan in promoting particle aggregation and sedimentation processes for raw water with low NOM content; as its molecular structure facilitates effective bridging and adsorption mechanisms, leading to the formation of larger flocs for subsequent sedimentation. Comparable improved coagulation performance was also observed for raw water samples treated with QCS2 and QCS4, variants of quaternized

chitosan with differing degrees of charged groups, measured at 34.0% and 51.6%, respectively (**Figure B.17**). Notably, QCS4, featuring the highest degree of charged groups among the series of modified chitosans, yielded the finest flocs in the treated water.

It is notable that in the case of quaternized chitosan, the 'flocculation zone' cannot be reliably anticipated based on charge ratio, as it exhibits a notable deviation from the charge neutralization point. This stands in contrast to previous observations of pure, IHSS standard humic acid systems with much high concentration (40 mg/L), where flocculation region was more closely aligned with the charge neutralization point. The phase diagram in Figure B.4 reveals that substantially higher dosages are required to achieve flocculation for quaternized chitosans, owing to their intrinsic much lower charge density in comparison to PDADMAC. Regarding the differences between the raw water sample, with total organic carbon (TOC) equals to 3.16 mg/L, and the standard humic acid (HA) solution, typically characterized by a TOC value around 21.83 mg/L, such concentration effect may be potentially explained by the different complexation mechanism between the polyelectrolytes and natural organic matters under different concentrations. PDADMAC, which is fully charged with quite high charge density, shows greater resilience with water treatment at various concentration. At lower concentration, the active sites available for interaction with organic particles are relatively more accessible for branched quaternized chitosans, facilitating more effective binding and aggregation. Conversely, at higher concentration, the complexation with quaternized chitosan is sterically impeded while PDADMAC molecules are less hindered due to its linear chain conformation, thereby showing comparable flocculation efficacy.

The measured  $\zeta$ -potential of all treated water samples are shown in **Figure 4.9**, with a solid black dot represents the  $\zeta$ -potential of pure water samples, expected to exhibit a negative value due to the functional groups (– COOH, phenolic, etc.) commonly found in natural organic matter (NOM). A rapid jump can be observed for all cationic polyelectrolytes upon addition of 1 mg/l dose, followed by continuous increase as polyelectrolytes further added to the system.

Interestingly, despite bringing more positive charge to the system compared to quaternized chitosans, PDADMAC exhibits a lower negative  $\zeta$ -potential at low dosage range; with further addition of PDADMAC, a sharp increase in  $\zeta$ -potential is observed and reaches to the positive value. After this charge flip, the  $\zeta$ -potential of PDADMAC surpasses that of quaternized chitosans, suggesting difference in the surface charge distribution between PDADMAC and QCSs. In the case of QCSs, a consistent upward trend was observed with increasing dosage. Under the same dose, the value of  $\zeta$ -potentials follows a sequence of QCS2<QCS3<QCS4, mirroring the degree of substitution of GTMAC, as it determines the charge density of QCSs, which is proportional to the amount of positive charges brought to the system.

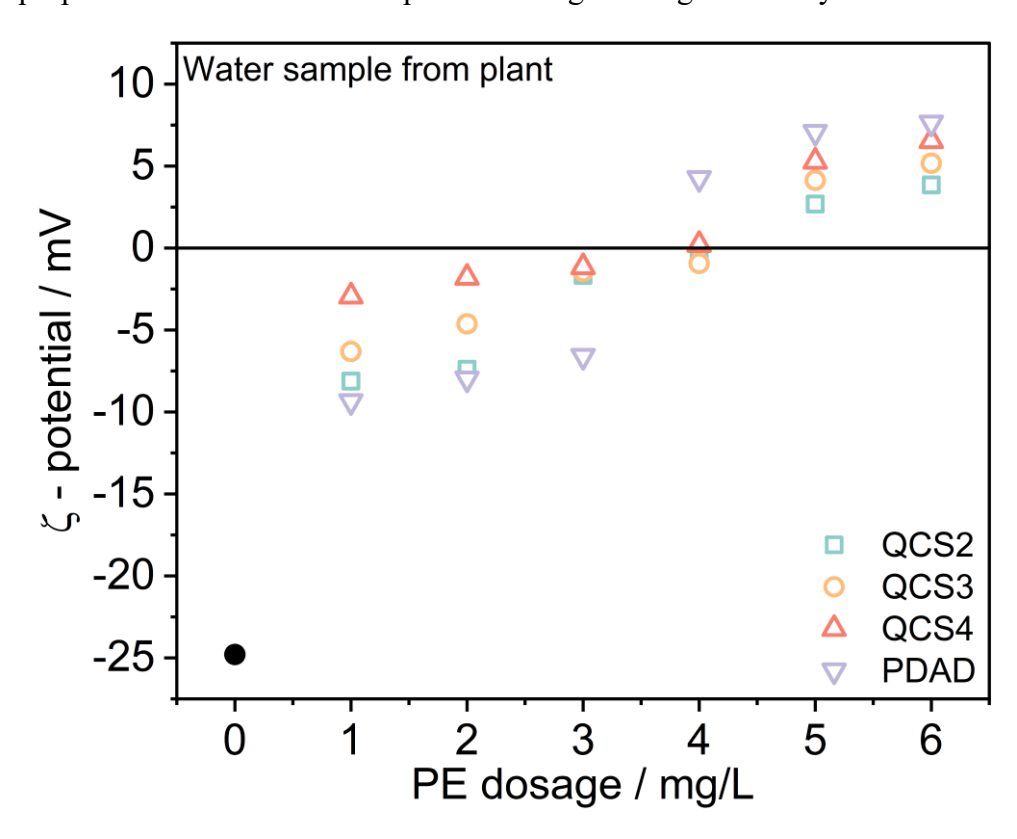


**Figure 4.9.** ζ-Potential for treated water samples with addition of different polyelectrolytes at different dosage. Solid black dot refers to raw water sample.

UV<sub>254</sub> absorbance, as a water quality test parameter that provides a quick measurement of the organic matter in water, was measured for of all treated water samples, as summarized in **Figure 4.10**. As the coagulant increased from 0 to 3 mg/L, a drop of the UV<sub>254</sub> absorbance can be observed among all polyelectrolytes, indicating the effective removal of organic matter. However, subsequent increases in coagulant dosage lead a reversal of this trend, with UV<sub>254</sub> absorbance showing a rise. Despite of the varying charge densities of the utilized polyelectrolytes, the optimal reduction in UV<sub>254</sub> absorbance consistently occurred at a coagulant dosage of 3 mg/L. This comparable 'optimal dosage point' contrasts with the previously mentioned results for UV254 absorbance for pure IHSS humic acid (HA) removed by the same series of cationic polyelectrolytes that shown in **Figure B.6**, where the lowest absorbance values for each cPE varied in a gradient manner, directly proportional to the degree of charge of the group. When the system is diluted to a certain degree, it is the mass ratio predominantly affects the phase behavior, rather than the charge ratio which typically governs under higher concentrations.

In the characterization of natural organic matter (NOM) in raw water samples through UV absorbance at 254nm, the detectable species are limited specifically to humic substances and similar compounds with conjugated aromatic rings that absorb UV light in that wavelength range. In the terms of removal efficiency, PDADMAC emerges as a superior candidate compared to QCSs in dealing with this subset of NOM. Within the QCS series, QCS3 (moderate degree of charged groups) exhibits better performance.

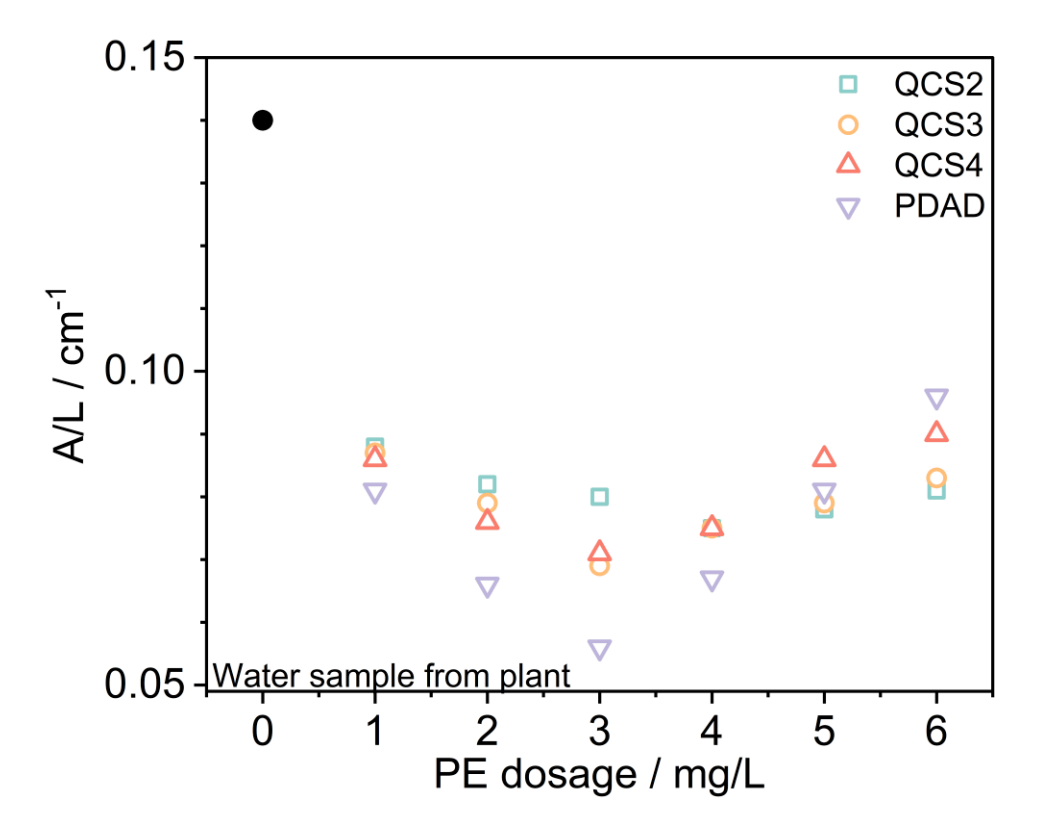


**Figure 4.10.** UV<sub>254</sub> absorbance for treated water samples with addition of different polyelectrolytes at different dosage. Solid black dot refers to raw water sample.

To enable a comprehensive detection of natural organic matter (NOM) in the treated water sample, total organic carbon (TOC) measurement was also employed apart from UV<sub>254</sub> absorbance test to quantify the total carbon content within organic compounds present in the samples, offering a comprehensive assessment irrespective of the chemical nature or structural properties of the organic molecules. Similar to the observation from UV<sub>254</sub> absorbance tests, an optimal dosage of 3 mg/L emerged with lowest TOC content for all polyelectrolytes (**Figure B.18**). However, due to the distinct sensitivity and selectivity between TOC and UV<sub>254</sub> absorbance methods, some differences reveal. In terms of the removal efficiency of total organic carbon (TOC), PDADMAC and QCSs exhibit comparable performance with optimal efficiency observed at a dosage of 3 mg/L for QCS3. For higher dosage above 5 mg/L, PDADMAC and QCS4, which have charge density up to 100%, and 51.6%, respectively, even TOC values

higher than untreated water sample were measured due to the dissolution of formed flocs that caused by charge reversal. For example, at dosage of 6 mg/L, the TOC of PDADMAC only was measured to be 1.92 mg/L and for QCS4 only is 1.55 mg/L. Such dissolution may also attribute to the higher solubility of PDADMAC and QCS4, owing to their higher charge densities compared to other polyelectrolyte.

# 4.4. Conclusion

In this paper, we looked at the potential application of chitosan in water treatment by increasing its solubility at natural pH via introducing different percentages of permanent positive charges by reacting the amino group with glycidyl trimethylammonium chloride (GTMAC). The interaction of the different modified chitosan (QCS) in the removal of negatively-charged humic acid (HA) was systematically investigated by determination of the phase diagrams as a function of the mixing ratio at a constant HA concentration of 40 mg/L. The commercial polycation polydiallyldimethylammonium chloride (PDADMAC) was used as a reference. To mimic the practical conditions in the water treatment process, measurements were performed at pH 7.0 and 9.0, respectively. For each pH condition, the charge ratio Z between the HA and quaternised chitosan with various degrees of substitution was varied to achieve a comprehensive understanding of the systems.

As seen in the macroscopic observation, humic acid can be precipitated out when the addition of fully-charged PDADMAC approaches the charge equilibrium; while such biphasic regions are seen much earlier for HA complexation with quaternised chitosans (QCSs), at lower Z the lower the charge density of the QCS. This can be explained by the structural and compositional characteristics of QCSs, where the greater flexibility of the charged groups and its intrinsic hydrophobicity of the backbone allow for more effective electrostatic and hydrophobic interactions with humic acid molecules, thus facilitating the phase separation of HA-QCS systems. Confocal microscopy was adopted to probe the morphology of the formed HA complexes with various QCSs, from which the positive relationship between packing density of flocs and the degree of GTMAC substitution was revealed. The biphasic region was shifted to lower Z at pH 7 compared to that at pH 9 due to the pH-dependence of the charge state of both humic acid and QCS molecules.

Besides the static behavior, the flocculation process of HA complexes was monitored through comprehensive laser light diffraction measurement. This study revealed distinct growth kinetics

and particle size evolution of HA complexes formed with various quaternised chitosan (QCSs). Notably, the complexes demonstrated a general pattern of rapid initial growth followed by a plateau phase of the size indicating quasi-stability, which can be fitted well by a logistic growth model. The degree of GTMAC substitution and the specific environmental pH significantly influence the flocculation dynamics, where the least charged QCS2 shows the fastest initial complexation followed by the slowest subsequent growth rate among all QCSs for a given charge ratio and ends up with larger particle sizes at a pseudo-equilibrium state after some minutes. On the other hand, it is PDADMAC with the highest charge density that shows the fastest flocculation kinetics and the corresponding smallest particles size in the plateau region. These findings underscore the critical role of cationic polyelectrolyte structure in tuning the flocculation behavior of HA complexes, providing valuable insights into the design and optimization of flocculation processes in water treatment applications.

In summary, it can be stated that QCS compares well to PDADMAC with respect to its performance in HA removal, with the advantage that by modulating its chemical structure one can tailor its performance correspondingly.

# 5. In Situ Investigation of Humic Acid - Quaternised

# Chitosan Complexation via Time-Resolved Small-angle X-

# ray Scattering

# 5.1. Introduction

Humic acid (HA), a major component of natural organic matter (NOM) in aquatic environment, brings significant challenges in water treatment due to its toxic disinfection byproducts during the necessary chlorination process. <sup>2-4</sup> Various methods have been explored for HA removal, of which coagulation-flocculation is widely adopted in practical water treatment process. <sup>15-17, 53, 54</sup> The choice of coagulant ranges from inorganic metal salts <sup>9, 10, 110</sup> (e.g. ferric chloride) to organic polymer electrolytes <sup>14, 21</sup>, with a growing demand for more efficient and environmentally-friendly options. Chitosan, a biopolymer derived from chitin, has received considerable attention due to its biodegradability and low-cost. <sup>27, 86, 91, 95</sup> It was reported that by conjugating glycidyl trimethylammonium chloride (GTMAC) onto chitosan chains, both solubility and charge density of the modified chitosan can be enhanced, which consequently allows to effectively interact with the anionic groups of HA thus demonstrate a promising approach for HA removal. <sup>98, 99</sup>

From a colloidal point of view, such interactions between humic acid and modified chitosan is the formation of a classical interpolyelectrolyte complex (IPEC) of oppositely charged polyelectrolytes.<sup>36</sup> This process typically begins with a rapid initial step where nanometric primary complexes are formed through charge neutralization<sup>60</sup>; following this, the primary complexes further grows to form secondary complexes, which involves effective bridge formation between the "dangling" chains of different primary complexes.<sup>37</sup> Such mesoscopic structure of the formed complexes affects their larger scale organization and propensity for

flocculation, contributing significantly to the effectiveness in water treatment application. However, although extensive literatures about the HA complexes at equilibrium state have been published, 40, 68, 77, 111, 112 the dynamic structural evolution of HA molecules upon complexation with coagulates at early stage remains a challenging task that rarely reported, which hinders the further innovation of coagulant materials.

Time-resolved small-angle X-ray scattering (TR-SAXS) has been reported to be an effective method for monitoring the structural evolution in mixtures of surfactants in the millisecond range, upon rapid mixing using a stopped-flow device<sup>113-115</sup>. This characterization has been also utilized in probing the kinetic processes of other systems including the self-assembly of ionizable amino-lipid<sup>116</sup>, adsorption of nanoparticles<sup>117</sup>, configuration change of proteins<sup>118-120</sup> and complexation of polyelectrolytes<sup>42, 121, 122</sup>. In a series of studies regarding a mixture of anionic-neutral and cationic-neutral block copolymers system, the fundamental intermolecular interactions and self-assembly behaviors were initially studied<sup>123</sup>, followed by the reversible vesicle to spherical micelle transition influenced by the copolymer mixing ratio and added sodium chloride (NaCl) concentration, demonstrating insights into the electrostatic and ionic strength driving factors <sup>124</sup>. These studies laid the groundwork for further kinetical investigations with TR-SAXS in real time, where the detailed the depolymerization of linear polycondensates and the random scission along the cylindrical micelle can be in-situ identified<sup>122</sup>, as well as a whole structural revolution of self-assemble that starting from spherical, cylindrical, disklike to the final vesicles formation<sup>121</sup>, demonstrating a vital role that TR-SAXS plays in revealing the transient intermediate structures of polyelectrolytes in colloidal science. Apart from salt concentration, vesicle formation was also reported to be determined by the initial concentration of surfactants that separate pathways were tracked above and below the critical micellar concentration of the more soluble component<sup>113</sup>. At lower concentration, the morphology of transient structures to forming unilamellar vesicles were more elongated compared to that at higher concentration. The homogeneous nature of the oppositely-charged sodium polyacrylate

(SPA) and polyallylamine hydrochloride (PAH), in contrast to above-mentioned heterogeneous surfactants/polymers, introduces unique polyelectrolyte complexation behavior starting from small aggregates formed through electrostatic interactions; as the polymer chains relax, the primary structure further aggregates and transient from mass fractal (random aggregate-like) to surface fractal (more compact) morphologies, exhibiting Porod behavior in the high q region<sup>125</sup>. In this work, we investigated the kinetics and structural changes during the HA and modified chitosan complexation by time-resolved small-angle X-ray scattering (TR-SAXS) with a stopped-flow device. A series of modified chitosans with varying molecular structures were synthesized in our lab by conjugating glycidyltrimethylammonium chloride (GTMAC) onto chitosan chains at different ratios<sup>98</sup>. This resulted in a series of chitosan derivatives with degrees group ranging from 34% to 52%. For comparative polydiallyldimethylammonium chloride (PDADMAC), one of the most commonly used cationic polyelectrolytes in water treatment, was used as a reference of which the degree of charged group can be regarded as 100%. These 4 mixing series were conducted under pH 7 and 9, respectively; the concentration of cationic polyelectrolytes was carefully adjusted for various nominal charge ratios Z = [+]/[-] ranging from 0.4 to 1.0, while the concentration of anionic humic acid was maintained at 40 mg/L. This setup was designed to compare the complexation behavior under different scenarios and provide a comprehensive description of the interaction dynamics across a wide range of dosages, based on the idea of simulating real conditions in conventional water treatment plants. By capturing the early-time interactions between HA and modified chitosans, this work helps to elucidate the formation pathways of the complexes, which are crucial for developing new materials tailored for the removal of humic acid, enhancing the efficiency of water treatment systems. Furthermore, by addressing the fundamental aspects of complexation between HA and modified chitosan, a system of relatively ill-defined oppositely-charged polyelectrolytes, this paper aims to contribute to the broader

application of this stopped-flow-coupled-TR-SAXS technique in practical industrial settings, enhancing its relevance and utility across various fields.

# **5.2.** Sample Preparation

HA is Suwannee River Humic Acid Standard III purchased from International Humic Substances Society (IHSS). 150 kDa polydiallyldimethylammonium chloride (PDADMAC) (low molecular weight, 100-200 kDa) was purchased from Sigma-Aldrich as 20 wt.% solutions in water and freeze-dried before usage. Chitosan (low molecular weight, 50-190 kDa) was purchased from Sigma-Aldrich. To remove any possible residual chloride ions from its production, chitosan was precipitated, washed and freeze-dried before usage. All samples were prepared by Milli-Q water ( $18.2 \text{ M}\Omega \cdot \text{cm}$  at  $25^{\circ}\text{C}$ ).

The stock solution of HA was prepared at 80 mg/L, which corresponds to a nominal charge concentration of 0.314 mM at pH 9, as calculated from the averaged molecular weight of the charged unit determined from titration (Mw(charge) = 255 g/mol; see the titration curve in **Figure B.1**). The pH of HA solutions was adjusted to 7.0 and 9.0 with 0.1 M NaOH solutions. The stock solutions of modified chitosans and PDADMAC were prepared to achieve a nominal charge concentration of 0.314 mM to make sure when mixed by stopped-flow instruments at 1 :1 ratio, the nominal charge ratio Z = 1.

# 5.3. Results and Discussion

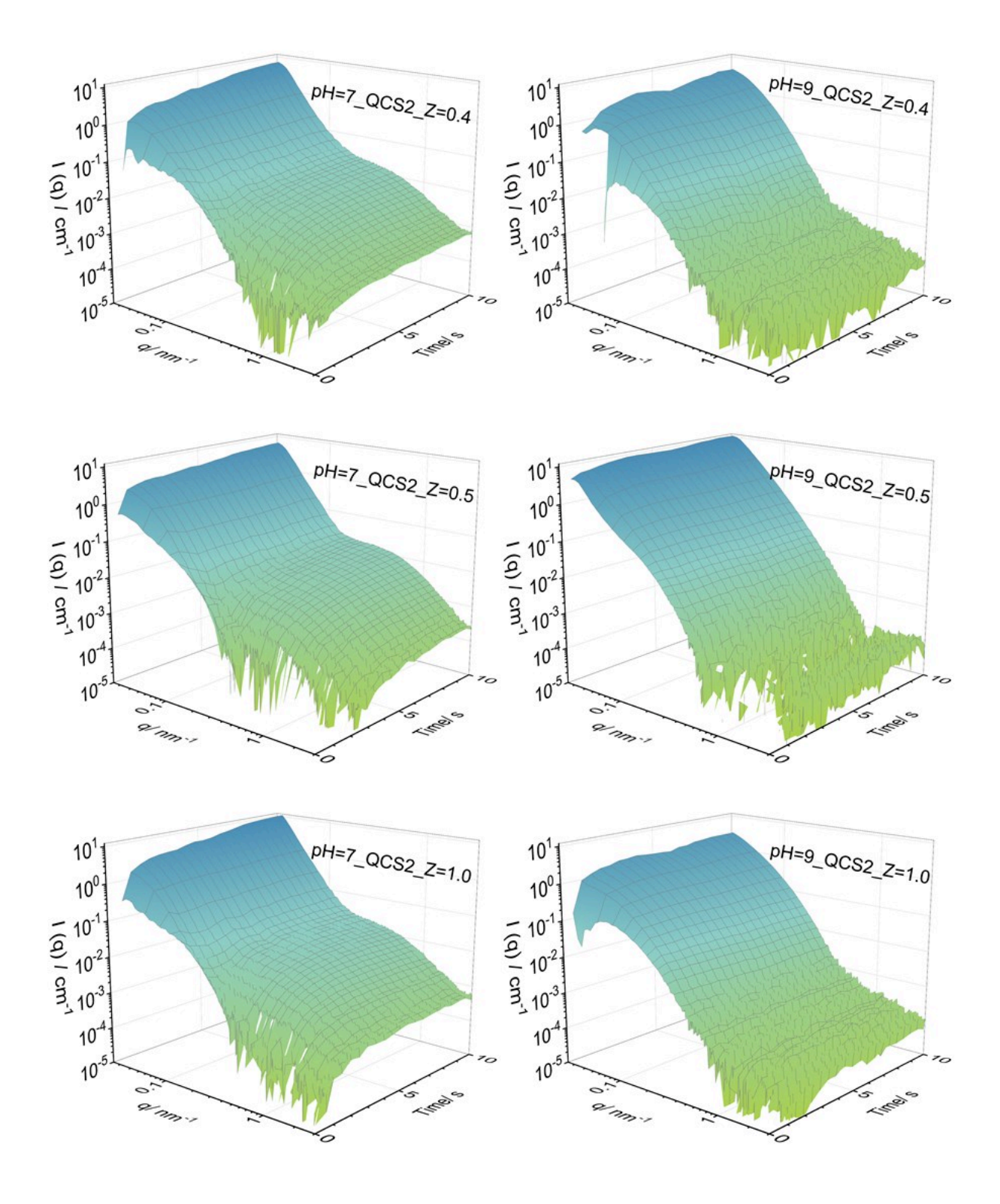
The macroscopic phase behavior of the polyelectrolyte complexes at a temperature of 25 °C and for a fixed HA concentration of 40 mg/L has been thoroughly studied in last chapter, with varied polyelectrolyte concentrations to achieve a specific nominal charge ratio Z ranging from 0 to 1.2 and samples were studied. In this part, we focus on time-resolved changes during the formation of HA complexes upon rapid mixing with cationic polyelectrolytes (cPEs) by timeresolved small-angle X-ray scattering (TR-SAXS) which coupled with a stopped-flow device. Identical with the static phase behavior studies, for cPEs we adopted three quaternised chitosans (QCS) with different molecular conjugating structures (obtained by glycidyltrimethylammonium chloride (GTMAC) onto chitosan chains with different ratios to achieve series of degree of quaternization ranging from 0.4 to 0.7) that were synthesized in our lab and most commonly employed cPE in water treatment polydiallyldimethylammonium chloride (PDADMAC) as a reference.

# 5.3.1. Influence of the pH value

The pH values of 7.0 and 9.0 were selected for this study to align with conditions commonly found in conventional water treatment plants. As discussed in last Chapter, at pH 9, the humic acid molecules are largely dissociated with the negligible protonation of the amino groups in chitosan; at pH 7, although nearly 20% of the amino groups in modified chitosan can be further protonated besides the permanent charge of the GTMAC-substituted molecules, the deprotonation degree of HA is reduced by approximately 20%, i.e. the charged HA molecules that can participate into the complexation are relatively limited so that slow down the whole process.

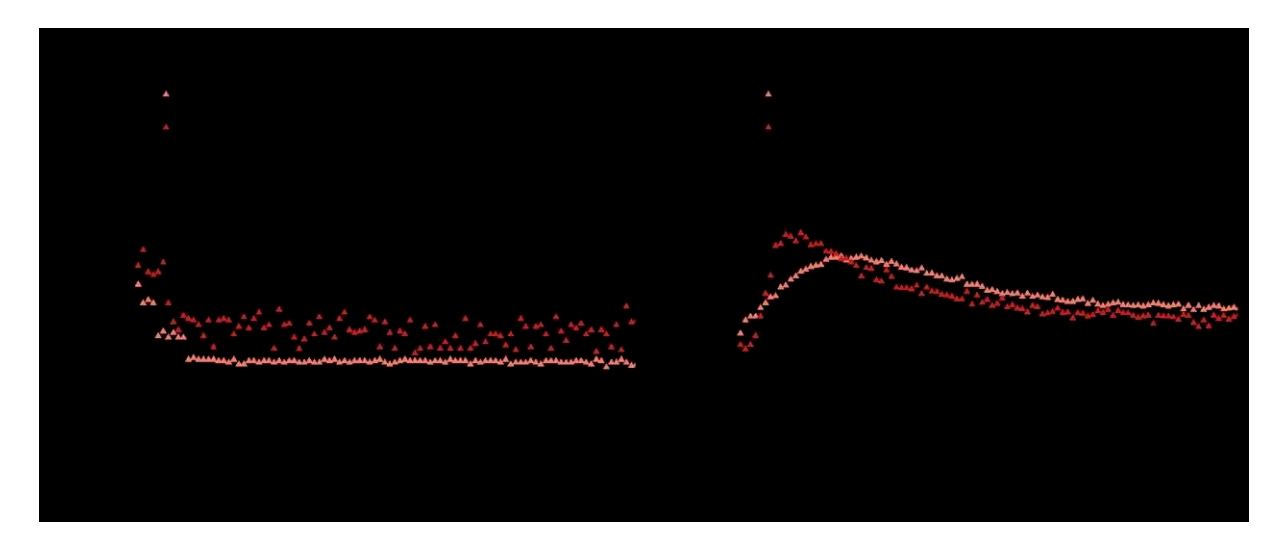
Specifically, for the HA-QCS2 complex formation at pH 7.0, as seen in **Figure 5.1** where q is the scattering vector and I(q) is the X-ray scattering intensity, the q values where notable

Figure C.1, the 'halo' structure can be observed roughly 3 s after mixing, suggesting the onset of primary structure formation of polyelectrolyte complexes between modified chitosan and HA. It leads to aggregates with characteristic sizes in the range of approximately 10 nm; while at pH 9.0, the variation between each time frame can be captured only for the initial 2-3 second without the formation of any primary structure. Similar variation between the two pH values can also be observed for HA-QCS3 system (Figure C.2 and Figure C.3).



**Figure 5.1.** 3D time-resolved SAXS curves illustrating the kinetic pathway of HA-QCS2 complex formation following rapid mixing at various Z charge ratios and pH values of 7.0 and 9.0. Each curve represents a time interval of 0.5s with 20 time frames recorded.

HA complexation with higher charged cPEs (QCS4 and PDADMAC) is too rapid to be monitored with a time interval of 0.5 s, as the variation between each time frame is hardly recognized thus instead 20 ms time interval was mainly adopted to probe the change over time. The 2D time-resolved SAXS curves (Figure C.4 and Figure C.5) does not clearly stated the change over time as well as the difference between each pH values. To highlight the changes upon complexation, SAXS curves were normalized to the curve of a pure 40 mg/L HA solution at corresponding pH values. Figure C.6 is an example of the normalized data indicating formation of HA-QCS4 (51.6 % quaternization) complexes after rapid mixing at different Z charge ratios where a peak can be observed. Those normalized data were further analyzed using custom python scripts to determine the peak position of all 100 curves for each sample set. A comparison between pH=7 and pH=9 for HA-QCS4 complexes at Z=0.5 regarding the q value at the peak position as well as the intensity of peak is shown below at Figure 5.2. It is clear that under both conditions a slight shift to lower q range around 0.1 nm<sup>-1</sup> is completed within 0.2 s upon mixing, with increasing peak intensity followed by the long-tail decreasing until reaches the plateau. Specifically, at pH 7, it takes longer time to reach the equilibrium state then that at pH 9, and the equilibrium q value is lower, indicating that larger aggregates are formed at the lower pH value. Those variation universally applied to HA-QCS4 complexes with other charge ratio Z values as well as HA-PDADMAC complexes, as shown in Figure C.7 and Figure C.8. This suggests that the environmental pH significantly influences the aggregation kinetics and the size of the resulting complexes.



**Figure 5.2.** Development of the peak position of the normalized results versus period upon mixing during the complexation of HA and QCS4 at charge ratio Z=0.5 and pH values of 7.0 and 9.0.

At larger length scale that was probed by q value done to 0.007 nm<sup>-1</sup>, the temporal changes in the complexation process between HA and cPEs is less distinct. Specifically, for HA-QCS4 complexes at a charge ratio Z=0.5, both at pH 7 and pH 9, the evolution of a globular structure is evidenced by the formation of a "peak" that shifts to the lower q range within 120 seconds as seen in **Figure 5.3**. This shift effectively allows the direct visualization of the growth of the formed complexes. The derived peak position of the normalized results over time shows that the peak shifts significantly from approximately 0.25 nm<sup>-1</sup> to 0.02 nm<sup>-1</sup>, indicating the formation of aggregates starting from a length scale of about 30 nm and expanding up to 400 nm.

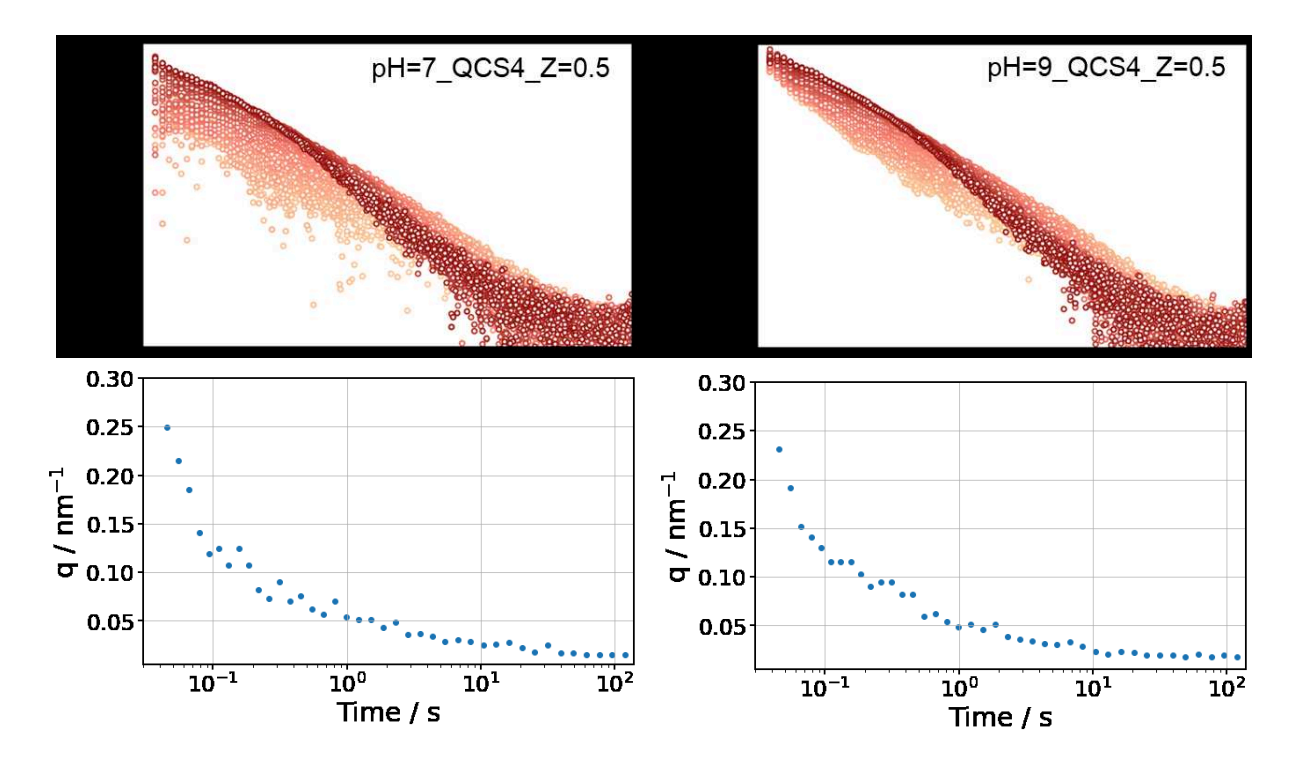


**Figure 5.3.** 2D time-resolved SAXS curves illustrating the kinetic pathway of HA-QCS4 complex formation following rapid mixing at charge ratio Z=0.5 and pH values of 7.0 and 9.0. Each mixing event was recorded over 40 frames throughout a total duration of 120 seconds, with intervals spaced by a power law.

## 5.3.2. Influence of the charge ratio

From the macroscopic phase observation of the final state after mixing, it was seen that for each sample set of humic acid and cationic polyelectrolyte, a noticeable transition from the monophasic to the biphasic region is observed, highlighting the destabilization of the system as positively-charged polyelectrolyte molecules interact with negatively-charged humic acid molecules. As the dosage of the cationic polyelectrolytes is further increased, the system can be restabilised, reverting to a clear solution with water-like viscosity. Such distinct variation between different charge ratios, however, was not revealed in the microscopic length scale smaller than ~50 nm at the initial complexation. As shown in **Figure C.9**, during the complexation of HA with various cationic polyelectrolytes (cPEs), comparable q values regarding the peak position are observed for different charge ratio Z values at the equilibrium

state. This indicates that the formation of primary structures at early stage does not depend on the charge ratio as the rapid complexation between anionic HA and cationic cPEs upon mixing is primarily driven by static electricity.

When the q value shifts to a lower range e.g. the exploration of larger length scales, the differences between various charge ratios become more pronounced for each HA complexation process, as indicated by the summary of scaled 2D SAXS curves in Figure 5.4, illustrating the kinetic pathways of humic acid complex formation following rapid mixing with various cPEs at different charge ratios and a pH value of 7.0 as color shifts from lighter to darker shades. Each mixing event was recorded over 40 frames during a total duration of 120 seconds, with intervals between frames determined by a power law. As the curves are scaled and presented separately, it becomes easier to observe the onset of a 'halo' in most of the sample sets that shifts to lower q ranges, indicating the growth of HA complexation over time. In the case of HA-QCS2 complexes, the onset of the 'halo' shape is observable at a very early time, within only 0.1 s of mixing, showing rapid structural changes upon initial contact between the components. Specifically, at charge ratio Z = 0.4, the halo rapidly shifts to the lower q range and gradually flattens, indicating a quick formation of large-scale structures that stabilize over time. In contrast, at charge ratio Z = 0.5, at which phase separation was observed in the macroscopic observation, the halo is markedly more intense and persistent even after two minutes. However, the shift of this halo in the q range 0.04 - 0.2 nm<sup>-1</sup> is quite negligible, suggesting that the size of the aggregates remains relatively constant. This indicates that although the aggregate size does not increase substantially, the internal structure becomes denser at this particular charge ratio, corresponding well to the enhanced HA removal efficiency that observed in static phase behavior that described in last Chapter. As the charge ratio further increases towards the one-phase diagram, a subsequent shift in the halo can be observed. However, this halo shape begins to diminish as time develops, suggesting a more uniformly distributed complexation environment, where the aggregates likely reach a bigger size at

equilibrium state while more loosely packed. From previous results of zeta potential measurements in Figure 4.4, those shifting and diminishing halo occurs at the charge ratios where larger absolute zeta potential values were measured. This observation reveals that when there is an excess of either positive or negative charge within the system, it promotes rearrangement into larger aggregates with greater length scales; while on the other hand, their density is substantially reduced. This inverse relationship between the size of the aggregates and their density can be attributed to the fact that while the aggregates grow larger due to the excess charge facilitating more extensive cross-linking or binding among the HA complexes, the internal structure of these aggregates becomes less compact. The zeta potential value serves as an indicator of the system's stability and the strength of the electrostatic interactions. Higher absolute values of zeta potential suggest stronger electrostatic repulsions between each HA complexes, leading to more robust particle stabilization but with less dense packing within the aggregates. For PDADMAC, which is a fully charged cationic polyelectrolyte, the behavior observed in SAXS measurements differs notably from other modified chitosans. The SAXS curve for the HA-PDADMAC complexation does not exhibit a halo structure or any noticeable shift, even at a charge ratio Z = 1, which is at the precipitation region as observed macroscopically. This lack of structural change in the SAXS data suggests the extremely rapid interactions between PDADMAC and humic acid that out of the detection window of current time-resolved SAXS setup; also, despite reaching charge neutralization point or not, the complexes formed are too small and lack of the ability of further formation of larger structured aggregates.

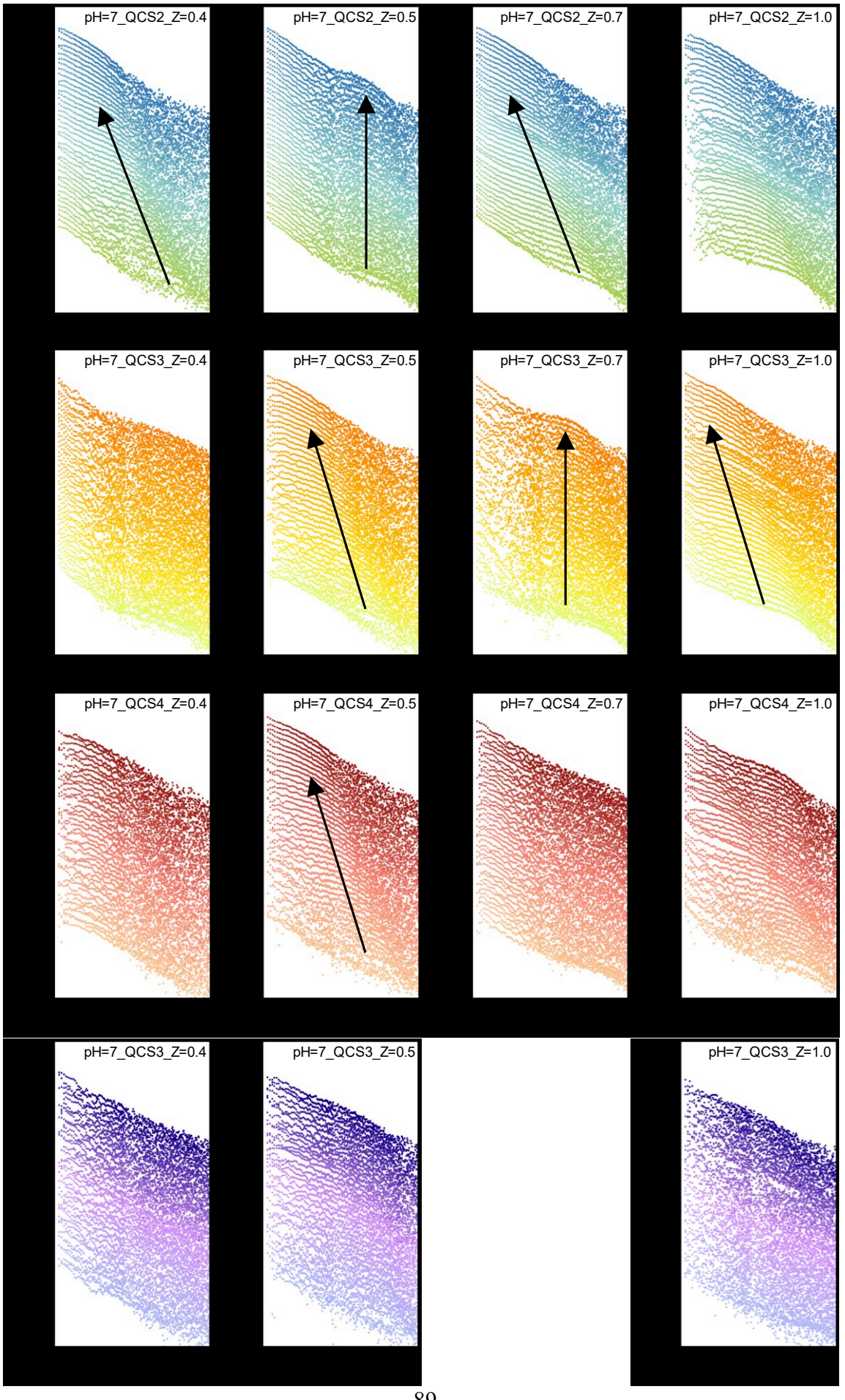


**Figure 5.4.** Scaled 2D time-resolved SAXS curves illustrating the kinetic pathway of HA complex formation following rapid mixing with various QCSs at various Z charge ratios and pH values of 7.0. Each mixing event was recorded over 40 frames throughout a total duration of 120 seconds, with intervals spaced by a power law. Additionally, the gradients of color in each figure represent temporal progression; curves start with lighter colors for earlier times and gradually darken as time advances.

To quantitate the changes of HA aggregates, SAXS curves were normalized as abovementioned to the curve of a pure 40 mg/L HA solution at pH 7. Figure C.10 is a summary of some of the normalized data indicating formation of HA-QCSs complexes after rapid mixing at different Z charge ratios. The normalized data was processed using custom python scripts to determine the peak position of all 40 curves for each sample set. This detailed analysis allowed for the precise tracking of changes in the q values of the peak positions over time and the results are comprehensively summarized in **Figure C.11**. This figure illustrates the temporal evolution of the q values for each sample set, providing a clear visual representation of how the peak positions shift throughout the experiment. Figure 5.5 shows an examples of HA complex formation following rapid mixing with QCS2 at charge ratio Z=1.0 and pH values of 7.0. A plateau in q value is evident after 30 seconds, indicating that the 120 s measurement timeframe utilized in this study sufficiently captures the essential dynamics of the system. A rapid decreasing of q can be observed within 0.2 s, corresponding to an increase in particle size from approximately 48.36 nm to 111.08 nm; this rapid aggregation gradually slows down and ultimately reaches up to 511.83 nm by 120 s. This stabilization of peak position suggests that significant structural changes of HA complexation reaches a steady state. The evolution of aggregation size over time was fitted to determine the rate constant of this initial complexation step via Logarithmic Growth model, which is often used in systems where growth slows down over time. Characterized by the equation

$$Size(t) = a * ln(bt + c)$$

where a is the scaling factor that adjusts the vertical stretch of the curve, b is the steepness of curve that influences the rate of growth and c is the horizontal shift factor that determines the starting point of growth on the time axis.

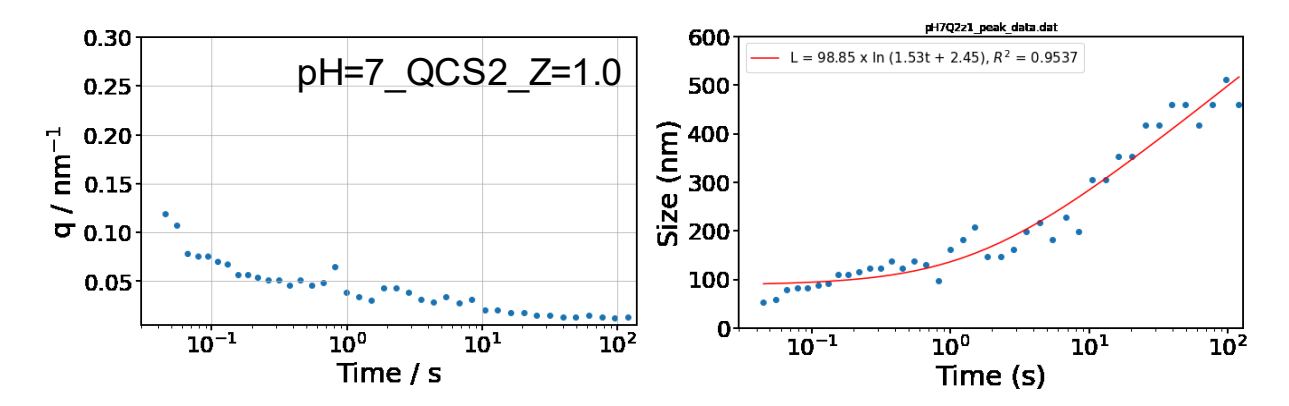


**Figure 5.5.** Development of the peak position for the normalized pH=7\_QCS2\_Z=1.0 sample set within 120s and the evolution of aggregation size over time. Red line refers to the fitted data from via Logarithmic Growth model.

The fitted curves for the pH=7\_QCS2 sample set at various Z charge ratios and pH values of 7.0 within 120s are displayed in **Figure C.12**. The results of these curve fittings are comprehensively summarized in **Table 5.1**. For the sample set with a charge ratio Z = 0.4, a peak growth rate revealed with value a equals to 91.95, suggesting a rapid initial increase in aggregation size that slowing considerably as time progresses; for Z = 0.7 and Z = 1.0, the growth rates are comparable high, but with differing coefficients b, which reflects the steepness of the growth curve. For Z = 1.0, the steepness factor b is considerably smaller around 1.53, suggesting a more gradual increase in size over time; in contrast, for Z = 0.4 and Z = 0.7, a much steeper growth curve was observed, reflecting a faster aggregation process early in the reaction. The data set with a charge ratio Z = 0.5, however, exhibits a much lower initial growth rate a as well as a much higher value of b, corresponding to the quite negligible increase in aggregate size over time within the detected time scale as previously discussed. It is necessary

to point out the relatively low  $R^2$  value around 0.75 for such complexation behavior, suggesting that the fit of the Logarithmic Growth model to the experimental data is less robust as the major complexation process at Z = 0.5 is too rapid to be appropriately captured within the current time scale of the instrumentation utilized.

**Table 5.1.** The fitted parameter and the corresponding goodness of fit  $R^2$  as determined by the Logarithmic Growth model for complexes of HA and various cationic polyelectrolytes with various charge ratio Z.

	Z	a	b	c	R <sup>2</sup>
pH=7_QCS2	0.4	91.95	5.52	1.18	0.93
	0.5	9.27	10.83	56.08	0.75
	0.7	87.38	5.99	1.69	0.94
	1	98.85	1.53	2.45	0.95

# 5.3.3. Influence of the degree of the quaternization

As summarized in **Table 4.1**, the degree of substitution in quaternized chitosan can be controlled by varying the molar ratio of GTMAC to chitosan during the modification process, which leads to a series of degree of charged group ranging from 34 % to 51.6 %. For comparative purposes, PDADMAC is used as a reference condition where the degree of charged group is 100%.

From the results collected at EMBL, where the complexation process was probed at a higher q range, it was observed that with an increase in the degree of charge of the groups, the peak around 0.9 nm<sup>-1</sup> was not detected, which can be seen more obviously in the Kratky– Porod plot, as shown in **Figure 5.6**. For the lower charged cationic polyelectrolytes, QCS2 and QCS3, the development of the peak position of the normalized results versus period upon mixing during the complexation was listed in **Figure C.13** and **Figure C.14**, respectively. The evolution of

peaks around 0.9 nm<sup>-1</sup> indicates the formation of stable complexes at the characteristic scattering lengths at 10 nm. The peak structure for HA-QCS2 complexes becomes apparent within 2 s after mixing, indicating rapid complexation kinetics for the primary structure. In contrast, for QCS3 of which the charge density is higher, the onset of a similar peak structure takes slightly longer, suggesting slower complexation process influenced by the higher solubilization of QCS3. Despite the swift formation of peak structures in both cases, the intensity of these peaks continues to increase until reaching to a plateau around 10 s after mixing. This behavior indicates that while the initial primary structure formation is rapid due to static electricity between oppositely charged polyelectrolytes, the subsequent growth of these complexes continues slowly as the system approaches to the equilibrium state.

However, for QCS4 and PDADMAC, which have higher degree of charge and enhanced solubility compared to QCS2 and QCS3, the SAXS results in **Figure C.7** and **Figure C.8** reveal distinct behavior. Notably, only a slight increase at q 0.1 nm<sup>-1</sup> is observed with the absence of peak at 0.9 nm<sup>-1</sup>, suggesting the formation of larger aggregates at the length scale around 50 nm. The equilibrium state for these higher charged polyelectrolytes is also reached significantly faster, with both the peak position and intensity stabilizing within just 1 s. The increased charge for QCS4 and PDADMAC significantly enhances their interaction with HA molecules, speeding up the initial binding and aggregation processes. However, the higher solubility of these polyelectrolytes also plays a role in forming more dispersed state of the complexes, which hinders the formation of more distinct aggregate structures.

Interestingly, the effects of pH on complexation process are different between lower charged and higher charged cationic polyelectrolytes. For QCS2 and QCS3, which have lower charge densities, adjusting the pH from 7 to 9 results in distinct phenomena that the complexes formation at the length scale of 10 nm cannot be observed anymore (**Figure 5.1** and **Figure C.2**); while for QCS4 and PDADMAC, changes in pH do not significantly alter the complexation behavior (**Figure C.4** and **Figure C.5**). This comparison indicates that the higher

charge density of these cationic polyelectrolytes may play a dominating role in determining the interaction dynamics, effectively overshadowing the effects of dissociation state of HA molecules and protonation state of the cationic polyelectrolytes at the different pH values.

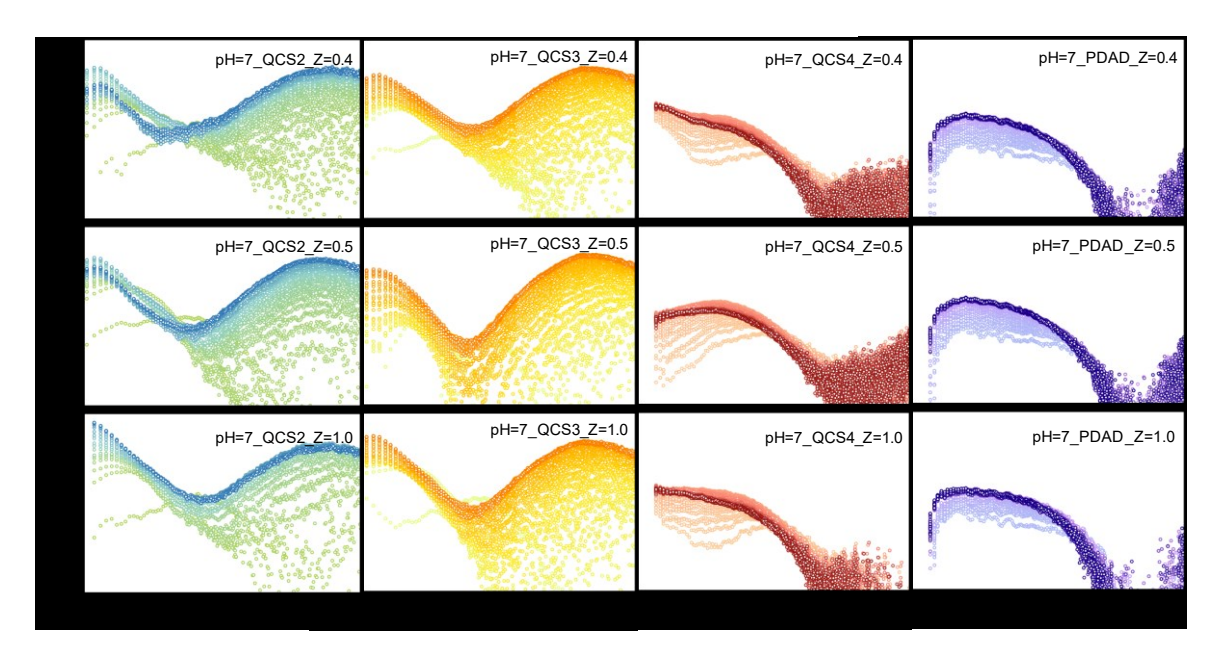


Figure 5.6. SAXS intensity  $I \times q2$  as a function of the magnitude of the scattering vector q for complexes of HA and various cationic polyelectrolytes following rapid mixing with various charge ratio Z at pH 7.

While regarding the results measured at ESRF, where the q range shifts to lower value, e.g. larger length scale can be probed, the differences between various QCSs are less pronounced, as shown in **Figure 5.4**, the SAXS curves for all QCSs display a temporal evolution of the peak towards the lower q range when complexed with HA molecules. Notably, as the degree of charged groups increases from QCS2 to QCS4, the emergence of this peak shape occurs at higher charge ratios, correlating well with the right shifted biphasic region that observed in macroscopic experiments. In the specific case of PDADMAC, which is a fully charged cationic polyelectrolyte, the evolution of a peak shift is rarely observed. As observed from previous results, PDADMAC binds with the negatively charged sites on HA too rapid upon mixing that the complexation process falls outside the detection window of the SAXS instrument.

A close examination of HA complexation with various cationic polyelectrolytes at charge ratio Z=0.5 reveals detailed insights into the complexation process. The progression of peak position alongside the corresponding development in complexes size are displayed in **Figure C.15**, providing a visual representation of how the complexes grow and stabilize. Also, the data have been analyzed using the Logarithmic Growth model of which the parameters derived are comprehensively tabulated in **Table 5.2**. The R<sup>2</sup> value of 0.56 for the PDADMAC complexation with HA is too low, indicating that the logarithmic growth model does not adequately fit the data. The comparison of growth rate constants among the QCS series, ranging from QCS2 to QCS4, shows an increase from 9.27 to 77.97. The highest value for QCS4 suggests a faster initial complexation with HA, likely due to its higher charge density. Conversely, the steepness of growth decreases with an increasing charge density across the QCS variants, highlighting a trade-off between rapid initial complexation and the rate of reaching near-maximum aggregation.

In general, the impact of different types of cationic polyelectrolytes on complexation at larger length scales seems to be less pronounced compared to their effect at smaller length scales. This observation suggests that although the formation of primary structures is highly sensitive to the specific properties of cationic polyelectrolytes regarding their various charge densities, such cPE factor become weaker in determining the subsequent aggregation processes that leading to larger scale complexes.

**Table 5.2.** The fitted parameter and the corresponding goodness of fit R<sup>2</sup> as determined by the Logarithmic Growth model for complexes of HA and various cationic polyelectrolytes at charge ratio Z=0.5 and pH values of 7.0.

	cPE	a	b	c	R <sup>2</sup>
pH=7_Z=0.5	QCS2	9.27	10.83	56.08	0.75
	QCS3	59.60	9.88	1.50	0.99
	QCS4	77.97	2.13	1.75	0.97
	PDAD		n/a		0.56

#### 5.4. Conclusion

In this work, we systematically explored the interaction between oppositely charged humic acid (HA) and polycation modified chitosans (qCs), focusing on the kinetics of these complexations at initial stage upon mixing via time-resolved Small-Angle X-ray Scattering (SAXS) combined with a stopped-flow instrument. Same to the system investigated in last Chapter, for cationic polyelectrolytes (cPEs), we employed three quaternized chitosans (QCS) with varying molecular structures. These were synthesized by conjugating glycidyltrimethylammonium chloride (GTMAC) onto chitosan chains at different ratios to achieve a series of degrees of quaternization ranging from 0.34 to 0.52. The most commonly employed cPE in water treatment polydiallyldimethylammonium chloride (PDADMAC) was also adopted as a reference. All of these investigations were done at pH 7.0 and 9.0, respectively, to mimic the realistic conditions in a water plant. To obtain a comprehensive view of the behavior of this system, the nominal charge ratios Z = [+]/[-], defined as the ratio of positive to negative charges was varied from 0.4 to 1.0.

Under varying pH conditions significant differences in complexation behavior was revealed at a smaller length scale, where complexation at pH 7 results in the formation of complexes with a characteristic size of approximately 10 nm. In contrast, at pH 9, the SAXS data did not indicate the formation of complexes of a comparable size. This suggests that the pH significantly influences the initial stages of complexation, potentially due to the ionization states of humic acid and the polycations molecules. At larger length scales, however, the differences between pH 7 and pH 9 diminish. In both cases, the evolution of complexes is observed with sizes expanding from about 30 nm to 400 nm within 120 s, as shown in **Figure 5.7**, indicating lower sensitivity to pH for the subsequent aggregation after the formation of initial complexes.

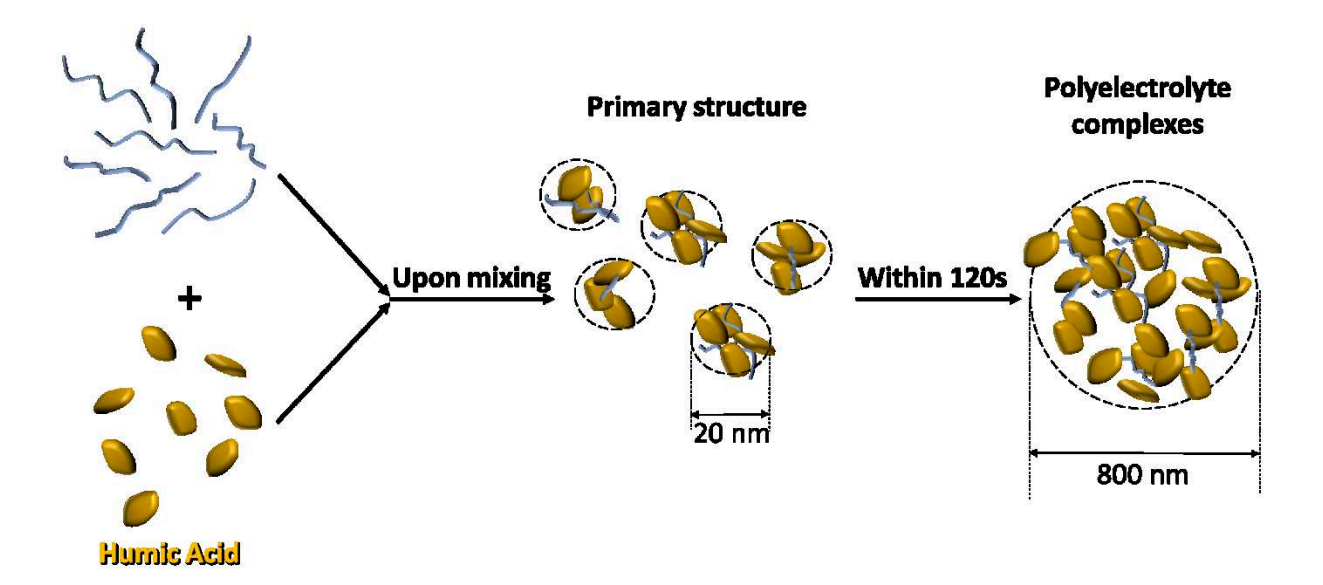


**Figure 5.7.** Schematic drawing of the complexation between cationic polyelectrolytes and anionic HA over time.

The influence of different charge ratios on the complexation process demonstrates distinct behaviors depending on the length scale explored. Notably, the SAXS results are comparable across various charge ratios at smaller length scales, suggesting that electrostatic force predominantly drives the initial stages of complexation regardless of the specific charge ratio. While at larger length scales as probed by smaller q ranges in SAXS, variations in the behavior of the complexes become apparent, particularly in the dynamics of the formed 'halo' features, which shifting to lower q ranges at varying rates and appearing after different periods depending on the charge ratio. This variation could be caused by different charge ratios between positive charges from cationic polyelectrolytes and negative charges from humic acid, which affect the intermolecular interaction thus leading to different time scale for further aggregation.

As the degree of charged group of cationic polyelectrolytes increases from 30% to 100%, the difference at higher q range is obvious that peak at 0.9 nm<sup>-1</sup> is no longer detectable, with the complexation behavior with humic acid molecules more rapid and largely unaffected by pH changing. The dominant role of higher charge densities shows a trade-off between high

complexation rate and the lack of distinct primary complexes formation around 10 nm. At lower q ranges, the differences in SAXS results among various QCSs become less pronounced with the peak shapes emerging at different charge ratios that correlating well with the biphasic region seen in macroscopic observation.

These findings elucidate the pathway of humic acid flocculation including the initial formation of primary structures at a constant size, followed by their aggregation into larger sizes, approximately in the length scale of several hundred nm. Several key factors that need to consider when analyzing the flocculation behavior were emphasized, such as the pH, the mixing ratio of the components, and the charge density of the cationic polyelectrolytes involved. Understanding how these variables affect the flocculation dynamics is crucial in optimizing conditions for more effective humic acid removal, keeping the balance between efficient initial complexation and further aggregation at larger scales.

#### 6. Conclusions & Outlook

The flocculation of humic acid (HA), a predominant component of natural organic matter (NOM) in raw water, have been a critical method in water treatment processes for HA removal. This can be achieved by adding polycations to facilitate the neutralization and subsequent precipitation of formed HA complexes, similar to the formation of classical interpolyelectrolyte complexes (IPEC) upon mixing of two oppositely charged polyelectrolytes as a result of electrostatic forces. Given the fundamental role of colloid science in understanding and optimizing this step in water treatment, this work mainly investigates the complexation of HA with various cationic polyelectrolytes (cPEs) ranging from synthetic (diallyldimethylammonium chloride) (PDADMAC) to natural derived modified chitosan.

# The Effect of Ca2+ on the Interaction Between Humic Acid and poly (diallyldimethylammonium chloride) (PDADMAC)

In Chapter 3, the influence of  $Ca^{2+}$  ions on the HA complexation process using poly(diallyldimethylammonium chloride) (PDADMAC) as the polycation was examined. A combination of light scattering, small-angle neutron scattering (SANS) and turbidimetry was employed to characterize the phase behavior and structural dynamics of the complexes in solution. It was indicated that increasing concentrations of  $Ca^{2+}$  result in the phase boundaries of the precipitation region shifting to lower concentration of PDADMAC, which aligns with a corresponding change in the  $\zeta$ -potential of the aggregates, suggesting alterations in their surface charge and stability. The quantitative analysis was supported by extensive characterization of the mesoscopic structure of the formed complexes using a combination of light scattering and neutron scattering techniques. Light scattering analysis revealed that aggregate formation typically features radii of 120–150 nm. Furthermore, SANS provided insight that the addition of  $Ca^{2+}$  contributes to a significant compaction within these aggregates, particularly in the size

range of 10–50 nm. Observations via confocal microscopy revealed more densely packed precipitates in the presence of Ca<sup>2+</sup>. Additionally, kinetic studies of precipitation via turbidimetry highlighted a substantial acceleration in the flocculation process, even at relatively low Ca<sup>2+</sup> concentrations of around 1 mg/L. These results affirm the pronounced impact of Ca<sup>2+</sup> on the phase behavior and precipitation kinetics in the complexation process of HA with polycations. Specifically, the presence of Ca<sup>2+</sup> not only facilitates the flocculation process at relatively low concentrations but also promotes a compaction of the formed structures within the mesoscopic size range. This enhanced understanding of the role of Ca<sup>2+</sup> in the complexation process is crucial for optimizing flocculation protocols in water treatment, aiming to improve the quality of drinking water delivered to consumers. This study's insights could lead to more effective and efficient water treatment strategies by tailoring the flocculation process to leverage the beneficial effects of Ca<sup>2+</sup> in complexation dynamics.

# From Waste Treatment to Water Treatment: Application of Quaternised Chitosan in Enhancing NOM Flocculation

In Chapter 4, to explore an environmentally friendly approach to water treatment, chitosan was selected to investigate its potential in altering synthetic PDADMAC for HA treatment due to its biocompatibility and the versatility offered by its chemical structure, which can be easily modified to adjust properties such as charge density, molecular weight and hydrophobicity. Considering the limited water solubility of chitosan at neutral and basic pH range, chitosan was further modified by the substitution of glycidyl trimethylammonium chloride (GTMAC) to achieve enhanced water solubility among all pH ranges as well as permanent charges. By varying the degree of GTMAC substitution, a series of quaternized chitosans (qCs) was engineered with different charge densities thus lead to various interaction capabilities with HA molecules. The application of those modified quaternized chitosans in the removal of HA under various pH conditions were investigated and compared to the commercially available, highly

charged polycation, poly(diallyldimethylammonium chloride) (PDADMAC). From the macroscopic phase behavior observation, the precipitation of HA-qCs complexes occurs at a lower charge mixing ratio compared to PDADMAC, likely due to the inherent hydrophobic domains within the qCs structure. Remarkably, the highest HA removal efficiency, observed at 88.0%, was achieved with a qCs that had a 34.0% GTMAC substitution at a charge ratio Z = 0.6, indicating a significant potential for qCs in enhancing flocculation efficacy through optimal charge density tuning. In addition, flocculation dynamics were monitored using laser light diffraction to provide a deeper understanding of the mechanisms. These measurements have highlighted how the structural properties of the cationic polyelectrolytes (cPEs) influence the flocculation process, offering valuable insights into the design and development of more effective flocculant materials for industrial water treatment applications. By understanding the impact of polymer charge density and structural properties on flocculation efficiency, this study contributes to the broader effort of improving water treatment technologies to meet environmental and health standards more sustainably.

### In Situ Investigation of Humic Acid - Quaternised Chitosan Complexation via Time-Resolved Small-angle X-ray Scattering

In Chapter 5, the temporal evolution of the complexation between humic acid and quaternised chitosan that studied last chapter was probed through kinetic investigations, monitoring the structural changes that occur during the initial complexation stage upon mixing in the combination of time-resolved small-angel X-ray scattering with stopped-flow instrument. This kinetic analysis will provide insights into how quickly and effectively HA can be bound and complexed under various pH conditions with different types of cationic polyelectrolytes, including quaternised chitosan with different degrees of charged groups and PDADMAC that is 100 % charged. By conducting the time-resolved SAXS experiments at two beamlines with distinct q range probed, the structural evolution at two length scales was investigated that affirm

the flocculation pathing consisting of the initial formation of primary structures at a constant size around 10 nm and followed aggregation into larger sizes with the length scale of approximately several hundred nanometers. Ultimately, this comprehensive kinetic characterization established systematic correlations between HA flocculation behavior with the pH environment, mixing ratio and the molecular structures of the cPEs. The significant influence of pH on the was revealed with primary structure detected at pH 7 while no comparable complexation at pH 9, followed by subsequent aggregation processes that are less influenced by pH changes, complexes size increasing from about 30 nm to 400 nm regardless of pH. The parameter of mixing ratio, however, showing negligible effect on the initial stage of complexation, as it is mainly dominated by electrostatic forces. On the contrary, the mixing ratio was able to determine the subsequent aggregation at larger length scale, where the formation of 'halo' features in SAXS data presented variable dynamics. Furthermore, as the charge density of the cationic polyelectrolytes increases from 30% to 100%, a trade-off between rapid complexation and the formation of distinct smaller complexes was highlighted for highly charged cPEs such as QCS4 and PDADMAC. These findings provide a comprehensive understanding of HA flocculation, from initial complex formation to subsequent aggregation, emphasizing the importance of pH, mixing ratio, and charge density in optimizing water treatment processes for effective HA removal.

#### **Outlook**

This research provided a deep fundamental understanding of the physio-chemical interactions between HA and various cationic polyelectrolytes under varying environmental conditions. The insights into how pH and charge density influence these interactions at different scales serve as a robust scientific foundation for future advancements in flocculants development for NOM removal from drinking water, addressing the significant technological challenges faced by humanity today. In addition to the primary research findings, the application of advanced

characterization techniques such as small-angle neutron scattering (SANS) and small-angle X-ray scattering (SAXS) to the complex system of humic acid and modified chitosan significantly enhances our understanding on these relatively ill-defined systems, demonstrating their potential universality a wider range of colloidal systems that can be utilized for practical industrial settings, such as pharmaceuticals, cosmetics and food technology.

## **List of Figures**

Figure 1.1. Stevenson's model for humic acid composition effectively integrates several key
components, offering a comprehensive framework that highlights the complex and
heterogeneous nature of humic substances. Taken from <sup>8</sup>
Figure 1.2. A schematic depiction of the formation of an interpolyelectrolyte complex (IPEC)
between polycations and polyanions with the low molecular weight counterions that were
previously balancing the charges of the polyelectrolytes are released into the solution. Taken
from <sup>36</sup>
Figure 2.1. Setup for time-resolved SAXS combined with stopped-flow mixing
<b>Figure 2.2</b> . Laser light diffraction experimental setup. Taken from <sup>52</sup>
Figure 3.1. Phase diagram of 40 mg/L HA and added 500 kDa PDADMAC, the added amount
being characterized by the nominal charge ratio $Z = [+]/[-]$ for different concentrations of $Ca^{2+}$
at pH 9.0. The inserts show confocal laser scanning microscopy (CLSM) images of precipitated
flocs at $Z = 1.0$ with no $Ca^{2+}$ and 0.250 mM $Ca^{2+}$ , respectively
Figure 3.2. ζ-potential for complexes of HA and 500 kDa PDADMAC for different Ca <sup>2+</sup>
concentrations at different charge ratio Z (measurements done at pH 9 and 25 °C). Open
symbols refer to monophasic regions while full symbols refer to the biphasic region. Error bars
are given or are smaller than the symbol size
Figure 3.3. Remaining percentage of HA in the supernatant 24 hours after mixing at different
charge ratio Z at 25 °C at pH 9 in the presence of different concentrations of Ca <sup>2+</sup> (open symbols:
monophasic (100%), filled symbols: biphasic, crossed symbol: in a metastable state, partly
precipitated). Error bars are given but always smaller than the symbol size

Figure 3.4. Static light scattering results: (a) Molecular weight Mw and (b) Radius of gyration
Rg for HA-PDADMAC complexes under varying Ca2+ concentrations as a function of the
charge ratio Z at 25 °C.
Figure 3.5. (a) Intensity auto-correlation functions from DLS experiments at 90° for HA
solutions for varying Ca <sup>2+</sup> concentrations at 25 °C and fits with a stretched exponential function
(solid black line). The insets show the normalized fit residuals, $(g^{(2)}-g^{(2)}_{fit})$ ; (b) Apparent
hydrodynamic radii Rh for HA-PDADMAC complexes under varying Ca2+ concentrations at
different charge ratio Z at 25 °C. Error bars for R <sub>h</sub> are given
Figure 3.6. SANS intensity as a function of the magnitude of the scattering vector q for
complexes of HA and 500 kDa PDADMAC (a) without added salt (the curves with added $CaCl_2$
are shown in Figure S13). Kratky-Porod plots for: (b) without added salt; (c) with 0.625 mM
CaCl <sub>2</sub> ; (d) with 3.125 mM CaCl <sub>2</sub> (all measured at 25 °C)
Figure 3.7. SANS intensity as a function of the magnitude of the scattering vector q for pure
HA ( $Z=0$ ) under various ionic conditions and for $HA$ -PDADMAC complexes under various
ionic conditions at $Z = 2$ and 3, respectively (c(HA) = 1.0 g/L)
Figure 3.8. Time dependence of the HA-PDADMAC mixture absorbance at 254 nm with
various (a) charge ratios Z (addition of PDADMAC) and (b) for different Ca <sup>2+</sup> concentrations
at fixed charge ratio Z=1
Figure 3.9. Schematic drawing of the complexation between cationic PDADMAC and anionic
HA in the presence and absence of Ca <sup>2+</sup> , respectively
Figure 4.1. Phase diagram of 40 mg/L HA and added polyelectrolytes, the added amount being
characterized by the nominal charge ratio $Z = [+]/[-]$ at pH 7 and pH 9, respectively (T =
25 °C). Open symbols refer to monophasic regions while full symbols refer to the biphasic
region55
Figure 4.2. Structure of quaternised chitosan (QCS) and polydiallyldimethylammonium
chloride (PDADMAC). The charged regions are highlighted

Figure 4.3. Confocal laser scanning microscopy (CLSM) images of precipitated flocs at $Z =$
$0.5$ for the different QCS with HA (size bar: $50~\mu m$ ).
<b>Figure 4.4.</b> ζ-potential for complexes of HA and polyelectrolytes at different charge ratio Z at
pH 7 and pH 9, respectively. (measurements done at 25 °C, full symbols denote samples located
in the biphasic region, but measurements were done before precipitation sets in)
Figure 4.5. Remaining percentage of HA in the supernatant 24 hour after mixing HA and
various polyelectrolytes under pH 7 and pH 9, respectively, at different charge ratio Z at 25 °C.
61
Figure 4.6. The extracted wavelength of the maximum emission $(\lambda_{max})$ and its emission
intensity ( $F_{\text{max}}$ ) of polarity-sensitive 1 $\mu M$ Prodan probe in varying concentration of humic acid,
at pH 7 and pH 9, respectively
Figure 4.7. The extracted wavelength of the maximum emission $(\lambda_{max})$ and its emission
intensity ( $F_{max}$ ) of polarity-sensitive 1 $\mu M$ Prodan probe in varying concentration of humic acid,
at pH 7 (open symbols) and pH 9 (full symbols), respectively
Figure 4.8. The trend diagram of the median particle size $(x(50\%))$ for complexes of HA and
various QCSs with charge ratio Z=0.4 at pH 7 and charge ratio Z=0.5 at pH 9. Solid lines are
fits with a logistic growth model
<b>Figure 4.9.</b> ζ-Potential for treated water samples with addition of different polyelectrolytes at
different dosage. Solid black dot refers to raw water sample
Figure 4.10. UV <sub>254</sub> absorbance for treated water samples with addition of different
polyelectrolytes at different dosage. Solid black dot refers to raw water sample
Figure 5.1. 3D time-resolved SAXS curves illustrating the kinetic pathway of HA-QCS2
complex formation following rapid mixing at various Z charge ratios and pH values of 7.0 and
9.0. Each curve represents a time interval of 0.5s with 20 time frames recorded

Figure 5.2. Development of the peak position of the normalized results versus period upon
mixing during the complexation of HA and QCS4 at charge ratio Z=0.5 and pH values of 7.0
and 9.0
Figure 5.3. 2D time-resolved SAXS curves illustrating the kinetic pathway of HA-QCS4
complex formation following rapid mixing at charge ratio Z=0.5 and pH values of 7.0 and 9.0.
Each mixing event was recorded over 40 frames throughout a total duration of 120 seconds,
with intervals spaced by a power law
Figure 5.4. Scaled 2D time-resolved SAXS curves illustrating the kinetic pathway of HA
complex formation following rapid mixing with various QCSs at various Z charge ratios and
pH values of 7.0. Each mixing event was recorded over 40 frames throughout a total duration
of 120 seconds, with intervals spaced by a power law. Additionally, the gradients of color in
each figure represent temporal progression; curves start with lighter colors for earlier times and
gradually darken as time advances
<b>Figure 5.5.</b> Development of the peak position for the normalized pH=7_QCS2_Z=1.0 sample
set within 120s and the evolution of aggregation size over time. Red line refers to the fitted data
from via Logarithmic Growth model
Figure 5.6. SAXS intensity $I \times q2$ as a function of the magnitude of the scattering vector q for
complexes of HA and various cationic polyelectrolytes following rapid mixing with various
charge ratio Z at pH 794
Figure 5.7. Schematic drawing of the complexation between cationic polyelectrolytes and
anionic HA over time
<b>Figure A.1.</b> Potentiometric titration curve of humic acid with a solution of HCl
Figure A.2. Photos of samples containing 40 mg/L HA at different charge ratio Z at pH 9 and
for varying Ca <sup>2+</sup> concentrations. 122
<b>Figure A.3.</b> Confocal laser scanning microscopy (CLSM) images of precipitated flocs at Z =
1.0 for varying $Ca^{2+}$ concentrations 122

Figure A.4. (a) UV-vis spectra of humic acid solutions of different concentrations at $pH = 9$ .
(b) Calibration curve for HA concentration as a function of UV absorbance at 254 nm 123
Figure A.5. Decadic UV-absorbance at 254 nm per optical path length (UV254) of HA-
PDADMAC systems (whole solution for monophasic region and supernatant for biphasic
region) 24 hour after mixing under varying Ca <sup>2+</sup> concentrations at different charge ratio Z at 25
°C. The HA concentration was 40 mg/L and the pH 9.0
Figure A.6. SLS intensities of HA-PDADMAC complexes under varying Ca <sup>2+</sup> concentrations
at different charge ratio Z at 25 °C
Figure A.7. The static intensity at zero angle, I <sub>0</sub> under varying Ca <sup>2+</sup> concentrations as a function
of the charge ratio Z at 25 °C.
<b>Figure A.8.</b> Intensity auto-correlation function $g^{(2)}(\tau)$ at 90° for HA-PDADMAC complexes at
(a) $Z = 0.4$ and (b) $Z = 1.6$ under varying $Ca^{2+}$ concentrations at 25 °C (c(HA) = 40 mg/L), as
determined from the DLS experiments with a stretched exponential fit; The insets show the fit
residuals, $g^{(2)}$ - $g^{(2)}$ <sub>fit</sub>
Figure A.9. Ratio of radius of gyration and hydrodynamic radius Rg/Rh for HA-PDADMAC
complexes under varying Ca <sup>2+</sup> concentrations at different charge ratio Z at 25 °C 128
Figure A.10. Intensity auto-correlation function at 90° for HA-PDADMAC complexes at Z
=1.0 under varying $Ca^{2+}$ concentrations (c(HA) = 40 mg/L). All the measurements were
conducted 5 min after mixing
Figure A.11. Combined SLS and SANS spectra for HA-PDADMAC complexes without added
salt. To superimpose both techniques we plot converted the scattering intensity of SLS to the
one of SANS by the corresponding contrast term, which is given by
Figure A.12. Photos of HA-PDADMAC complexes measured at ISIS with 1000 mg/L HA and
different charge ratio Z values under different ionic conditions. Photos were taken after an aging
time of 24 hours after mixing

Figure A.13. Scattering intensity as a function of the magnitude of the scattering vector q for
HA-PDADMAC complexes with (a) 0.625 mM CaCl <sub>2</sub> and (b) 3.125 mM CaCl <sub>2</sub> , respectively
(c(HA) = 1.0  g/L). 130
Figure A.14. Scattering intensity as a function of the magnitude of the scattering vector q for
HA-PDADMAC complexes without added salt (a), with 0.625 mM CaCl <sub>2</sub> (b), with 3.125 mM
CaCl <sub>2</sub> (c) normalised to the respective pure HA intensity (I/I <sub>Z=0</sub> ) and the corresponding Kratky-
Porod plot of the pure HA aggregates $(Z = 0)$ (d)
Figure A.15. Scattering intensity as a function of the magnitude of the scattering vector q for
HA-PDADMAC complexes for $Z = 2.0$ (a) and $Z = 3.0$ (b) for different addition of CaCl <sub>2</sub> ,
normalized to the respective system without added CaCl <sub>2</sub>
Figure A.16. SANS intensity as a function of the magnitude of the scattering vector q for HA-
PDADMAC complexes with addition of (a) 9.375 mM Na <sup>+</sup> and (b) 3.125 mM Mg <sup>2+</sup>
respectively, and the corresponding Kratky-Porod plots (c(HA) = 1.0 g/L) (c) and (d) 133
<b>Figure A.17.</b> SANS intensity $I^*q^2$ as a function of the magnitude of the scattering vector q for
complexes of HA and 500 kDa PDADMAC under various ionic conditions with $Z = 0$ , 2 and
3, respectively
Figure A.18. Scattering intensity as a function of the magnitude of the scattering vector q for
HA complexes $(c(HA) = 1.0 \text{ g/L})$ at $Z = 0$ under various ionic conditions normalized to the
intensity of pure HA without added salt (I/I <sub>Ref</sub> )
Figure A.19. Corresponding residuals for fit of SANS data for 500kDa PDADMAC-HA
complexes under various ionic conditions at $Z = 2$ with the two-power law model (left column)
and Beaucage model (right column)
Figure A.20. Corresponding residuals for fit of SANS data for 500kDa PDADMAC-HA
complexes under various ionic conditions at $Z = 2$ with the two-power law model and Beaucage
model 127

Figure B.1. Potentiometric titration curve of humic acid with a solution of HCl and the
corresponding degree of dissociation as a function of pH
Figure B.2. Determination of the degree of deacetylation (DDA) from potentiometric titration
of chitosan
Figure B.3. Determination of the degree of substitution (DS) of modified chitosan from
conductometric titration with AgNO <sub>3</sub>
Figure B.4. Phase diagram of 40 mg/L HA and added polyelectrolytes, the added amount being
characterised by the concentration of polyelectrolytes at pH 7 and pH 9, respectively ( $T = 25$ °C).
Open symbols refer to monophasic regions while full symbols refer to the biphasic region. 142
Figure B.5. UV-vis spectra of humic acid solutions of different concentrations and the
corresponding calibration curve for HA concentration as a function of UV absorbance at 254
nm
Figure B.6. Decadic UV-absorbance at 254 nm per optical path length (UV254) of HA-PE
systems (supernatant for biphasic region) 24 hours after mixing at pH 7 and pH 9, respectively,
for different charge ratios Z at 25 °C.
Figure B.7. The fluorescence emission spectra of polarity-sensitive 1 $\mu M$ Prodan probe in
varying concentrations of humic acid at different pH
Figure B.8. Fluorescence emission spectra of 40 mg/L humic acid at pH 7 and pH 9,
respectively
Figure B.9. Fluorescence spectra of the various HA (40 mg/L)-cPE complexes containing 1
$\mu M$ Prodan at pH 7 for different charge ratio Z at 25 $^{\circ} C$ and the extracted wavelength of the
maximum emission ( $\lambda_{max}$ ) and its emission intensity ( $F_{max}$ )
Figure B.10. Fluorescence spectra of the various HA (40 mg/L)-cPE complexes containing 1
$\mu M$ Prodan at pH 9 for different charge ratio Z at 25 $^{\circ} C$ and the extracted wavelength of the
maximum emission $(\lambda_{max})$ and its emission intensity $(F_{max})$ .

<b>Figure B.11.</b> Laser diffraction particle size distribution density $q_3^*$ and cumulative mass
distribution Q3 as a function of particle size recorded for complexes of HA and various QCSs
with charge ratio Z=0.4 at pH 7 upon mixing. For HA-PDADMAC complexes, the charge ratio
is 0.8. Each curve represents time interval of 10 s, in which the red one refers to the
measurement at 300 s
Figure B.12. Laser diffraction particle size distribution density $q_3^*$ and cumulative mass
distribution Q <sub>3</sub> as a function of particle size recorded for complexes of HA and various QCSs
with charge ratio Z=0.5 at pH 9. For HA-PDADMAC complexes, the charge ratio is 1.0. Each
curve represents time interval of 10 s, in which the red one refers to the measurement at 300 s.
<b>Figure B.13.</b> The trend diagram of the median particle size (x(50%)) for HA-PDADMAC
complexes with charge ratio Z=0.8 at pH 7 and charge ratio Z=1.0 at pH 9. Solid lines are fits
with a logistic growth model
<b>Figure B.14.</b> The trend diagram of the median particle size $(x(50\%))$ for HA-QCS2 complexes
with charge ratio Z=0.4 and HA-QCS4 complexes with charge ratio Z=0.5 under various pH
conditions
Figure B.15. Jar test of raw water treatment with PDADMAC
Figure B.16. Jar test of raw water treatment with QCS3
Figure B.17. Jar test of raw water treatment with QCS2 and QCS4
Figure B.18. TOC for treated water samples with addition of different polyelectrolytes at
different dosage. Solid black dot refers to raw water sample
Figure C.1. 2D time-resolved SAXS curves illustrating the kinetic pathway of HA-QCS2
complex formation following rapid mixing at various Z charge ratios and pH values of 7.0 and
9.0. Each curve represents a time interval of 0.5s with 30 time frames recorded (Except for
sample pH=9_QCS2_Z=1.0 only 20 time frames recorded). Curves have been offset for visual
alority 155

Figure C.2. 2D time-resolved SAXS curves illustrating the kinetic pathway of HA-QCS3
complex formation following rapid mixing at various Z charge ratios and pH values of 7.0 and
9.0. Each curve represents a time interval of 0.5s with 30 time frames recorded. Additionally,
the gradients of color in each figure represent temporal progression; curves start with lighter
colors for earlier times and gradually darken as time advances
Figure C.3. 2D time-resolved SAXS curves illustrating the kinetic pathway of HA-QCS3
complex formation following rapid mixing at various Z charge ratios and pH values of 7.0 and
9.0. Each curve represents a time interval of 0.5s with 30 time frames recorded. Curves have
been offset for visual clarity
Figure C.4. 2D time-resolved SAXS curves illustrating the kinetic pathway of HA-QCS4
complex formation following rapid mixing at various Z charge ratios and pH values of 7.0 and
9.0. Each curve represents a time interval of 20 ms with 100 time frames recorded. Additionally,
the gradients of color in each figure represent temporal progression; curves start with lighter
colors for earlier times and gradually darken as time advances
Figure C.5. 2D time-resolved SAXS curves illustrating the kinetic pathway of HA-PDAD
complex formation following rapid mixing at various $Z$ charge ratios and $pH$ values of $7.0$ and
complex formation following rapid mixing at various Z charge ratios and pH values of 7.0 and 9.0. Each curve represents a time interval of 20 ms with 100 time frames recorded. Additionally,
9.0. Each curve represents a time interval of 20 ms with 100 time frames recorded. Additionally,
9.0. Each curve represents a time interval of 20 ms with 100 time frames recorded. Additionally, the gradients of color in each figure represent temporal progression; curves start with lighter
9.0. Each curve represents a time interval of 20 ms with 100 time frames recorded. Additionally, the gradients of color in each figure represent temporal progression; curves start with lighter colors for earlier times and gradually darken as time advances
9.0. Each curve represents a time interval of 20 ms with 100 time frames recorded. Additionally, the gradients of color in each figure represent temporal progression; curves start with lighter colors for earlier times and gradually darken as time advances
9.0. Each curve represents a time interval of 20 ms with 100 time frames recorded. Additionally, the gradients of color in each figure represent temporal progression; curves start with lighter colors for earlier times and gradually darken as time advances

Figure C.7. Development of the peak position of the normalized results versus period upon
mixing during the complexation of HA and QCS4 at various Z charge ratios and pH values of
7.0 and 9.0161
Figure C.8. Development of the peak position of the normalized results versus period upon
mixing during the complexation of HA and PDADMAC at various Z charge ratios and pH
values of 7.0 and 9.0
Figure C.9. Peak position of the normalized results for the final time frame of HA complex
formation following rapid mixing with various QCSs at various Z charge ratios and pH values
of 7.0
Figure C.10. Normalized 2D time-resolved SAXS curves illustrating the kinetic pathway of
HA complex formation following rapid mixing with various QCSs at various Z charge ratios
and pH values of 7.0. Each mixing event was recorded over 40 frames throughout a total
duration of 120 seconds, with intervals spaced by a power law. Additionally, the gradients of
color in each figure represent temporal progression; curves start with lighter colors for earlier
times and gradually darken as time advances
Figure C.11. Development of the peak position for the normalized HA complex formation
following rapid mixing with various QCSs at various Z charge ratios and pH values of 7.0
within 120s
<b>Figure C.12.</b> The evolution of aggregation size over time for the pH=7_QCS2 sample set at
various Z charge ratios and pH values of 7.0 within 120s. Red line refers to the fitted data from
via Logarithmic Growth model
Figure C.13. Development of the peak position of the normalized results versus period upon
mixing during the complexation of HA and QCS2 at various Z charge ratios and pH values of

Figure C.14. Development of the peak position of the normalized results versus period upon
mixing during the complexation of HA and QCS3 at various Z charge ratios and pH values of
7.0 and 9.0
Figure C.15. Development of the peak position of the normalized results versus period upon
mixing during the complexation of HA and various cPEs and the evolution of aggregation size
over time at charge ratio Z=0.5 and pH values of 7.0. Red line refers to the fitted data from via
Logarithmic Growth model

### **List of Tables**

Table 3.1. Fitted power law exponent p1 at low q and p2 at high q, respectively of HA
complexes with different charge ratio Z values under different ionic conditions, as determined
from the SANS experiments
Table 4.1. Composition, feed ratio, ratios of the functional groups, molecular weights, and
charge densities for the different samples of quaternised chitosans and PDADMAC (PDAD).
53
<b>Table 5.1.</b> The fitted parameter and the corresponding goodness of fit R <sup>2</sup> as determined by the
Logarithmic Growth model for complexes of HA and various cationic polyelectrolytes with
various charge ratio Z92
<b>Table 5.2.</b> The fitted parameter and the corresponding goodness of fit R <sup>2</sup> as determined by the
Logarithmic Growth model for complexes of HA and various cationic polyelectrolytes at charge
ratio Z=0.5 and pH values of 7.096
<b>Table A.1.</b> ζ-potential for complexes of HA (40 mg/L) and 500 kDa PDADMAC for different
$Ca^{2+}$ concentrations at different charge ratio Z (T = 25 °C)
Table A.2. Decadic UV-absorbance at 254 nm per optical path length (UV254) of HA-
PDADMAC systems
<b>Table A.3.</b> Characteristic stretching exponent α of HA-PDADMAC complexes under varying
Ca <sup>2+</sup> concentrations at different charge ratio Z at 25 °C
Table A.4. Radius of gyration at larger scale R <sub>g1</sub> and smaller scale R <sub>g2</sub> as well as the
corresponding scaling pre-factor G, power law scattering pre-factor B and power law exponent
P as determined by the Beaucage model from the SANS data of HA complexes with different
charge ratio Z values under different ionic conditions

<b>Table B.1.</b> ζ-potential for complexes of HA (40 mg/L) and different cationic polyelectrolytes,
at pH 7 and pH 9, respectively, for different charge ratios Z ( $T = 25$ °C)
Table B.2. Decadic UV-absorbance at 254 nm per optical path length (UV254) for complexes
of HA (40 mg/L) and different cationic polyelectrolytes, at pH 7 and pH 9, respectively, for
different charge ratios Z (T = $25$ °C)
<b>Table B.3.</b> The maximum size $x(50\%)_M$ of the HA complexes, the growth rate k, the time $t_0$ at
which the particle size is half of L and the corresponding goodness of fit R <sup>2</sup> as determined by
the logistic growth model (eq. 1) from the laser light diffraction data for complexes of HA and
various cationic polyelectrolytes with various charge ratio Z
<b>Table B.4.</b> Characterized results of raw water sample received from water plant

## Appendix A. Chapter 3

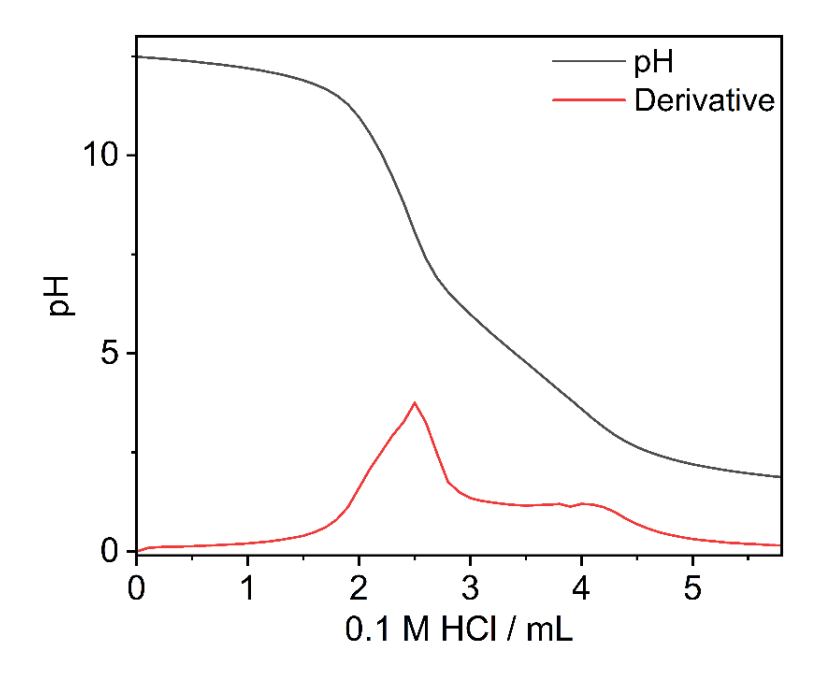
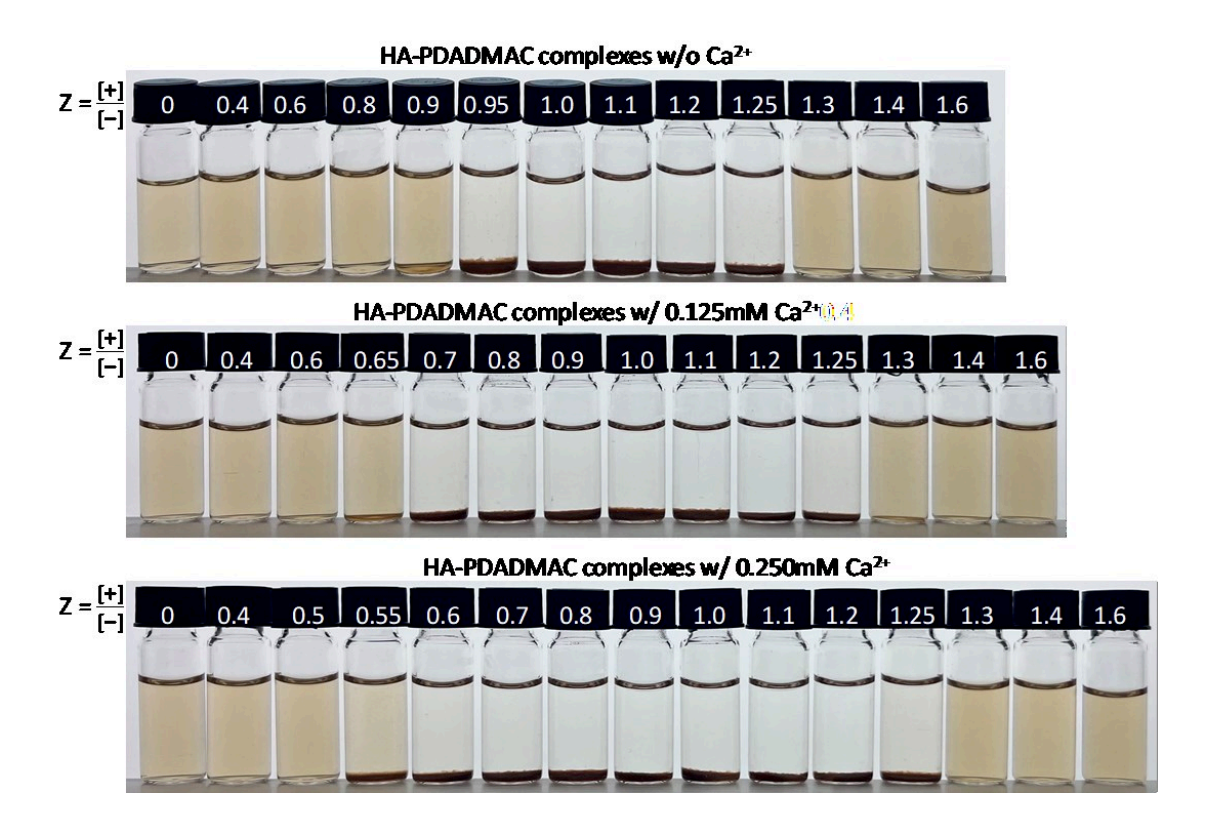
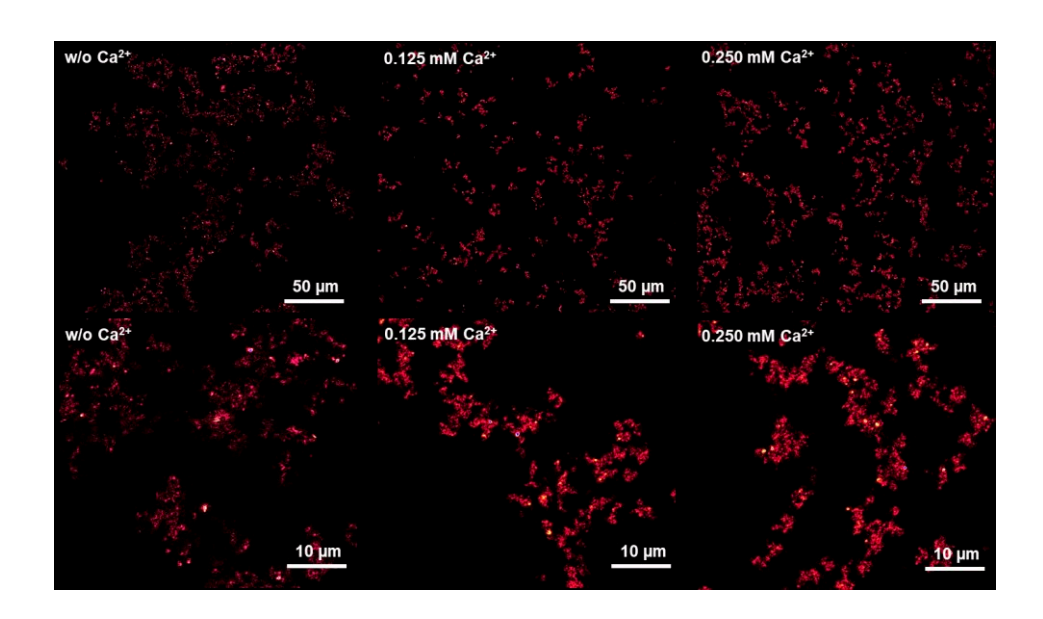


Figure A.1. Potentiometric titration curve of humic acid with a solution of HCl.



**Figure A.2.** Photos of samples containing 40 mg/L HA at different charge ratio Z at pH 9 and for varying Ca<sup>2+</sup> concentrations.



**Figure A.3.** Confocal laser scanning microscopy (CLSM) images of precipitated flocs at Z = 1.0 for varying  $Ca^{2+}$  concentrations

**Table A.1.**  $\zeta$ -potential for complexes of HA (40 mg/L) and 500 kDa PDADMAC for different Ca<sup>2+</sup> concentrations at different charge ratio Z (T = 25 °C).

z	0	0.4	0.5	0.6	0.7	0.8	0.9	1	1.1	1.2	1.3	1.4	1.6
	ζ, mV	ζ, mV	$\zeta$ , mV	ζ, mV									
w/o Ca <sup>2+</sup>	-30.9	-29.3		-25.3		-20.9	-16.8	-16.9	-16.5	-1.4	14.7	16.6	23.4
w/o Ca-	(2.4)	(1.1)		(0.7)		(0.8)	(0.6)	(1.1)	(0.6)	(0.5)	(0.4)	(0.5)	(0.9)
0.125mM Ca <sup>2+</sup>	-25.6	-23.3		-19.1	-16.5	-13.9	-7.7	-4.0	-3.5	1.0	10.3	18.3	24.3
	(0.8)	(0.7)		(0.7)	(1.3)	(1.2)	(0.7)	(0.6)	(0.2)	(0.5)	(0.4)	(1.1)	(1.0)
0.250mM Ca <sup>2+</sup>	-18.4	-18.6	-16.8	-11.0	-10.5	-6.5	-7.0	-3.5	0.7	0.7	13.6	18.9	23.3
	(0.5)	(1.0)	(0.6)	(0.6)	(0.8)	(0.7)	(0.2)	(0.4)	(0.4)	(0.5)	(0.6)	(0.5)	(1.5)

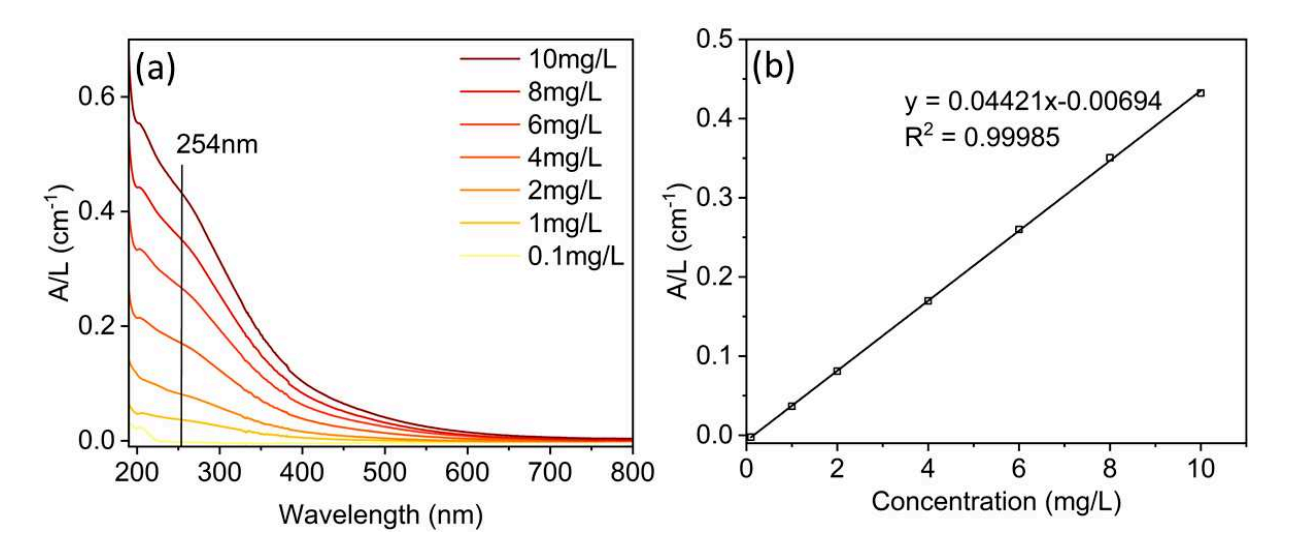


**Figure A.4.** (a) UV-vis spectra of humic acid solutions of different concentrations at pH = 9. (b) Calibration curve for HA concentration as a function of UV absorbance at 254 nm.

**Table A.2.** Decadic UV-absorbance at 254 nm per optical path length (UV254) of HA-PDADMAC systems.

		w/o	Ca <sup>2+</sup>		0.125 n	nM Ca <sup>2+</sup>	0.250 mM Ca <sup>2+</sup>				
Z	A/L	HA conc	Removal efficiency	A/L	HA conc	Removal efficiency	A/L	HA conc	Removal efficiency		
	cm <sup>-1</sup>	mg/L	%	cm <sup>-1</sup>	mg/L	%	cm <sup>-1</sup>	mg/L	%		
0.4	1.78			1.76			1.77				
0.5							1.77				
0.6	1.79			1.79			0.44	10.1	74.7		
0.7				0.41	9.4	76.5	0.34	7.8	80.6		
0.8	1.81			0.32	7.3	81.7	0.29	6.7	83.2		
0.9	1.57	35.7	10.8	0.26	6.0	84.9	0.24	5.6	86.0		
1	0.29	6.7	83.4	0.21	4.8	87.9	0.19	4.6	88.6		
1.1	0.19	4.4	88.9	0.17	4.0	90.0	0.15	3.6	90.9		
1.2	0.14	3.2	91.9	0.13	3.1	92.3	0.14	3.4	91.5		
1.3	1.73			1.68			1.83				
1.4	1.77			1.75			1.76				
1.6	1.78			1.79			1.80				

\*the supernatant of samples was measured 24 hours after mixing for different Ca<sup>2+</sup> concentrations at different charge ratio Z at 25 °C. For the biphasic region the corresponding HA concentration and removal efficiency were calculated.

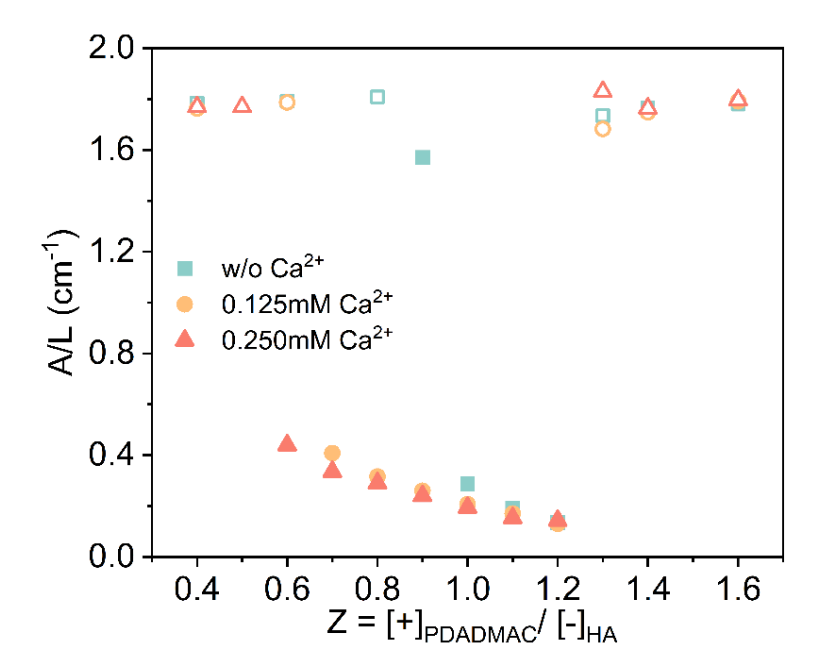


**Figure A.5.** Decadic UV-absorbance at 254 nm per optical path length (UV254) of HA-PDADMAC systems (whole solution for monophasic region and supernatant for biphasic region) 24 hour after mixing under varying Ca<sup>2+</sup> concentrations at different charge ratio Z at 25 °C. The HA concentration was 40 mg/L and the pH 9.0.

According to classical solubility product K = [HA]\*[PDADMAC] (concentrations in mass per volume), assuming a simple precipitation behavior in which a certain percentage x of the PDADMAC relative to the humic acid (HA) becomes precipitated out of solution, one arrives

$$[HA] = -\frac{[P]_0 - x \cdot [HA]_0}{2 \cdot x} + \sqrt{\left(\frac{[P]_0 - x \cdot [HA]_0}{2 \cdot x}\right)^2 + \frac{K}{x}}$$
$$[P]_0 = Z \cdot [HA]_0 \cdot \frac{\text{Mw(charge)}_{PDADMAC}}{\text{Mw(charge)}_{HA}}$$

Substitute the factors in remaining HA (%) =  $\left(\frac{C}{C_0}\right)$  \* 100% to derive the theoretical remaining HA

Theoretical remaining HA

$$= -\frac{Z \cdot Mw(charge)_{PDADMAC}}{2 \cdot x \cdot Mw(charge)_{HA}} + \frac{1}{2}$$

$$+ \sqrt{\frac{Z \cdot \frac{Mw(charge)_{PDADMAC}}{Mw(charge)_{HA}} - x}{2 \cdot x}}^2 + \frac{K}{x \cdot [HA]_0^2}$$

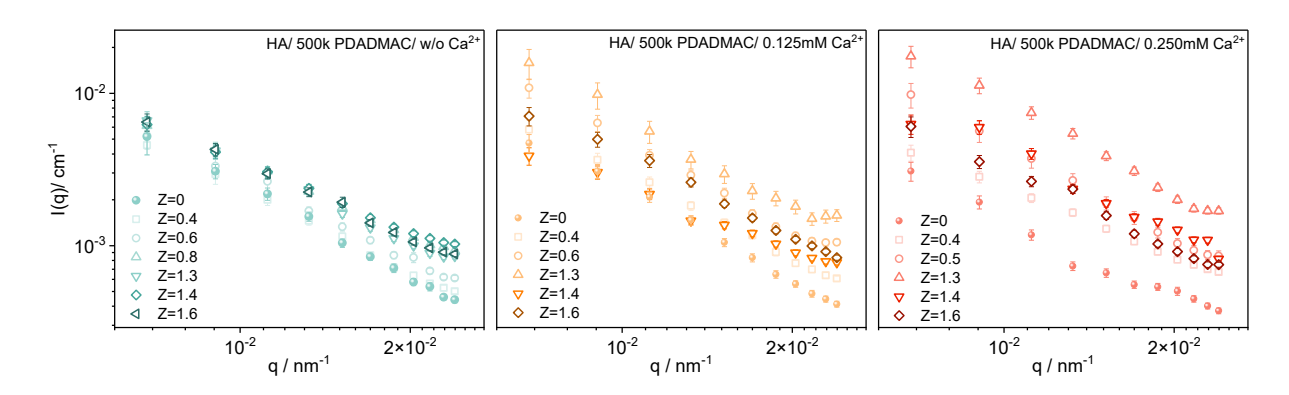


**Figure A.6.** SLS intensities of HA-PDADMAC complexes under varying Ca<sup>2+</sup> concentrations at different charge ratio Z at 25 °C.

**Table A.3.** Characteristic stretching exponent  $\alpha$  of HA-PDADMAC complexes under varying  $Ca^{2+}$  concentrations at different charge ratio Z at 25 °C.

Z	0	0.4	0.5	0.6	0.8	1.3	1.4	1.6
w/o Ca <sup>2+</sup>	0.941	0.926		0.897	0.895	0.888	0.913	0.884
0.125mM Ca <sup>2+</sup>	0.926	0.872		0.882		0.803	0.889	0.899
0.250mM Ca <sup>2+</sup>	0.941	0.927	0.797			0.895	0.883	0.909

<sup>\*</sup>determined from the DLS experiments with a stretched exponential fit

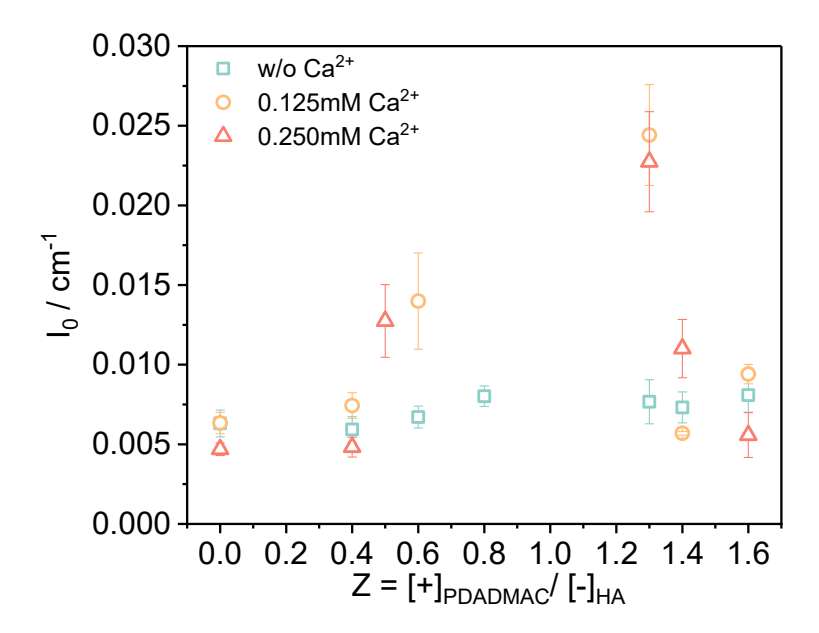


**Figure A.7.** The static intensity at zero angle,  $I_0$  under varying  $Ca^{2+}$  concentrations as a function of the charge ratio Z at 25 °C.

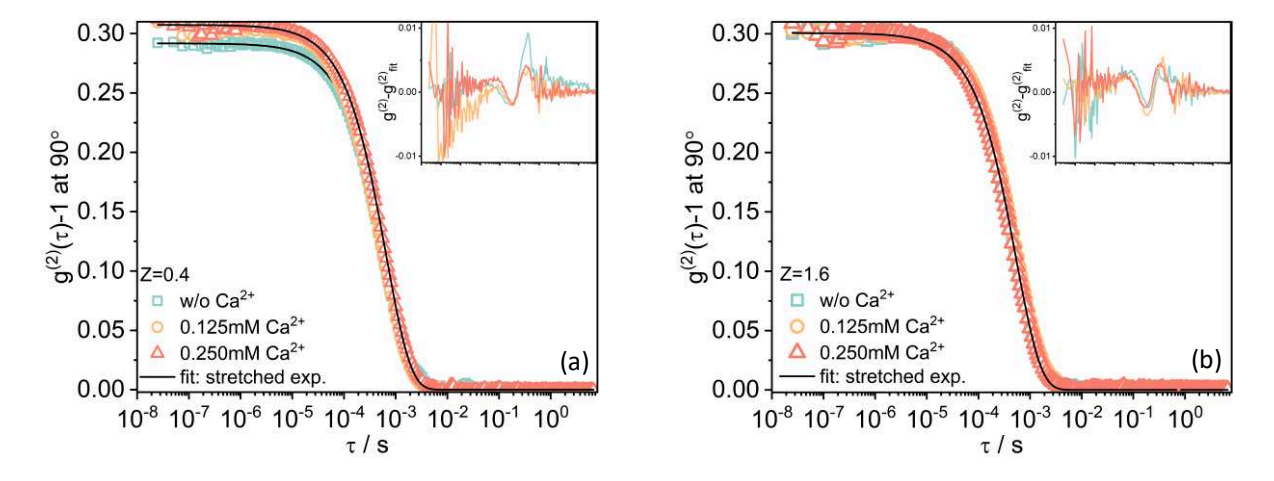


**Figure A.8.** Intensity auto-correlation function  $g^{(2)}(\tau)$  at 90° for HA-PDADMAC complexes at (a) Z = 0.4 and (b) Z = 1.6 under varying  $Ca^{2+}$  concentrations at 25 °C (c(HA) = 40 mg/L), as determined from the DLS experiments with a stretched exponential fit; The insets show the fit residuals,  $g^{(2)}-g^{(2)}_{fit}$ .

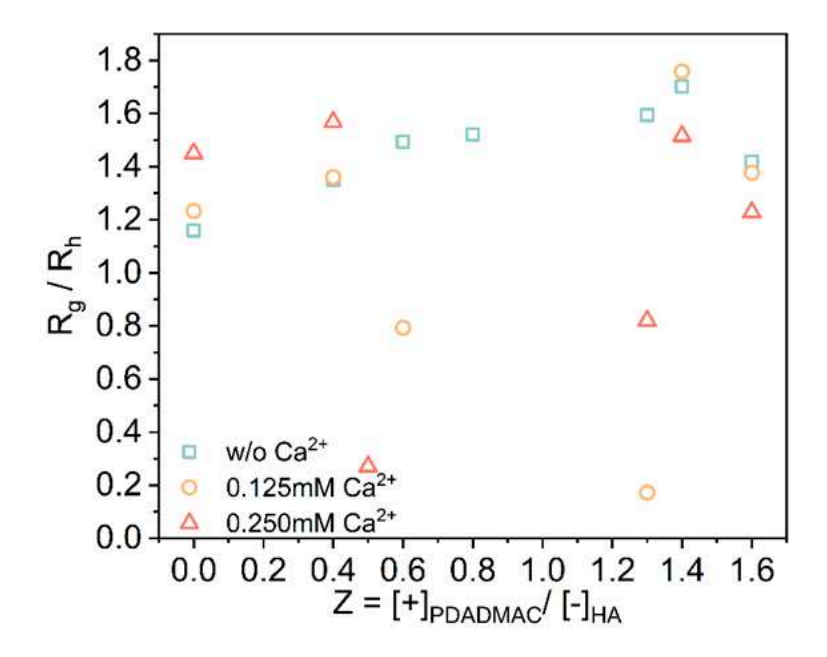


**Figure A.9.** Ratio of radius of gyration and hydrodynamic radius Rg/Rh for HA-PDADMAC complexes under varying Ca<sup>2+</sup> concentrations at different charge ratio Z at 25 °C

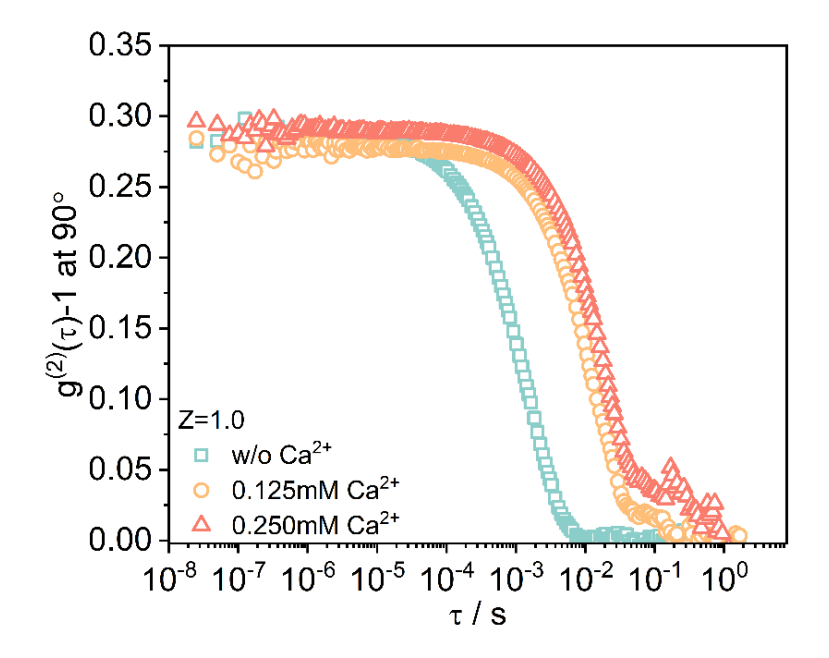


**Figure A.10.** Intensity auto-correlation function at 90° for HA-PDADMAC complexes at Z = 1.0 under varying  $Ca^{2+}$  concentrations (c(HA) = 40 mg/L). All the measurements were conducted 5 min after mixing.

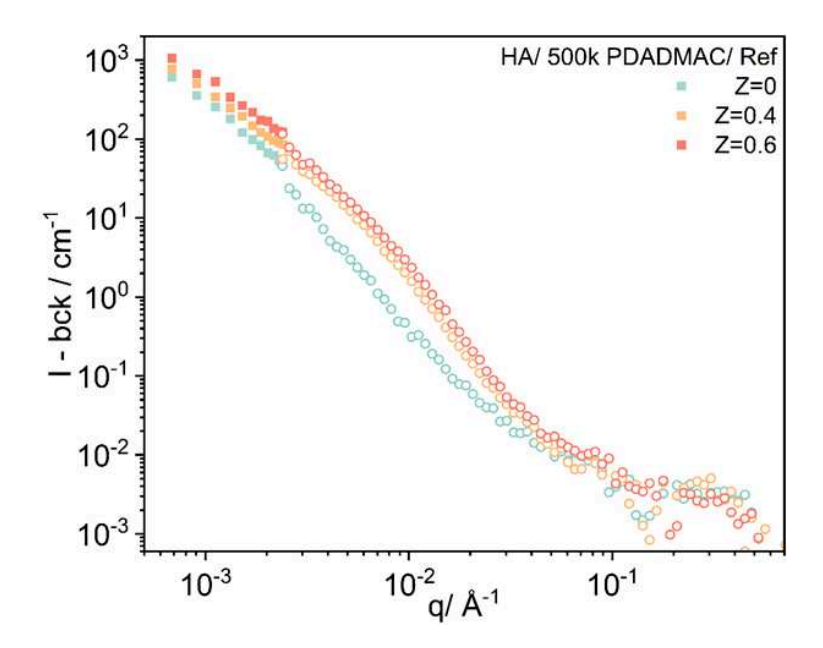


**Figure A.11.** Combined SLS and SANS spectra for HA-PDADMAC complexes without added salt. To superimpose both techniques we plot converted the scattering intensity of SLS to the one of SANS by the corresponding contrast term, which is given by

$$I(q)SANS = I(q)SLS \frac{\lambda^4 \phi \Delta SLD^2}{4\pi^2 n^2 (\frac{dn}{dc})^2 c \rho_{agg}},$$

where  $\lambda$  is the wavelength of the incident light beam,  $\phi$  is the volume fraction of all scattering particles,  $\Delta SLD$  is the difference in scattering length density between particle and solvent, n is the refractive index of the solvent, (dn/dc) the refractive index increment, c is the mass concentration of solute and  $\rho_{agg}$  is the mean density of scattering particles.

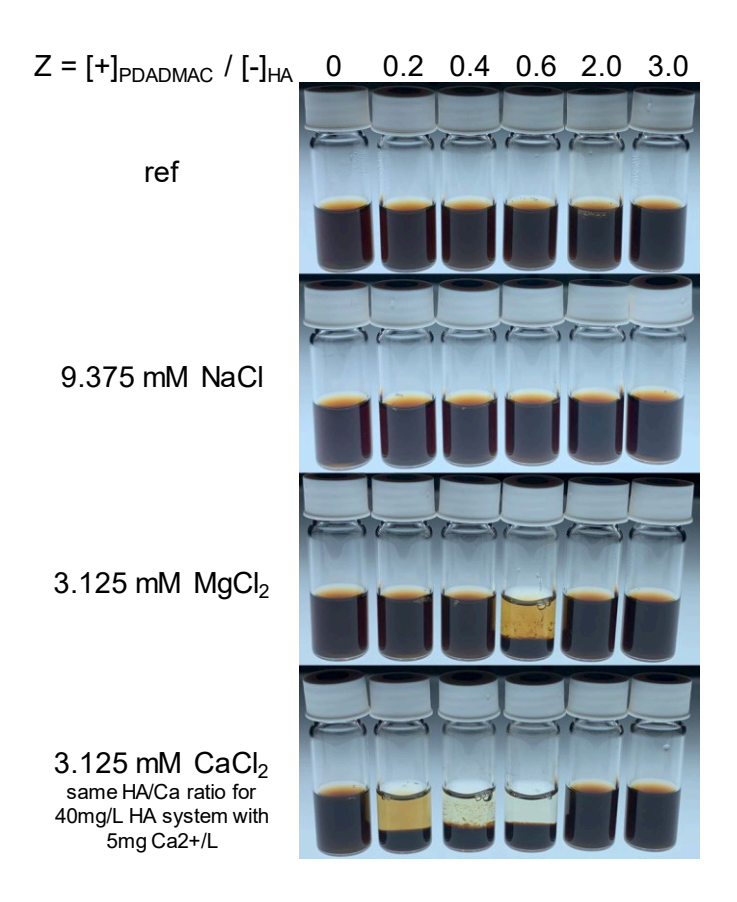


**Figure A.12.** Photos of HA-PDADMAC complexes measured at ISIS with 1000 mg/L HA and different charge ratio Z values under different ionic conditions. Photos were taken after an aging time of 24 hours after mixing.

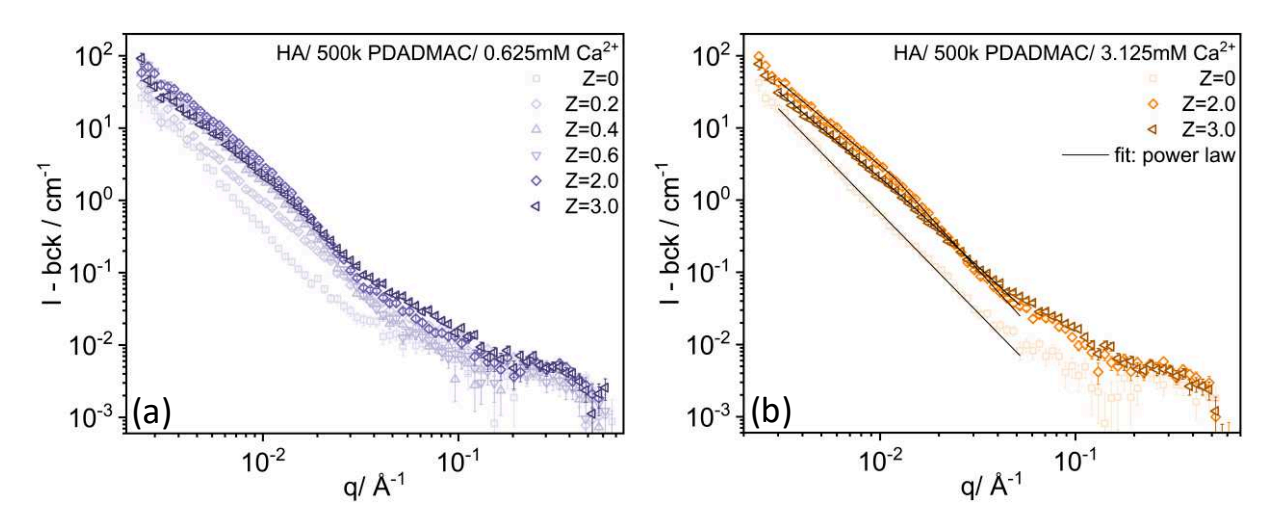


**Figure A.13.** Scattering intensity as a function of the magnitude of the scattering vector q for HA-PDADMAC complexes with (a) 0.625 mM CaCl<sub>2</sub> and (b) 3.125 mM CaCl<sub>2</sub>, respectively (c(HA) = 1.0 g/L).

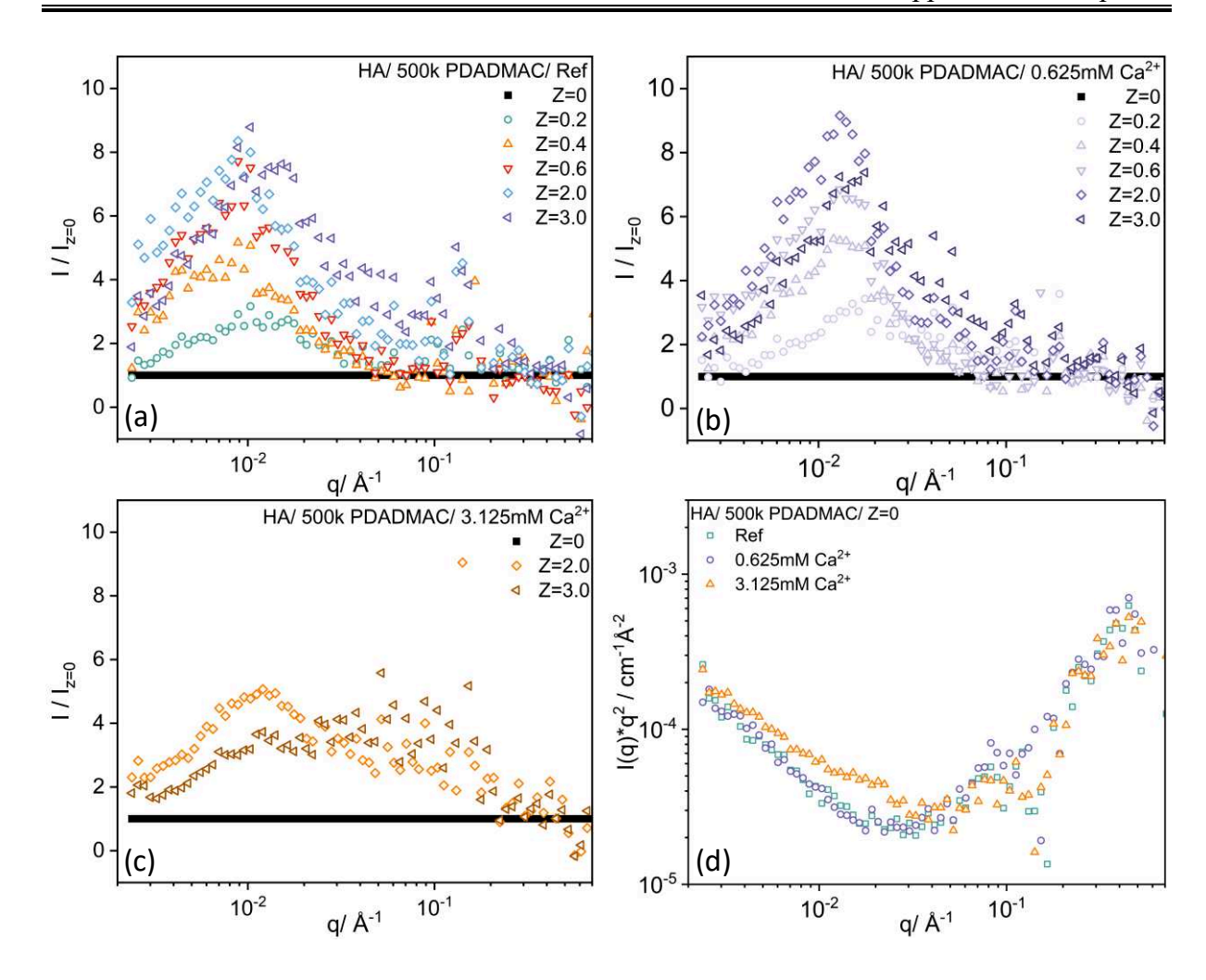


**Figure A.14.** Scattering intensity as a function of the magnitude of the scattering vector q for HA-PDADMAC complexes without added salt (a), with 0.625 mM  $CaCl_2$  (b), with 3.125 mM  $CaCl_2$  (c) normalised to the respective pure HA intensity (I/I<sub>Z=0</sub>) and the corresponding Kratky-Porod plot of the pure HA aggregates (Z = 0) (d).

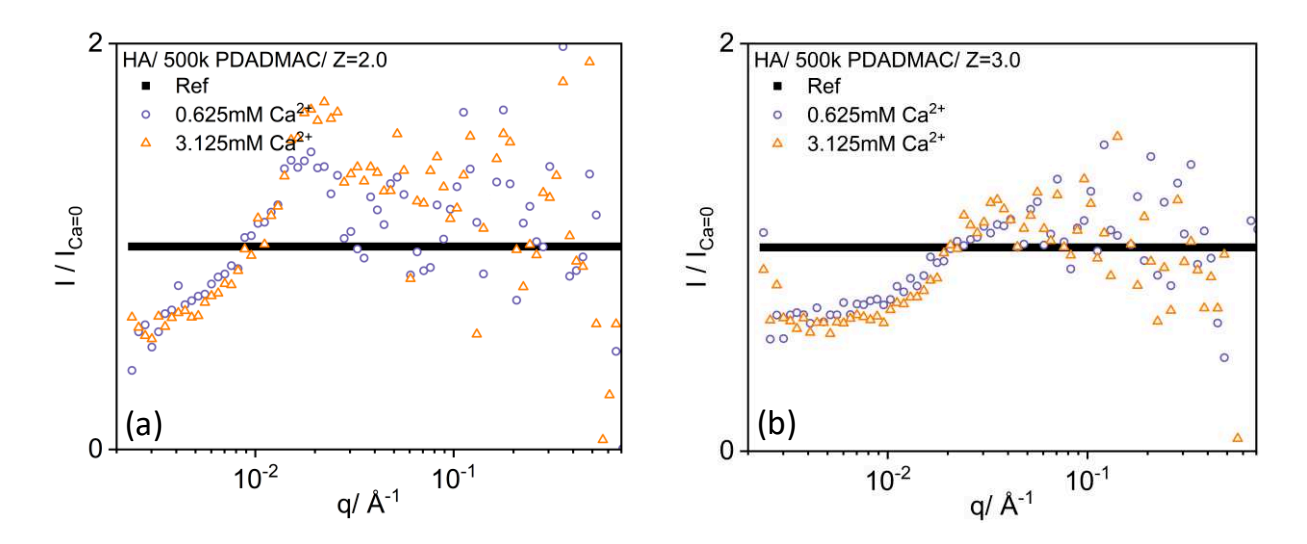


**Figure A.15.** Scattering intensity as a function of the magnitude of the scattering vector q for HA-PDADMAC complexes for Z = 2.0 (a) and Z = 3.0 (b) for different addition of CaCl<sub>2</sub>, normalized to the respective system without added CaCl<sub>2</sub>.

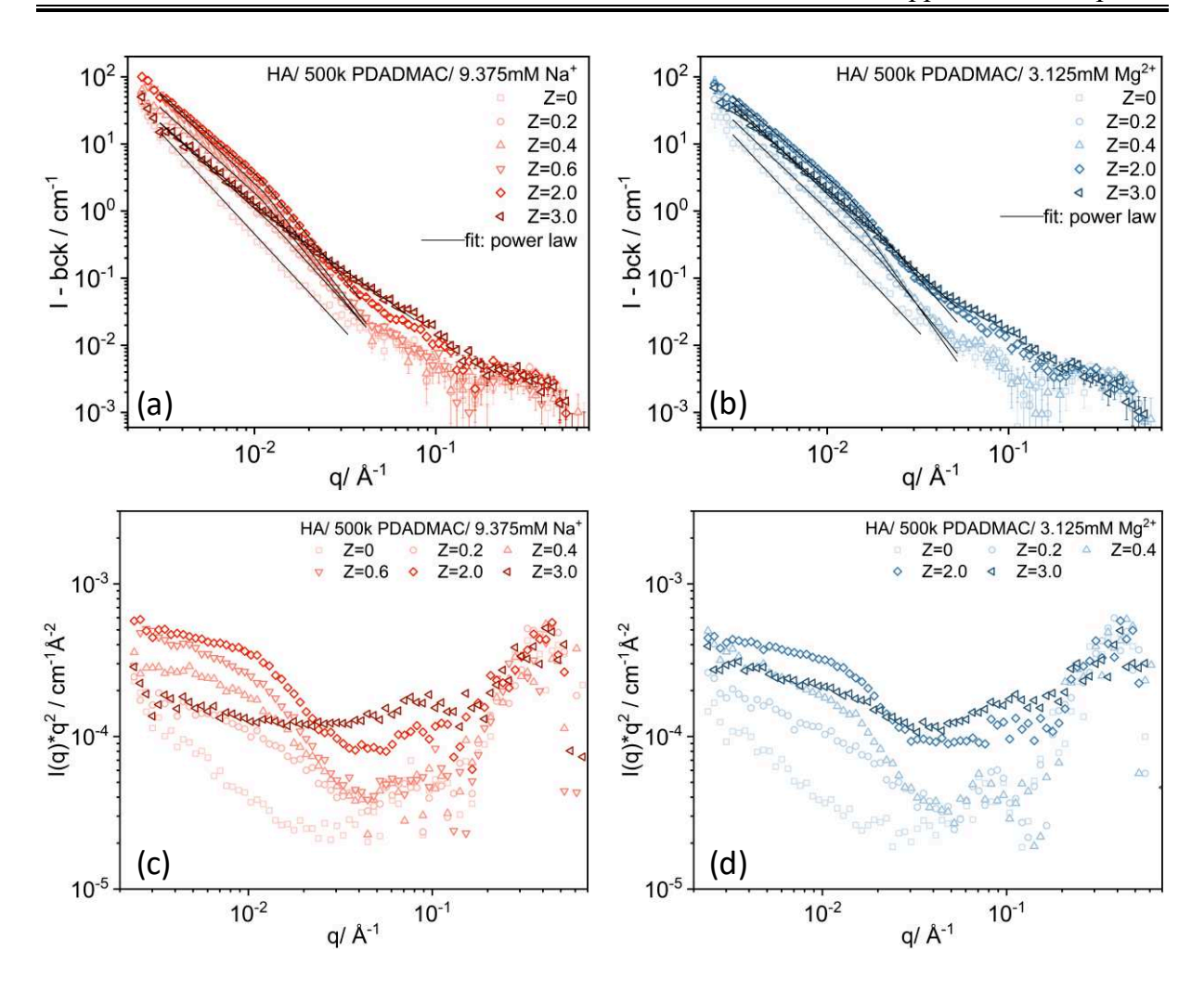


**Figure A.16.** SANS intensity as a function of the magnitude of the scattering vector q for HA-PDADMAC complexes with addition of (a) 9.375 mM Na<sup>+</sup> and (b) 3.125 mM Mg<sup>2+</sup>, respectively, and the corresponding Kratky-Porod plots (c(HA) = 1.0 g/L) (c) and (d).

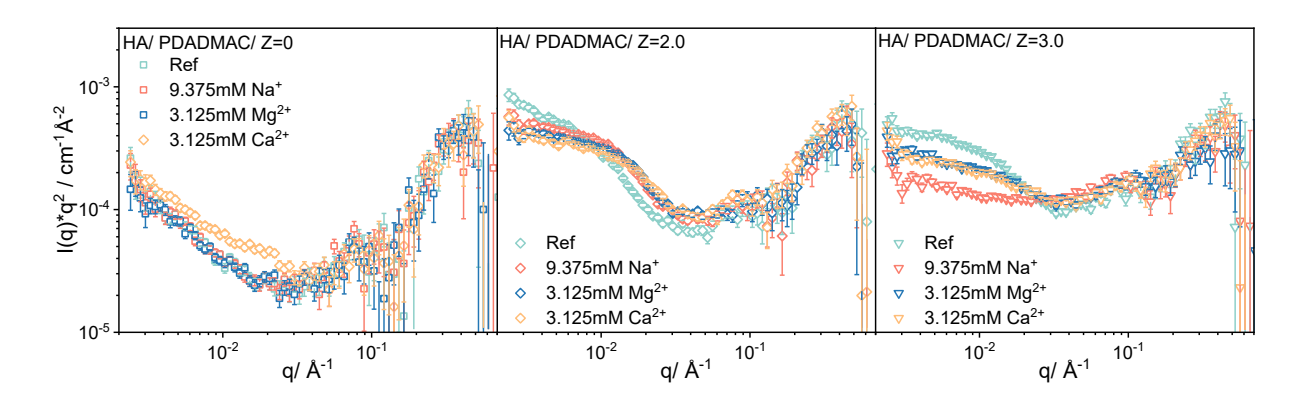


**Figure A.17.** SANS intensity  $I^*q^2$  as a function of the magnitude of the scattering vector q for complexes of HA and 500 kDa PDADMAC under various ionic conditions with Z = 0, 2 and 3, respectively.

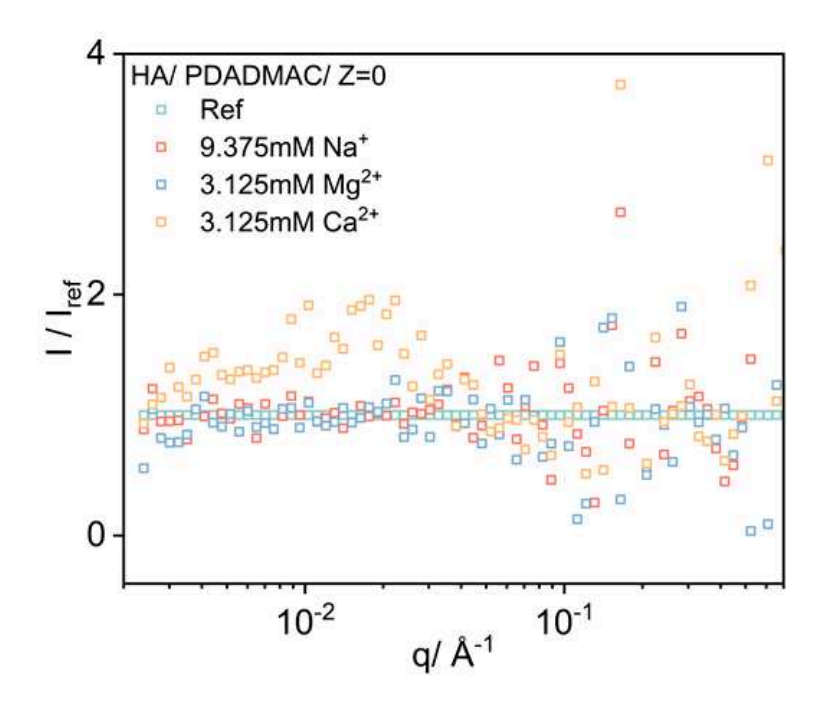


**Figure A.18.** Scattering intensity as a function of the magnitude of the scattering vector q for HA complexes (c(HA) = 1.0 g/L) at Z = 0 under various ionic conditions normalized to the intensity of pure HA without added salt ( $I/I_{Ref}$ ).

**Table A.4.** Radius of gyration at larger scale  $R_{g1}$  and smaller scale  $R_{g2}$  as well as the corresponding scaling pre-factor G, power law scattering pre-factor B and power law exponent P as determined by the Beaucage model from the SANS data of HA complexes with different charge ratio Z values under different ionic conditions.

	Z	R <sub>g1</sub> , nm	$P_1$	B <sub>1</sub> , 10 <sup>-6</sup> cm <sup>-1</sup> nm <sup>-p</sup>	G <sub>1</sub> , cm <sup>-1</sup>	R <sub>g2</sub> , nm	P <sub>2</sub>	B <sub>2</sub> , 10 <sup>-3</sup> cm <sup>-1</sup> nm <sup>-p</sup>	G <sub>2</sub> , cm <sup>-1</sup>
	0	43.7	2.06	2.37	15.6				
	0.2	56.1	2.79	2.96	51.2	5.19	0.78	1.31	0.03
C	0.4	58.2	3.44	2.33	95.8	5.51	0.46	1.52	0.01
ref	0.6	62.4	2.91	4.41	154	7.68	1.24	0.42	0.11
	2	76.8	2.85	6.83	331	9.01	1.36	0.52	0.25
	3	95.5	2.31	8.18	341	9.60	1.45	0.57	0.49
	0	43.0	1.98	3.27	14.9				
	0.2	60.8	2.77	3.12	50.1	2.34	0.22	1.97	0.01
No	0.4	53.6	2.79	5.26	65.2	6.24	0.99	0.63	0.06
Na	0.6	63.4	2.57	2.15	143	8.39	1.25	0.42	0.14
	2	64	2.5	1.40	156	10.2	1.59	3.10	0.52
	3	52.9	2.74	3.72	38.5	8.05	1.77	0.30	0.48
	0	44.4	2.14	1.72	16.2				
	0.2	58.6	2.59	7.49	53.9	4.45	0.56	1.46	0.02
Mg	0.4	108	2.40	3.29	508	7.47	0.82	0.96	0.06
	2	56.3	3.55	1.54	94.1	13.7	1.73	0.23	3.80
	3	59.4	2.28	6.17	84.8	8.25	1.63	0.39	0.40
	0	56.1	2.49	6.38	41.9				
Ca	2	86.8	2.12	1.42	278	8.30	1.37	0.61	0.30
	3	102	2.30	0.52	324	7.41	1.55	0.48	0.31

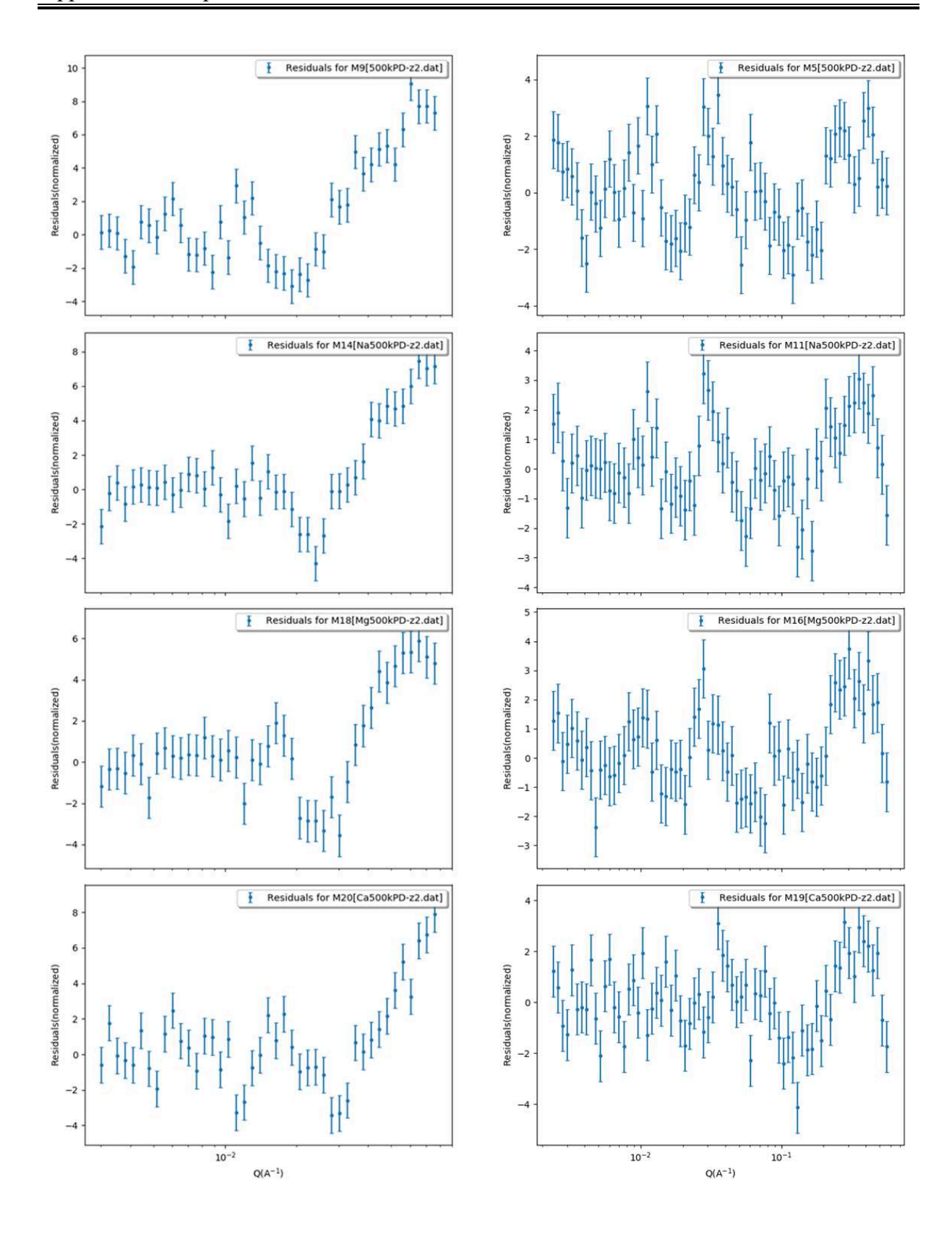


**Figure A.19.** Corresponding residuals for fit of SANS data for 500kDa PDADMAC-HA complexes under various ionic conditions at Z = 2 with the two-power law model (left column) and Beaucage model (right column).

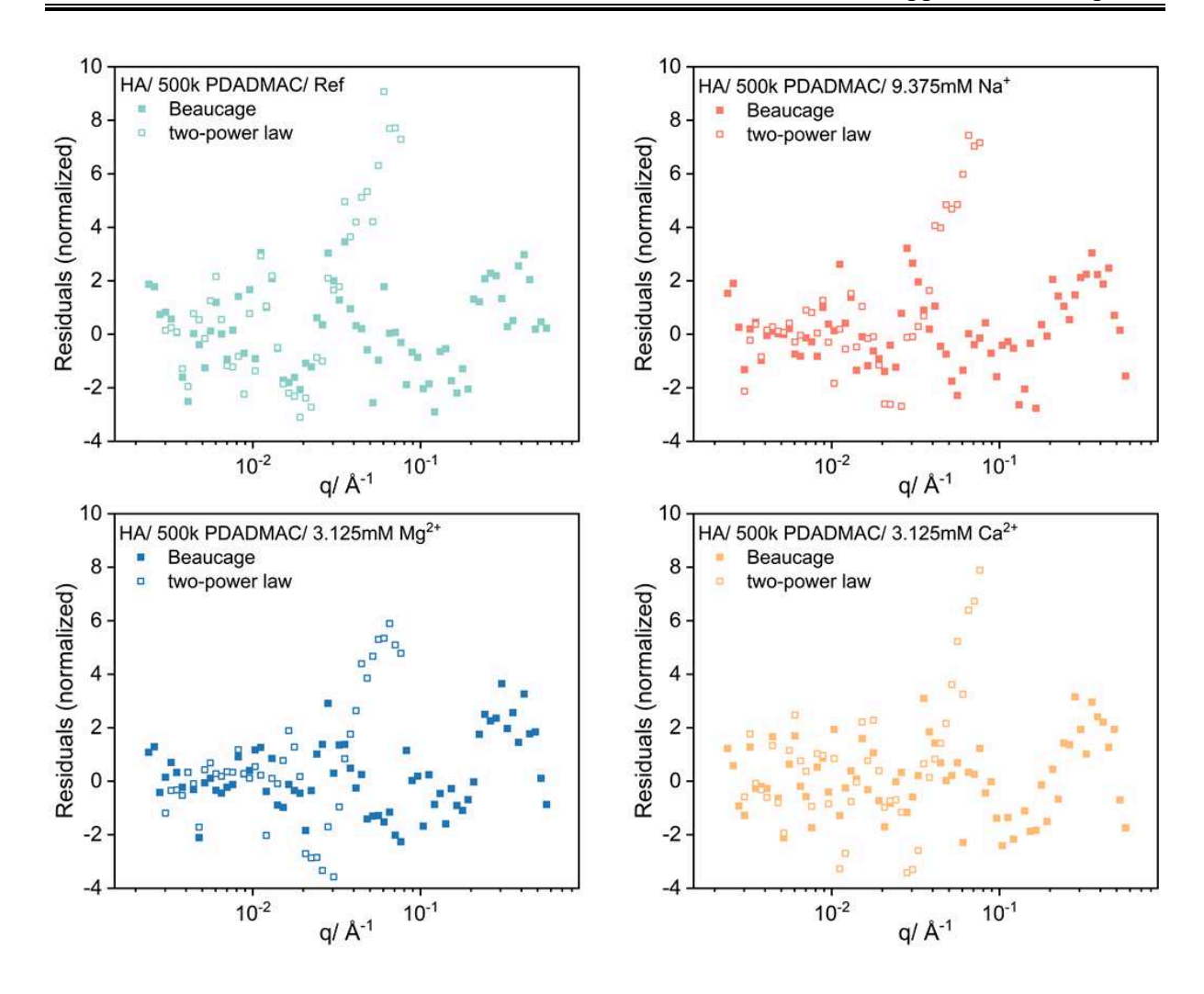


**Figure A.20.** Corresponding residuals for fit of SANS data for 500kDa PDADMAC-HA complexes under various ionic conditions at Z = 2 with the two-power law model and Beaucage model.

# Appendix B. Chapter 4

## Characterization of IHSS (International Humic Substances Society)-HA

The average molecular weight of the charged unit was determined using potentiometric titration with a 0.1 M HCl solution. From the titration curve, three inflection points were identified. The consumption of the acid solution between the first and second inflection points corresponds to the protonation of hydroxide anions from the HA molecules, while the consumption between the second and third inflection points corresponds to the protonation of carboxylate anions. The charge per of humic acid can be calculated by the overall consumption between the first and the third inflection points.

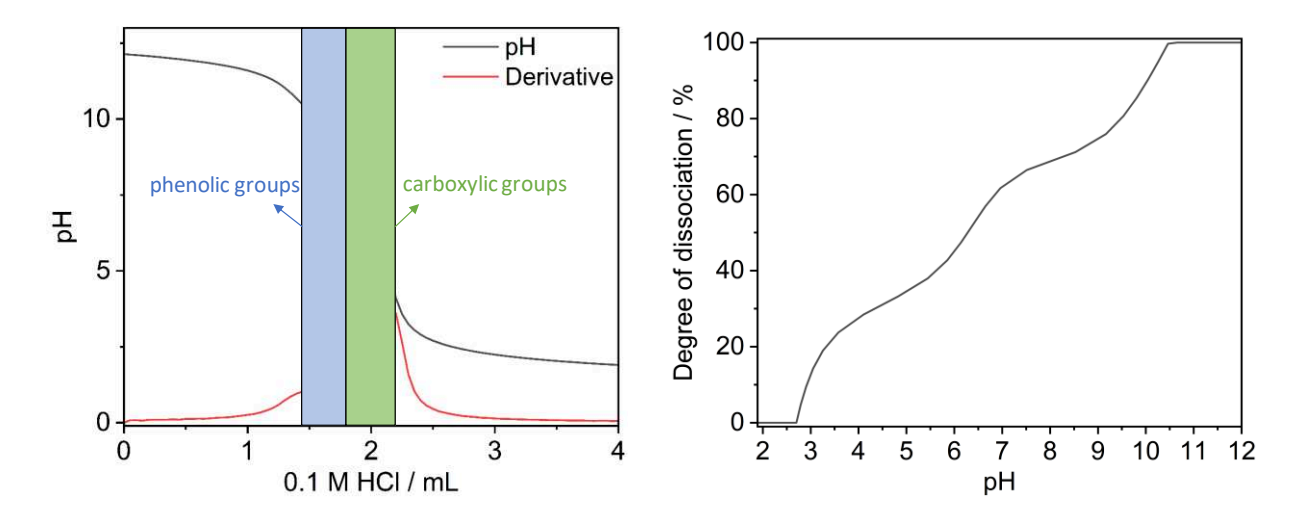


**Figure B.1.** Potentiometric titration curve of humic acid with a solution of HCl and the corresponding degree of dissociation as a function of pH.

### Degree of deacetylation (DDA) of chitosan

The degree of deacetylation (DDA) was determined by potentiometric titration with 0.1 M sodium hydroxide solution<sup>126</sup>. From the titration curve in **Figure S2** two inflexion points were derived, between which the consumption of basic solution indicating the deprotonation of ammonium cations from the chitosan. This parameter allows the calculation of the degree of deacetylation (DDA), which was determined to be 73%.

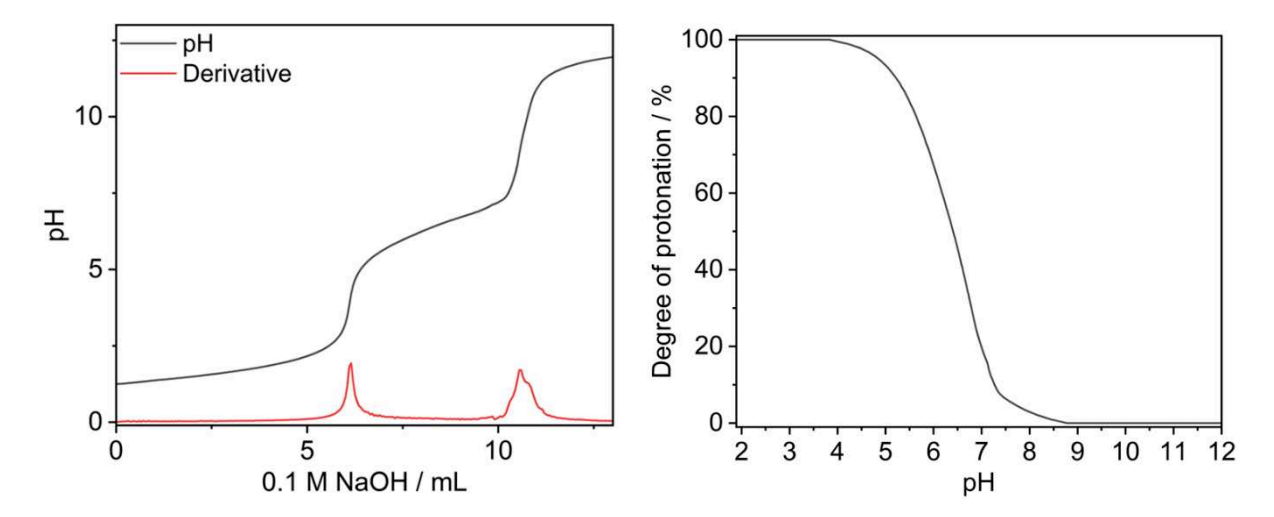


**Figure B.2.** Determination of the degree of deacetylation (DDA) from potentiometric titration of chitosan.

#### **QCSs** characterization

The DS for each QCS variant was determined through a titration method reliant on conductivity measurements with the addition of 0.01 M AgNO<sub>3</sub><sup>98</sup>. The formation of an insoluble salt between Ag<sup>+</sup> ions and the Cl<sup>-</sup> (counterions of GTMAC) leads to an initial decrease in the conductivity of the QCS solutions, followed by an increase. The inflection point in this trend corresponds to the stoichiometric balance between the substituted GTMAC and the added Ag<sup>+</sup>, thereby enabling the calculation of the substitution degree of GTMAC and of the permanent charge density of each QCS based on the average molecular weight of the substituted unit.

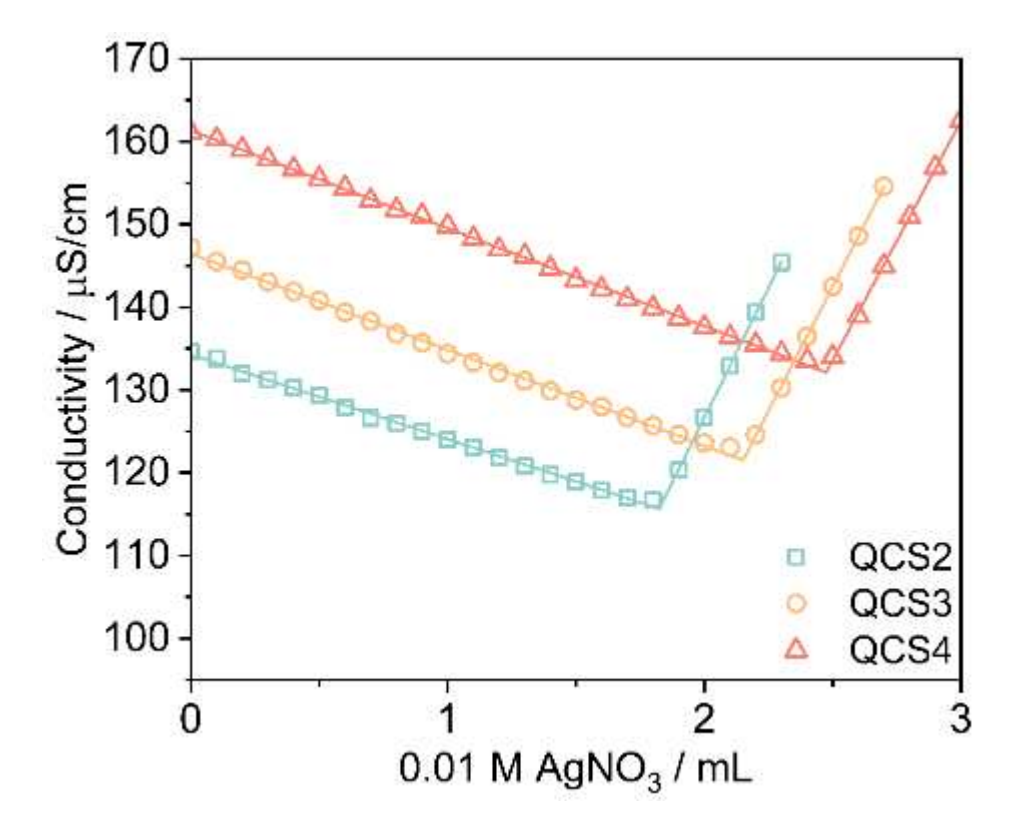


**Figure B.3.** Determination of the degree of substitution (DS) of modified chitosan from conductometric titration with AgNO<sub>3</sub>.

### **Phase Diagram**

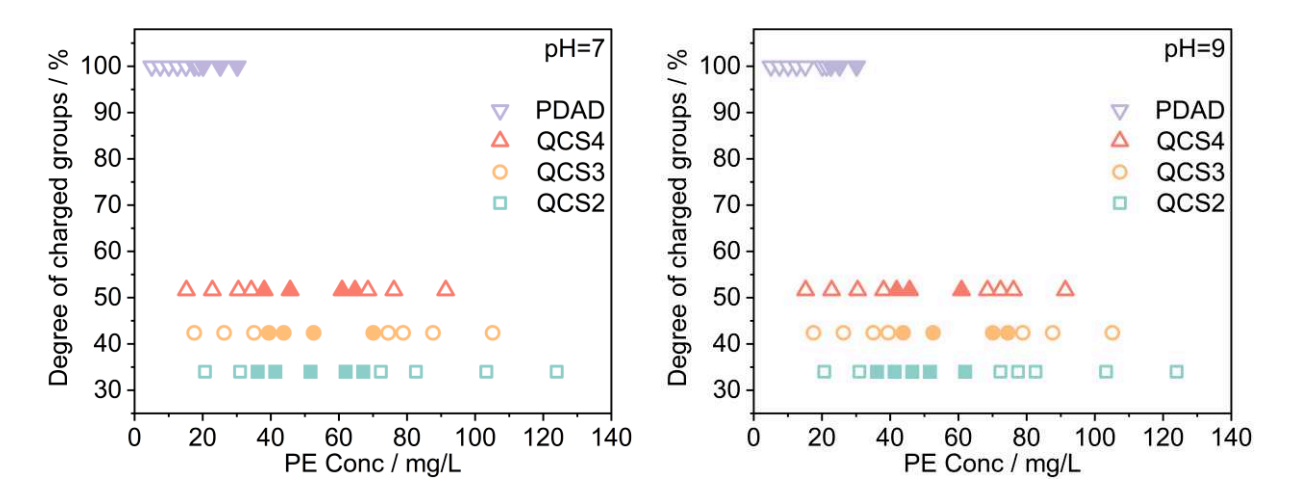


**Figure B.4.** Phase diagram of 40 mg/L HA and added polyelectrolytes, the added amount being characterised by the concentration of polyelectrolytes at pH 7 and pH 9, respectively (T = 25 °C). Open symbols refer to monophasic regions while full symbols refer to the biphasic region.

**Table B.1.**  $\zeta$ -potential for complexes of HA (40 mg/L) and different cationic polyelectrolytes, at pH 7 and pH 9, respectively, for different charge ratios Z (T = 25 °C).

		pН	[=7		pH=9				
Z	QCS2	QCS3	QCS4	<b>PDAD</b>	QCS2	QCS3	QCS4	<b>PDAD</b>	
	ξ, mV	ξ, mV	ξ, mV	ξ, mV	ξ, mV	ξ, mV	ξ, mV	ξ, mV	
0	-26.2(1.5)				-33.0(1.6)				
0.2	-28.6(1.2)	-31.1(1.1)	-31.3(1.3)	-29.6(1.1)	-35.5(1.4)	-33.3(1.6)	-28.7(1.4)	-28.3(1.8)	
0.3	-24.5(1.3)	-27.6(1.8)	-26.5(1.5)	-26.5(1.8)	-27.5(1.7)	-30.0(1.9)	-23.9(2.0)	-27.7(1.3)	
0.4	-20.8(0.9)	-19.5(0.8)	-22.2(0.9)	-28.7(2.5)	-16.9(1.0)	-17.6(1.4)	-20.6(1.0)	-27.3(0.6)	
0.5	-15.0(1.0)	-18.7(0.8)	-18.4(0.7)	-22.6(1.9)	-14.6(1.0)	-17.8(0.7)	-21.2(0.5)	-22.2(1.3)	
0.6	-2.8(0.3)	-6.5(0.5)	-6.6(0.3)	-23.8(0.7)	2.1(0.3)	-9.5(0.5)	-13.0(0.4)	-21.5(0.4)	
0.8	16.0(0.4)	11.9(0.2)	6.5(0.1)	-19.8(0.8)	7.0(0.4)	10.7(0.3)	5.2(0.4)	-20.1(0.7)	
1	21.2(1.0)	19.4(1.1)	21.3(1.4)	-10.9(0.5)	17.3(0.6)	19.5(0.8)	16.8(0.5)	-13.2(0.9)	
1.2	21.7(1.0)	24.2(1.1	24.4(0.7)	1.5(0.1)	19.7(0.8)	23.7(0.8)	24.1(0.8)	0.4(0.2)	

### Removal efficiency of humic acid – UV-vis monitoring

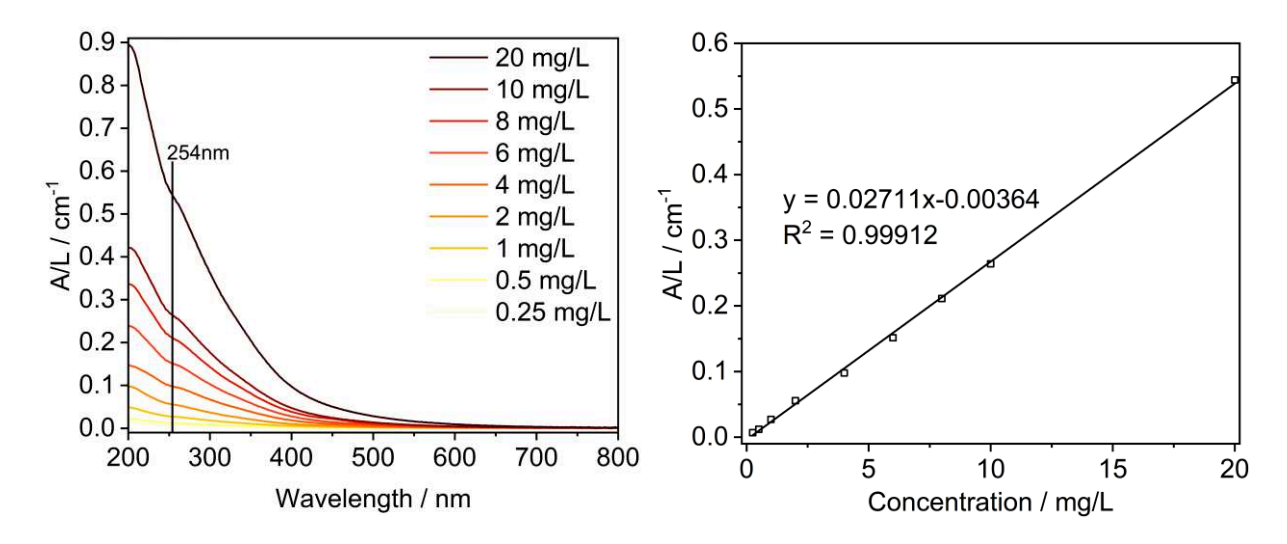


**Figure B.5.** UV-vis spectra of humic acid solutions of different concentrations and the corresponding calibration curve for HA concentration as a function of UV absorbance at 254 nm.

**Table B.2.** Decadic UV-absorbance at 254 nm per optical path length (UV254) for complexes of HA (40 mg/L) and different cationic polyelectrolytes, at pH 7 and pH 9, respectively, for different charge ratios Z (T = 25 °C).

	7	A/L (cm-1)			HA conc (mg/L)			Remaining HA (%)					
	Z	QCS2	QCS3	QCS4	PDAD	QCS2	QCS3	QCS4	PDAD	QCS2	QCS3	QCS4	PDAD
	0.4	0.26				9.8				24.4			
	0.5	0.18	0.26	0.41		7.0	9.9	15.1		17.4	24.8	37.7	
nII_7	0.6	0.18	0.27	0.18		6.9	10.2	7.0		17.2	25.5	17.4	
pH=7	0.8		0.48	0.18	0.31		17.7	6.7	11.5		44.3	16.7	28.8
	1				0.27				10.0				24.9
	1.2				0.17				6.6				16.4
	0.4												
	0.5	0.17	0.25			6.2	9.3			15.6	23.3		
pH=9	0.6	0.13	0.19	0.23		4.8	7.1	8.6		12.0	17.8	21.5	
	0.8		0.25	0.16			9.3	5.9			23.3	14.8	
	1				0.21				7.9				19.7
	1.2				0.11				4.3				10.8

<sup>\*</sup>the supernatant of samples with biphasic region was measured 24 hours after mixing for different cationic polyelectrolytes at different charge ratio Z at 25 °C. The corresponding HA concentration and remaining HA percentage were calculated.

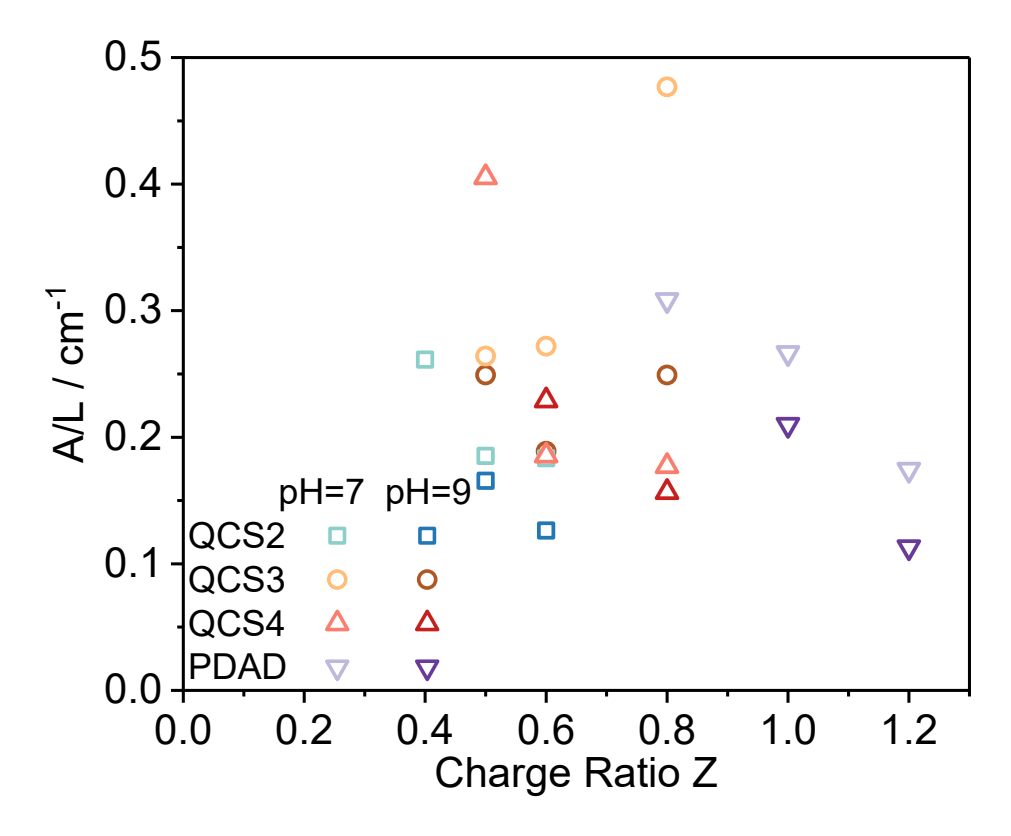


**Figure B.6.** Decadic UV-absorbance at 254 nm per optical path length (UV254) of HA-PE systems (supernatant for biphasic region) 24 hours after mixing at pH 7 and pH 9, respectively, for different charge ratios Z at 25 °C.

#### **Fluorescence Probe Studies**

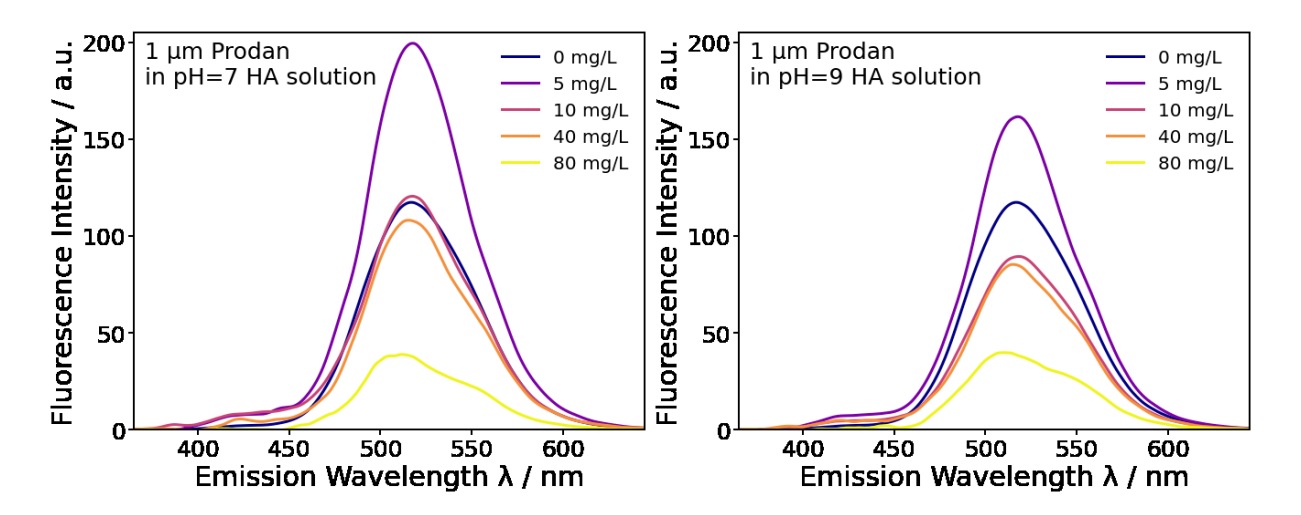


**Figure B.7.** The fluorescence emission spectra of polarity-sensitive 1 μM Prodan probe in varying concentrations of humic acid at different pH

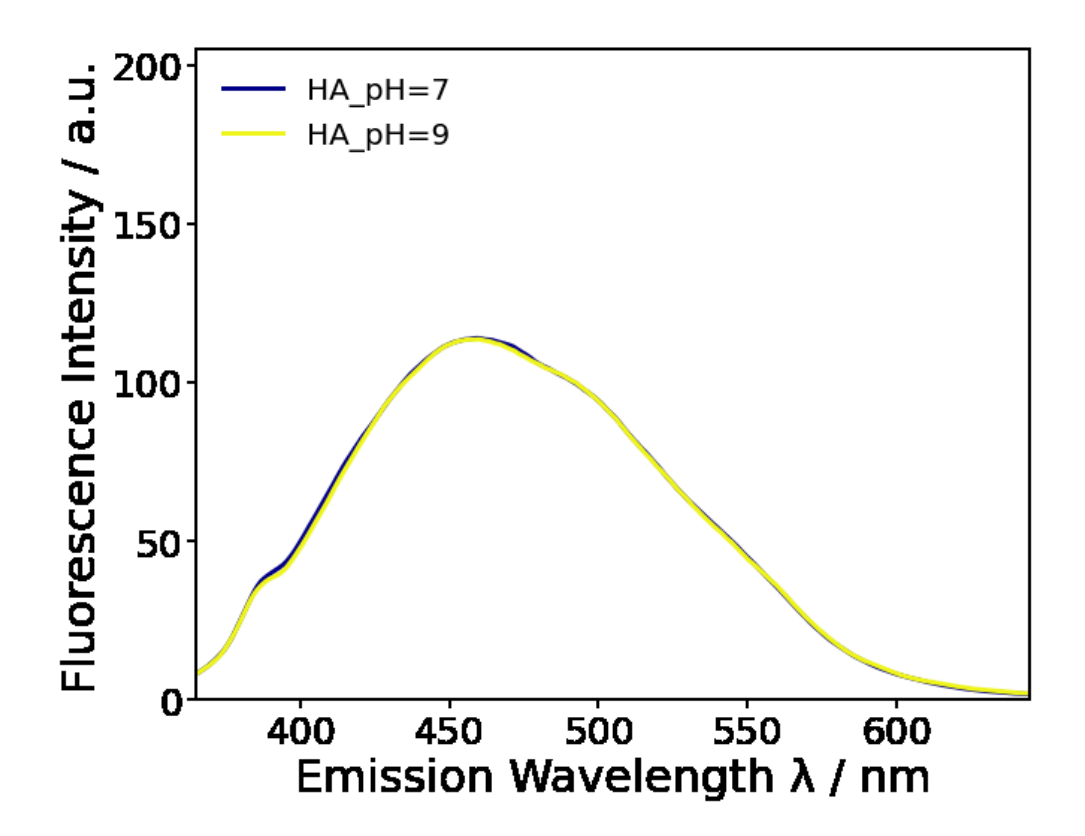


**Figure B.8.** Fluorescence emission spectra of 40 mg/L humic acid at pH 7 and pH 9, respectively.

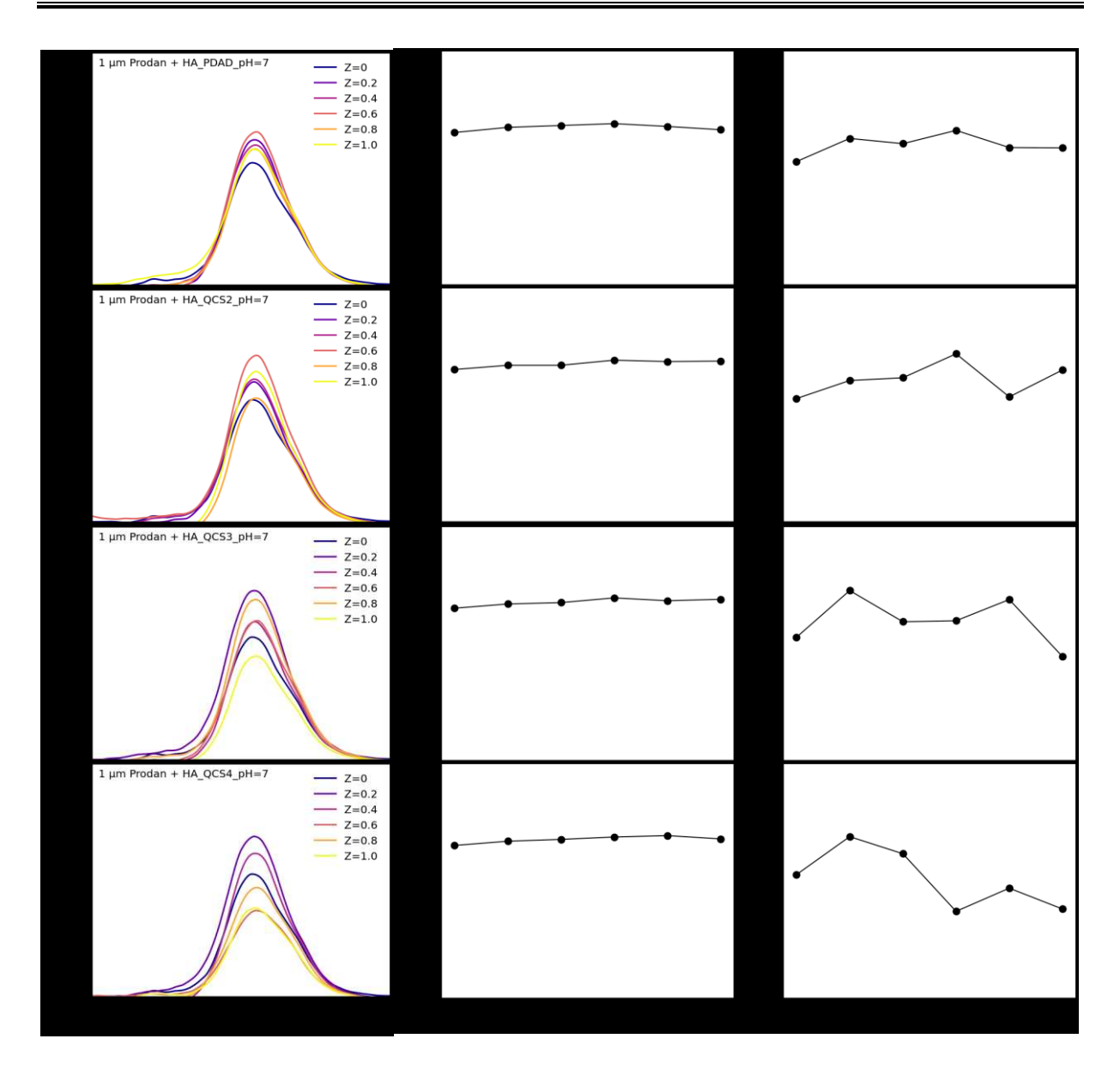


**Figure B.9.** Fluorescence spectra of the various HA (40 mg/L)-cPE complexes containing 1  $\mu$ M Prodan at pH 7 for different charge ratio Z at 25 °C and the extracted wavelength of the maximum emission ( $\lambda_{max}$ ) and its emission intensity ( $F_{max}$ ).

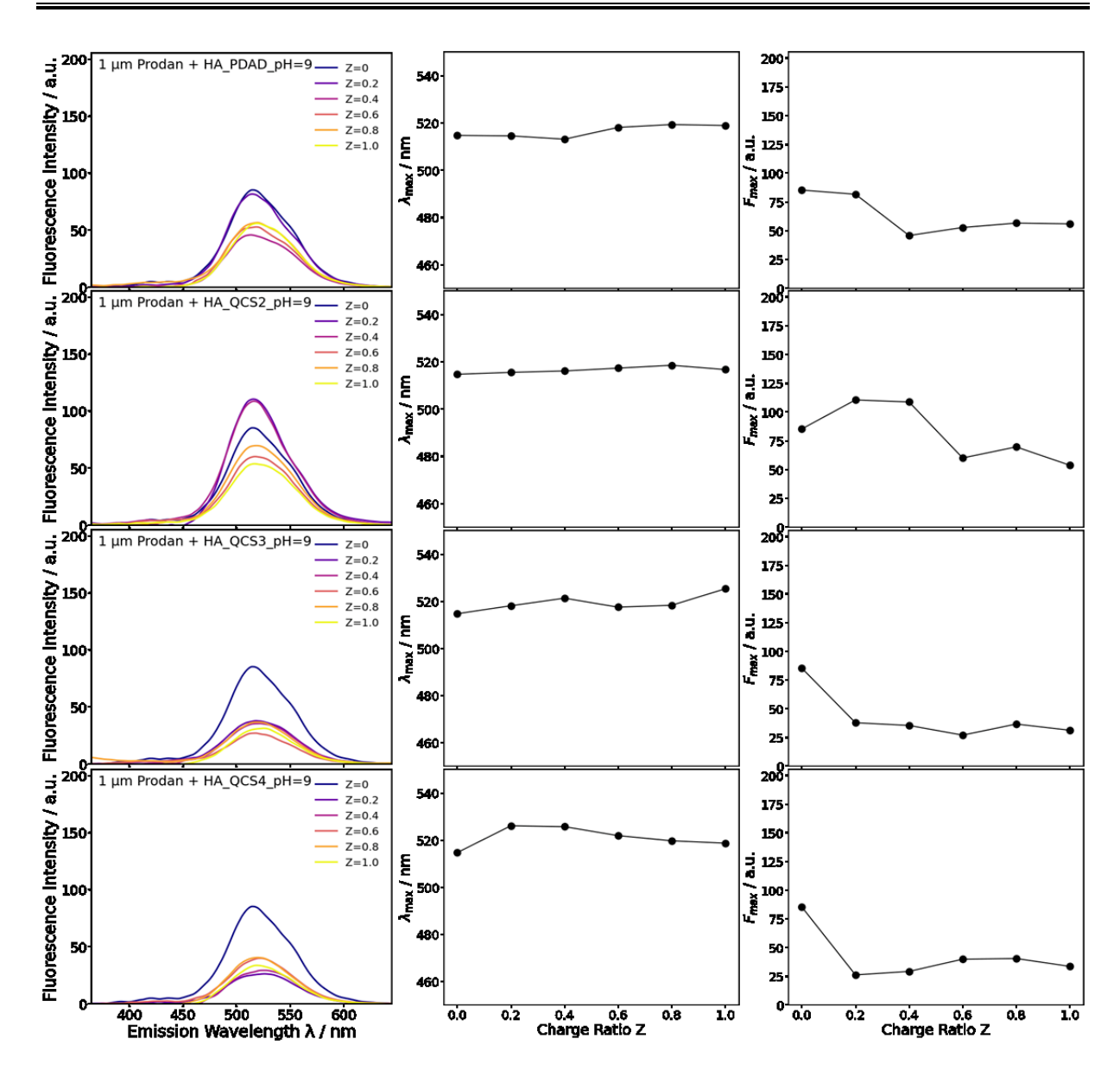


**Figure B.10.** Fluorescence spectra of the various HA (40 mg/L)-cPE complexes containing 1  $\mu$ M Prodan at pH 9 for different charge ratio Z at 25 °C and the extracted wavelength of the maximum emission ( $\lambda_{max}$ ) and its emission intensity ( $F_{max}$ ).

#### Flocculation of HA complexes via light diffraction

Two factors including size distribution density q3\* and cumulative mass distribution  $Q_3$  were utilized to elaborate the flocculation process of HA complexes. Specifically, size distribution density  $q_3^*$  represents the probability of finding a particle with certain diameter within the population, whereas the cumulative mass distribution  $Q_3$  is the integral curve for the size distribution, indicating the percentage of particles that are smaller than a specific diameter. The median percentiles of the particle size distribution, which are measured as the middle of cumulative mass distribution  $Q_3$  curve, was denoted as x(50%). This parameter was adopted to provide a direct quantification of particle size during the flocculation process.

The change of the median percentiles of the particle size distribution x(50%) over time, characteristic of the size growth of HA complexes, was analyzed with the logistic growth model, with

$$P(t) = \frac{L}{1 + e^{-k(t - t_0)}}$$

Where P(t) is the particle size at time t, L is the maximum size the HA complexes can achieve, k is the growth rate and  $t_0$  is the time at which the particle size is half of L.

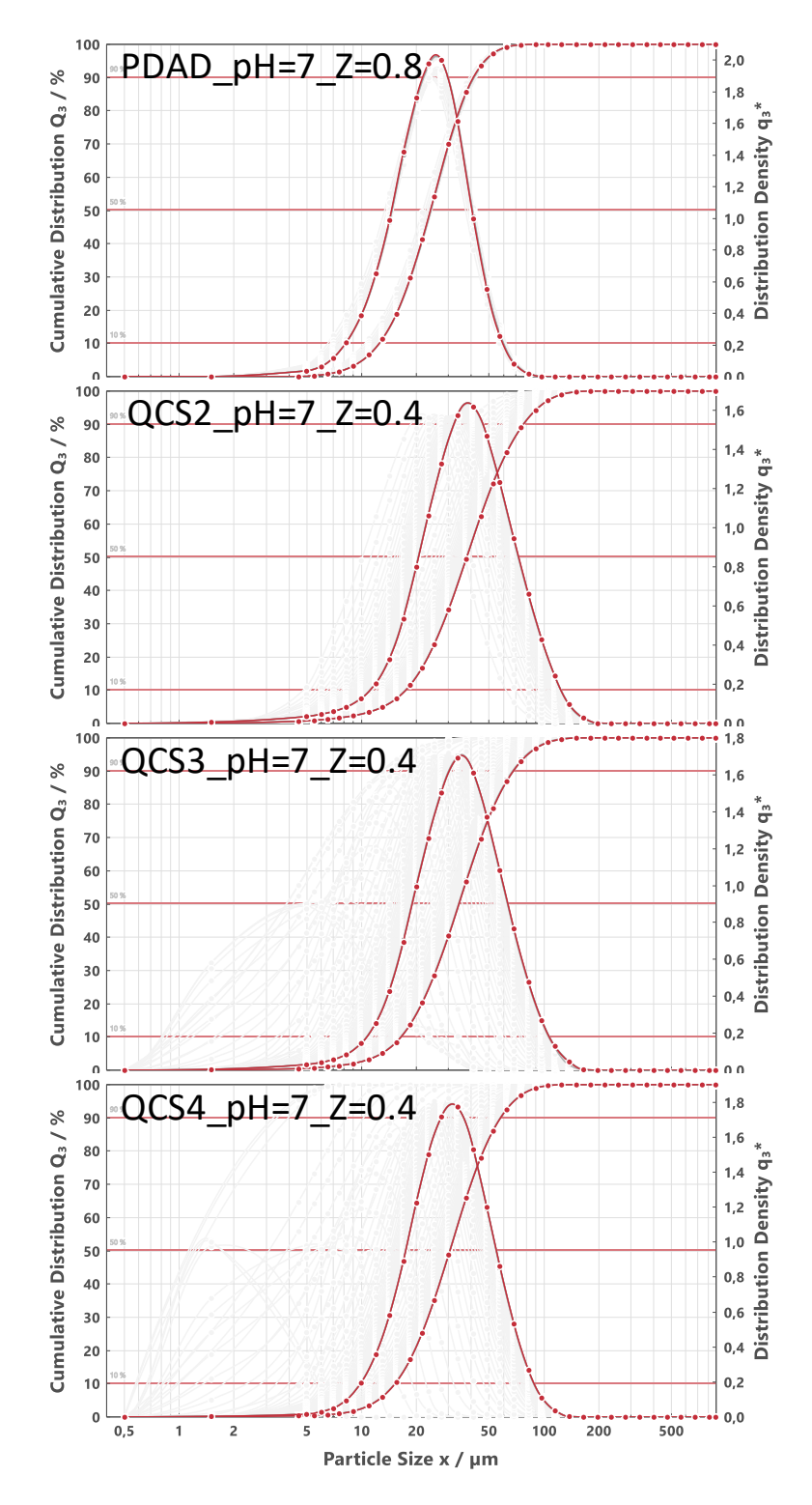


**Figure B.11.** Laser diffraction particle size distribution density q<sub>3</sub>\* and cumulative mass distribution Q<sub>3</sub> as a function of particle size recorded for complexes of HA and various QCSs with charge ratio Z=0.4 at pH 7 upon mixing. For HA-PDADMAC complexes, the charge ratio is 0.8. Each curve represents time interval of 10 s, in which the red one refers to the measurement at 300 s.

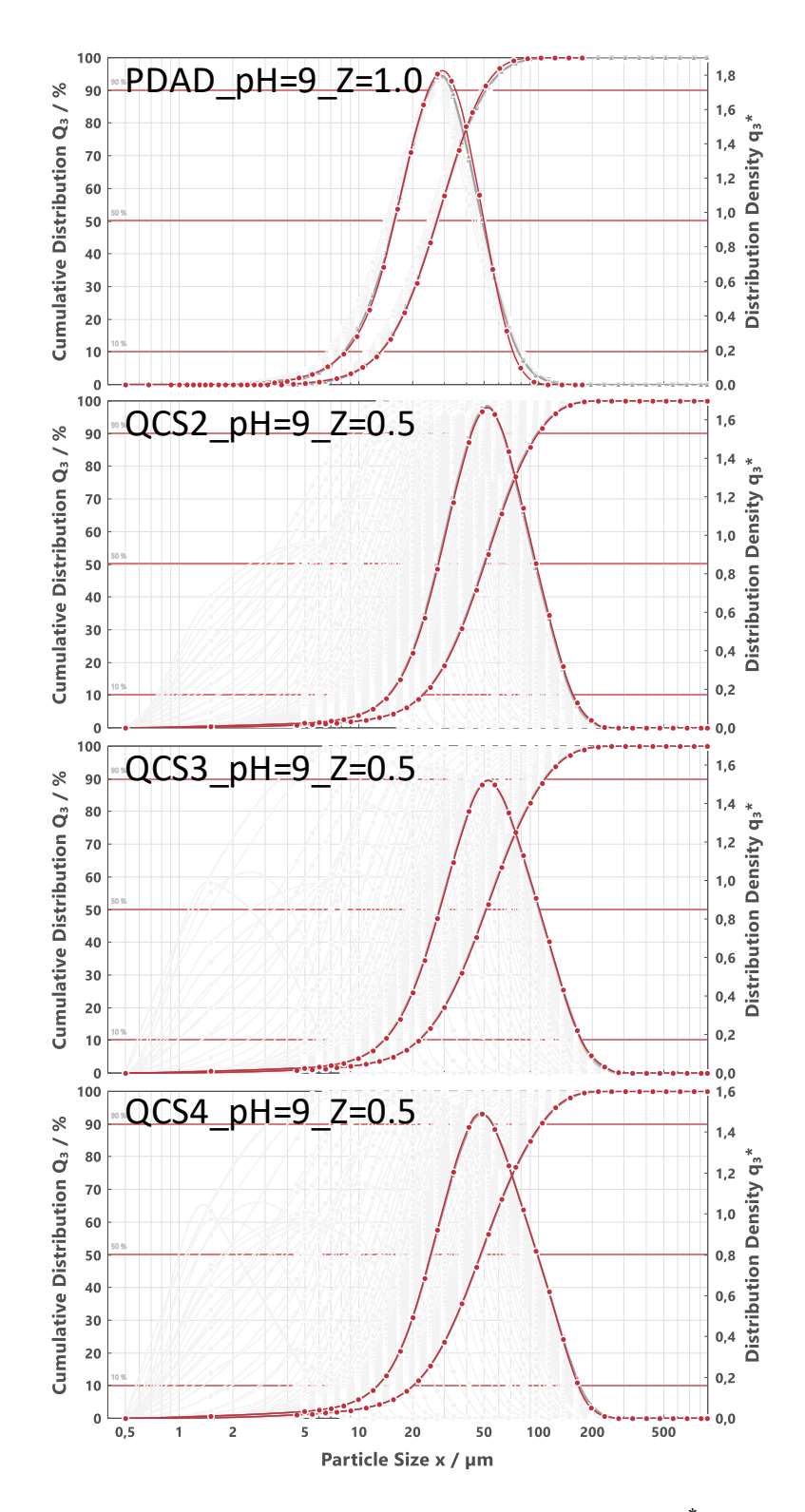


**Figure B.12.** Laser diffraction particle size distribution density  $q_3^*$  and cumulative mass distribution  $Q_3$  as a function of particle size recorded for complexes of HA and various QCSs with charge ratio Z=0.5 at pH 9. For HA-PDADMAC complexes, the charge ratio is 1.0. Each curve represents time interval of 10 s, in which the red one refers to the measurement at 300 s.

**Table B.3.** The maximum size  $x(50\%)_M$  of the HA complexes, the growth rate k, the time  $t_0$  at which the particle size is half of L and the corresponding goodness of fit  $R^2$  as determined by the logistic growth model (eq. 1) from the laser light diffraction data for complexes of HA and various cationic polyelectrolytes with various charge ratio Z.

		Z	L, µm	k, s <sup>-1</sup>	t <sub>0</sub> , s	$\mathbb{R}^2$
	QCS2	0.4	37.65	0.012	-17.05	0.9907
	QCS3	0.4	34.24	0.017	106.47	0.99
<b>pH=7</b>	0004	0.4	30.49	0.02	141.35	0.9913
	QCS4	0.5	39.05	0.013	43.35	0.9926
	PDAD	0.8	24.01	0.045	-48.66	0.9615
	QCS2	0.4	46.77	0.018	134.05	0.9891
	QCS2	0.5	48.71	0.009	203.26	0.9916
pH=0	QCS3	0.5	51.12	0.015	194.97	0.9922
pH=9	QCS4	0.5	46.14	0.016	221.16	0.9958
	QC54	0.6	65.12	0.005	413.65	0.9863
	PDAD	1.0	27.33	0.042	-46.15	0.9381

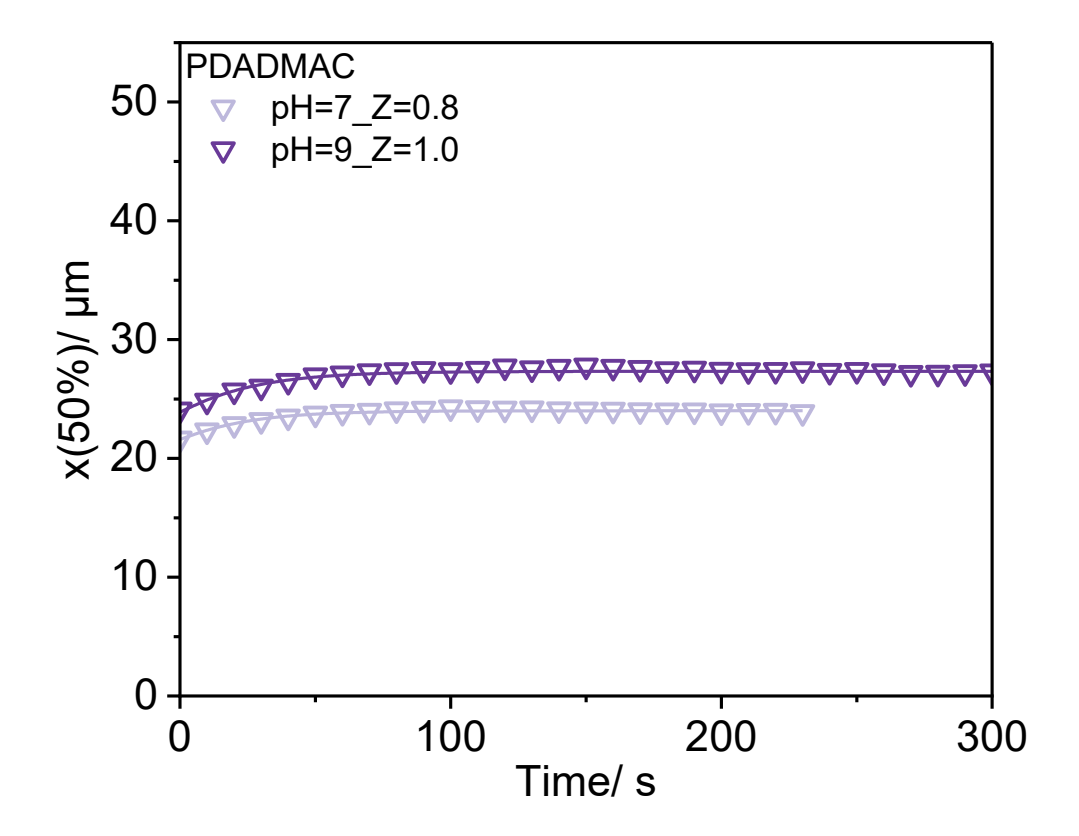


**Figure B.13.** The trend diagram of the median particle size (x(50%)) for HA-PDADMAC complexes with charge ratio Z=0.8 at pH 7 and charge ratio Z=1.0 at pH 9. Solid lines are fits with a logistic growth model.

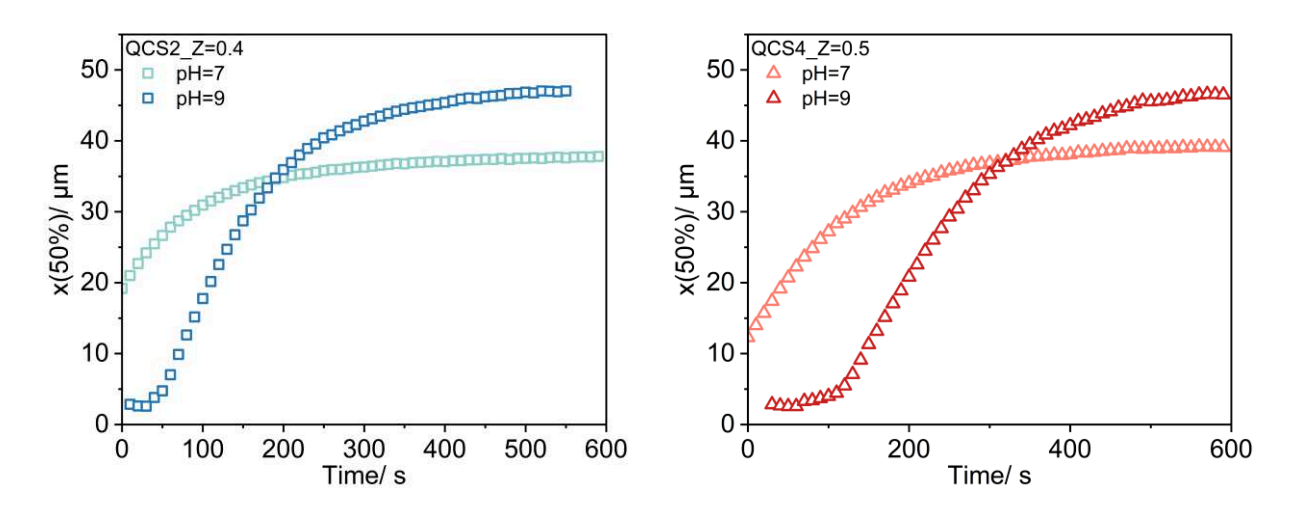


**Figure B.14.** The trend diagram of the median particle size (x(50%)) for HA-QCS2 complexes with charge ratio Z=0.4 and HA-QCS4 complexes with charge ratio Z=0.5 under various pH conditions.

Table B.4. Characterized results of raw water sample received from water plant

ζ-potential (mV)	UV254	TOC (mg/L)	рН
-24.80	0.140	3.16	7.05

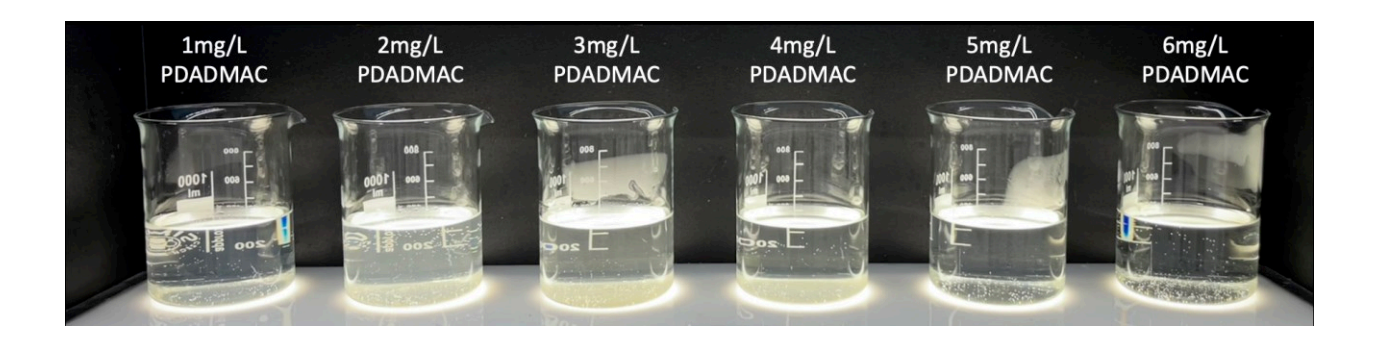


Figure B.15. Jar test of raw water treatment with PDADMAC.

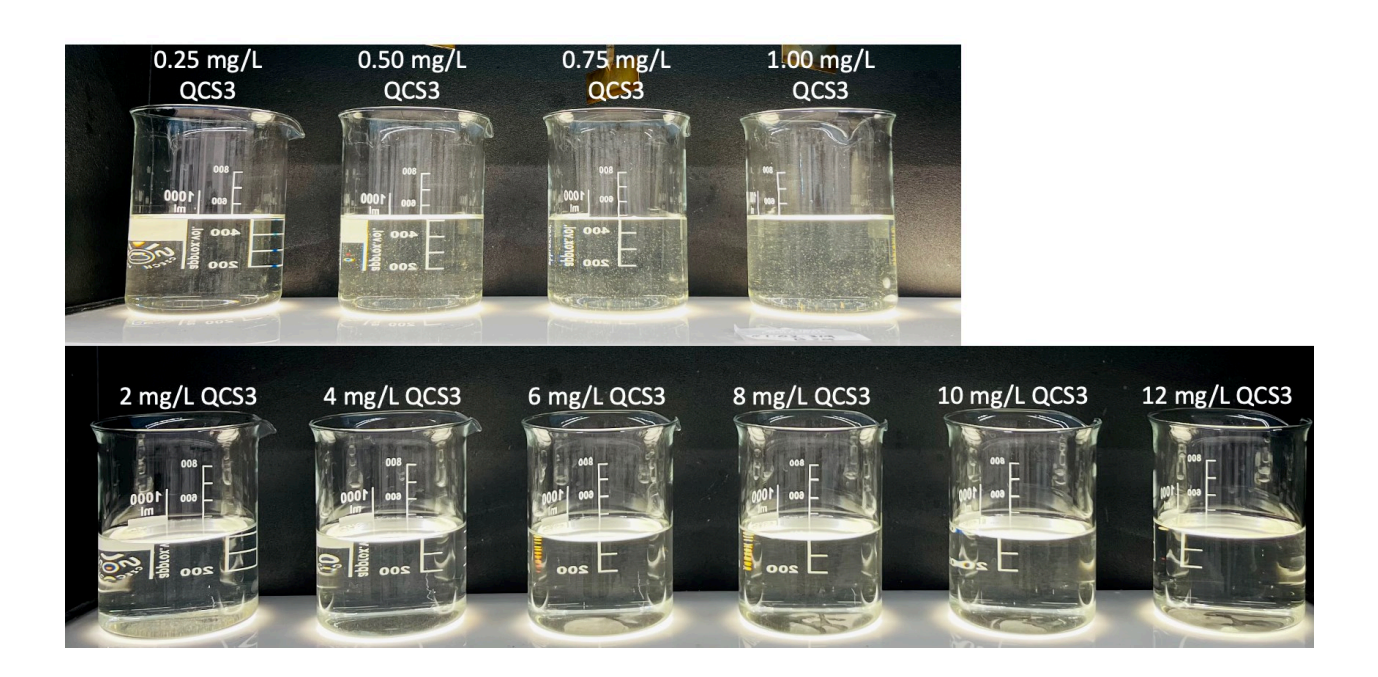


Figure B.16. Jar test of raw water treatment with QCS3.

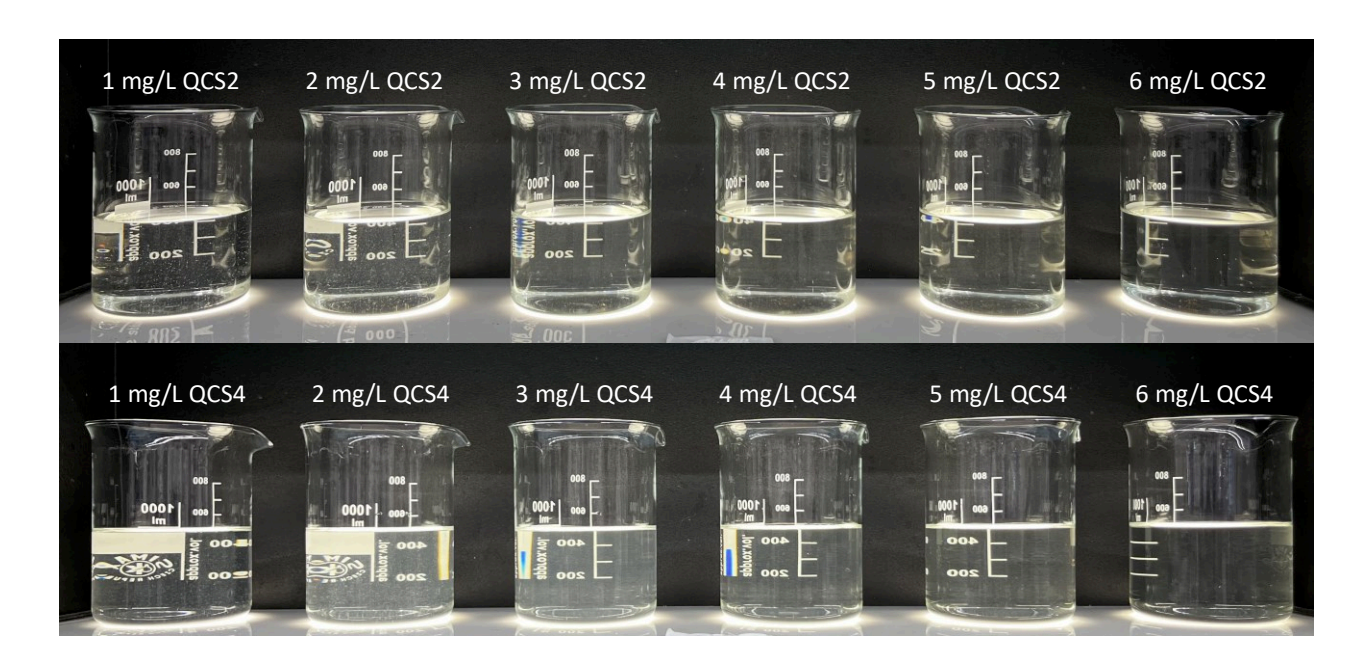
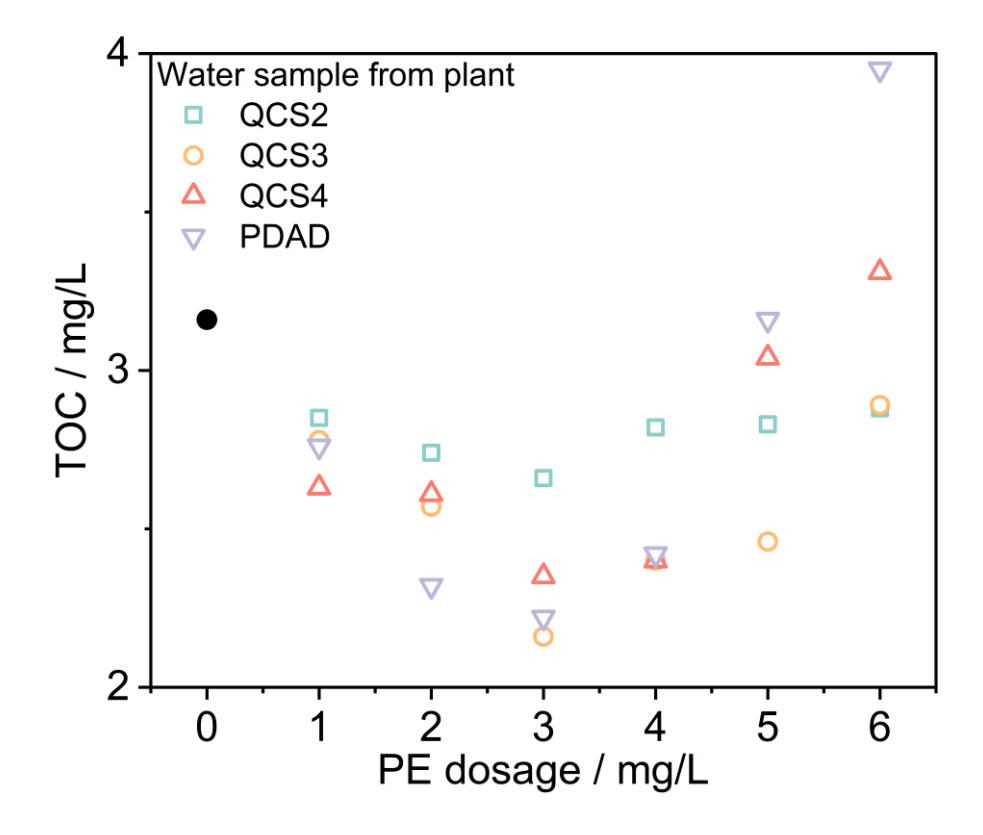
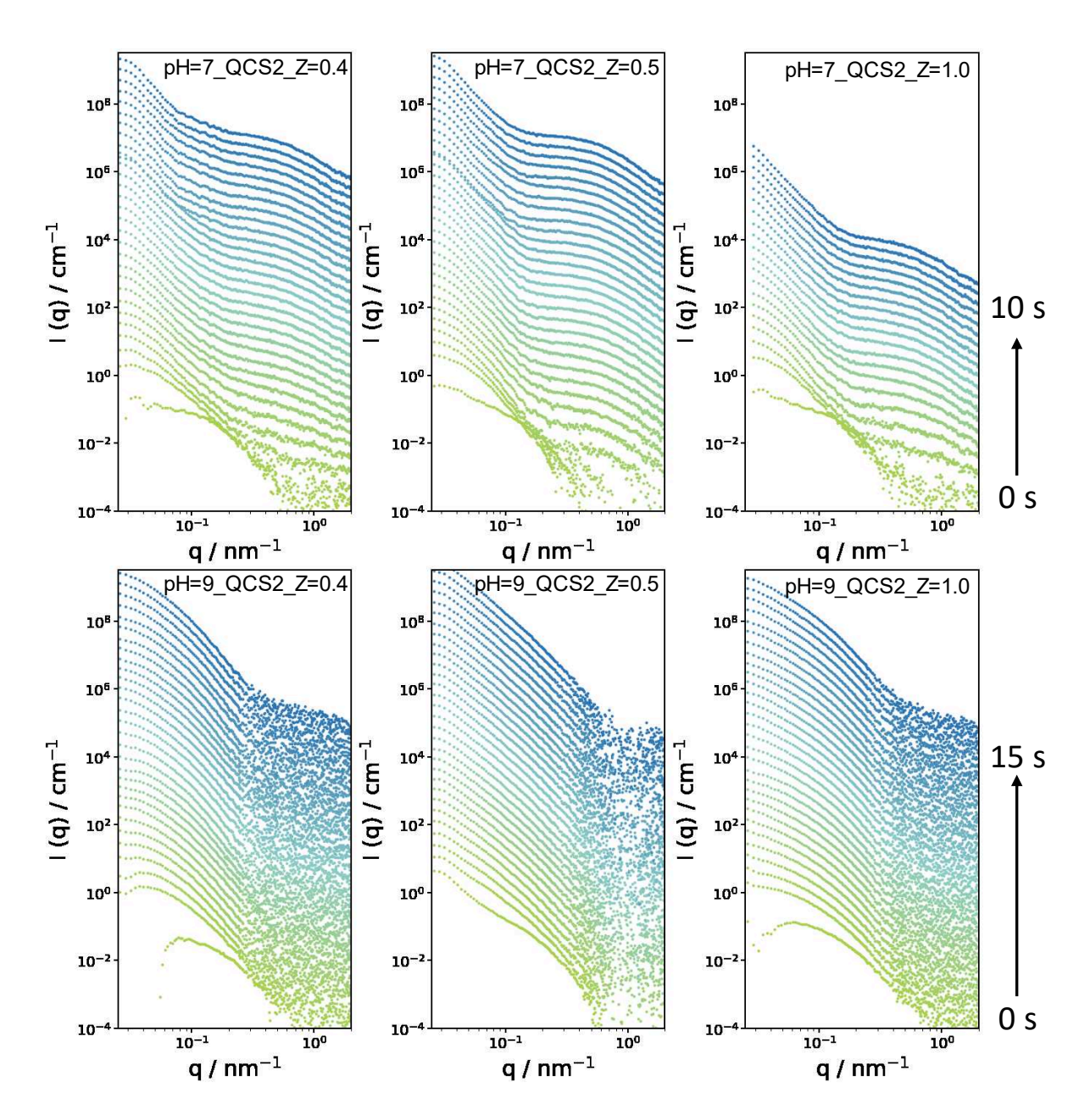


Figure B.17. Jar test of raw water treatment with QCS2 and QCS4



**Figure B.18.** TOC for treated water samples with addition of different polyelectrolytes at different dosage. Solid black dot refers to raw water sample.

# Appendix C. Chapter 5



**Figure C.1.** 2D time-resolved SAXS curves illustrating the kinetic pathway of HA-QCS2 complex formation following rapid mixing at various Z charge ratios and pH values of 7.0 and 9.0. Each curve represents a time interval of 0.5s with 30 time frames recorded (Except for sample pH=9\_QCS2\_Z=1.0 only 20 time frames recorded). Curves have been offset for visual clarity.

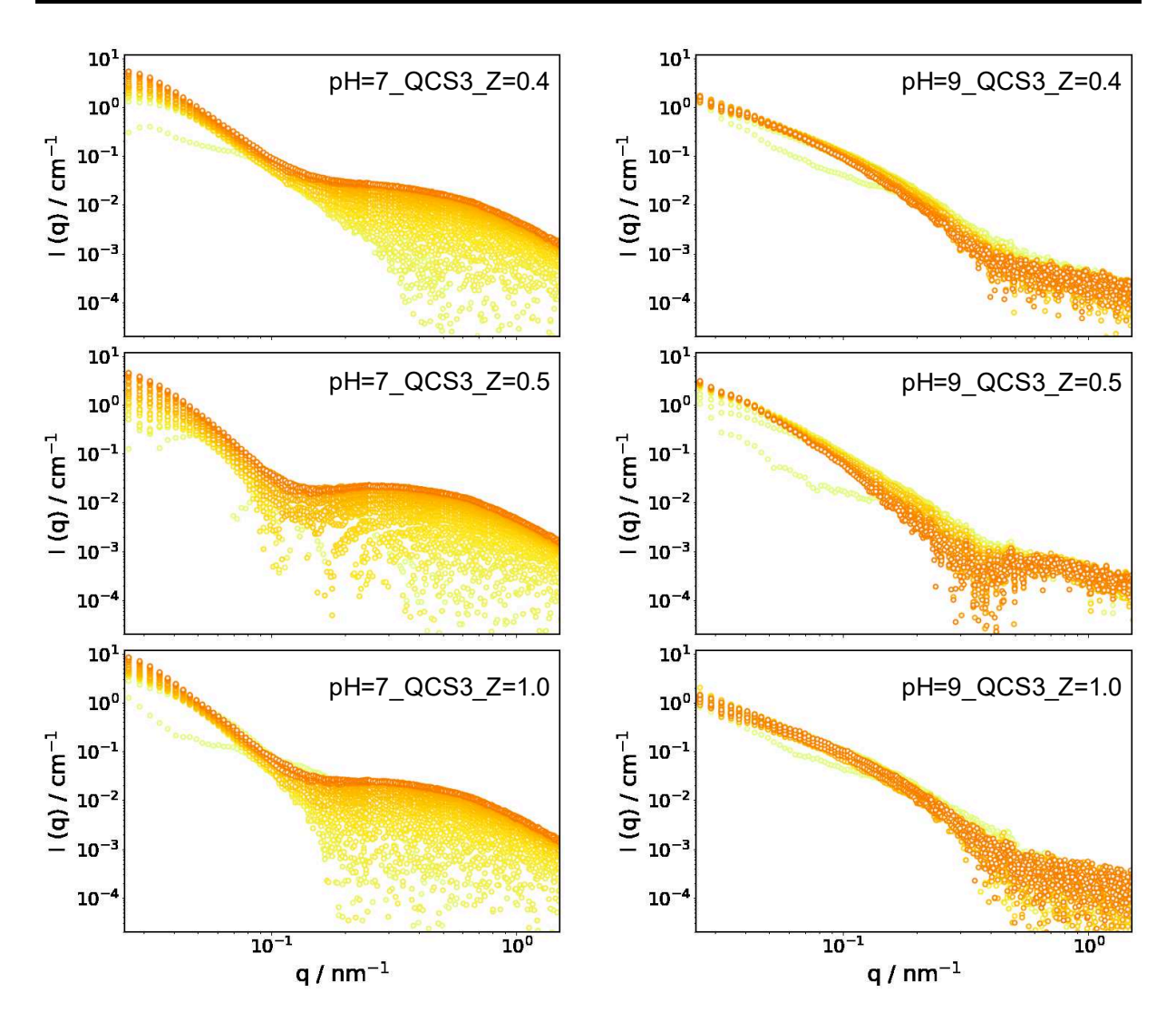


**Figure C.2.** 2D time-resolved SAXS curves illustrating the kinetic pathway of HA-QCS3 complex formation following rapid mixing at various Z charge ratios and pH values of 7.0 and 9.0. Each curve represents a time interval of 0.5s with 30 time frames recorded. Additionally, the gradients of color in each figure represent temporal progression; curves start with lighter colors for earlier times and gradually darken as time advances.

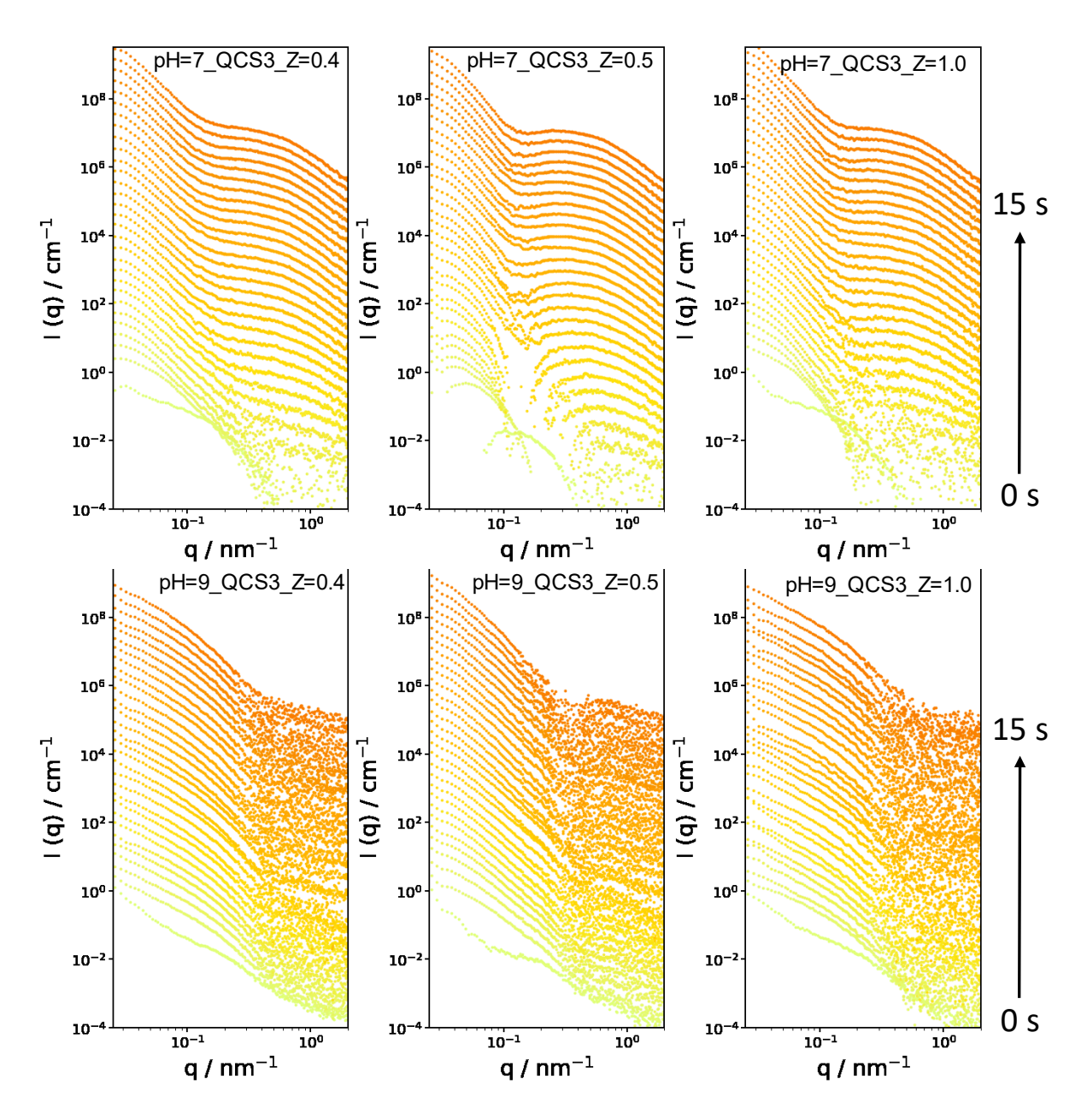


**Figure C.3.** 2D time-resolved SAXS curves illustrating the kinetic pathway of HA-QCS3 complex formation following rapid mixing at various Z charge ratios and pH values of 7.0 and 9.0. Each curve represents a time interval of 0.5s with 30 time frames recorded. Curves have been offset for visual clarity.

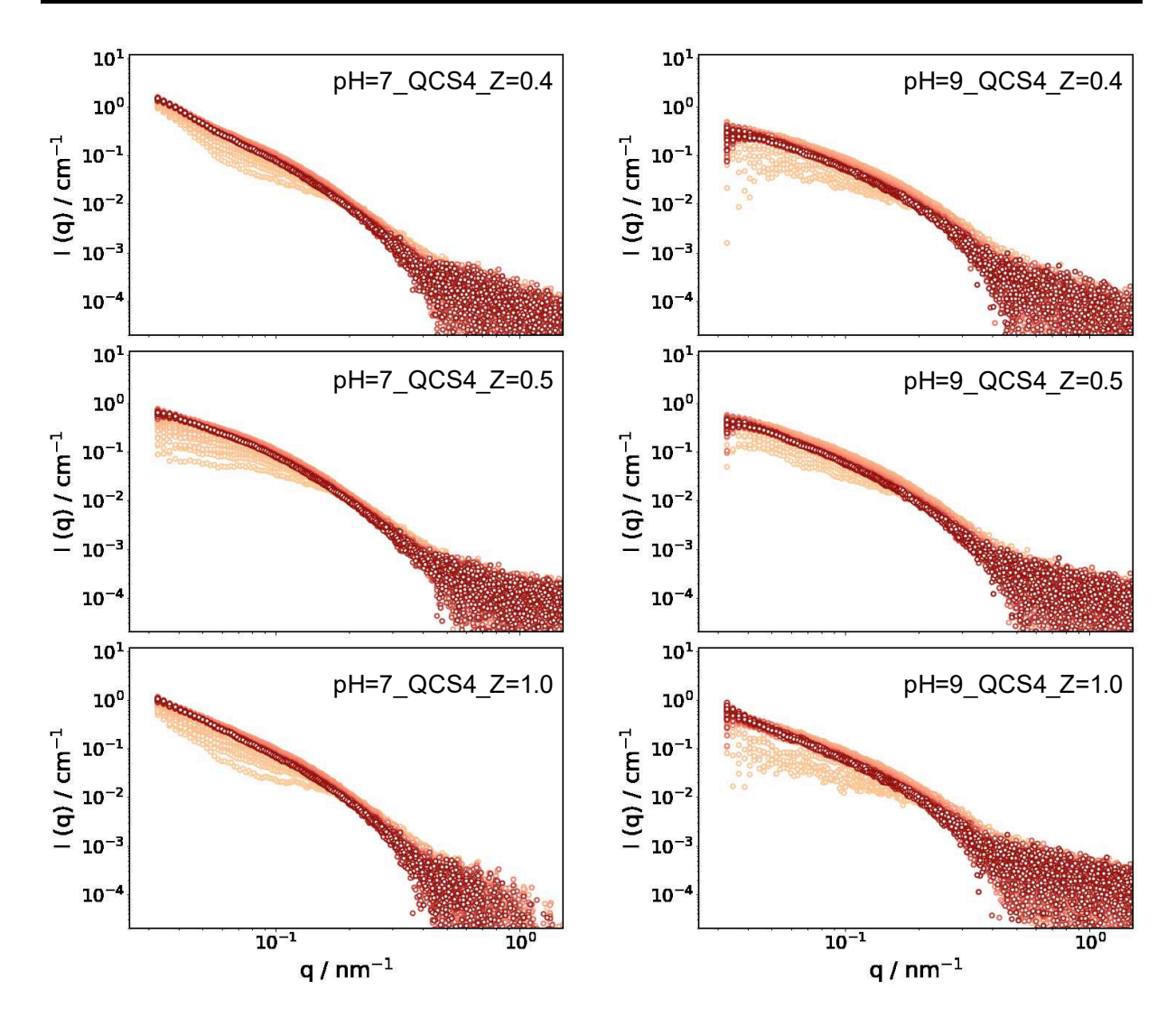


**Figure C.4.** 2D time-resolved SAXS curves illustrating the kinetic pathway of HA-QCS4 complex formation following rapid mixing at various Z charge ratios and pH values of 7.0 and 9.0. Each curve represents a time interval of 20 ms with 100 time frames recorded. Additionally, the gradients of color in each figure represent temporal progression; curves start with lighter colors for earlier times and gradually darken as time advances.

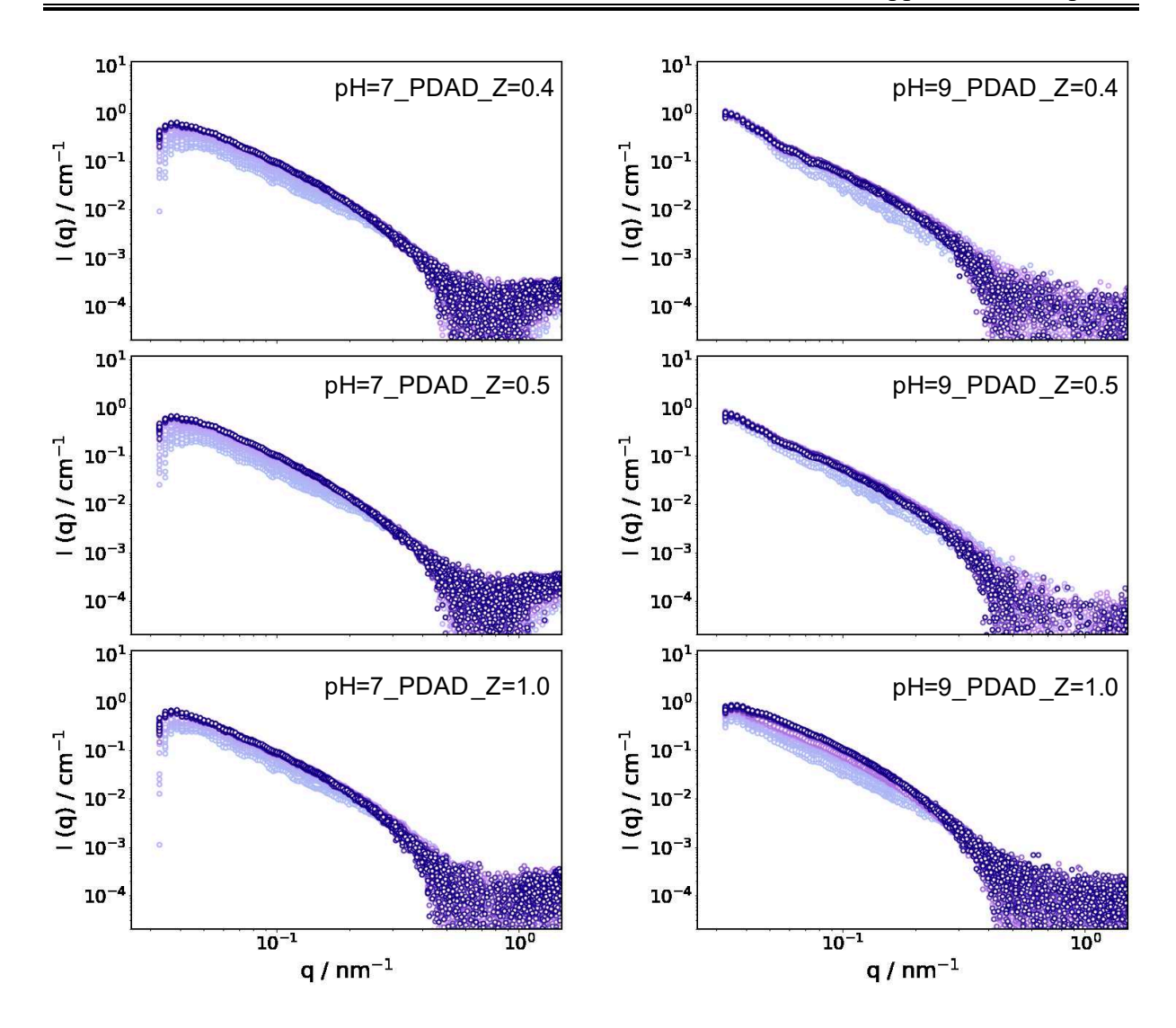


**Figure C.5.** 2D time-resolved SAXS curves illustrating the kinetic pathway of HA-PDAD complex formation following rapid mixing at various Z charge ratios and pH values of 7.0 and 9.0. Each curve represents a time interval of 20 ms with 100 time frames recorded. Additionally, the gradients of color in each figure represent temporal progression; curves start with lighter colors for earlier times and gradually darken as time advances.

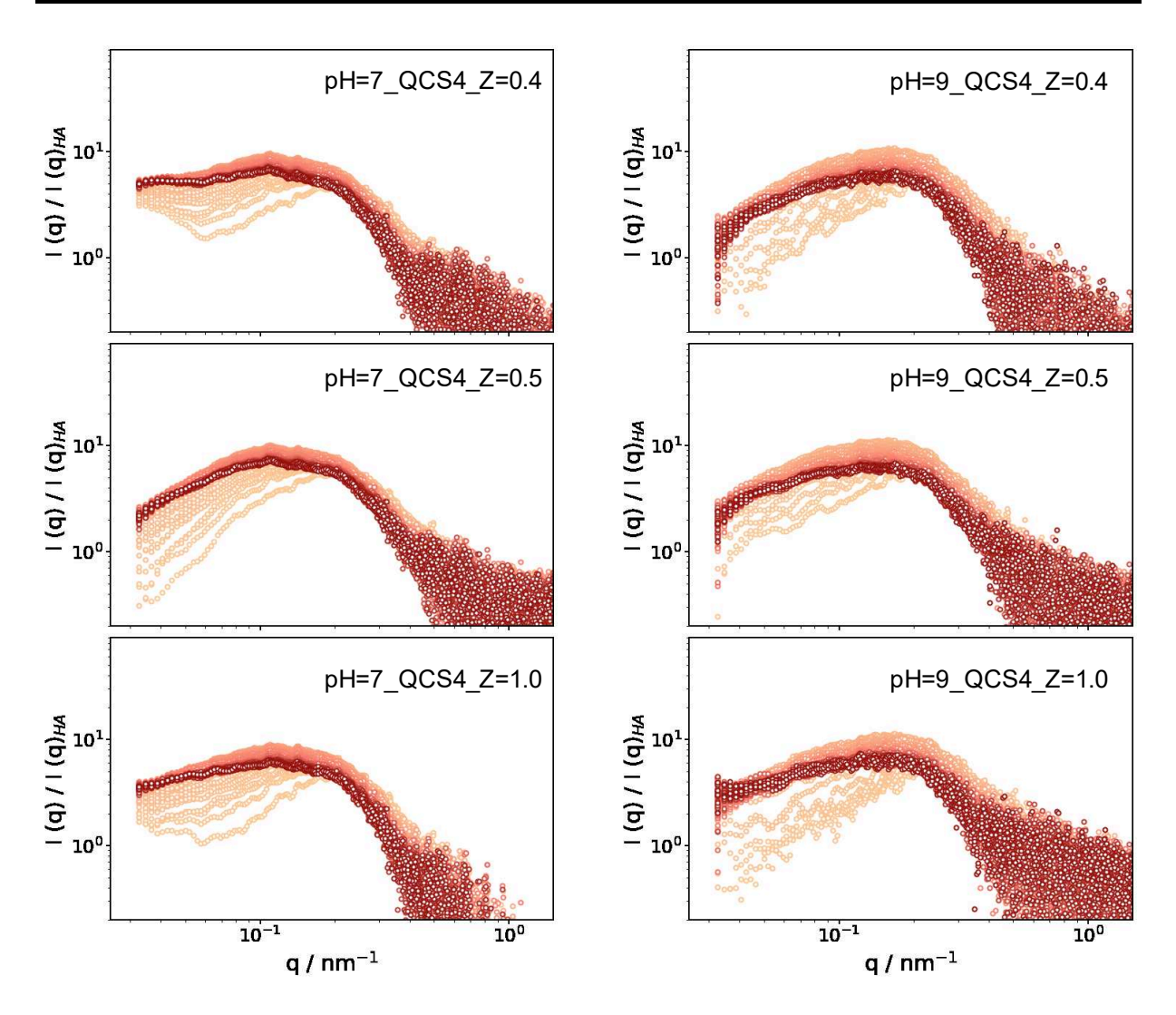


**Figure C.6.** 2D normalized time-resolved SAXS curves illustrating the kinetic pathway of HA-QCS3 complex formation following rapid mixing at various Z charge ratios and pH values of 7.0 and 9.0. Each curve represents a time interval of 20 ms, with 100 time frames recorded. The scattering intensity, plotted against the magnitude of the scattering vector q, is normalized to the curve of pure 40 mg/L HA solution at corresponding pH values ( $I(q)_{HA}$ ).

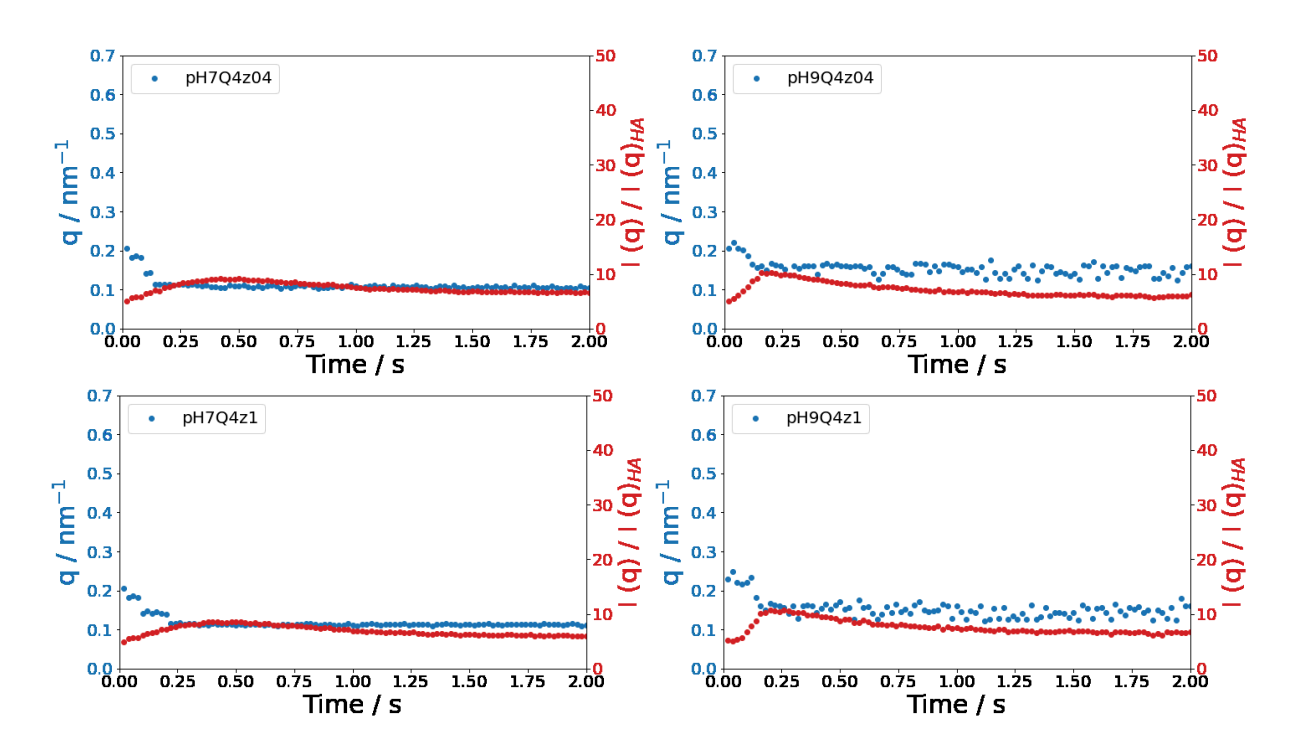


**Figure C.7.** Development of the peak position of the normalized results versus period upon mixing during the complexation of HA and QCS4 at various Z charge ratios and pH values of 7.0 and 9.0.

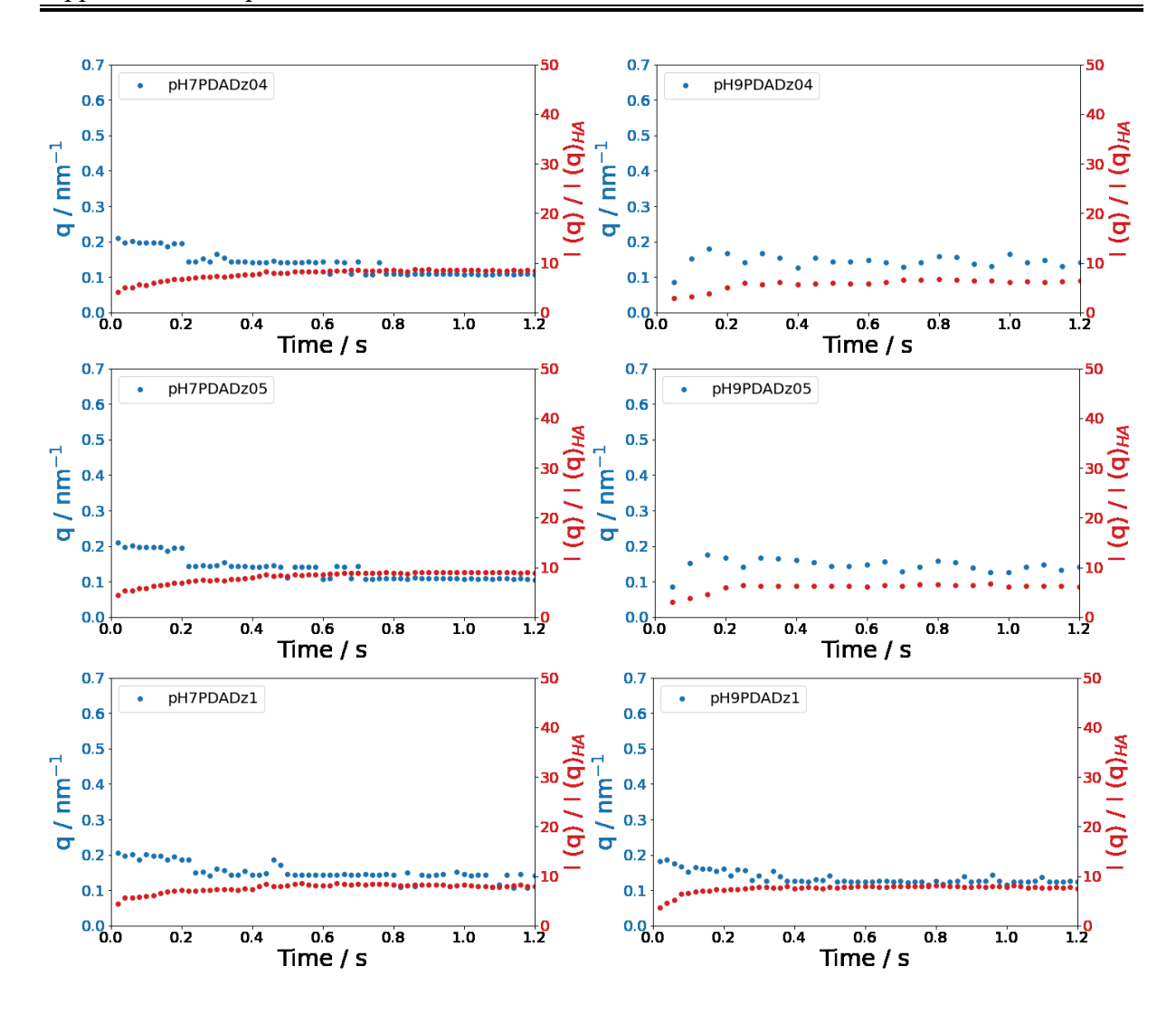


**Figure C.8.** Development of the peak position of the normalized results versus period upon mixing during the complexation of HA and PDADMAC at various Z charge ratios and pH values of 7.0 and 9.0.

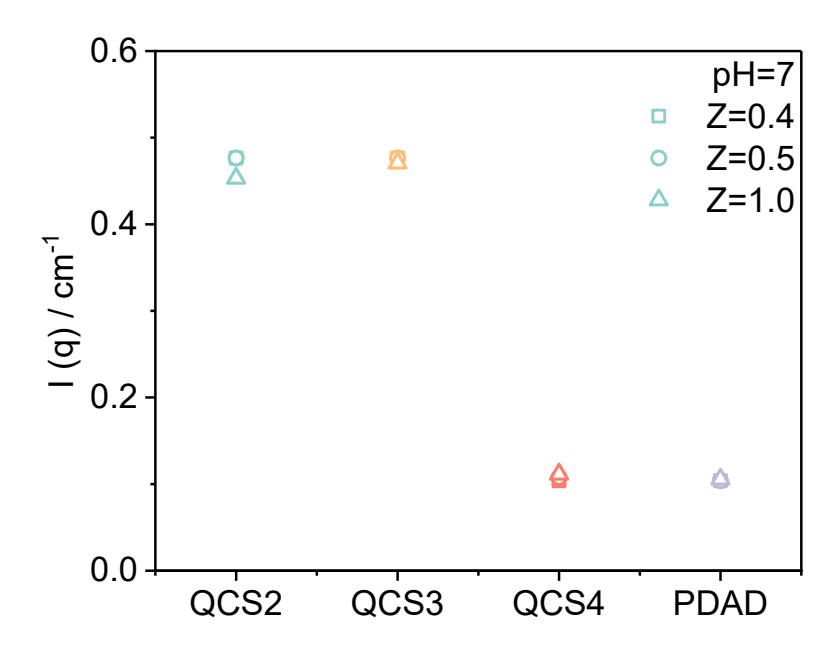


**Figure C.9.** Peak position of the normalized results for the final time frame of HA complex formation following rapid mixing with various QCSs at various Z charge ratios and pH values of 7.0.

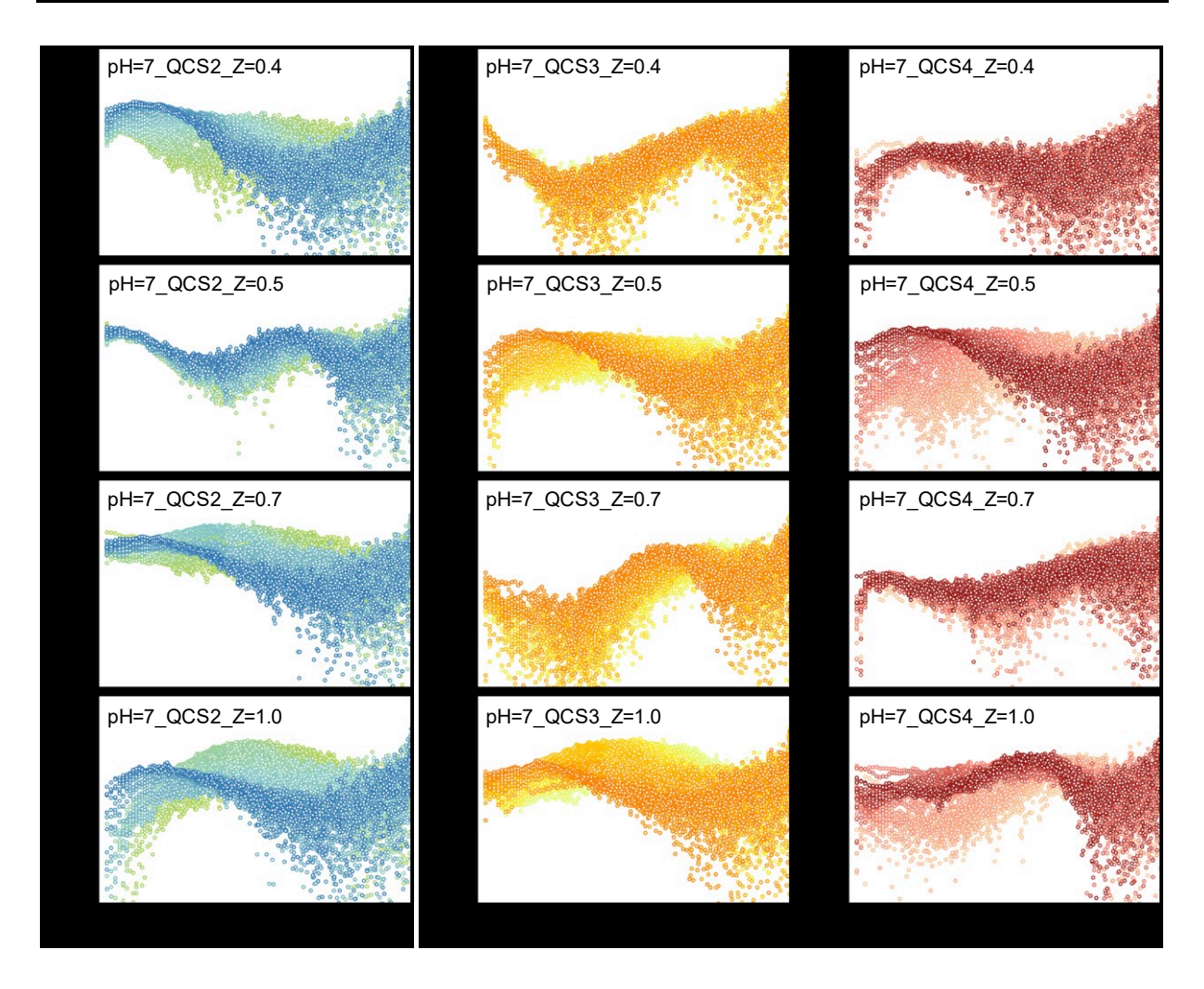
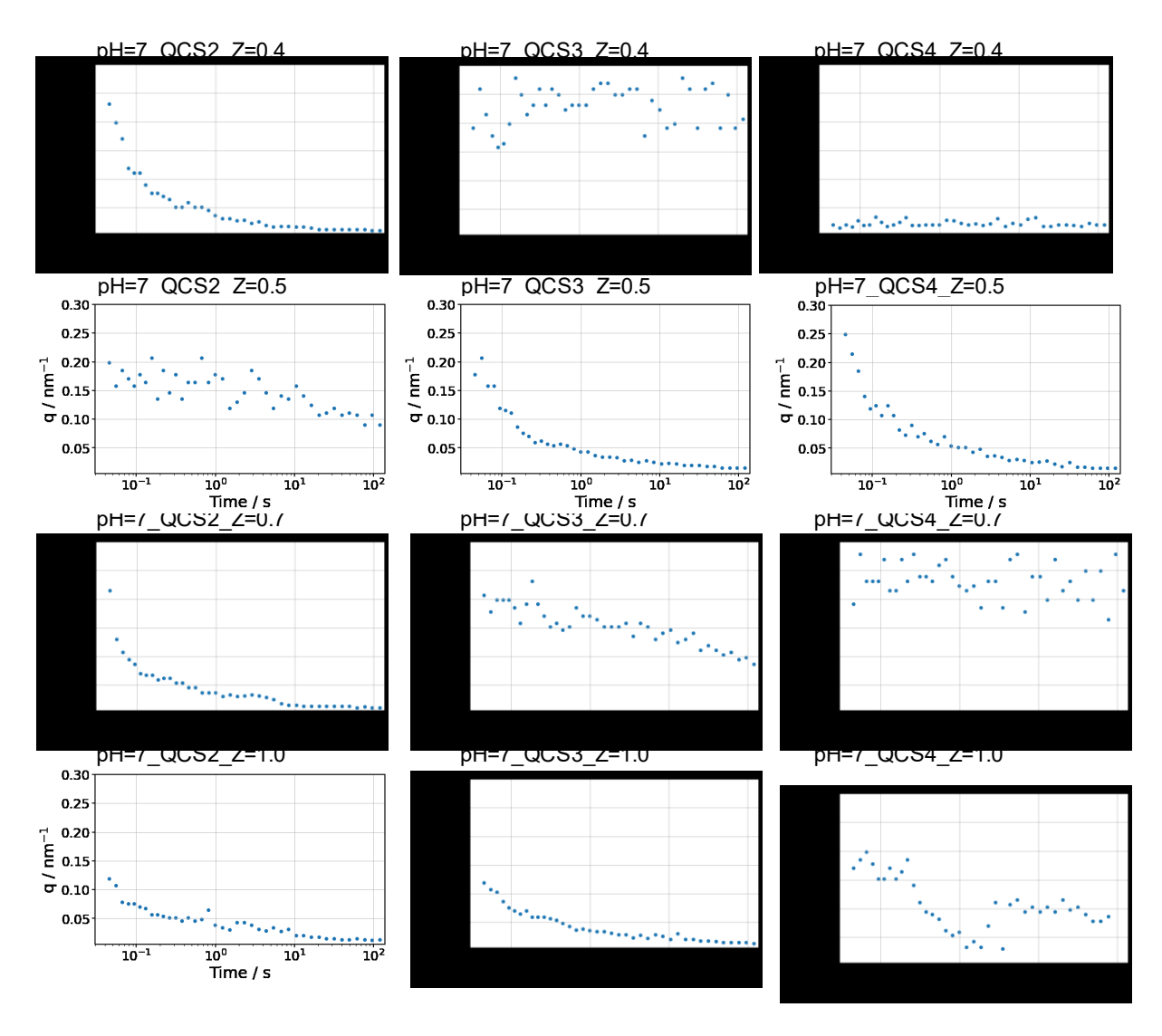
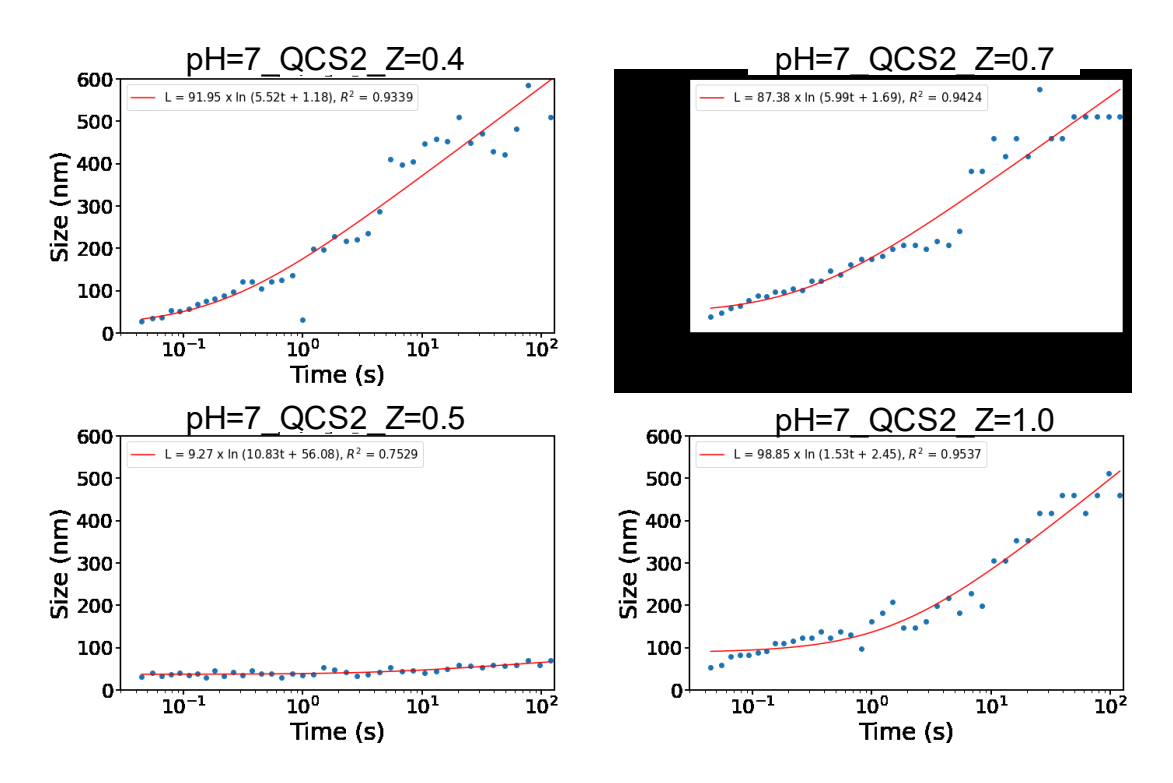


Figure C.10. Normalized 2D time-resolved SAXS curves illustrating the kinetic pathway of HA complex formation following rapid mixing with various QCSs at various Z charge ratios and pH values of 7.0. Each mixing event was recorded over 40 frames throughout a total duration of 120 seconds, with intervals spaced by a power law. Additionally, the gradients of color in each figure represent temporal progression; curves start with lighter colors for earlier times and gradually darken as time advances.



**Figure C.11.** Development of the peak position for the normalized HA complex formation following rapid mixing with various QCSs at various Z charge ratios and pH values of 7.0 within 120s



**Figure C.12.** The evolution of aggregation size over time for the pH=7\_QCS2 sample set at various Z charge ratios and pH values of 7.0 within 120s. Red line refers to the fitted data from via Logarithmic Growth model.

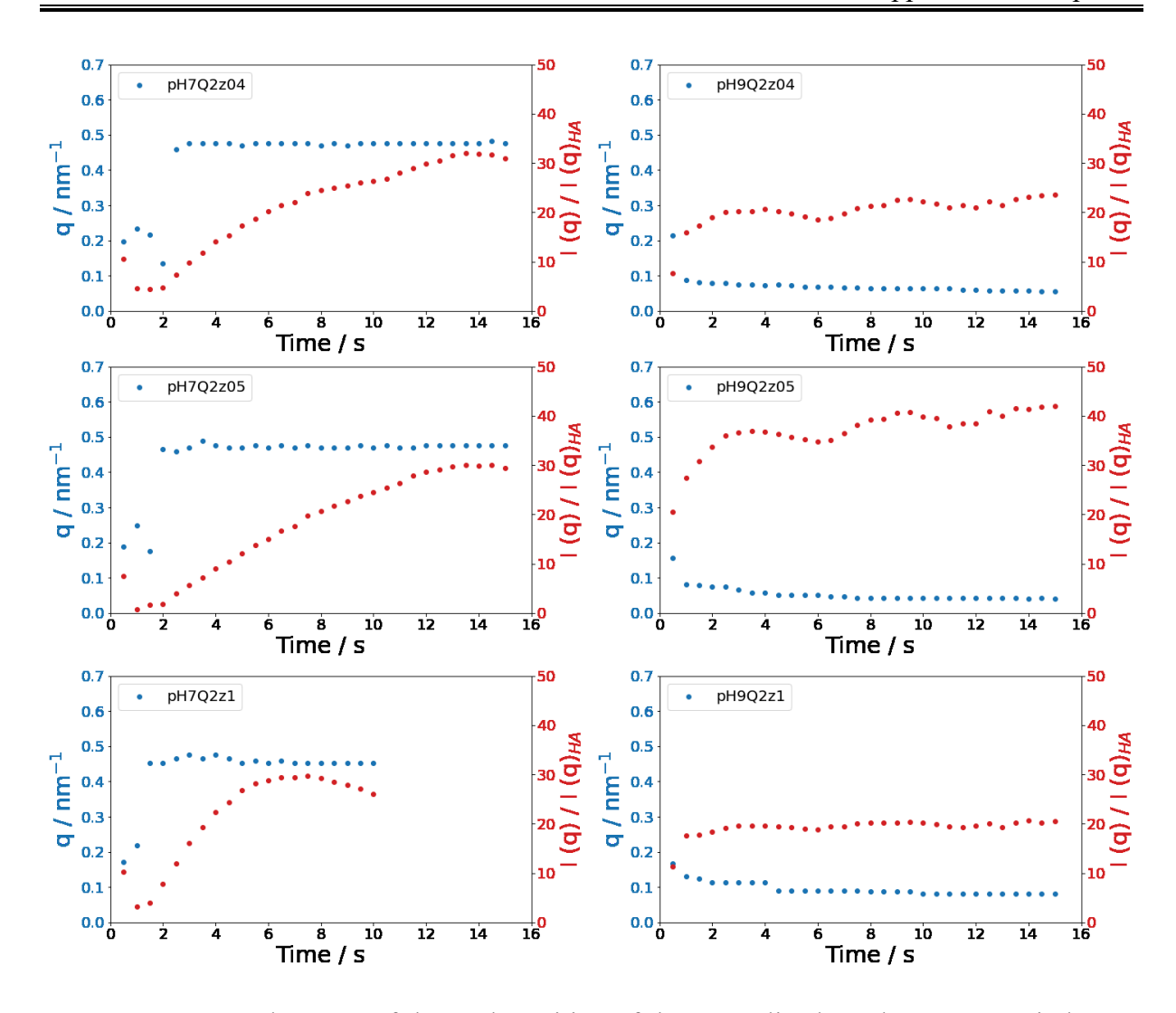


**Figure C.13.** Development of the peak position of the normalized results versus period upon mixing during the complexation of HA and QCS2 at various Z charge ratios and pH values of 7.0 and 9.0.

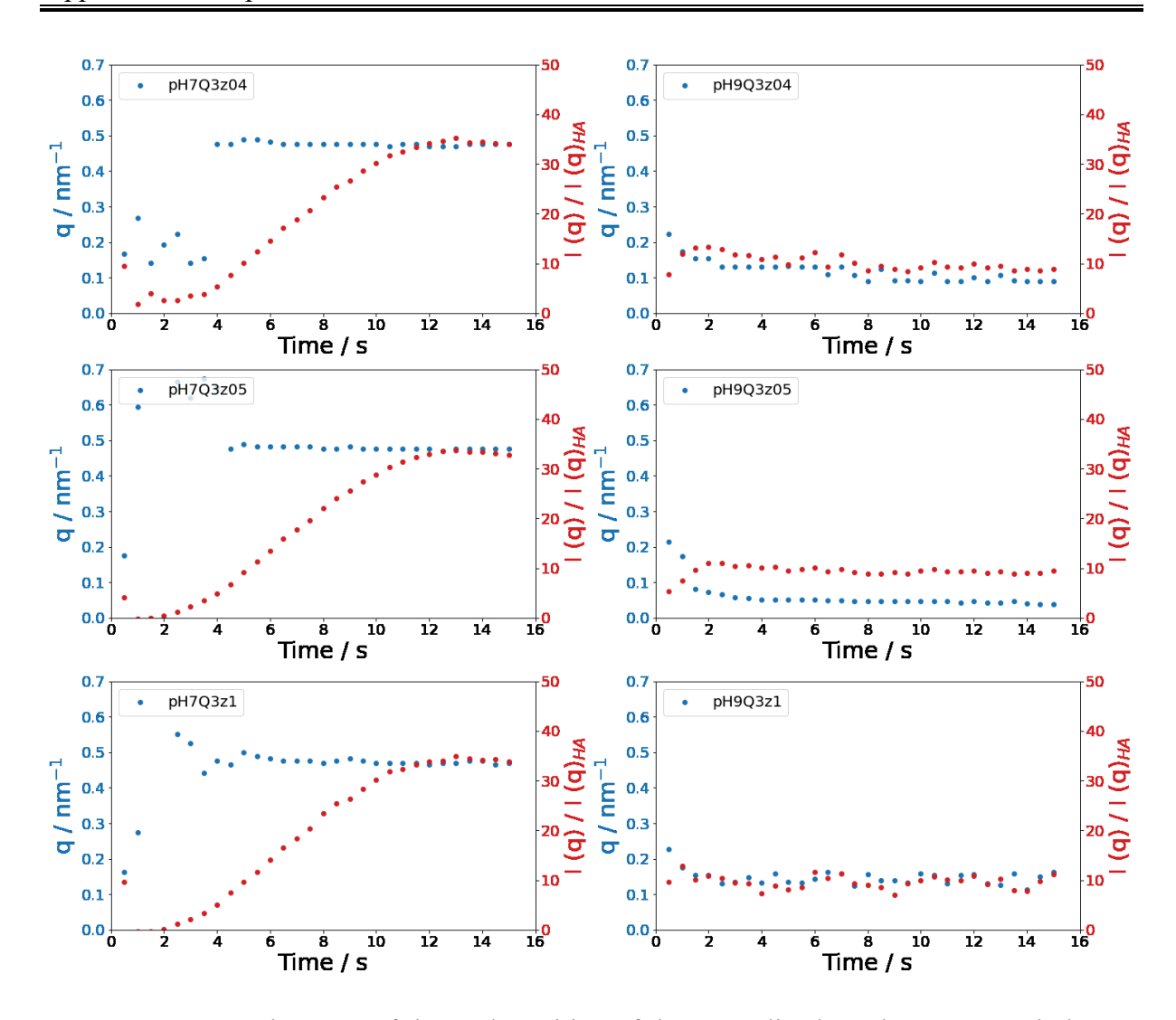


**Figure C.14.** Development of the peak position of the normalized results versus period upon mixing during the complexation of HA and QCS3 at various Z charge ratios and pH values of 7.0 and 9.0.

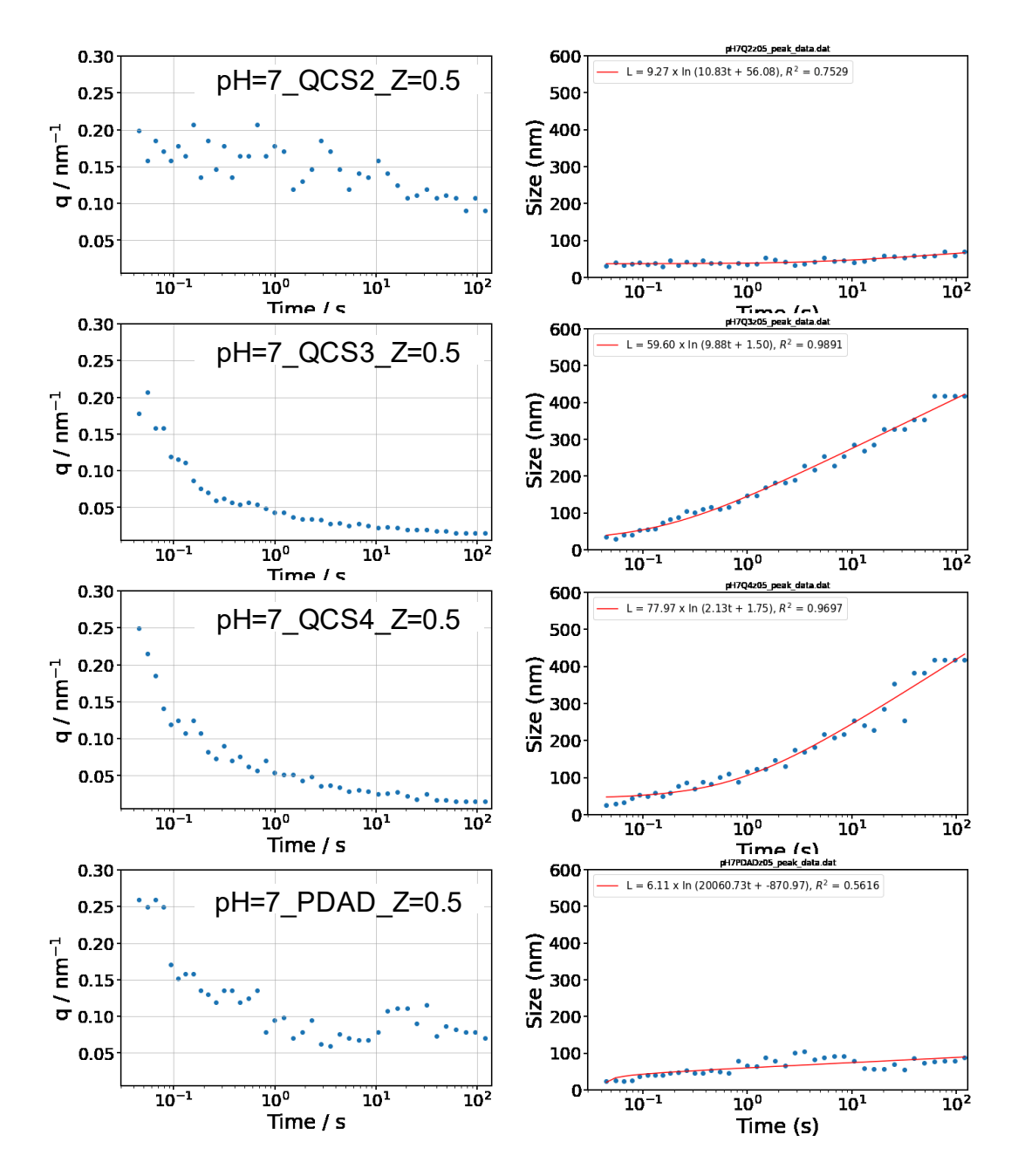


**Figure C.15.** Development of the peak position of the normalized results versus period upon mixing during the complexation of HA and various cPEs and the evolution of aggregation size over time at charge ratio Z=0.5 and pH values of 7.0. Red line refers to the fitted data from via Logarithmic Growth model.

## **List of Reference**

- 1. Ahmed, A. T.; El Gohary, F.; Tzanakakis, V. A.; Angelakis, A. N., Egyptian and Greek water cultures and hydro-technologies in ancient times. *Sustainability* **2020**, *12* (22), 9760.
- 2. Peña-Méndez, E. M.; Havel, J.; Patočka, J., Humic substances-compounds of still unknown structure: applications in agriculture, industry, environment, and biomedicine. *J. Appl. Biomed* **2005**, *3* (1), 13-24.
- 3. Sharp, E. L.; Parsons, S. A.; Jefferson, B., Seasonal variations in natural organic matter and its impact on coagulation in water treatment. *Sci. Total Environ.* **2006**, *363* (1-3), 183-194.
- 4. Singer, P. C., Humic substances as precursors for potentially harmful disinfection by-products. *Water Sci. Technol.* **1999**, *40* (9), 25-30.
- 5. Chowdhury, S., Heterotrophic bacteria in drinking water distribution system: a review. *Environ. Monit. Assess.* **2012**, *184*, 6087-6137.
- 6. Li, L.; Zhao, Z.; Huang, W.; Sheng, G.; Fu, J., Characterization of humic acids fractionated by ultrafiltration. *Org. Geochem.* **2004**, *35* (9), 1025-1037.
- 7. Stevenson, F., Humus chemistry: Genesis, composition, reactions. John Wiley & Sons: 1994.
- 8. Stevenson, F. J., *Humus chemistry: genesis, composition, reactions.* John Wiley & Sons: 1994.
- 9. Duan, J.; Gregory, J., Coagulation by hydrolysing metal salts. *Advances in colloid and interface science* **2003**, *100*, 475-502.
- 10. Duan, J.; Wang, J.; Graham, N.; Wilson, F., Coagulation of humic acid by aluminium sulphate in saline water conditions. *Desalination* **2002**, *150* (1), 1-14.
- 11. Trefalt, G.; Borkovec, M., Overview of DLVO theory. *Laboratory of Colloid and Surface Chemistry, University of Geneva, Switzerland* **2014**, *304*.
- 12. Iwuozor, K. O., Prospects and challenges of using coagulation-flocculation method in the treatment of effluents. *Advanced Journal of Chemistry-Section A* **2019**, *2* (2), 105-127.
- 13. Fisher, I.; Kastl, G.; Sathasivan, A.; Chen, P.; Van Leeuwen, J.; Daly, R.; Holmes, M., Tuning the enhanced coagulation process to obtain best chlorine and THM profiles in the distribution system. *Water science and technology: water supply* **2004**, *4* (4), 235-243.
- 14. Bolto, B. A., Soluble polymers in water purification. *Prog. Polym. Sci.* **1995**, *20* (6), 987-1041.
- 15. Matilainen, A.; Vepsäläinen, M.; Sillanpää, M., Natural organic matter removal by coagulation during drinking water treatment: A review. *Advances in colloid and interface science* **2010**, *159* (2), 189-197.

- 16. Sillanpää, M.; Ncibi, M. C.; Matilainen, A.; Vepsäläinen, M., Removal of natural organic matter in drinking water treatment by coagulation: A comprehensive review. *Chemosphere* **2018**, *190*, 54-71.
- 17. Yu, J.; Sun, D.; Tay, J., Characteristics of coagulation-flocculation of humic acid with effective performance of polymeric flocculant and inorganic coagulant. *Water Sci. Technol.* **2003**, *47* (1), 89-95.
- 18. Hess, M.; Jones, R. G.; Kahovec, J.; Kitayama, T.; Kratochvíl, P.; Kubisa, P.; Mormann, W.; Stepto, R.; Tabak, D.; Vohlídal, J., Terminology of polymers containing ionizable or ionic groups and of polymers containing ions (IUPAC Recommendations 2006). *Pure Appl. Chem.* **2006**, 78 (11), 2067-2074.
- 19. Bolto, B.; Gregory, J., Organic polyelectrolytes in water treatment. *Water Res.* **2007**, *41* (11), 2301-2324.
- 20. Dobrynin, A. V.; Rubinstein, M., Theory of polyelectrolytes in solutions and at surfaces. *Prog. Polym. Sci.* **2005**, *30* (11), 1049-1118.
- 21. Kam, S.-K.; Gregory, J., The interaction of humic substances with cationic polyelectrolytes. *Water Res.* **2001**, *35* (15), 3557-3566.
- 22. Bolto, B. A.; Dixon, D. R.; Eldridge, R. J.; King, S., The use of cationic polymers as primary coagulants in water treatment. In *Chemical water and wastewater treatment V*, Springer: 1998; pp 173-185.
- 23. Wilts, E. M.; Herzberger, J.; Long, T. E., Addressing water scarcity: cationic polyelectrolytes in water treatment and purification. *Polym. Int.* **2018**, *67* (7), 799-814.
- 24. Wandrey, C.; Jaeger, W., Copolymerization of dimethyl diallyl ammonium chloride and acryl amide. *Acta polymerica* **1985**, *36* (2), 100-102.
- 25. Vorchheimer, N., Synthetic polyelectrolytes. *Polyelectrolytes for Water and Wastewater Treatment* **1981,** *1*.
- 26. Hoover, M. F., Cationic quaternary polyelectrolytes—a literature review. *Journal of Macromolecular Science—Chemistry* **1970**, *4* (6), 1327-1418.
- 27. Yang, R.; Li, H.; Huang, M.; Yang, H.; Li, A., A review on chitosan-based flocculants and their applications in water treatment. *Water Res.* **2016**, *95*, 59-89.
- 28. Rinaudo, M., Chitin and chitosan: properties and applications. *Progress in polymer science* **2006**, *31* (7), 603-632.
- 29. Chiappisi, L.; Prévost, S.; Grillo, I.; Gradzielski, M., Chitosan/alkylethoxy carboxylates: a surprising variety of structures. *Langmuir* **2014**, *30* (7), 1778-1787.
- 30. Jia, S.; Yang, Z.; Ren, K.; Tian, Z.; Dong, C.; Ma, R.; Yu, G.; Yang, W., Removal of antibiotics from water in the coexistence of suspended particles and natural organic matters using amino-acid-modified-chitosan flocculants: A combined experimental and theoretical study. *Journal of hazardous materials* **2016**, *317*, 593-601.
- 31. Li, X.; Zheng, H.; Wang, Y.; Sun, Y.; Xu, B.; Zhao, C., Fabricating an enhanced sterilization chitosan-based flocculant: Synthesis, characterization, evaluation of sterilization and flocculation. *Chemical Engineering Journal* **2017**, *319*, 119-130.

- 32. Yang, Z.; Li, H.; Yan, H.; Wu, H.; Yang, H.; Wu, Q.; Li, H.; Li, A.; Cheng, R., Evaluation of a novel chitosan-based flocculant with high flocculation performance, low toxicity and good floc properties. *Journal of hazardous materials* **2014**, *276*, 480-488.
- 33. Fuoss, R. M.; Sadek, H., Mutual interaction of polyelectrolytes. *Science* **1949**, *110* (2865), 552-554.
- 34. Bakeev, K. N.; Izumrudov, V. A.; Kuchanov, S.; Zezin, A. B.; Kabanov, V. A., Kinetics and mechanism of interpolyelectrolyte exchange and addition reactions. *Macromolecules* **1992**, *25* (17), 4249-4254.
- 35. Izumrudov, V. A.; Zezin, A. B.; Kabanov, V. A., Equilibria in interpolyelectrolyte reactions and the phenomenon of molecular" recognition" in solutions of interpolyelectrolyte complexes. *Russian Chemical Reviews* **1991**, *60* (7), 792.
- 36. Pergushov, D. V.; Müller, A. H.; Schacher, F. H., Micellar interpolyelectrolyte complexes. *Chem. Soc. Rev.* **2012**, *41* (21), 6888-6901.
- 37. Ruehrwein, R.; Ward, D., Mechanism of clay aggregation by polyelectrolytes. *Soil science* **1952**, *73* (6), 485-492.
- 38. Koetz, J.; Kosmella, S., *Polyelectrolytes*. Springer: 2007.
- 39. Barany, S.; Meszaros, R.; Kozakova, I.; Skvarla, I., Kinetics and mechanism of flocculation of bentonite and kaolin suspensions with polyelectrolytes and the strength of floccs. *Colloid J.* **2009**, *71*, 285-292.
- 40. Yuan, M.; Bustamante, H.; Mahmoudi, N.; Gradzielski, M., Colloidal Chemistry in Water Treatment: The Effect of Ca2+ on the Interaction between Humic Acid and Poly (diallyldimethylammonium chloride)(PDADMAC). *Langmuir* **2024**.
- 41. Kuzminskaya, O.; Riemer, S.; Dalgliesh, R.; Almásy, L.; Hoffmann, I.; Gradzielski, M., Structure and Phase Behavior of Interpolyelectrolyte Complexes of PDADMAC and Hydrophobically Modified PAA (HM-PAA). *Macromol. Chem. Phys.*, 2200276.
- 42. Amann, M.; Diget, J. S.; Lyngsø, J.; Pedersen, J. S.; Narayanan, T.; Lund, R., Kinetic pathways for polyelectrolyte coacervate micelle formation revealed by time-Resolved synchrotron SAXS. *Macromolecules* **2019**, *52* (21), 8227-8237.
- 43. Chen, S.; Zhang, P.; Wang, Z.-G., Complexation between oppositely charged polyelectrolytes in dilute solution: Effects of charge asymmetry. *Macromolecules* **2022**, *55* (10), 3898-3909.
- 44. Arnold, O.; Bilheux, J.-C.; Borreguero, J.; Buts, A.; Campbell, S. I.; Chapon, L.; Doucet, M.; Draper, N.; Leal, R. F.; Gigg, M., Mantid—Data analysis and visualization package for neutron scattering and μ SR experiments. *Nuclear instruments and methods in physics research section a: accelerators, spectrometers, detectors and associated equipment* **2014,** 764, 156-166.
- 45. Heenan, R.; Penfold, J.; King, S., SANS at pulsed neutron sources: present and future prospects. *J. Appl. Crystallogr.* **1997**, *30* (6), 1140-1147.
- 46. SasView for Small Angle Scattering Analysis. sasview.org/index.html.
- 47. Beaucage, G., Approximations leading to a unified exponential/power-law approach to small-angle scattering. *J. Appl. Crystallogr.* **1995**, *28* (6), 717-728.

- 48. Beaucage, G., Small-angle scattering from polymeric mass fractals of arbitrary mass-fractal dimension. *J. Appl. Crystallogr.* **1996**, *29* (2), 134-146.
- 49. Hammouda, B., Analysis of the Beaucage model. J. Appl. Crystallogr. **2010**, 43 (6), 1474-1478.
- 50. Orthaber, D.; Bergmann, A.; Glatter, O., SAXS experiments on absolute scale with Kratky systems using water as a secondary standard. *J. Appl. Crystallogr.* **2000**, *33* (2), 218-225.
- 51. Mylonas, E.; Svergun, D. I., Accuracy of molecular mass determination of proteins in solution by small-angle X-ray scattering. *J. Appl. Crystallogr.* **2007**, *40* (s1), s245-s249.
- 52. SO 13320: Edition 2009/10: Particle size analysis Laser diffraction methods.
- 53. Dayarathne, H.; Angove, M. J.; Aryal, R.; Abuel-Naga, H.; Mainali, B., Removal of natural organic matter from source water: Review on coagulants, dual coagulation, alternative coagulants, and mechanisms. *J. Water Process. Eng.* **2021**, *40*, 101820.
- 54. Krzeminski, P.; Vogelsang, C.; Meyn, T.; Köhler, S.; Poutanen, H.; de Wit, H.; Uhl, W., Natural organic matter fractions and their removal in full-scale drinking water treatment under cold climate conditions in Nordic capitals. *Journal of Environmental Management* **2019**, *241*, 427-438.
- 55. Miikki, V.; Senesi, N.; Hänninen, K., Characterization of humic material formed by composting of domestic and industrial biowastes: Part 2 spectroscopic evaluation of humic acid structures. *Chemosphere* **1997**, *34* (8), 1639-1651.
- 56. Pronk, W.; Ding, A.; Morgenroth, E.; Derlon, N.; Desmond, P.; Burkhardt, M.; Wu, B.; Fane, A. G., Gravity-driven membrane filtration for water and wastewater treatment: a review. *Water Res.* **2019**, *149*, 553-565.
- 57. Wei, C.; Zhang, F.; Hu, Y.; Feng, C.; Wu, H., Ozonation in water treatment: the generation, basic properties of ozone and its practical application. *Rev. Chem. Eng.* **2017**, *33* (1), 49-89.
- 58. Shah, J.; Židonis, A.; Aggidis, G., State of the art of UV water treatment technologies and hydraulic design optimisation using computational modelling. *J. Water Process. Eng.* **2021**, *41*, 102099.
- 59. Swift, R., Molecular weight, size, shape, and charge characteristics of humic substances: some basic considerations. *Humic substances II: In search of structure* **1989**, 449-466.
- 60. Napper, D. H., *Polymeric stabilization of colloidal dispersions*. Academic Pr. 1983; Vol. 3.
- 61. Hankins, N. P.; Lu, N.; Hilal, N., Enhanced removal of heavy metal ions bound to humic acid by polyelectrolyte flocculation. *Sep. Purif. Technol.* **2006**, *51* (1), 48-56.
- 62. Mohd Amin, M.; Heijman, S.; Rietveld, L., The potential use of polymer flocculants for pharmaceuticals removal in wastewater treatment. *Environmental Technology Reviews* **2014**, *3* (1), 61-70.
- 63. Palmer, N. E.; von Wandruszka, R., Dynamic light scattering measurements of particle size development in aqueous humic materials. *Fresenius' journal of analytical chemistry* **2001**, *371*, 951-954.

- 64. Shaffer, L.; von Wandruszka, R., Temperature induced aggregation and clouding in humic acid solutions. *Advances in Environmental Chemistry* **2015**, *2015*.
- 65. Wang, Z.; Stumm, W., Heavy metal complexation by surfaces and humic acids: a brief discourse on assessment by acidimetric titration. *Netherlands journal of agricultural science* **1987**, *35* (3), 231-240.
- 66. Yoon, S.-H.; Lee, C.-H.; Kim, K.-J.; Fane, A. G., Effect of calcium ion on the fouling of nanofilter by humic acid in drinking water production. *Water Res.* **1998**, *32* (7), 2180-2186.
- 67. Von Wandruszka, R.; Ragle, C.; Engebretson, R., The role of selected cations in the formation of pseudomicelles in aqueous humic acid. *Talanta* **1997**, *44* (5), 805-809.
- 68. Tan, L.; Tan, X.; Mei, H.; Ai, Y.; Sun, L.; Zhao, G.; Hayat, T.; Alsaedi, A.; Chen, C.; Wang, X., Coagulation behavior of humic acid in aqueous solutions containing Cs+, Sr2+ and Eu3+: DLS, EEM and MD simulations. *Environ. Pollut.* **2018**, *236*, 835-843.
- 69. Gonzalez-Perez, A.; Hägg, K.; Duteil, F., Optimizing NOM Removal: Impact of Calcium Chloride. *Sustainability* **2021**, *13* (11), 6338.
- 70. Wu, Z.; Zhang, X.; Pang, J.; Zhang, X.; Li, J.; Li, J.; Zhang, P., Humic acid removal from water with PAC-Al30: effect of calcium and kaolin and the action mechanisms. *ACS omega* **2020**, *5* (27), 16413-16420.
- 71. Al-Heety, E.; Turky, A.; Al-Othman, E., Physico-chemical assessment of Euphrates river between Heet and Ramadi cities, Iraq. *Journal of Water Resource and Protection* **2011**, *3* (11), 812-823.
- 72. Potasznik, A.; Szymczyk, S., Magnesium and calcium concentrations in the surface water and bottom deposits of a river-lake system. *Journal of Elementology* **2015**, *20* (3).
- 73. Morfesis, A.; Jacobson, A. M.; Frollini, R.; Helgeson, M.; Billica, J.; Gertig, K. R., Role of zeta ( $\zeta$ ) potential in the optimization of water treatment facility operations. *Industrial & Engineering Chemistry Research* **2009**, 48 (5), 2305-2308.
- 74. Nobbmann, U.; Morfesis, A.; Billica, J.; Gertig, K., The role of zeta potential in the optimization of water treatment. *Nanotech* **2010**, *3*, 605-607.
- 75. Altmann, J.; Massa, L.; Sperlich, A.; Gnirss, R.; Jekel, M., UV254 absorbance as real-time monitoring and control parameter for micropollutant removal in advanced wastewater treatment with powdered activated carbon. *Water Res.* **2016**, *94*, 240-245.
- 76. Burchard, W.; Schmidt, M.; Stockmayer, W., Information on polydispersity and branching from combined quasi-elastic and intergrated scattering. *Macromolecules* **1980**, *13* (5), 1265-1272.
- 77. Hakim, A.; Suzuki, T.; Kobayashi, M., Strength of humic acid aggregates: effects of divalent cations and solution pH. ACS omega 2019, 4 (5), 8559-8567.
- 78. Zhang, Y.; Cremer, P. S., Interactions between macromolecules and ions: the Hofmeister series. *Curr. Opin. Chem. Biol.* **2006**, *10* (6), 658-663.
- 79. Gradzielski, M.; Hoffmann, I., Polyelectrolyte-surfactant complexes (PESCs) composed of oppositely charged components. *Current opinion in colloid & interface science* **2018**, *35*, 124-141.

- 80. Yan, W.; Wang, Y.; Chen, Y., Effect of conditioning by PAM polymers with different charges on the structural and characteristic evolutions of water treatment residuals. *Water Res.* **2013**, *47* (17), 6445-6456.
- 81. Zeng, Y.; Yang, C.; Zhang, J.; Pu, W., Feasibility investigation of oily wastewater treatment by combination of zinc and PAM in coagulation/flocculation. *J. Hazard. Mater.* **2007**, *147* (3), 991-996.
- 82. Xiong, B.; Loss, R. D.; Shields, D.; Pawlik, T.; Hochreiter, R.; Zydney, A. L.; Kumar, M., Polyacrylamide degradation and its implications in environmental systems. *NPJ Clean Water* **2018**, *1* (1), 17.
- 83. Cumming, J.; Hawker, D.; Chapman, H.; Nugent, K., The fate of polymeric quaternary ammonium salts from cosmetics in wastewater treatment plants. *Water, Air, & Soil Pollution* **2011,** *216*, 441-450.
- 84. Isik, M.; Fernandes, A. M.; Vijayakrishna, K.; Paulis, M.; Mecerreyes, D., Preparation of poly (ionic liquid) nanoparticles and their novel application as flocculants for water purification. *Polymer Chemistry* **2016**, *7* (8), 1668-1674.
- 85. Dharani, M.; Balasubramanian, S., Synthesis, characterization and application of acryloyl chitosan anchored copolymer towards algae flocculation. *Carbohydr. Polym.* **2016**, *152*, 459-467.
- 86. Loganathan, P.; Gradzielski, M.; Bustamante, H.; Vigneswaran, S., Progress, challenges, and opportunities in enhancing NOM flocculation using chemically modified chitosan: a review towards future development. *Environ. Sci.: Water Res. Technol.* **2020,** *6* (1), 45-61.
- 87. Brasselet, C.; Pierre, G.; Dubessay, P.; Dols-Lafargue, M.; Coulon, J.; Maupeu, J.; Vallet-Courbin, A.; De Baynast, H.; Doco, T.; Michaud, P., Modification of chitosan for the generation of functional derivatives. *Applied Sciences* **2019**, *9* (7), 1321.
- 88. Casettari, L.; Vllasaliu, D.; Castagnino, E.; Stolnik, S.; Howdle, S.; Illum, L., PEGylated chitosan derivatives: Synthesis, characterizations and pharmaceutical applications. *Prog. Polym. Sci.* **2012**, *37* (5), 659-685.
- 89. Bhattarai, N.; Ramay, H. R.; Gunn, J.; Matsen, F. A.; Zhang, M., PEG-grafted chitosan as an injectable thermosensitive hydrogel for sustained protein release. *J. Controlled Release* **2005**, *103* (3), 609-624.
- 90. Xu, T.; Xin, M.; Li, M.; Huang, H.; Zhou, S., Synthesis, characteristic and antibacterial activity of N, N, N-trimethyl chitosan and its carboxymethyl derivatives. *Carbohydr. Polym.* **2010**, *81* (4), 931-936.
- 91. Mourya, V.; Inamdar, N. N., Chitosan-modifications and applications: Opportunities galore. *React. Funct. Polym.* **2008**, *68* (6), 1013-1051.
- 92. Jia, Z.; Xu, W., Synthesis and antibacterial activities of quaternary ammonium salt of chitosan. *Carbohydr. Res.* **2001**, *333* (1), 1-6.
- 93. Rúnarsson, Ö. V.; Holappa, J.; Jónsdóttir, S.; Steinsson, H.; Másson, M., N-selective 'one pot'synthesis of highly N-substituted trimethyl chitosan (TMC). *Carbohydr. Polym.* **2008**, *74* (3), 740-744.

- 94. Sashiwa, H.; Kawasaki, N.; Nakayama, A.; Muraki, E.; Yajima, H.; Yamamori, N.; Ichinose, Y.; Sunamoto, J.; Aiba, S.-i., Chemical modification of chitosan. Part 15: Synthesis of novel chitosan derivatives by substitution of hydrophilic amine using N-carboxyethylchitosan ethyl ester as an intermediate. *Carbohydr. Res.* **2003**, *338* (6), 557-561.
- 95. Yang, Z.; Shang, Y.; Lu, Y.; Chen, Y.; Huang, X.; Chen, A.; Jiang, Y.; Gu, W.; Qian, X.; Yang, H., Flocculation properties of biodegradable amphoteric chitosan-based flocculants. *Chem. Eng. J.* **2011**, *172* (1), 287-295.
- 96. Zhang, X.; Geng, X.; Jiang, H.; Li, J.; Huang, J., Synthesis and characteristics of chitin and chitosan with the (2-hydroxy-3-trimethylammonium) propyl functionality, and evaluation of their antioxidant activity in vitro. *Carbohydr. Polym.* **2012**, *89* (2), 486-491.
- 97. Loubaki, E.; Ourevitch, M.; Sicsic, S., Chemical modification of chitosan by glycidyl trimethylammonium chloride. Characterization of modified chitosan by 13C-and 1H-NMR spectroscopy. *European Polymer Journal* **1991**, *27* (3), 311-317.
- 98. Cho, J.; Grant, J.; Piquette-Miller, M.; Allen, C., Synthesis and physicochemical and dynamic mechanical properties of a water-soluble chitosan derivative as a biomaterial. *Biomacromolecules* **2006**, 7 (10), 2845-2855.
- 99. Lim, S.-H.; Hudson, S. M., Synthesis and antimicrobial activity of a water-soluble chitosan derivative with a fiber-reactive group. *Carbohydr. Res.* **2004**, *339* (2), 313-319.
- 100. Jarvis, P.; Jefferson, B.; Gregory, J.; Parsons, S. A., A review of floc strength and breakage. *Water Res.* **2005**, *39* (14), 3121-3137.
- 101. Bean, E. L.; Campbell, S. J.; Anspach, F. R., Zeta potential measurements in the control of coagulation chemical doses. *Journal-American Water Works Association* **1964**, *56* (2), 214-227.
- 102. Krasner, S. W.; Croué, J. P.; Buffle, J.; Perdue, E. M., Three approaches for characterizing NOM. *Journal-American Water Works Association* **1996**, *88* (6), 66-79.
- 103. Martin-Mousset, B.; Croue, J.; Lefebvre, E.; Legube, B., Distribution and characterization of dissolved organic matter of surface waters. *Water Res.* **1997**, *31* (3), 541-553.
- 104. Sun, S.; Heitz, M. P.; Perez, S. A.; Colon, L. A.; Bruckenstein, S.; Bright, F. V., 6-Propionyl-2-(N, N-dimethylamino) naphthalene (PRODAN) revisited. *Applied spectroscopy* **1997**, *51* (9), 1316-1322.
- 105. Kucherak, O. A.; Didier, P.; Mély, Y.; Klymchenko, A. S., Fluorene analogues of prodan with superior fluorescence brightness and solvatochromism. *The Journal of Physical Chemistry Letters* **2010**, *I* (3), 616-620.
- 106. Prause, A.; Hechenbichler, M.; Schmidt, R. F.; Simon, M.; Prevost, S.; Cavalcanti, L. P.; Talmon, Y.; Laschewsky, A.; Gradzielski, M., Rheological Control of Aqueous Dispersions by Thermoresponsive BAB\* Copolymers of Different Architectures. *Macromolecules* **2022**, *56* (1), 104-121.
- 107. Angelico, R.; Colombo, C.; Di Iorio, E.; Brtnický, M.; Fojt, J.; Conte, P., Humic substances: From supramolecular aggregation to fractal conformation—Is there time for a new paradigm? *Applied Sciences* **2023**, *13* (4), 2236.

- 108. Gadad, P.; Nanny, M. A., Influence of cations on noncovalent interactions between 6-propionyl-2-dimethylaminonaphthalene (PRODAN) and dissolved fulvic and humic acids. *Water Res.* **2008**, *42* (19), 4818-4826.
- 109. Tsoularis, A.; Wallace, J., Analysis of logistic growth models. *Mathematical biosciences* **2002**, *179* (1), 21-55.
- 110. Duan, J.; Graham, N.; Wilson, F., Coagulation of humic acid by ferric chloride in saline (marine) water conditions. *Water Sci. Technol.* **2003**, *47* (1), 41-48.
- 111. Wei, J.; Gao, B.; Yue, Q.; Wang, Y.; Li, W.; Zhu, X., Comparison of coagulation behavior and floc structure characteristic of different polyferric-cationic polymer dual-coagulants in humic acid solution. *Water Res.* **2009**, *43* (3), 724-732.
- 112. Calero, J.; Ontiveros-Ortega, A.; Aranda, V.; Plaza, I., Humic acid adsorption and its role in colloidal-scale aggregation determined with the zeta potential, surface free energy and the extended-DLVO theory. *European Journal of Soil Science* **2017**, *68* (4), 491-503.
- 113. Gummel, J.; Sztucki, M.; Narayanan, T.; Gradzielski, M., Concentration dependent pathways in spontaneous self-assembly of unilamellar vesicles. *Soft matter* **2011**, *7* (12), 5731-5738.
- 114. Weiss, T. M.; Narayanan, T.; Gradzielski, M., Dynamics of spontaneous vesicle formation in fluorocarbon and hydrocarbon surfactant mixtures. *Langmuir* **2008**, *24* (8), 3759-3766.
- 115. Weiss, T.; Narayanan, T.; Wolf, C.; Gradzielski, M.; Panine, P.; Finet, S.; Helsby, W., Dynamics of the self-assembly of unilamellar vesicles. *Phys. Rev. Lett.* **2005**, *94* (3), 038303.
- 116. Yu, H.; Angelova, A.; Angelov, B.; Dyett, B.; Matthews, L.; Zhang, Y.; El Mohamad, M.; Cai, X.; Valimehr, S.; Drummond, C. J., Real-Time pH-Dependent Self-Assembly of Ionisable Lipids from COVID-19 Vaccines and In Situ Nucleic Acid Complexation. *Angew. Chem.* **2023**, *135* (35), e202304977.
- 117. Bekir, M.; Hörmann, A.; Brückner, C.; Hoffmann, I.; Prevost, S.; Gradzielski, M., Adsorption Kinetics of Oppositely Charged Hard and Soft Nanoparticles with Phospholipid Membranes. *Langmuir* **2021**, *37* (8), 2800-2809.
- 118. Josts, I.; Gao, Y.; Monteiro, D. C.; Niebling, S.; Nitsche, J.; Veith, K.; Gräwert, T. W.; Blanchet, C. E.; Schroer, M. A.; Huse, N., Structural kinetics of MsbA investigated by stopped-flow time-resolved small-angle X-ray scattering. *Structure* **2020**, *28* (3), 348-354. e3.
- 119. Fislage, M.; Brosens, E.; Deyaert, E.; Spilotros, A.; Pardon, E.; Loris, R.; Steyaert, J.; Garcia-Pino, A.; Versées, W., SAXS analysis of the tRNA-modifying enzyme complex MnmE/MnmG reveals a novel interaction mode and GTP-induced oligomerization. *Nucleic Acids Res.* **2014**, *42* (9), 5978-5992.
- 120. Kikhney, A. G.; Svergun, D. I., A practical guide to small angle X-ray scattering (SAXS) of flexible and intrinsically disordered proteins. *FEBS Lett.* **2015**, *589* (19), 2570-2577.
- 121. Takahashi, R.; Narayanan, T.; Yusa, S.-i.; Sato, T., Formation kinetics of polymer vesicles from spherical and cylindrical micelles bearing the polyelectrolyte complex core studied by time-resolved USAXS and SAXS. *Macromolecules* **2022**, *55* (2), 684-695.
- 122. Takahashi, R.; Narayanan, T.; Yusa, S.-i.; Sato, T., Kinetics of morphological transition between cylindrical and spherical micelles in a mixture of anionic–neutral and cationic–neutral

block copolymers studied by time-resolved SAXS and USAXS. *Macromolecules* **2018**, *51* (10), 3654-3662.

- 123. Takahashi, R.; Sato, T.; Terao, K.; Yusa, S.-i., Intermolecular interactions and self-assembly in aqueous solution of a mixture of anionic–neutral and cationic–neutral block copolymers. *Macromolecules* **2015**, *48* (19), 7222-7229.
- 124. Takahashi, R.; Sato, T.; Terao, K.; Yusa, S.-i., Reversible vesicle–spherical micelle transition in a polyion complex micellar system induced by changing the mixing ratio of copolymer components. *Macromolecules* **2016**, *49* (8), 3091-3099.
- 125. Takahashi, R.; Narayanan, T.; Sato, T., Growth kinetics of polyelectrolyte complexes formed from oppositely-charged homopolymers studied by time-resolved ultra-small-angle X-ray scattering. *The Journal of Physical Chemistry Letters* **2017**, *8* (4), 737-741.
- 126. Tolaimate, A.; Desbrieres, J.; Rhazi, M.; Alagui, A.; Vincendon, M.; Vottero, P., On the influence of deacetylation process on the physicochemical characteristics of chitosan from squid chitin. *Polymer* **2000**, *41* (7), 2463-2469.